Jefferson Lab High Precision Proton Radius Measurement Experiment: PRad

Xinzhan Bai

Shandong, China

A Dissertation Presented to the Graduate Faculty

of the University of Virginia in Candidacy for the Degree of

Doctor of Philosophy

Department of Physics

University of Virginia

April, 2020

Abstract

Proton is not a point-like particle; it has a finite size and an internal structure. The proton charge radius is usually measured through two different methods: using spectroscopy of hydrogen atoms, or through electron-proton ($e-p$) elastic scattering at low momentum transfer. In 2010, Phol et al [1] published a new measurement for proton charge radius obtained using the spectroscopy method from muonic hydrogen atoms. An ordinary hydrogen (H) atom is a bound state of an electron orbiting a proton. Likewise, a muonic hydrogen atom has a muon orbiting a proton. Since a muon has 200 times more mass than an electron, resulting in a much smaller orbiting radius, its orbit is much more sensitive to the proton charge distribution in space than the electron's of an ordinary H-atom. Thus, the measurement from muonic hydrogen provides a 10 times more precise result than the previous methods. The radius from the muonic hydrogen measurement reported in [1] was significantly smaller than all the previous measurements combined. The difference between the two values is more than 5σ away. This large discrepancy triggered the so-called Proton Charge Radius Crisis. In order to investigate the proton charge radius, the PRad experiment was performed in experimental hall B at Jefferson Lab in June, 2016. PRad experiment used a novel $e-p$ elastic scattering method. Considering the limitations introduced by magnetic spectrometers in all previous $e-p$ elastic scattering experiments, PRad adopted a magnetic-spectrometer-free, calorimetric method for electron detection. Its detector system consisted of a high energy resolution hybrid calorimeter, closely installed around the beam line, and a pair of large area, high spatial resolution GEM detectors, which improved the experiment position resolution by a factor of 20. The absence of magnetic spectrometers enabled PRad to reach very forward electron scattering angles, and allowed collection of data in a very small momentum transfer region ($Q^2 = 2 \times 10^{-4} - 6 \times 10^{-2}$ $(\mathrm{GeV}/c)^2$), which had never been reached before. The PRad experiment used a windowless gas flow hydrogen target to remove the background from target cell walls, and a vacuum box to further reduce the background

from the beam line. To better control the uncertainties, the $e-p$ elastic cross section was normalized to the well-known Møller (electron-electron elastic scattering) cross section; the Møller scattered electrons were collected simultaneously with the $e-p$ electrons within the same detector acceptance for both beam energy settings used for the experiment (1.1 GeV and 2.2 GeV). The result from PRad experiment is $r_p = 0.833 \pm 0.007_{stat.} \pm 0.012_{syst.}\ fm$, in agreement with the muonic hydrogen result within the experimental uncertainty.

Acknowledgments

First and foremost, I would like to thank my advisor Prof. Nilanga Liyanage for his guidance, support, care, knowledge and enthusiasm. Pursuing a PhD in physics is a long journey filled with joyful and stressful moments. I cannot imagine how things would turn without his support. I deeply appreciate his optimistic attitude when facing challenging situations. Those obstacles we encountered in developing various most innovative detectors could not be conquered without his optimism and knowledge.

I would like to thank Prof. Xiaochao Zheng for her enlightening, concise conversations with me, for her wonderful lectures in elementary particles, for her spending time reading through the whole thesis, for her dinners with many friends during holidays which brought me the feeling of family, and for her support.

Then I would like to thank the PRad collaboration especially the senior members: Dr. Ashot Gasparian, Dr. Haiyan Gao, Dr. Mahbub Khandaker, Dr. Dipangkar Dutta, Dr. Eugene Pasyuk for their valuable suggestions throughout the analysis, and for all the questions from them that pushed the analysis becoming better and better.

I would like to thank the members in my group: Dr. Kondo Gnanvo, Dr. Huong Nguyen, Dr. Vladimir Nelyubin, Dr. Danning Di, Siyu Jian, John Matter, John Boyd, Anuruddha Rathnayake. I always enjoyed being around them. They gave me countless help and brought me great joy in this journey.

I would like to thank Dr. Chao Peng, Dr. Weizhi Xiong, Dr. Li Ye, for their priceless help on the analysis, for all the time we spent together preparing the experiment and analyzing the experimental data.

I would like to thank Dr. Chao Gu, Dr. Xuefei Yan, Dr. Maxime Levillain, Dr. Krishna Adhikari, Dr. Aleksandr Glamazdin for their important contributions to this experiment. Without them, I am sure the analysis will take much longer.

I would also like to thank Prof. Blaine Norum, Prof. Roger Chevalier for being my committee members in such a stressful COVID-19 pandemic time.

I would like to thank Dr. Xiaomei Li. Without her guidance and encouragement, I couldn't begin this fruitful journey.

Lastly, I would like to take this chance to show my deepest appreciation to my parents and my sisters for their understanding, love, and support. I especially want to thank my elder sister, who took care of my parents for me when I am not home.

Contents

List of Figures

List of Tables

Chapter 1

Introduction

The search for the fundamental constituents of the universe and the study for their properties has always been an important research interest in physics. In 1911, Rutherford discovered the atomic nucleus through a scattering experiment [33]. In the experiment, a beam of α (^{4}He) particles was aimed at a thin Gold foil. Most of the α particles passed through the foil without deflecting from their original direction, while a few particles were deflected by large angles. Rutherford concluded that a dense, small and positively charged nucleus must exist inside an atom to cause the deflection. Today we know that the nucleus consists of protons and neurons, collectively known as nucleons. The nucleons are the building blocks of visible matter in the universe; more than 99.9% of the visible matter is made of protons and neutrons.

Protons and neutrons are made of elementary particles called quarks and gluons. Electrons and muons are elementary particles by themselves. Elementary particles are described by the standard model, as shown in Fig. 1-1. In the standard model, there are three generations of quarks and leptons, governed by four interactions: strong, weak, gravitational and electromagnetic. Different interactions are mediated by different mesons (force carriers): gluons are the mediators for strong interaction, photons for electromagnetic, W and Z bosons for weak interaction. Except for the gravitational interaction, the three interactions described by the standard model can be determined by the rotation symmetry of the corresponding Lagrangian in an abstract space defined by the gauge group. A classical analogy for this is the rotation of

the Lagrangian in ordinary space: the symmetry of the rotation leads to the angular momentum conservation. The gauge transformation not only predicts conservation laws, but also predicts the existence of gauge bosons (spin 1 vector particles) and the existence of coupling constants between them and fermions [34]. However, it is found that the mass term of the gauge bosons breaks the symmetry of rotation. While the mass term of scalar particles (spin 0) keeps the symmetry. This mechanism is used to give mass to gauge bosons and fermions, which acquire mass through absorbing scalar bosons. This is called the Higgs mechanism, and the scalar boson is called the Higgs boson, discovered at CERN [35] in 2012. The Higgs mechanism does not work for neutrinos, the origin of neutrino mass is still under investigation.

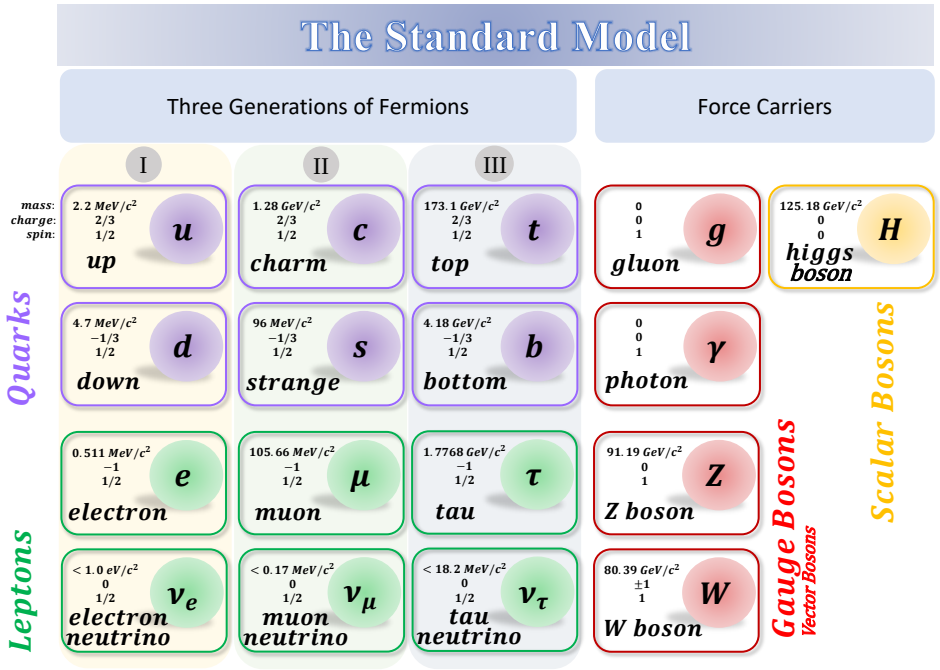

Figure 1-1: Elementary particles in the standard model.

The discovery of the Higgs boson proved the consistency of the standard model. In fact, the standard model has been very successful in describing and predicting the phenomena from all interactions except gravitational interaction. In the standard model, electrons, muons and τ leptons all respond to the same interactions. This is known as the "lepton universality".

In 1950s, electron proton (ep) scattering experiments at Stanford [5] found that proton is not a point-like elementary particle, but an extended particle with a radius of around 0.8 fm, as shown in Fig. 1-2. In the plot $k = (E_e, \boldsymbol{k})$ and $p = (E_p, \boldsymbol{p})$ are the

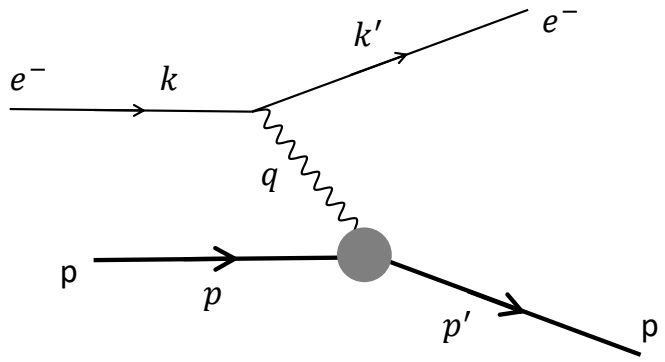

Figure 1-2: Feynman diagram of elastic electron-proton scattering.

four-momenta of the incoming electron and proton; k' and p' are the four-momenta of the scattered particles; q is the four-momentum of the exchanged virtual photon given by:

$$q = k - k' = p' - p. \tag{1.1}$$

The proton charge radius soon became an important physics quantity. Theories were developed to interpret the structure of the proton. A classical interpretation of the proton is that it is like a blob with a charge distribution $\rho(\boldsymbol{r})$, and the proton charge radius is defined as:

$$\langle r_p^2 \rangle \equiv \int \rho(\boldsymbol{r}) \boldsymbol{r}^2 d^3\boldsymbol{r}. \tag{1.2}$$

One can do a Fourier transform for the charge distribution function $\rho(\boldsymbol{r})$, and obtain the corresponding function, the form factor, in the momentum space:

$$G_E^p(Q^2) = F(\boldsymbol{q}^2) = \int \rho(\boldsymbol{r}) e^{i\boldsymbol{q}\cdot\boldsymbol{r}} d^3\boldsymbol{r}, \tag{1.3}$$

where $Q^2 = -q^2$ is the four momentum transfer squared. In the Breit frame $Q^2 = \boldsymbol{q}^2$, as shown in Fig. 1-3; $G_E^p(Q^2)$ is called the proton electric form factor. When q is

small, the above formula can be expressed by a series expansion over $\boldsymbol{q} \cdot \boldsymbol{r}$:

$$F(\boldsymbol{q}^2) = \int \rho(\boldsymbol{r})(1 + i\boldsymbol{q} \cdot \boldsymbol{r} - \frac{1}{2}(\boldsymbol{q} \cdot \boldsymbol{r})^2 + \cdots)d^3\boldsymbol{r}. \tag{1.4}$$

From the above equation, the proton charge radius can be obtained from the slope of G_E^p as Q^2 approaches zero:

$$\langle r_p^2 \rangle = -6\frac{dG_E^p(Q^2)}{dQ^2}\bigg|_{Q^2=0}. \tag{1.5}$$

In relativistic situation, the interaction of ep scattering is described by QED (Quan-

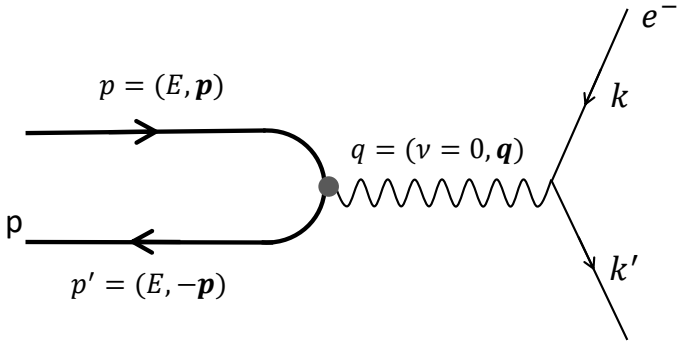

Figure 1-3: The ep elastic scattering in the Breit frame. In this frame, no energy is transferred: $\nu = 0$; the proton bounces back with the same energy and momentum magnitude after absorbing the virtual photon, the momentum direction is flipped.

tum electrodynamics), the form factor can be defined through a construction of a Lorentz Invariant matrix element for the proton line, as shown by Eq. (8.15) in [36].

The proton electric form factor is usually extracted from the differential cross section of ep scattering. Besides the ep scattering method, the proton charge radius can also be measured using hydrogen spectroscopy method in atomic physics, where r_p is an input parameter for the calculation of the transition frequency between two energy levels in a hydrogen atom. One can extract the proton charge radius by measuring the energy difference between the two energy levels (such as $2S_{1/2} - 2P_{1/2}$). Prior to 2010, the radius results from the two methods were consistent, with both values around 0.88 fm.

In 2010, Pohl et al [1] published results from a new measurement for proton charge radius using muonic hydrogen spectroscopy method. A normal hydrogen is a bound state of an electron orbiting a proton, while a muonic hydrogen has the electron replaced by a muon. Since a muon is more than 200 times heavier than an electron, its orbit is much closer to the proton, and the spectroscopy result is highly sensitive to the proton charge radius. The result was:

$$r_p = 0.84184 \pm 0.00067 \ fm, \tag{1.6}$$

with an uncertainty smaller than 0.1%, more than 20 times smaller than the uncertainties from normal hydrogen spectroscopy. The discrepancy between muonic hydrogen result and the combined result from all electron-proton measurements (CODATA-2014) [4] including both spectroscopy and *ep* scattering is more than 5σ away, where σ is the uncertainty for the combined previous result. This discrepancy led to the so called "proton charge radius puzzle".

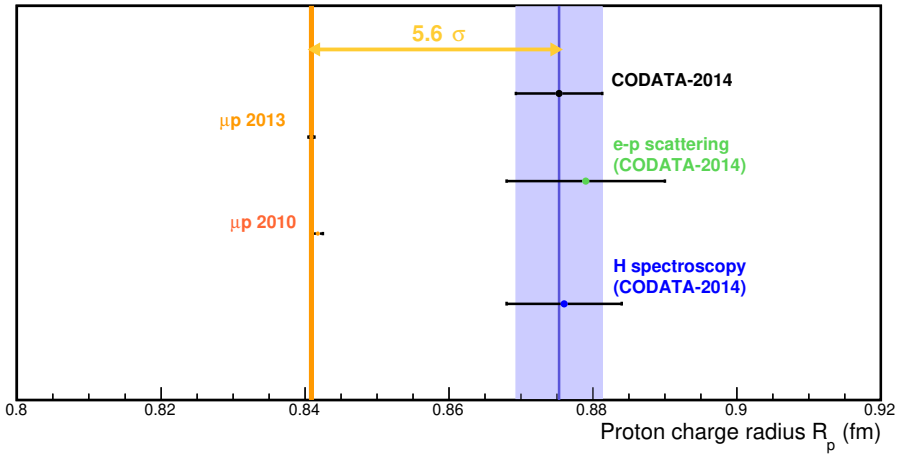

Figure 1-4: The proton radius puzzle. This plot was produced using data from [1], [2] and the world data compilations [3] [4].

The discrepancy between the muonic hydrogen and normal hydrogen results has been intensively studied. The bound-state QED calculation for muonic hydrogen spectroscopy [37] and normal hydrogen spectroscopy [38] have both been reviewed thoroughly, but no evidence could be found to explain the large discrepancy.

In order to resolve the different proton radii from muonic hydrogen and normal hydrogen, a violation to the lepton universality was also proposed, which suggested a new particle with stronger coupling constant mediating the interaction between muons and protons [39], indicating a fifth interaction beyond the standard model.

In order to investigate the proton charge radius puzzle, various experiments were carried out. Some of the completed experiments have produced inconsistent results. For example, a measurement in 2017 from normal hydrogen spectroscopy [40] gave a result $r_p = 0.8335(95)\ fm$, which is consistent with the muonic hydrogen result; while in 2018, a result of $r_p = 0.877(13)\ fm$ [41] from the normal hydrogen spectroscopy was published, which agrees with previous normal hydrogen spectroscopy. These contradictions make the subject even more interesting.

The Proton charge Radius (PRad) experiment was proposed at Jefferson Lab in 2011 in order to address the proton radius puzzle. The goal for PRad was to measure the proton charge radius using ep elastic scattering with high precision. Compared with previous ep elastic scattering experiments, PRad used a magnetic-spectrometer-free calorimetry method. This allowed PRad to reach very forward scattering angles. The Q^2 coverage for PRad was around $2.1 \times 10^{-4} - 6 \times 10^{-2}$ $(\mathrm{GeV}/c)^2$, which is unprecedentedly low. The form factor data in low Q^2 region is crucial in the radius extraction. A novel windowless gas flow hydrogen target was used, enabling the electron beam to pass through two orifices on the target cell without hitting anything but the target gas. The absence of target cell windows removed possible background from target cell walls, a major background source for previous ep scattering experiments. A two-stage vacuum window was installed between the target and detectors to reduce the background from the beam line. The energy measurement of the scattered electrons was done by a hybrid calorimeter (HyCal) with high energy resolution. A pair of Gas Electron Multiplier (GEM) detectors was designed and built in the detector lab at the University of Virginia to improve the position resolution of the scattered electrons. These GEM detectors improved the experimental position resolution by at least 20 times.

In this dissertation, the physics background, the introduction to form factors

and cross sections will be provided in Chapter 2. The detailed introduction to the PRad experimental setup will be given in Chapter 3. Chapter 4 will be dedicated to GEM detectors, including the construction, commission and performance in PRad experiment. The details of the data analysis, the cross section and the form factor extraction will be given in Chapter 5. Lastly, the radius extraction and a conclusion will be given in Chapter 6.

Chapter 2

Formalism for Lepton Scattering

2.1 Overview

The general method to study the structure and the interactions of sub-atomic particles is through scattering. Almost everything we know about sub-atomic physics has been discovered through scattering experiments. Starting from Rutherford's experiment in 1911 [33]; through the scattering of α particles off Au atoms, Rutherford discovered the small, dense nucleus inside an atom for the first time; all the way to the proton-proton collision experiment in 2012 [35] at CERN where the Higgs boson was discovered.

Scattering experiments also provided a powerful tool to investigate the structure of the nucleon. In 1950s [5], Hofstadter studied the proton charge radius using electron proton elastic scattering, and extracted the size of proton $r_p \approx 0.8\ fm$, see Fig. 2-1. Extensive, similar works using different techniques followed at several other facilities, such as MAMI[42], Jefferson Lab[43] [44] [45] [6], DESY [46] [47], with improved electron beam luminosity, polarization techniques for electron beam and nucleon target, recoil polarimetry, and large detector acceptance. The electromagnetic form factors for nucleons have been intensively investigated at various Q^2 range, where Q^2 is the 4-momentum transfer squared between electron and nucleon during scattering. Before the PRad experiment in 2016, the lowest Q^2 for e-p scattering reached 0.004 GeV^2 [48].

Nucleons are made of quarks and gluons, the interaction that quarks and gluons respond to is strong interaction, which is described by the Quantum Chromodynamics (QCD) theory. QCD has two features, asymptotic freedom and confinement. Asymptotic freedom means the strong interaction coupling constant becomes smaller when the energy involved becomes higher; confinement means that isolated quarks and gluons do not exist, quarks exist only in the form of hadrons. Due to the first feature, QCD theory has a very good agreement with high energy scattering experiment, where perturbation theory applies because the strong coupling constant is weak. The knowledge on QCD in the confinement region with large coupling constant is very limited. To better study QCD using the nucleon structure, a precise understanding of the nucleon ground state properties, such as the charge radius, is also required.

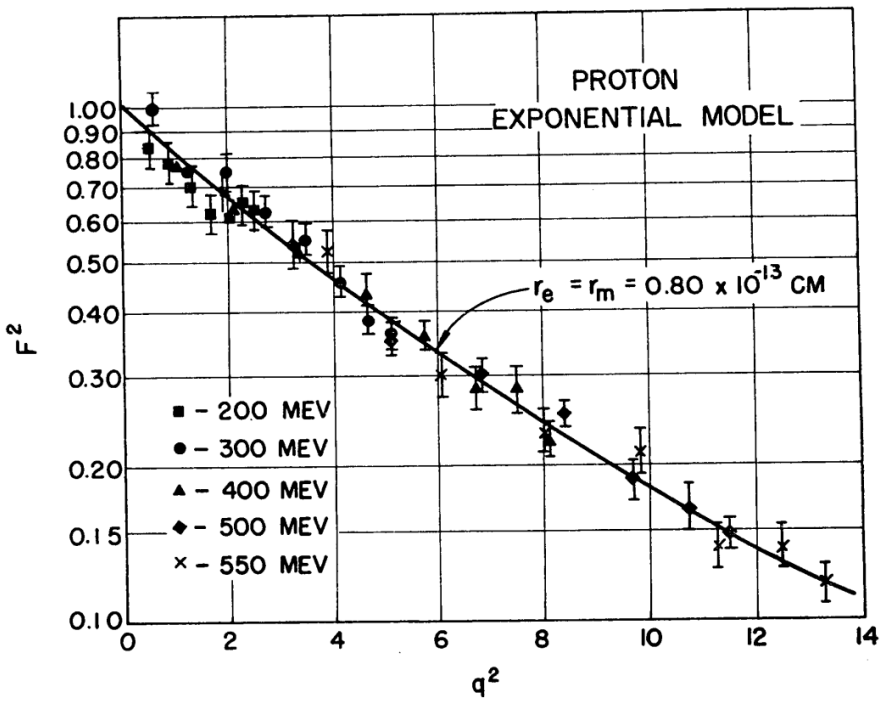

Figure 2-1: A comparison of proton form factors [5] between the proton exponential model with $r_p = 0.8\ fm$ and the experimental points. q^2 is given in the unit of $10^{26}\ cm^{-2}$, where $10^{26}\ cm^{-2} = 3.88 \times 10^{-3}\ (\mathrm{GeV}/c)^2$.

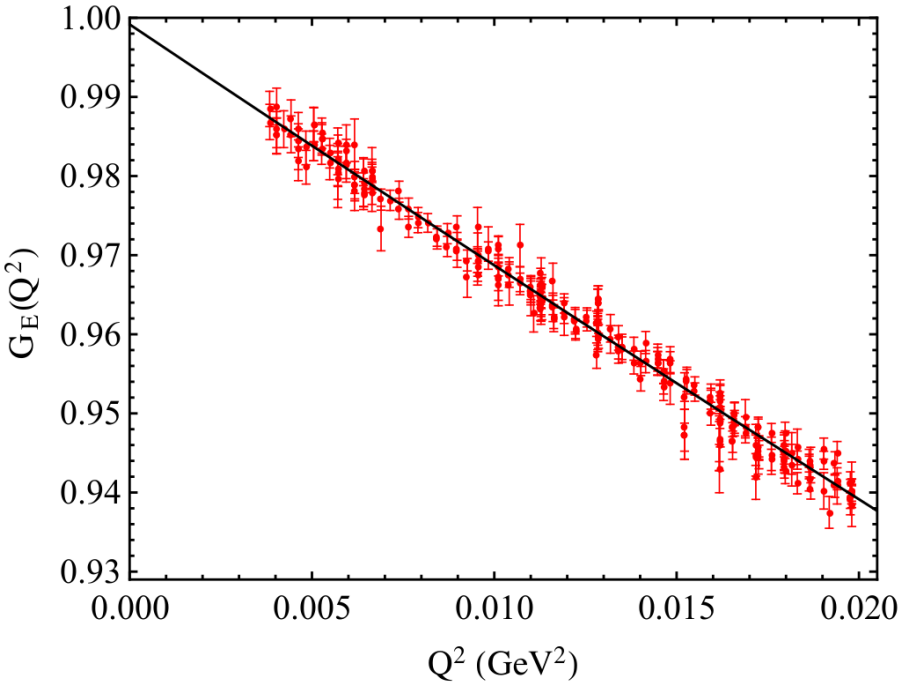

Figure 2-2: Mainz data (2010) on proton electric form factor at low $Q^2 = (0.004 - 0.02)$ $(\mathrm{GeV}/c)^2$. The black line is a linear plus quadratic fit using model: $G_E(Q^2) = c_1(1 + c_2Q^2 + c_3Q^4)$ [6].

2.2 Scattering Cross Sections

In a scattering process, one important quantity is the cross section [49] defined as the number of interactions per unit time per target particle over incident flux, which means the probability that a process takes place in a collision of two particles. In this section, we will describe the tools that we need to calculate cross sections, and we will use these tools to calculate Møller (electron electron scattering) and $e-p$ (electron proton scattering) elastic scattering cross sections.

2.2.1 Recapitulation of Fermi's Golden Rule

In quantum mechanics, particle scattering or decay corresponds to transitions between different states, the transition rate is obtained through Fermi's Golden rule [50]. In non-relativistic approximation, suppose we have a system with Hamiltonian H_0 and a corresponding complete set of states: $S = \{|1\rangle, |2\rangle, ..., |n\rangle, ..., |N\rangle\}$, where:

$$H_0 |n\rangle = E_n |n\rangle . \tag{2.1}$$

S constructs the so-called Hilbert space, where wave function of the system in this space can be expressed as:

$$\psi = \sum_n c_n |n\rangle , \tag{2.2}$$

where $|c_n|^2$ means the probability of finding the system stays in $|n\rangle$ state.

Initially, the system stays at $|i\rangle \in S$, if we apply an interaction Hamiltonian H_I on the system:

$$(H_0 + H_I)\psi = i\frac{d}{dt}\psi,$$

(here we use natural units $\hbar = c = 1$), the system will transit from initial state $|i\rangle$ to some other state $|f\rangle \in S$. Using the completeness of S and adding back the time dependence:

$$(H_0 + H_I) \sum_n c_n |n\rangle e^{-iE_n t} = i\frac{d}{dt} \sum_n c_n |n\rangle e^{-iE_n t}, \tag{2.3}$$

where c_n is time dependent $c_n = c_n(t)$, The transition amplitude for $|i\rangle \to |f\rangle$ can be

obtained by multiplying $\langle f|$ on both sides of the above equation:

$$\langle f| (H_0 + H_I) \sum_n c_n |n\rangle e^{-iE_n t} = \langle f| i\frac{d}{dt} \sum_n c_n |n\rangle e^{-iE_n t}, \tag{2.4}$$

which can be further expanded into:

$$\sum_n c_n \langle f| H_I |n\rangle e^{-iE_n t} + \sum_n c_n \langle f| H_0 |n\rangle e^{-iE_n t} = i\sum_n \langle f| \frac{dc_n}{dt} |n\rangle e^{-iE_n t} + i\sum_n \langle f| c_n |n\rangle \frac{d}{dt} e^{-iE_n t},$$

using the orthogonality $\langle f|n\rangle = \delta_{nf}$, the second term on both sides cancel out, and we get:

$$\sum_n c_n \langle f| H_I |n\rangle e^{-iE_n t} = i\sum_n \langle f| \frac{dc_n}{dt} |n\rangle e^{-iE_n t} = i\frac{dc_f}{dt} e^{-iE_f t}. \tag{2.5}$$

Initially, system stays at $|i\rangle$[1], in first order approximation $c_n(t) = \delta_{ni}$, so

$$\frac{dc_f}{dt} = -i \langle f| H_I |i\rangle e^{i(E_f - E_i)t}, \tag{2.6}$$

$\langle f| H_I |i\rangle$ is called transition matrix element, with its dimension being energy. It is symbolized by $T_{fi} = \langle f| H_I |i\rangle$. From Eq. (2.6), the transition at time T:

$$c_f(T) = -i \int_0^T T_{fi} e^{i(E_f - E_i)t} dt. \tag{2.7}$$

For scattering or decay, T_{fi} is usually time independent. The probability of a transition:

$$P_{fi} = |c_f(T)|^2 = |T_{fi}|^2 \int_0^T \int_0^T e^{i(E_f - E_i)t} e^{-i(E_f - E_i)t'} dt dt', \tag{2.8}$$

[1]Regarding this, there are two possible interpretations, the first interpretation for things down to quantum level is that we cannot determine the specific state for a single particle, instead we are describing an ensemble, "system stays at $|i\rangle$" means the majority part of the ensemble are in $|i\rangle$ state, the minor rest stay at other states; the second interpretation goes as system/particle has a probability for staying at one specific state, "system stay at $|i\rangle$" means if wave function collapsed, most probably we will find it in $|i\rangle$ state, but still has small probability system could collapse at other state. The math process for both interpretations are the same, in first order approximation: $c_n(0) = \delta_{ni}$ for both.

and the transition rate:

$$d\Gamma_{fi} = \frac{P_{fi}}{T} = |T_{fi}|^2 \frac{1}{T} \int_0^T \int_0^T e^{i(E_f - E_i)t} e^{-i(E_f - E_i)t'} dt dt', \tag{2.9}$$

using the inverse δ function Fourier transform[2]:

$$\delta(x) = \frac{1}{2\pi} \int_{-\infty}^{\infty} e^{ikx} dk,$$

the integration over dt' in Eq. (2.9) can be replaced by the δ function,

$$d\Gamma_{fi} = |T_{fi}|^2 \int_{-T/2}^{T/2} \frac{2\pi}{T} e^{i(E_f - E_i)t} \delta(E_f - E_i) dt. \tag{2.10}$$

In the above equation, the integral part ensures $E_f = E_i$. If there's only one possible final state $|f\rangle$, then transition rate will be $2\pi|T_{fi}|^2$. In the realistic scenario, there can be multiple states in energy E_f, for example in the phase space, states lie in the same shell all have the same E_f. Thus, a density of state is introduced:

$$\rho(E_f) = \left| \frac{dn}{dE} \right|_{E=E_f}, \tag{2.11}$$

and the transition rate:

$$\Gamma_{fi} = 2\pi |T_{fi}|^2 \rho(E_f). \tag{2.12}$$

Up to here we have given a detailed derivation of Eq. (2.12), named the Fermi's Golden rule, which we will frequently refer to in the following sections. Cross section calculation is usually based on calculating T_{fi} and $\rho(E_f)$.

The density of state (Eq. (2.11)) can be expressed using the δ function,

$$\rho(E_f) = \int \left| \frac{dn}{dE} \right| \delta(E - E_f) dE = \int \delta(E - E_f) dn,$$

[2]Fourier transform for $\delta(x)$: $F(k) = \int \delta(x) e^{-ikx} dk = 1$, so the opposite direction leads to a delta function in Fourier series form: $\delta(x) = \frac{1}{2\pi} \int e^{ikx} dk$

leading to a more concrete Fermi's Golden rule:

$$\Gamma_{fi} = 2\pi |T_{fi}|^2 \int \delta(E - E_f) dn. \tag{2.13}$$

In phase space, following [50], the unit volume occupied by a single state is $(2\pi)^3/V$, with V the total volume of the system. Usually wave functions are normalized over V, letting $V = 1$ leads to:

$$dn = 4\pi p^2 \frac{dp}{(2\pi)^3} = \frac{d\boldsymbol{p}}{(2\pi)^3}.$$

For an N particle system, we have $N - 1$ (momentum conservation) independent variables:

$$dn = \prod_j^{N-1} \frac{d\boldsymbol{p_j}}{(2\pi)^3}.$$

A more general form is:

$$dn = (2\pi)^3 \delta(\sum_j^N \boldsymbol{p_j} - \boldsymbol{p_f}) \prod_j^N \frac{d\boldsymbol{p_j}}{(2\pi)^3}.$$

Now Eq. (2.13) becomes:

$$\Gamma_{fi} = \int |T_{fi}|^2 2\pi \delta(E - E_f)(2\pi)^3 \delta(\sum_j^N \boldsymbol{p_j} - \boldsymbol{p_f}) \prod_j^N \frac{d\boldsymbol{p_j}}{(2\pi)^3}. \tag{2.14}$$

In Eq. (2.14), T_{fi} is not Lorentz invariant, because wave functions are normalized by V, and V is not Lorentz invariant due to length contraction. The Lorentz invariant form would be wave functions being normalized by $2E \times V$. The Lorentz invariant wave function $\psi' = \sqrt{2E}\psi$ leads to the Lorentz invariant transition matrix element:

$$M_{fi} = \langle \psi'_f | H_I | \psi'_i \rangle = \prod_j^N \sqrt{2E_j 2E_f} T_{fi}.$$

Here, i, f represents all particles in the initial and final states respectively, and the

Lorentz invariant form of Eq. (2.14) is:

$$\Gamma_{fi} = \frac{1}{2E_f} \int |M_{fi}|^2 2\pi\delta(E - E_f)(2\pi)^3\delta(\sum_j^N \boldsymbol{p_j} - \boldsymbol{p_f}) \prod_j^N \frac{d\boldsymbol{p_j}}{(2\pi)^3 2E_j}. \tag{2.15}$$

2.2.2 Differential Cross Sections

Cross section is defined as the number of interactions per unit time per target particle over incident flux. Consider a scattering system of $a + b \to 1 + 2$ [7] in CM (Center of Mass) frame, in this case the incident flux would be $v_a + v_b$ if we assume particle density $n_a = 1$. Using the transition rate Eq. (2.15) divided by the incident flux, the cross section would be:

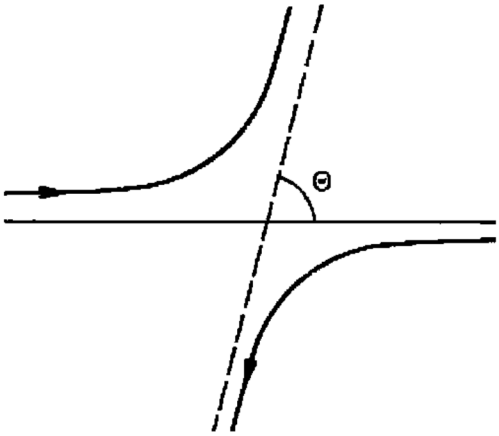

Figure 2-3: Scattering of two particles in CM frame [7].

$$\sigma = \frac{1}{2E_a 2E_b(v_a + v_b)} \int |M_{fi}|^2 2\pi\delta(E_a + E_b - E_1 - E_2)\times \\ (2\pi)^3\delta(\boldsymbol{p_a} + \boldsymbol{p_b} - \boldsymbol{p_1} - \boldsymbol{p_2}) \frac{d\boldsymbol{p_1}}{(2\pi)^3 2E_1} \frac{d\boldsymbol{p_2}}{(2\pi)^3 2E_2}, \tag{2.16}$$

where $F = 2E_a 2E_b(v_a + v_b)$ is called Lorentz invariant flux (see Appendix A.1),

$$F = 4E_a E_b(\frac{p_a}{E_a} + \frac{p_b}{E_b}) = 4\sqrt{(p_a \cdot p_b)^2 - m_a^2 m_b^2}.$$

Equation (2.16) is Lorentz invariant. It is easier to solve it in CM frame, where

$$\boldsymbol{p_a} + \boldsymbol{p_b} = \boldsymbol{p_1} + \boldsymbol{p_2} = 0.$$

Using the Mandelstam variable s, defined as:

$$s = (p_a + p_b)^2 = (E_a + E_b)^2,$$

with $p_a = (E_a, \boldsymbol{p_a})$ the 4-momentum, Eq. (2.16) becomes[3]:

$$\begin{aligned}
\sigma &= \frac{(2\pi)^4}{F} \int |M_{fi}|^2 \delta(\sqrt{s} - E_1 - E_2) \delta(\boldsymbol{p_1} + \boldsymbol{p_2}) \frac{d\boldsymbol{p_1}}{(2\pi)^3 2E_1} \frac{d\boldsymbol{p_2}}{(2\pi)^3 2E_2} \\
&= \frac{1}{4\pi^2 F} \int |M_{fi}|^2 \delta(\sqrt{s} - E_1 - E_2) \delta(\boldsymbol{p_1} + \boldsymbol{p_2}) \frac{d\boldsymbol{p_1}}{2E_1} \frac{d\boldsymbol{p_2}}{2E_2} \\
&= \frac{1}{4\pi^2 F} \frac{\mathrm{p}^\ddagger}{4\sqrt{s}} \int |M_{fi}|^2 d\Omega,
\end{aligned}$$

where we use p for $|\boldsymbol{p}|$, italic p for 4-momentum $(E, \boldsymbol{p})$, and $\mathrm{p}^\ddagger$ satisfies $\sqrt{s} - \sqrt{m_1^2 + \mathrm{p}^{\ddagger 2}} - \sqrt{m_2^2 + \mathrm{p}^{\ddagger 2}} = 0$.

In the CM frame:

$$F = 4E_a E_b (v_a + v_b) = 4E_a E_b (\mathrm{p}_i^\star / E_a + \mathrm{p}_i^\star / E_b) = 4\mathrm{p}_i^\star \sqrt{s},$$

and $\mathrm{p}^\ddagger = \mathrm{p}_f^\star$, where $\mathrm{p}_f^\star$ is the final state particle momentum in the CM frame, so:

$$\begin{aligned}
\sigma &= \frac{1}{4\pi^2 F} \frac{\mathrm{p}^\ddagger}{4\sqrt{s}} \int |M_{fi}|^2 d\Omega \\
&= \frac{1}{64\pi^2 s} \frac{\mathrm{p}_f^\star}{\mathrm{p}_i^\star} \int |M_{fi}|^2 d\Omega^\star,
\end{aligned} \tag{2.17}$$

in which $\star$ represents the CM frame.

[3]Here, relation $\int g(p)\delta(f(p))dp = g(p^\ddagger)\left|\frac{df(p)}{dp}\right|^{-1}_{p^\ddagger}$ was used, where $p^\ddagger$ satisfies $f(p^\ddagger) = 0$.

2.2.3 Coordinate Transform

Equation (2.17) is in the CM frame, in order to compare calculations with experimental measurements, we need to express it in the lab frame. The approach here is to re-write it in the Lorentz invariant form, which means it applies in any inertial coordinate system (the other approach is multiplying the Jacobian factor [51] to Eq. (2.17) for transformation between two moving frames). Following [50], we use the Lorentz invariant Mandelstam variable t, defined as:

$$t = (p_1 - p_3)^2,$$

For a scattering system $1 + 2 \to 3 + 4$, in CM frame:

$$t = (p_1^\star - p_3^\star)^2 \tag{2.18}$$

$$\Rightarrow t = m_1^2 + m_3^2 - 2p_1^\star p_3^\star \tag{2.19}$$

$$\Rightarrow t = m_1^2 + m_3^2 - 2E_1^\star E_3^\star + 2\mathrm{p}_1^\star \mathrm{p}_3^\star \cos\theta^\star. \tag{2.20}$$

In CM frame, E_1, E_3, p_1 and p_3 are already known by momentum and energy conservation, so

$$dt = 2\mathrm{p}_1^\star \mathrm{p}_3^\star d(\cos\theta^\star). \tag{2.21}$$

In CM frame, clearly, $\mathrm{p}_i^\star = \mathrm{p}_1^\star$ and $\mathrm{p}_f^\star = \mathrm{p}_3^\star$ so,

$$dt = 2\mathrm{p}_i^\star \mathrm{p}_f^\star d(\cos\theta^\star), \tag{2.22}$$

using

$$d\Omega^\star = d(\cos\theta^\star) d\phi^\star, \tag{2.23}$$

thus, $d\Omega^\star$ can be expressed in Lorentz invariant form using Mandelstam variable t:

$$d\Omega^\star = \frac{dt}{2\mathrm{p}_i^\star \mathrm{p}_f^\star} d\phi^\star. \tag{2.24}$$

and since scattering system is ϕ symmetric, $d\phi^\star$ can be integrated out:

$$\int d\phi^\star = 2\pi. \tag{2.25}$$

Substituting Eq. (2.24) into Eq. (2.17) cancels out $\mathrm{p}_f^\star$, then we need to write $|\mathrm{p}_i^\star|^2$ into Lorentz invariant form. Similarly, we use Mandelstam variable s: for scattering system $1+2 \to 3+4$, in CM frame $p_1^\star = (E_1^\star,\ \mathrm{p}_i^\star)$ and $p_2^\star = (E_2^\star,\ -\mathrm{p}_i^\star)$,

$$p_1^\star \cdot p_2^\star = E_1^\star E_2^\star + \mathrm{p}_i^{\star 2},$$

$$\mathrm{p}_i^{\star 2} = p_1^\star \cdot p_2^\star - E_1^\star E_2^\star,$$

considering that:

$$s = (p_1^\star + p_1^\star)^2,$$

$$\Rightarrow s = m_1^2 + m_2^2 + 2p_1^\star \cdot p_2^\star,$$

$$\Rightarrow p_1^\star \cdot p_2^\star = (s - m_1^2 - m_2^2)/2,$$

and $E_1^{\star 2} = m_1^2 + \mathrm{p}_i^{\star 2}$, $E_2^{\star 2} = m_2^2 + \mathrm{p}_i^{\star 2}$ so,

$$\mathrm{p}_i^{\star 2} = \frac{s - m_a^2 - m_b^2}{2} - \sqrt{m_a^2 + \mathrm{p}_i^{\star 2}}\sqrt{m_b^2 + \mathrm{p}_i^{\star 2}},$$

simplify the above equation, we get the Lorentz invariant form:

$$\mathrm{p}_i^{\star 2} = \frac{1}{4s}[s - (m_a + m_b)^2][s - (m_a - m_b)^2]. \tag{2.26}$$

Combining Eqs. (2.17), (2.24), (2.25) and (2.26), we get a Lorentz invariant form differential cross section for any inertial frame:

$$\frac{d\sigma}{dt} = \frac{1}{16\pi}\frac{1}{[s - (m_a + m_b)^2][s - (m_a - m_b)^2]}|M_{fi}|^2. \tag{2.27}$$

2.2.4 *ee*, *ep* Cross Sections in Lab Frame

Starting from Eq. (2.27), we can get cross sections for Møller and $e-p$ elastic scattering in Lab frame.

For $e-p$ **scattering** case $1+2 \to 3+4$, as shown in Fig. 2-4:

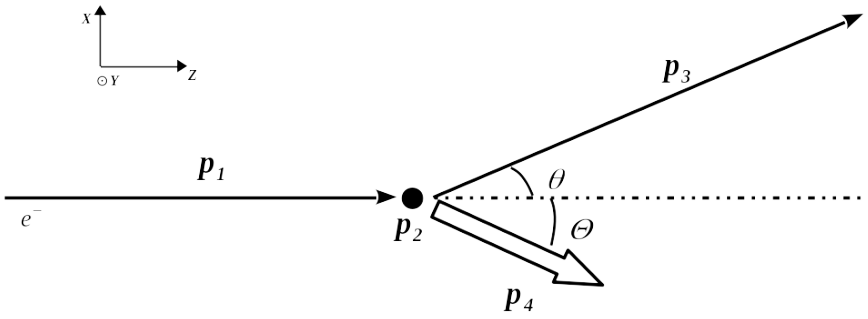

Figure 2-4: Unpolarized electron proton elastic scattering in Lab frame.

in lab frame, we have:

$$\begin{aligned} p_1 &= (E, 0, 0, E), \\ p_2 &= (m_p, 0, 0, 0), \\ p_3 &= (E', 0, E'\sin\theta, E'\cos\theta), \\ p_4 &= (E_4, \boldsymbol{p_4}), \end{aligned}$$

so,

$$\begin{aligned} t = (p_1 - p_3)^2 &= (E - E', 0, -E'\sin\theta, E - E'\cos\theta)^2, \\ \Rightarrow t &= (E - E')^2 - E'^2\sin^2\theta - (E - E'\cos\theta)^2, \\ \Rightarrow t &= 2EE'(\cos\theta - 1). \end{aligned} \tag{2.28}$$

Need to find E', using

$$t = (p_2 - p_4)^2 = 2{m_p}^2 - 2p_2 \cdot p_4 = 2{m_p}^2 - 2m_p E_4,$$

and energy conservation,

$$E + m_p = E' + E_4,$$

we have:

$$t = 2{m_p}^2 - 2m_p(E + m_p - E') = 2m_p(E' - E), \tag{2.29}$$

combining with Eq. (2.28), we have:

$$E' = \frac{m_p E}{E(1 - \cos\theta) + m_p}. \tag{2.30}$$

To get the cross section,

$$\frac{d\sigma}{d\Omega} = \frac{d\sigma}{dt}\frac{dt}{d\Omega} = \frac{d\sigma}{dt d\phi}\frac{dt}{d\cos\theta},$$

according to Eq. (2.29),

$$\frac{dt}{d\cos\theta} = 2m_p\frac{dE'}{d\cos\theta},$$

according to Eq. (2.30)

$$\frac{dE'}{d\cos\theta} = \frac{m_p E^2}{(E - E\cos\theta + m_p)^2} = \frac{E'^2}{m_p},$$

so,

$$\frac{d\sigma}{d\Omega} = 2E'^2\frac{d\sigma}{dt d\phi},$$

with

$$s = (p_1 + p_2)^2 = (E + m_p)^2 - E^2 = m_p(2E + m_p),$$

and combining with Eq. (2.27):

$$\frac{d\sigma}{d\Omega} = 2E'^2\frac{1}{d\phi}\frac{d\sigma}{dt} = \frac{2E'^2}{d\phi}\frac{1}{16\pi}\frac{1}{(2Em_p)^2}|M_{fi}|^2,$$

$$\frac{d\sigma}{d\Omega} = \frac{2E'^2}{32\pi^2}\frac{1}{(2Em_p)^2}|M_{fi}|^2,$$

$$\frac{d\sigma}{d\Omega} = \frac{1}{64\pi^2}\frac{{E_\prime}^2}{(m_p E)^2}|M_{fi}|^2,$$

then the cross section becomes,

$$\boxed{\frac{d\sigma}{d\Omega} = \frac{1}{64\pi^2}\frac{1}{(E - E\cos\theta + m_p)^2}|M_{fi}|^2.} \tag{2.31}$$

In the above equation, the differential actually means:

$$\boxed{\frac{d\sigma}{d\Omega} = \frac{d\sigma}{\sin\theta d\theta},} \tag{2.32}$$

the ϕ has been integrated out using Eq. (2.25). Since references [36] [50] still write it as $d\sigma/d\Omega$, to keep this thesis consistent with these references, we will follow their convention. However, when comparing Eq. (2.31) with experimental measurement, one need to properly handle the $\sin\theta$ factor in Eq. (2.32).

For **Møller scattering** case $1 + 2 \to 3 + 4$, Fig. 2-5:

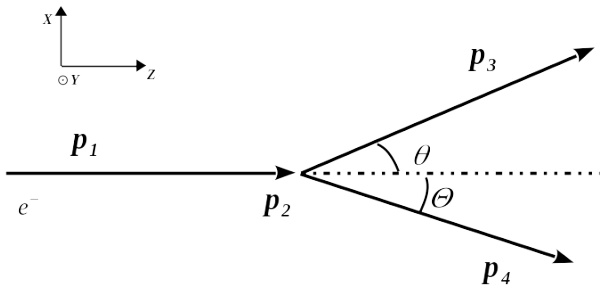

Figure 2-5: Unpolarized Møller elastic scattering in Lab Frame.

in lab frame

$$\begin{aligned} p_1 &= (E, 0, 0, P_1), \\ p_2 &= (m_e, 0, 0, 0), \\ p_3 &= (E_3, 0, P_3\sin\theta, P_3\cos\theta), \\ p_4 &= (E_4, 0, P_4\sin\Theta, P_4\cos\Theta). \end{aligned} \tag{2.33}$$

here we use p for 4-momentum, P for the magnitude of three momentum $\boldsymbol{P}$. Using Mandelstam variable to find scattered electron energy E_3:

$$t = (p_1 - p_3)^2 = (p_2 - p_4)^2, \tag{2.34}$$

namely $p_1 \cdot p_3 = p_2 \cdot p_4$, substituting Eq. (2.33),

$$EE_3 - P_1 P_3 \cos\theta = m_e E_4, \tag{2.35}$$

energy conservation,

$$E_4 = E + m_e - E_3. \tag{2.36}$$

Combining Eq. (2.35) and Eq. (2.36),

$$EE_3 - P_1 P_3 \cos\theta = m_e(E + m_e - E_3).$$

From the above equation, using $E^2 = P^2 + m^2$, we get the relationship between scattered energy vs scattering angle for Møller,

$$\cos\theta = \sqrt{\frac{E + m_e}{E - m_e}\frac{E_3 - m_e}{E_3 + m_e}}, \tag{2.37}$$

$$E_3 = \frac{2m_e}{1 - \frac{E - m_e}{E + m_e}\cos^2\theta} - m_e. \tag{2.38}$$

Equation (2.38) for 2.2 GeV beam energy is shown in Fig. 2-6. Similar as in ep case, combining Eqs. (2.34), (2.36) and (2.37),

$$\frac{dt}{d\cos\theta} = -\frac{2m_e dE_4}{d\cos\theta} = \frac{2m_e dE_3}{d\cos\theta} = \frac{2m_e}{d\cos\theta/dE_3},$$

$$\frac{dt}{d\cos\theta} = 2m_e \cdot \sqrt{\frac{E - m_e}{E + m_e}}\frac{(E_3 + m_e)\sqrt{E_3^2 - m_e^2}}{m_e}, \tag{2.39}$$

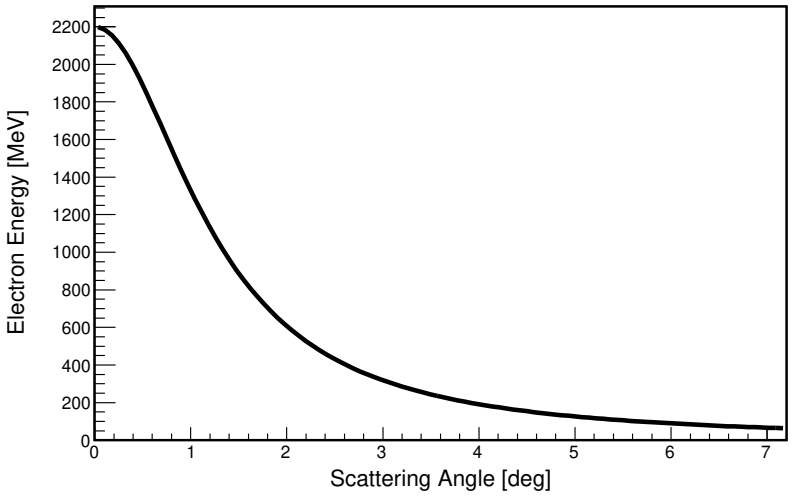

Figure 2-6: Møller electron energy vs scattering angle for 2.2 GeV electron beam.

or use Eq. (2.38),

$$\frac{dt}{d\cos\theta} = 2m_e \frac{dE_3}{d\cos\theta} = 8m_e^2 \frac{\frac{E-m_e}{E+m_e}\cos\theta}{(1-\frac{E-m_e}{E+m_e}\cos^2\theta)^2}. \tag{2.40}$$

From Eq. (2.27), we also need to find s, combining Eq. (2.33),

$$s = (p_1+p_2)^2 = 2m_e^2 + 2p_1\cdot p_2 = 2m_e^2 + 2m_e E.$$

So cross section for Møller:

$$\begin{aligned}
\frac{d\sigma}{d\Omega} &= \frac{d\sigma}{dt}\frac{dt}{d\Omega} = \frac{dt}{d\Omega}\frac{1}{16\pi}\frac{1}{[s-(m_a+m_b)^2][s-(m_a-m_b)^2]}|M_{fi}|^2 \\
&= \frac{dt}{d\Omega}\frac{1}{16\pi}\frac{1}{(s-4m_e^2)s}|M_{fi}|^2 \\
&= \frac{dt}{d\Omega}\frac{1}{16\pi}\frac{1}{4m_e^2(E^2-m_e^2)}|M_{fi}|^2 \\
&= \frac{dt}{d\cos\theta}\frac{1}{32\pi^2}\frac{1}{4m_e^2(E^2-m_e^2)}|M_{fi}|^2,
\end{aligned}$$

if $E \gg m_e$, and combining Eq. (2.39),

$$\begin{aligned}\frac{d\sigma}{d\Omega} &= \frac{dt}{d\cos\theta}\frac{1}{32\pi^2}\frac{1}{4m_e^2(E^2-m_e^2)}|M_{fi}|^2 \\ &= \frac{dt}{d\cos\theta}\frac{1}{128\pi^2}\frac{1}{m_e^2E^2}|M_{fi}|^2 \\ &= 2m_e\cdot\frac{(E_3+m_e)\sqrt{E_3^2-m_e^2}}{m_e}\frac{1}{128\pi^2}\frac{1}{m_e^2E^2}|M_{fi}|^2,\end{aligned}$$

where the $d\sigma/d\Omega$ has the same meaning with Eq. (2.32); then the cross section for Møller becomes:

$$\boxed{\frac{d\sigma}{d\Omega} = \frac{(E_3+m_e)\sqrt{E_3^2-m_e^2}}{64\pi^2}\frac{1}{m_e^2E^2}|M_{fi}|^2,} \tag{2.41}$$

Or combining Eq. (2.40) we get:

$$\begin{aligned}\frac{d\sigma}{d\Omega} &= 8m_e^2\frac{\frac{E-m_e}{E+m_e}\cos\theta}{(1-\frac{E-m_e}{E+m_e}\cos^2\theta)^2}\frac{1}{128\pi^2}\frac{1}{m_e^2(E^2-m_e^2)}|M_{fi}|^2 \\ &= \frac{1}{16\pi^2(E^2-m_e^2)}\frac{\frac{E-m_e}{E+m_e}\cos\theta}{(1-\frac{E-m_e}{E+m_e}\cos^2\theta)^2}|M_{fi}|^2.\end{aligned} \tag{2.42}$$

Compared with Eq. (2.41), Eq. (2.42) kept the electron mass m_e in its phase space integral process.

2.3 Møller Scattering

In the last section, we have given the expression for Møller scattering cross section in lab frame, Eq. (2.41) and Eq. (2.42). In this section, we will give a detailed expression for the the transition matrix element M_{fi} in Born level approximation. The Born approximation takes into account only the one photon exchange process, see Fig. 2-7. Conventions and terminology in this section follow [36]. In QED, M_{fi} is calculated through the following Feynman diagrams:

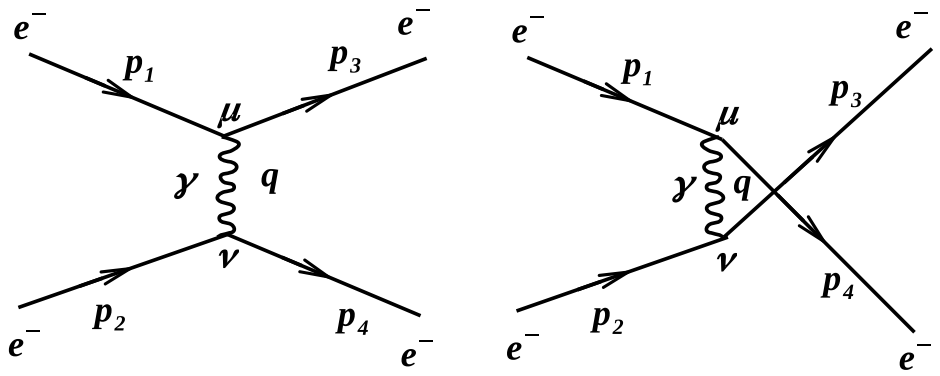

Figure 2-7: One photon exchange (Born level) t channel (left) and u channel (right) Feynman Diagrams for Møller scattering.

For Møller scattering at the Born level, we have two possible reaction channels: t and u channels. Following Feynman rules in [36], for the t channel (the left part in Figure 2-7), the matrix element is evaluated as:

$$-iM_1 = [\bar{u}(p_3)(-i(-e)\gamma^\mu)u(p_1)]\frac{-ig_{\mu\nu}}{q^2}[\bar{u}(p_4)(-i(-e)\gamma^\nu)u(p_2)]$$

$$\Rightarrow M_1 = -\frac{e^2}{q^2}[\bar{u}(p_3)\gamma^\mu u(p_1)][\bar{u}(p_4)\gamma_\mu u(p_2)], \tag{2.43}$$

where $u(p)$ are Dirac spinors, constructed by the four base vectors from solutions of Dirac equations on particles $(\gamma^\mu p_\mu - m)u = 0$. Similarly the Dirac equation for anti-particles $(\gamma^\mu p_\mu + m)v = 0$ leads to antiparticle spinors $v(p)$, which is not used

here.

The Dirac spinors are:

$$u_1(p) = \sqrt{E+m}\begin{pmatrix} 1 \\ 0 \\ \frac{p_z}{E+m} \\ \frac{p_x+ip_y}{E+m} \end{pmatrix}, u_2(p) = \sqrt{E+m}\begin{pmatrix} 0 \\ 1 \\ \frac{p_x-ip_y}{E+m} \\ \frac{-pz}{E+m} \end{pmatrix}, \tag{2.44}$$

$$v_1(p) = \sqrt{E+m}\begin{pmatrix} \frac{p_x-ip_y}{E+m} \\ \frac{-p_z}{E+m} \\ 0 \\ 1 \end{pmatrix}, v_2(p) = \sqrt{E+m}\begin{pmatrix} \frac{p_z}{E+m} \\ \frac{p_x+ip_y}{E+m} \\ 1 \\ 0 \end{pmatrix}, \tag{2.45}$$

and $\bar{u} = u^+\gamma^0$, with γ matrices:

$$\gamma^0 = \beta,\ \gamma^1 = \beta\alpha_x,\ \gamma^2 = \beta\alpha_y,\ \gamma^3 = \beta\alpha_z,$$

where

$$\beta = \begin{pmatrix} I & 0 \\ 0 & -I \end{pmatrix}, \alpha_i = \begin{pmatrix} 0 & \sigma_i \\ \sigma_i & 0 \end{pmatrix}, \tag{2.46}$$

with $\sigma_{i=x,y,z}$ the Pauli matrix.

With 4-vector current given by $j^\mu = \bar{u}(p_3)\gamma^\mu u(p_1)$, M_1 is often written as:

$$M_1 = -\frac{e^2}{q^2} j^\mu j_\mu.$$

For u channel:

$$M_2 = -\frac{e^2}{q^2}[\bar{u}(p_4)\gamma^\mu u(p_1)][\bar{u}(p_3)\gamma_\mu u(p_2)]. \tag{2.47}$$

For M_1, $q = p_1 - p_3 = \sqrt{t}$ in Eq. (2.43); for M_2, $q = p_1 - p_4 = \sqrt{u}$ in Eq. (2.47).

Following Feynman anti-symmetric rule, the total amplitude M:

$$\begin{aligned} M &= M_1 - M_2 \\ &= -\frac{e^2}{t}[\bar{u}(p_3)\gamma^\mu u(p_1)][\bar{u}(p_4)\gamma_\mu u(p_2)] + \frac{e^2}{u}[\bar{u}(p_4)\gamma^\mu u(p_1)][\bar{u}(p_3)\gamma_\mu u(p_2)]. \end{aligned} \tag{2.48}$$

To calculate the scattering cross section, we need to find

$$|M|^2 = |M_1|^2 + |M_2|^2 - M_1 M_2^\star - M_2 M_1^\star.$$

When sum all spins up, one can use trace theorem to calculate each term in the above equation:

$$\sum_{\text{all spins}} |M_1|^2 = \sum_{\text{all spins}} \frac{e^4}{t^2}[\bar{u}(p_3)\gamma^\mu u(p_1)][\bar{u}(p_4)\gamma_\mu u(p_2)][\bar{u}(p_3)\gamma^\mu u(p_1)]^\star[\bar{u}(p_4)\gamma_\mu u(p_2)]^\star \tag{2.49}$$

$$= \frac{e^4}{t^2} Tr[\not{p}_3\gamma^\mu \not{p}_1\gamma^\nu] \cdot Tr[\not{p}_4\gamma_\mu \not{p}_2\gamma_\nu], \tag{2.50}$$

where $\not{p} = \gamma^\mu p_\mu$. Here, we will omit the $\sum$ symbol before $|M|^2$ to make the derivation clear to follow.

Similarly,

$$|M_2|^2 = \frac{e^4}{u^2} Tr[\not{p}_4\gamma^\mu \not{p}_1\gamma^\nu] \cdot Tr[\not{p}_3\gamma_\mu \not{p}_2\gamma_\nu], \tag{2.51}$$

$$M_1 M_2^\star = \frac{e^4}{ut} Tr[\not{p}_3\gamma^\mu \not{p}_1\gamma^\nu \not{p}_4\gamma_\mu \not{p}_2\gamma_\nu], \tag{2.52}$$

$$M_2 M_1^\star = \frac{e^4}{ut} Tr[\not{p}_4\gamma^\mu \not{p}_1\gamma^\nu \not{p}_3\gamma_\mu \not{p}_2\gamma_\nu]. \tag{2.53}$$

To simplify, we use

$$\gamma^\mu \not{p}_1\gamma^\nu \not{p}_4\gamma_\mu = -2\not{p}_4\gamma^\nu \not{p}_1,$$

$$\gamma^\nu \not{p}_2\not{p}_2\gamma_\nu = 4p_1 \cdot p_2$$

to obtain

$$M_1 M_2^\star = M_2 M_1^\star = -32\frac{e^4}{ut}(p_1 \cdot p_2)(p_3 \cdot p_4) \tag{2.54}$$

and

$$|M_1|^2 = \frac{32e^4}{t^2}[(p_1 \cdot p_2)(p_3 \cdot p_4) + (p_1 \cdot p_4)(p_2 \cdot p_3)], \tag{2.55}$$

$$|M_2|^2 = \frac{32e^4}{u^2}[(p_1 \cdot p_2)(p_3 \cdot p_4) + (p_1 \cdot p_3)(p_2 \cdot p_4)]. \tag{2.56}$$

In $E \gg m_e$ case, it is easy to show:

$$p_3 \cdot p_4 = p_1 \cdot p_2 = s/2,$$

$$p_2 \cdot p_3 = p_1 \cdot p_4 = -u/2,$$

$$p_1 \cdot p_3 = p_2 \cdot p_4 = -t/2,$$

so the above M equations can be expressed by Mandelstam variables:

$$|M_1|^2 = \frac{32e^4}{t^2}[\frac{s^2}{4} + \frac{u^2}{4}], \tag{2.57}$$

$$|M_2|^2 = \frac{32e^4}{u^2}[\frac{s^2}{4} + \frac{t^2}{4}], \tag{2.58}$$

$$M_1 M_2^\star = M_2 M_1^\star = -\frac{32e^4}{ut}\frac{s^2}{4}. \tag{2.59}$$

Combining the above three equations, we can separate $|M|^2$ into two parts $|M|^2 = M^t + M^u$, with:

$$M^t = \frac{32e^4}{t^2}[\frac{s^2+u^2}{4}] + \frac{32e^4}{ut}\frac{s^2}{4}, \tag{2.60}$$

$$M^u = \frac{32e^4}{u^2}[\frac{s^2+t^2}{4}] + \frac{32e^4}{ut}\frac{s^2}{4}. \tag{2.61}$$

Then the spin averaged amplitude:

$$\langle|M|\rangle^2 = \frac{1}{4}\sum_{\text{all spins}}|M|^2 = \frac{1}{4}(M^t + M^u). \tag{2.62}$$

Combining the Golden rule Eq. (2.42) and Eq. (2.62), yields the fully expressed

Born level Møller differential cross section:

$$\boxed{\frac{d\sigma}{d\Omega} = \frac{1}{16\pi^2(E^2 - m_e^2)} \frac{\frac{E-m_e}{E+m_e}\cos\theta}{(1 - \frac{E-m_e}{E+m_e}\cos^2\theta)^2}(\frac{M^t + M^u}{4}).} \tag{2.63}$$

The $d\phi$ dependency has been divided out since the cross section is symmetric over ϕ, as shown by Eq. (2.32). The Møller cross section using Eq. (2.63) for 2.2 GeV electron beam has been shown in Fig. 2-8, in comparison with the calculation from Akushevich [8] used in PRad simulation.

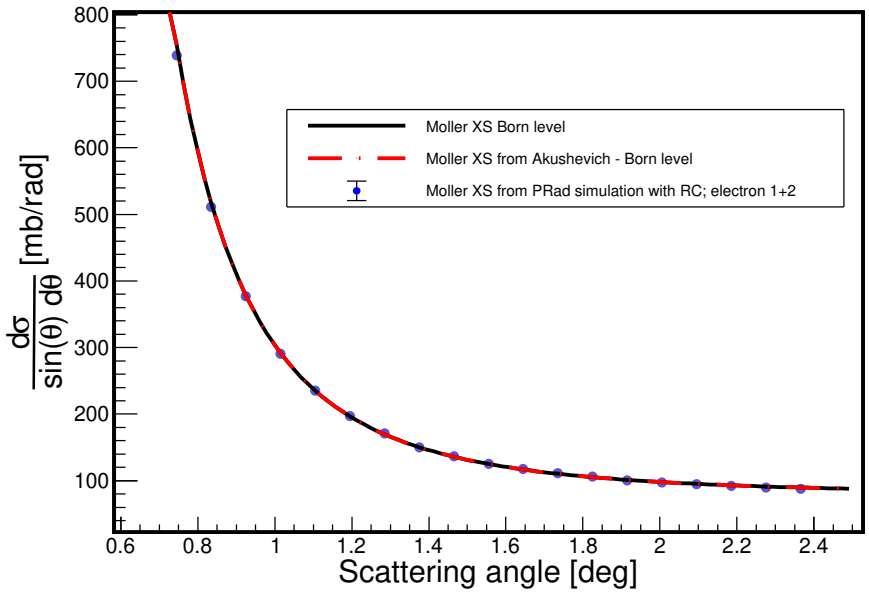

Figure 2-8: Møller scattering cross section comparison. a) the black line is the calculated Born-level Møller cross section using Eq. (2.63); b) the blue dots are the generated cross section with radiative correction using generator in PRad simulation; c) The dotted line represents the calculated Møller cross section from Akushevich [8].

2.4 Electron Proton Elastic Scattering

In this section, we will give a detailed description of the Born level (one photon exchange) cross section for the unpolarized electron proton elastic scattering as illustrated by the Feynman diagram shown in Fig. 2-9. The conventions and terms used

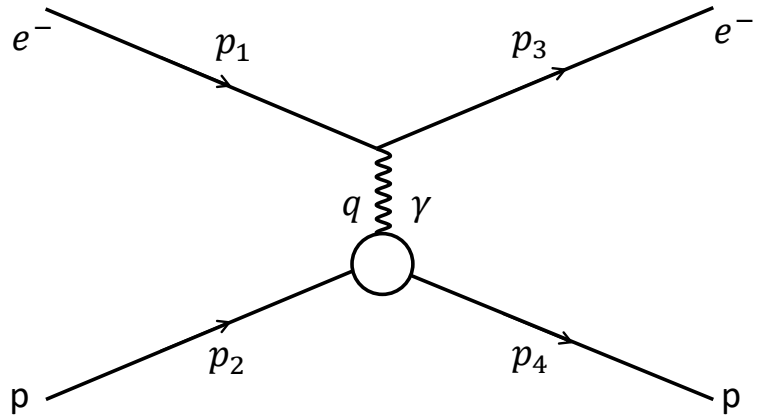

Figure 2-9: One photon exchange Feynman diagram for ep elastic scattering

in this derivation follow [36].

First we calculate the Mott scattering cross section which assumes the target particle (the proton) is a point-like particle with mass M_p, which can be described by Dirac spinors. Similar to the last section, the Lorentz Invariant transition matrix element for a point-like target can be written as:

$$-iM = [\bar{u}_3(-i(-1)e\gamma^\mu)u_1](-\frac{ig_{\mu\nu}}{q^2})[\bar{u}_4(-ie\gamma^\nu)u_2],$$

$$\Rightarrow M = \frac{e^2}{q^2}[\bar{u}_3\gamma^\mu u_1][\bar{u}_4\gamma_\mu u_2]. \tag{2.64}$$

To find $|M|^2$ in the Golden rule for $e-p$ scattering (Eq. (2.31)), we use trace theorem:

$$\begin{aligned} |M|^2 &= \frac{e^4}{q^4}\sum_{all\ spins}[\bar{u}_3\gamma^\mu u_1][\bar{u}_4\gamma_\mu u_2][\bar{u}_1\gamma^\nu u_3][\bar{u}_2\gamma_\nu u_4] \\ &= \frac{e^4}{q^4}Tr[(\not{p}_3 + m_e)\gamma^\mu(\not{p}_1 + m_e)\gamma^\nu] \times Tr[(\not{p}_4 + M_p)\gamma_\mu(\not{p}_2 + M_p)\gamma_\nu], \end{aligned} \tag{2.65}$$

where m_e is electron mass, M_p is proton mass. The first term is:

$$Tr[(\not{p}_3+m_e)\gamma^\mu(\not{p}_1+m_e)\gamma^\nu] = Tr[\not{p}_3\gamma^\mu\not{p}_1\gamma^\nu+m_e^2\gamma^\mu\gamma^\nu] = Tr[\gamma^\rho {p_3}_\rho\gamma^\mu\gamma^\sigma {p_1}_\sigma\gamma^\nu+m_e^2\gamma^\mu\gamma^\nu]$$
$$= {p_3}_\rho {p_1}_\sigma Tr[\gamma^\rho\gamma^\mu\gamma^\sigma\gamma^\nu] + m_e^2 Tr[\gamma^\mu\gamma^\nu] = 4{p_3}_\rho {p_1}_\sigma(g^{\rho\mu}g^{\sigma\nu} - g^{\rho\sigma}g^{\mu\nu} + g^{\rho\nu}g^{\mu\sigma}) + 4m_e^2 g^{\mu\nu}$$
$$= 4[{p_3}^\mu {p_1}^\nu - (p_3\cdot p_1)g^{\mu\nu} + {p_3}^\nu {p_1}^\mu] + 4m_e^2 g^{\mu\nu}. \quad (2.66)$$

The second term is:

$$Tr[(\not{p}_4+M_p)\gamma_\mu(\not{p}_2+M_p)\gamma_\nu] = Tr[\not{p}_4\gamma_\mu\not{p}_2\gamma_\nu+M_p^2\gamma_\mu\gamma_\nu] = Tr[\gamma_\rho {p_4}^\rho\gamma_\mu\gamma_\sigma {p_2}^\sigma\gamma_\nu+M_p^2\gamma_\mu\gamma_\nu]$$
$$= {p_4}^\rho {p_2}^\sigma Tr[\gamma_\rho\gamma_\mu\gamma_\sigma\gamma_\nu] + M_p^2 Tr[\gamma_\mu\gamma_\nu] = 4{p_4}^\rho {p_2}^\sigma(g_{\rho\mu}g_{\sigma\nu} - g_{\rho\sigma}g_{\mu\nu} + g_{\rho\nu}g_{\mu\sigma}) + 4M_p^2 g_{\mu\nu}$$
$$= 4[{p_4}_\mu {p_2}_\nu - (p_4\cdot p_2)g_{\mu\nu} + {p_4}_\nu {p_2}_\mu] + 4M_p^2 g_{\mu\nu}. \quad (2.67)$$

Combining Eq. (2.66) and Eq. (2.67), and omitting the leading factor 16, Eq. (2.65) becomes:

$$[{p_3}^\mu {p_1}^\nu - (p_3\cdot p_1)g^{\mu\nu} + {p_3}^\nu {p_1}^\mu + m_e^2 g^{\mu\nu}][{p_4}_\mu {p_2}_\nu - (p_4\cdot p_2)g_{\mu\nu} + {p_4}_\nu {p_2}_\mu + M_p^2 g_{\mu\nu}]$$
$$= (p_3\cdot p_4)(p_1\cdot p_2) - (p_3\cdot p_1)(p_2\cdot p_4) + (p_1\cdot p_4)(p_2\cdot p_3) + M_p^2(p_1\cdot p_3)$$
$$- (p_1\cdot p_3)(p_2\cdot p_4) + 4(p_1\cdot p_3)(p_2\cdot p_4) - (p_1\cdot p_3)(p_2\cdot p_4) - 4M_p^2(p_1\cdot p_3)$$
$$+ (p_1\cdot p_4)(p_2\cdot p_3) - (p_1\cdot p_3)(p_2\cdot p_4) + (p_1\cdot p_2)(p_3\cdot p_4) + M_p^2(p_1\cdot p_3)$$
$$+ m_e^2(p_4\cdot p_2) - 4m_e^2(p_4\cdot p_2) + m_e^2(p_4\cdot p_2) + 4M_p^2 m_e^2$$
$$= 2(p_1\cdot p_2)(p_3\cdot p_4) + 2(p_1\cdot p_4)(p_2\cdot p_3) - 2M_p^2(p_1\cdot p_3) - 2m_e^2(p_4\cdot p_2) + 4M_p^2 m_e^2.$$

So,

$$\sum_{all\ \ spins} |M|^2 = \frac{32e^4}{q^4}[(p_1\cdot p_2)(p_3\cdot p_4)+(p_1\cdot p_4)(p_2\cdot p_3)-M_p^2(p_1\cdot p_3)-m_e^2(p_4\cdot p_2)+2M_p^2 m_e^2].$$

Note that the spin averaged result:

$$\langle|M|^2\rangle = \frac{1}{4}\sum_{all\ \ spins}|M|^2,$$

$$\langle|M|^2\rangle = \frac{8e^4}{q^4}[(p_1{\cdot}p_2)(p_3{\cdot}p_4)+(p_1{\cdot}p_4)(p_2{\cdot}p_3)-M_p^2(p_1{\cdot}p_3)-m_e^2(p_4{\cdot}p_2)+2M_p^2m_e^2]. \quad (2.68)$$

In the lab frame, as shown in Fig. 2-4, for scattering $1+2 \to 3+4$, we have:

$$\begin{aligned} p_1 &= (E, 0, 0, E), \\ p_2 &= (M_p, 0, 0, 0), \\ p_3 &= (E_3, 0, E_3 \sin\theta, E_3 \cos\theta), \\ p_4 &= (E_4, 0, \mathrm{P}_4 \sin\Theta, \mathrm{P}_4 \cos\Theta), \end{aligned}$$

where E is electron beam energy, E_3 is scattered electron energy, E_4 is recoil proton energy. Using Mandelstam variables, we have:

$$s = (p_1+p_2)^2 = (p_3+p_4)^2, \quad u = (p_1-p_4)^2 = (p_2-p_3)^2,$$

which leads to:

$$\boxed{p_3 \cdot p_4 = p_1 \cdot p_2 = M_p E,} \quad (2.69)$$

$$\boxed{p_1 \cdot p_4 = p_2 \cdot p_3 = M_p E_3.} \quad (2.70)$$

And from

$$t = (p_1-p_3)^2 = (p_2-p_4)^2,$$

we have:

$$2m_e^2 - 2p_1 \cdot p_3 = 2M_p^2 - 2p_2 \cdot p_4,$$

$$EE_3(1-\cos\theta) = M_p E_4 - M_p^2.$$

From the above equation, we get:

$$E_4 = \frac{EE_3(1-\cos\theta)}{M_p} + M_p,$$

combining with energy conservation

$$E + M_p = E_3 + E_4,$$

we get

$$\boxed{E_3 = \frac{M_p E}{M_p + E(1-\cos\theta)},} \tag{2.71}$$

$$\boxed{p_1 \cdot p_3 = E E_3 (1-\cos\theta),} \tag{2.72}$$

$$\boxed{p_2 \cdot p_4 = E E_3 (1-\cos\theta) + M_p^2,} \tag{2.73}$$

combining all the above boxed equations, we get

$$\begin{aligned}
\langle |M|^2 \rangle &= \frac{8e^4}{q^4}[(p_1\cdot p_2)(p_3\cdot p_4) + (p_1\cdot p_4)(p_2\cdot p_3) - M_p^2(p_1\cdot p_3) - m_e^2(p_4\cdot p_2) + 2M_p^2 m_e^2] \\
&= \frac{8e^4}{q^4}[M_p^2E^2 + M_p^2E_3^2 - M_p^2 E E_3(1-\cos\theta) - m_e^2[E E_3(1-\cos\theta) + M_p^2] + 2M_p^2 m_e^2] \\
&= \frac{8e^4}{q^4}[M_p^2(E^2+E_3^2) - (M_p^2+m_e^2)E E_3(1-\cos\theta) + M_p^2 m_e^2] \\
&= \frac{8e^4}{q^4} M_p^2[E^2 + E_3^2 - E E_3(1-\cos\theta)],
\end{aligned}$$

where

$$q^2 = (p_1 - p_3)^2 = -2p_1\cdot p_3 = -2EE_3(1-\cos\theta),$$

$$\boxed{Q^2 = -q^2 = 2EE_3(1-\cos\theta) = 4EE_3\sin^2(\theta/2).} \tag{2.74}$$

To approach Form Factors, we need to reformat the above $\langle |M|^2 \rangle$

$$\begin{aligned}
\langle |M|^2 \rangle &= \frac{8e^4}{q^4} M_p^2[E^2 + E_3^2 - E E_3(1-\cos\theta)] \\
&= \frac{8e^4 M_p^2}{16E^2E_3^2\sin^4(\theta/2)}[E^2 + E_3^2 - E E_3(1-\cos\theta)] \\
&= \frac{e^4 M_p^2}{E E_3 \sin^4(\theta/2)} \frac{1}{2EE_3}\left(E^2 + E_3^2 - 2EE_3\sin^2\frac{\theta}{2}\right) \\
&= \frac{e^4 M_p^2}{E E_3 \sin^4\frac{\theta}{2}}\left(\frac{E}{2E_3} + \frac{E_3}{2E} - \sin^2\frac{\theta}{2}\right),
\end{aligned}$$

using Eq. (2.71), namely $E_3 = M_p E/(M_p + 2E\sin^2\frac{\theta}{2})$, and substituting it into the

above equation, we get:

$$\langle|M|^2\rangle = \frac{e^4 M_p^2}{E E_3 \sin^4\frac{\theta}{2}}\left(\frac{E}{2E_3} + \frac{E_3}{2E} - \sin^2\frac{\theta}{2}\right) \tag{2.75}$$

$$= \frac{e^4 M_p^2}{E E_3 \sin^4\frac{\theta}{2}}\left[\frac{M_p + 2E\sin^2\frac{\theta}{2}}{2M_p} + \frac{M_p}{2(M_p + 2E\sin^2\frac{\theta}{2})} - \sin^2\frac{\theta}{2}\right] \tag{2.76}$$

$$= \frac{e^4 M_p^2}{E E_3 \sin^4\frac{\theta}{2}}\left[\cos^2\frac{\theta}{2} + \frac{Q^2}{2M_p^2}\sin^2(\theta/2)\right], \tag{2.77}$$

namely,

$$\langle|M|^2\rangle = \frac{e^4 M_p^2}{E E_3 \sin^4\frac{\theta}{2}}\left[\cos^2\frac{\theta}{2} + \frac{Q^2}{2M_p^2}\sin^2(\theta/2)\right]. \tag{2.78}$$

Substituting Eq. (2.78) into Eq. (2.31) (Golden rule):

$$\frac{d\sigma}{d\Omega} = \frac{1}{64\pi^2}\frac{1}{(2E\sin^2(\theta/2) + M_p)^2}|M_{fi}|^2$$

$$= \frac{1}{64\pi^2}\frac{E_3^2}{M_p^2 E^2}\frac{e^4 M_p^2}{E E_3 \sin^4(\theta/2)}\left[\cos^2(\theta/2) + \frac{Q^2}{2M_p^2}\sin^2(\theta/2)\right], \tag{2.79}$$

which is

$$\boxed{\frac{d\sigma}{d\Omega} = \frac{1}{64\pi^2}\frac{e^4}{E^2\sin^4(\theta/2)}\frac{E_3}{E}\left\{\cos^2(\theta/2) + \frac{Q^2}{2M_p^2}\sin^2(\theta/2)\right\},} \tag{2.80}$$

the full expression for Born level Mott scattering cross section. In Eq. (2.80), the factor E_3/E is due to the proton recoil; the second term in the curly brackets is purely due to the spin-spin interaction between electron and proton (electron and proton are both spin-1/2 particles).

2.4.1 The Rosenbluth Formula

Equation (2.64) only applies for Mott case, where proton was treated as a spin-1/2 structure-less point particle. To introduce the structure of the proton, we first reorganize Eq. (2.64) into two parts: electron current j^μ and proton current J^μ,

$$j^\mu = -e[\bar{u}_3\gamma^\mu u_1],$$

$$J^\mu = e[\bar{u}_4 \gamma^\mu u_2],$$

In the above current j^μ for electron, the vertex part γ^μ is for structure-less spin-1/2 Dirac particles. Thus, the γ^μ in the proton current J^μ needs to be modified to account for its structure [52] like the following:

$$J^\mu = e[\bar{u}_4 \Gamma^\mu u_2]. \tag{2.81}$$

Γ^μ must be Lorentz invariant and transforms as a vector like γ^μ does. Thus, it must be a combination of p_2, p_4, q and Dirac γ-matrices. Since $q = p_4 - p_2$, one can use p_2, p_4 and Dirac γ-matrices to construct Γ^μ, the most general form is:

$$\Gamma^\mu = A \cdot \gamma^\mu + B \cdot (p_4^\mu + p_2^\mu) + C \cdot (p_4^\mu - p_2^\mu), \tag{2.82}$$

where A, B and C are coefficients composed of q^2 and the production of p and γ-matrices: $\gamma^\mu p_{2,\mu}$, $\gamma^\mu p_{4,\mu}$. Using the Dirac equation $(\gamma^\mu p_\mu - M_p)u(p) = 0$, $\gamma^\mu p_\mu$ can be replaced by a number M_p. So A, B and C can be purely functions of q^2. It is shown in [52] that the following Ward identity[4] must hold for Γ^μ:

$$q_\mu \Gamma^\mu = 0. \tag{2.83}$$

Given that $q_\mu \gamma^\mu = (p_{4,\mu} - p_{2,\mu})\gamma^\mu = (M_p - M_p) = 0$ and $q_\mu(p_4^\mu + p_2^\mu) = (p_{4,\mu} - p_{2,\mu})(p_4^\mu + p_2^\mu) = 0$, so C must be 0 in order to hold the Ward identity. Using the following Dirac equation and its Hermitian conjugate:

$$\begin{aligned} (\gamma^\mu p_{2,\mu} - M_p)u(p_2) &= 0 \\ \bar{u}(p_4)(\gamma^\mu p_{4,\mu} - M_p) &= 0, \end{aligned} \tag{2.84}$$

it is easy to show the Gordon identity (see Appendix A.2):

$$\bar{u}(p_4)\gamma^\mu u(p_2) = \bar{u}(p_4)\Big[\frac{p_4^\mu + p_2^\mu}{2M_p} + \frac{i\sigma^{\mu\nu}q_\nu}{2M_p}\Big]u(p_2), \tag{2.85}$$

[4] Current conservation.

where

$$\sigma^{\mu\nu} = \frac{i}{2}(\gamma^\mu\gamma^\nu - \gamma^\nu\gamma^\mu). \tag{2.86}$$

One can re-organize the Gordon identity into the following form:

$$\bar{u}(p_4)\Big[\frac{p_4^\mu + p_2^\mu}{2M_p}\Big]u(p_2) = \bar{u}(p_4)\Big[\gamma^\mu - \frac{i\sigma^{\mu\nu}q_\nu}{2M_p}\Big]u(p_2), \tag{2.87}$$

and substitute the above equation into Eq. (2.82), we get:

$$\Gamma^\mu = \left[F_1(q^2)\gamma^\mu + \frac{\kappa}{2M_p}F_2(q^2)i\sigma^{\mu\nu}q_\nu\right], \tag{2.88}$$

where the first term is called Dirac current, the second term is called Pauli current; F_1 and F_2 are two independent factors that describe the proton structure, called Dirac and Pauli form factors; and κ is the anomalous magnetic moment. Substitute Eq. (2.88) back into Eq. (2.64), and repeat what we did for Mott scattering, we get the modified differential cross section:

$$\frac{d\sigma}{d\Omega} = \frac{\alpha^2}{4E^2\sin^4(\theta/2)}\frac{E_3}{E}\left\{\left(F_1^2 - \frac{\kappa^2q^2}{4M_p^2}F_2^2\right)\cos^2\frac{\theta}{2} - \frac{q^2}{2M_p^2}(F_1+\kappa F_2)^2\sin^2\frac{\theta}{2}\right\}, \tag{2.89}$$

where $\alpha = e^2/4\pi$ is the fine structure constant. In practice, it is often to use the linear combinations of F_1, F_2 [53],

$$G_E = F_1 + \frac{\kappa q^2}{4M_p^2}F_2, \tag{2.90}$$

$$G_M = F_1 + \kappa F_2, \tag{2.91}$$

Then the cross section Eq. (2.89) becomes,

$$\frac{d\sigma}{d\Omega} = \frac{\alpha^2}{4E^2\sin^4(\theta/2)}\frac{E_3}{E}\left(\frac{G_E^2 + \tau G_M^2}{1+\tau}\cos^2\frac{\theta}{2} + 2\tau G_M^2\sin^2\frac{\theta}{2}\right), \tag{2.92}$$

where $\tau = -q^2/4M^2$, G_E and G_M are called electric and magnetic form factors or the Sachs form factor [54] [55]. Equation (2.92) is known as the Rosenbluth formula. For

structure-less Mott scattering, $G_E = G_M = 1$, and Eq. (2.92) reduces to Eq. (2.80).

The Born level cross section from Eq. (2.92) using Kelly form factors [9] for G_E and G_M has been shown in Fig. 2-10, in comparison with the cross section with radiative corrections from PRad simulation using an *ep* generator from [8].

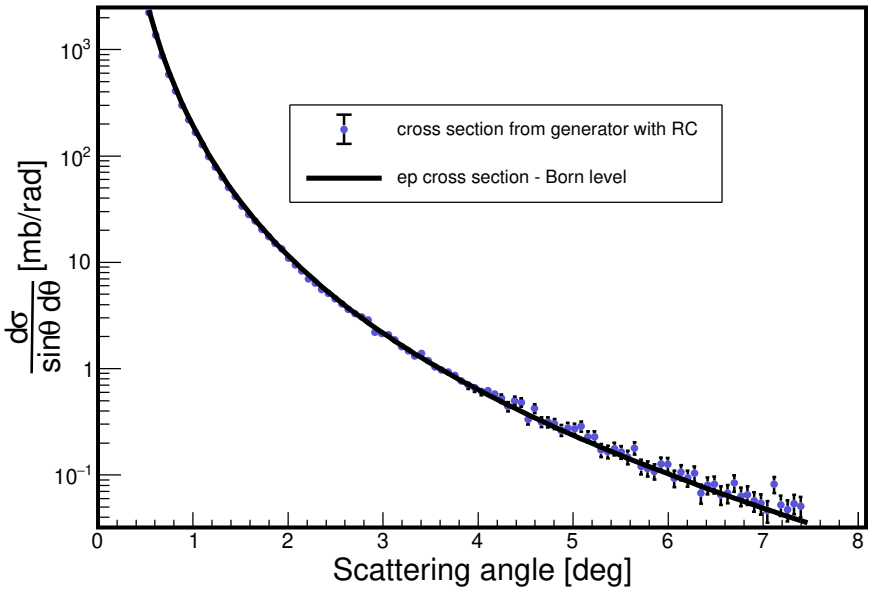

Figure 2-10: $e - p$ elastic scattering cross sections. 1) the dots are the cross sections with radiative correction from PRad simulation generator; 2) the black line represents the Born level cross section Eq. (2.92) using Kelly form factors [9] for G_E and G_M.

2.5 Nucleon Form Factors

In the previous section, we have given the detailed differential cross section for electron proton elastic scattering, including contributions from electromagnetic form factors, Eq. (2.92). There are several methods to measure G_E and G_M, such as polarized or un-polarized e-p elastic scattering, polarization transfer measurement, etc. In the time earlier than 1990s, the "Rosenbluth separation" technique was used to measure G_E and G_M [10]. The Rosenbluth separation requires measurements of the cross section at different kinematics for a fixed Q^2, typically by using different scattering angles and incident electron beam energies.

Equation (2.92) can be normalized the by Mott cross section (Eq. (2.80)):

$$\frac{d\sigma}{d\Omega} = \left(\frac{d\sigma}{d\Omega}\right)_{Mott} \times \left[G_E^2 + \frac{\tau}{\epsilon}G_M^2\right]/(1+\tau), \tag{2.93}$$

where $\epsilon = [1 + 2(1+\tau)\tan^2(\theta/2)]^{-1}$ is called the virtual photon polarization, θ is the electron scattering angle, and $\tau = -q^2/4M^2$. In earlier versions of Rosenbluth separation method, a reduced cross section was introduced:

$$\left(\frac{d\sigma}{d\Omega}\right)_{reduced} = \frac{\epsilon(1+\tau)}{\tau}\left(\frac{d\sigma}{d\Omega}\right)_{exp} / \left(\frac{d\sigma}{d\Omega}\right)_{Mott} = G_M^2 + \frac{\epsilon}{\tau}G_E^2, \tag{2.94}$$

where $(d\sigma/d\Omega)_{exp}$ is the measured cross section. Once the $Q^2 = -q^2$ is fixed, τ will be fixed with it. After measuring a series of cross sections at the same Q^2, a linear fit with Eq. (2.94) over ϵ on the measured data would give an interception G_M^2 and a slope G_E^2/τ, as shown in Fig. 2-11. In this plot, the data were normalized by the dipole form factor:

$$G_D = \frac{1}{(1 + Q^2/0.71\text{GeV}^2)^2}. \tag{2.95}$$

Another method would be using models or parameterizations to approach G_E and G_M, and then fit the measured cross sections using these models/parameterizations, and take the fitting results as form factors directly. For low Q^2 region, where the contribution from G_M is small, one can safely assume a model or parameterization

for G_M, and assign a systematic uncertainty to the extracted G_E. This works for PRad situation, which has the unprecedentedly low Q^2 region: $2.1 \times 10^{-4} - 1.6 \times 10^{-2}$ $(\mathrm{GeV}/c)^2$.

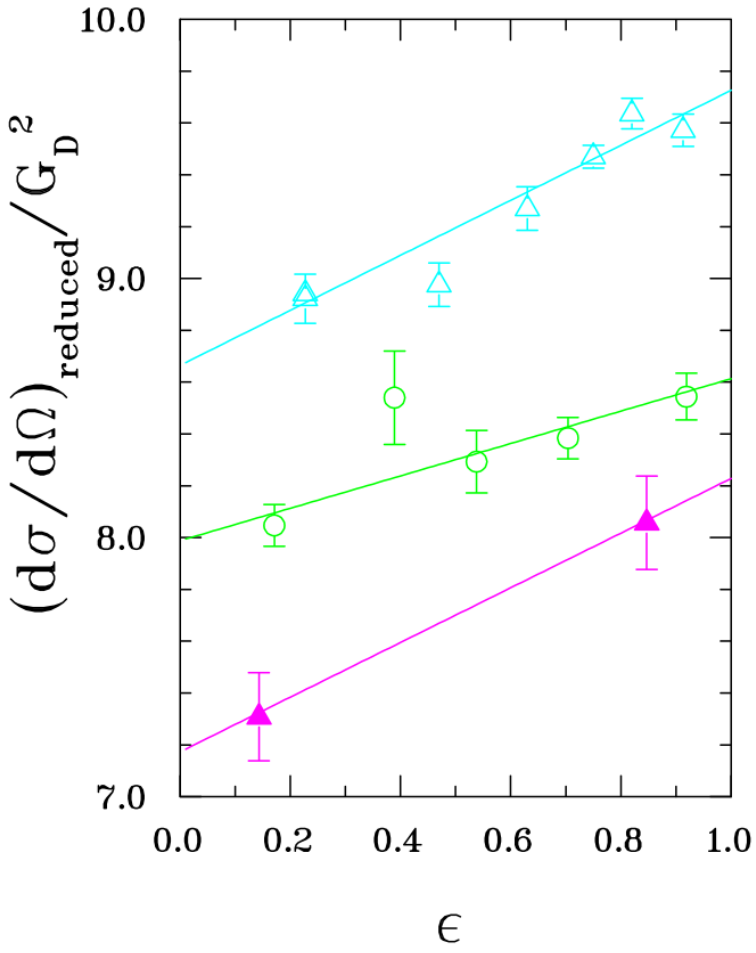

Figure 2-11: A demonstration for the Rosenbluth separation method [10]. The data with cyan triangles are for $Q^2 = 2.5$ GeV^2, green circle $Q^2 = 5.0$ GeV^2, purple triangle $Q^2 = 7.0$ GeV^2. The straight lines are fittings from Eq. (2.94).

Prior to PRad experiment, the lowest Q^2 range was reached by the Mainz 2010 measurement [56], in which about 1400 cross section points from electron-proton elastic scattering were measured in the Q^2 range $0.004-1.0$ $(\mathrm{GeV}/c)^2$, with statistical uncertainty below 0.2%. The extracted G_E^p and G_M^p parameterizations from Mainz

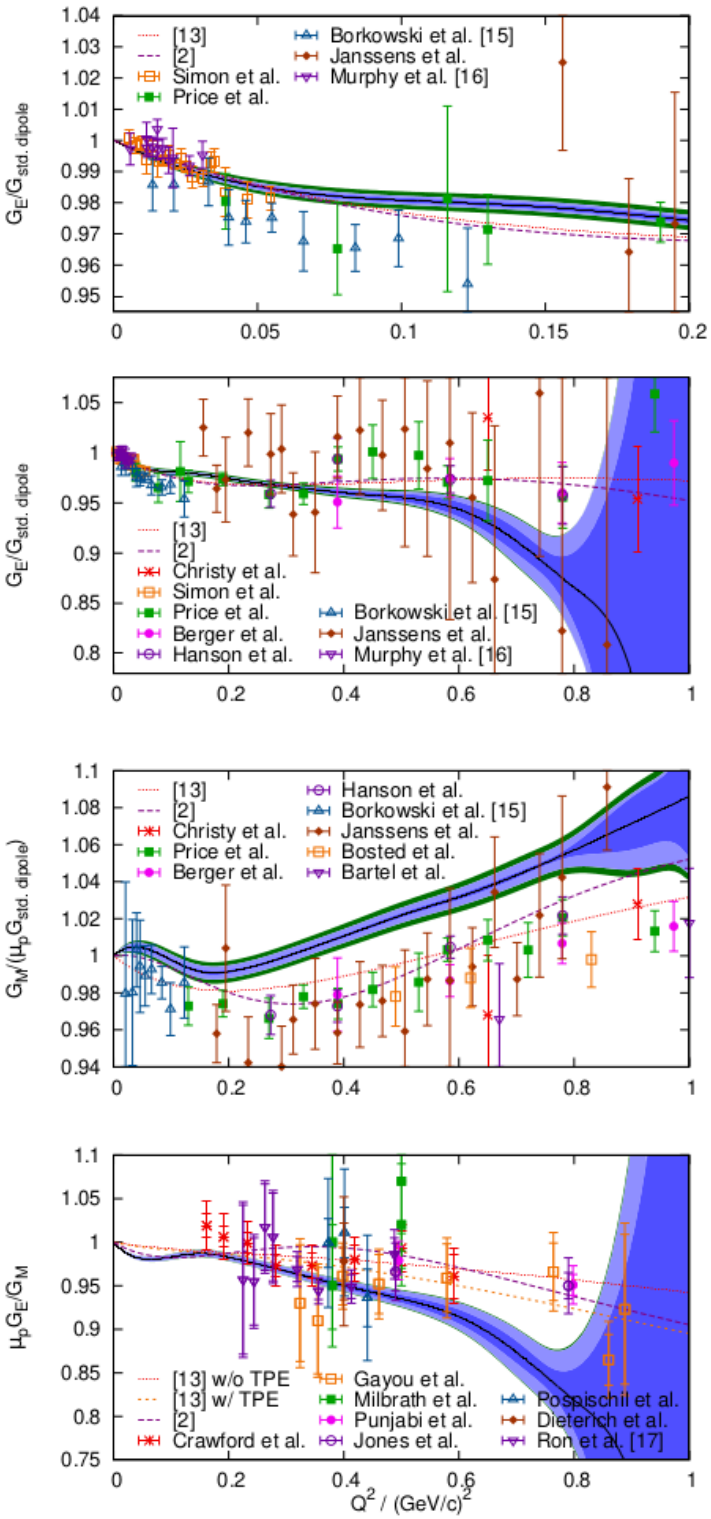

Figure 2-12: The proton form factors G_E and G_M normalized to the standard dipole model and G_E/G_M as a function of Q^2 from Mainz data. The plot was taken from [11].

[42] are shown in Fig. 2-12. The extracted proton charge and magnetic radii are [11]:

$$\sqrt{\langle r_E^2 \rangle} = 0.879(5)_{stat.}(4)_{syst.}(2)_{model}(4)_{group}\ fm, \tag{2.96}$$

and

$$\sqrt{\langle r_M^2 \rangle} = 0.777(13)_{stat.}(9)_{syst.}(5)_{model}(2)_{group}\ fm. \tag{2.97}$$

There are limitations on Rosenbluth separation method. The Rosenbluth separation (Eq. (2.94)) works best in situations where both G_E and G_M contribute to the cross section considerably. However, due to the factor τ/ϵ in front of G_M, see Eq. (2.93), in low Q^2 range, the contribution from G_M^p is negligible, G_E^p dominate the cross section; while in high Q^2 range, G_M^p dominates. For example, at $Q^2 = 2.0$ (GeV/c)^2, the magnetic form factor contributes about 95% of total cross section. In these cases the extracted form factors would have large uncertainties. On the other hand, the Rosenbluth separation also need cross section measurements in a wide range of beam energy, which potentially increased the systematic uncertainties that are beam energy dependent, such as uncertainties from luminosity, detector efficiency, and acceptance. For such situations, polarization techniques were introduced [26] [57] [58] using polarized electron beams and/or polarized targets. Among these, the polarization transfer experiment can directly measure the ratio of G_E^p/G_M^p using a longitudinally polarized electron beam and an unpolarized proton target. The polarization of electrons will be transferred to the recoil proton by [59]:

$$P_t = -hP_e\sqrt{\frac{2\epsilon(1-\epsilon)}{\tau}}\frac{G_E G_M}{G_M^2 + \frac{\epsilon}{\tau}G_E^2}, \tag{2.98}$$

$$P_l = hP_e\sqrt{1-\epsilon^2}\frac{G_M^2}{G_M^2 + \frac{\epsilon}{\tau}G_E^2}, \tag{2.99}$$

$$\frac{G_E}{G_M} = -\frac{P_t}{P_l}\sqrt{\frac{\tau(1+\epsilon)}{2\epsilon}}, \tag{2.100}$$

where P_t, P_l are the perpendicular and parallel polarization components of the recoil proton in the scattering plane, respectively; $h = \pm 1$ is the helicity of the electron, see

Fig. 2-13.

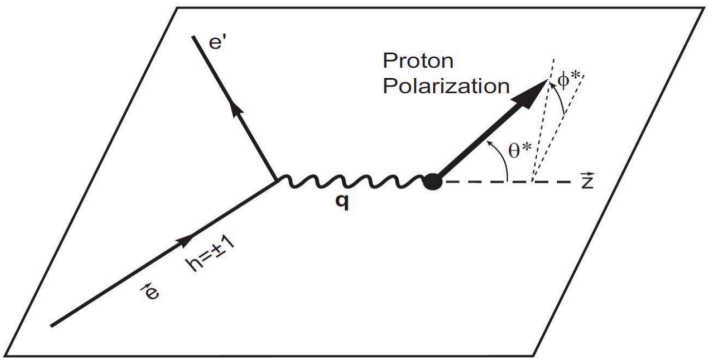

Figure 2-13: Spin dependent elastic *ep* scattering in Born level approximation.

The extraction of G_E/G_M using polarization transfer technique (Eq. (2.100)) has been an active research field at Jefferson Lab in recent years [45] [21] [12] [13] [15] [18] [19], where the first experiment was done by Jones et al [45] [21] in Hall A using two identical high resolution spectrometers (HRS). A focal plane polarimeter (FPP) was installed in the hadron HRS which can determine the polarization of the recoil proton. The result of Jones et al demonstrated for the first time that the Q^2 dependence of G_E^p and G_M^p is significantly different in the range of $Q^2 = 0.49 - 3.47$ $(\mathrm{GeV}/c)^2$. The follow-up experiments in Hall A using the polarization transfer technique [12] [13] expanded the Q^2 to 5.6 $(\mathrm{GeV}/c)^2$. The measurements from [45] [12] [13] in the Q^2 range of $0.5 - 5.0$ $(\mathrm{GeV}/c)^2$ are shown in Fig. 2-14, where a linear fit of $\mu_p G_E^p/G_M^p$ over Q^2 is obtained.

The most recent measurement using polarization transfer technique at Jefferson Lab was done by Zhan et al [43] [26], where the ratio of $\mu_p G_E/G_M$ was measured in the small Q^2 range $0.3 - 0.7$ $(\mathrm{GeV}/c)^2$. The experiment was performed at Jefferson Lab in Hall A using recoil polarimetry, with a total uncertainty of approximately 1%. The measurement result was shown in Fig. 2-15, and the extracted proton radius is $\langle r_E^2 \rangle^{1/2} = 0.875 \pm 0.0010\ fm$.

There is another polarization technique, which is using longitudinally polarized electron beam and polarized target. This technique is called double polarization method, and the ratio of G_E/G_M can also be extracted from it. The elastic scattering

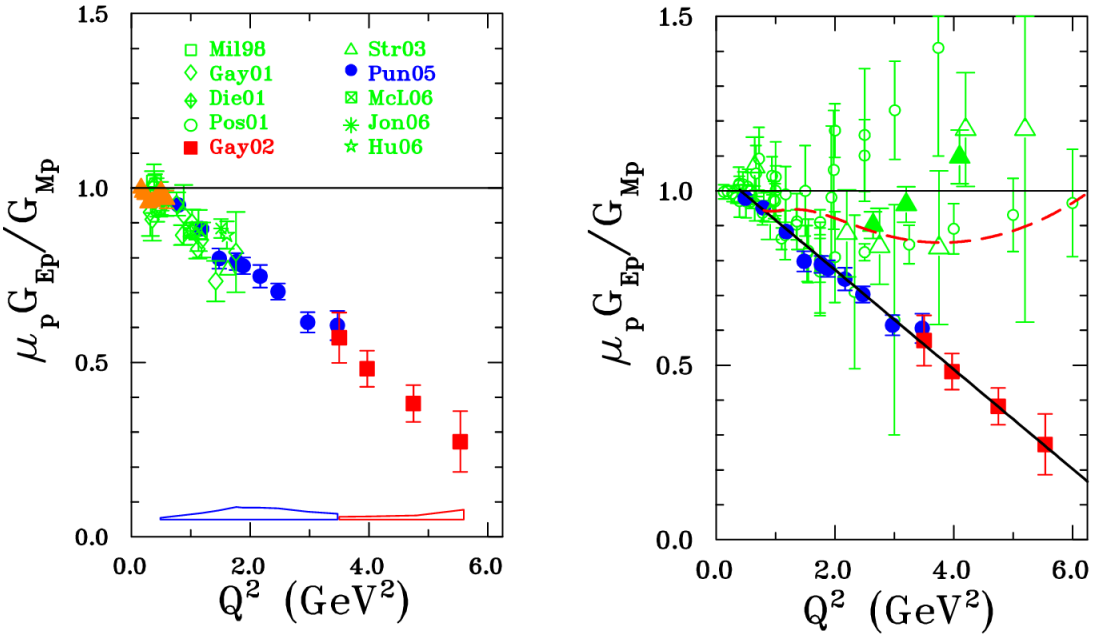

Figure 2-14: Left plot: G_E^p/G_M^p ratio from [12] [13] (solid circle and square), in compare with other polarization transfer experiments [14] [15] [16] [17] [18] [19] [20] [21]. Right plot is a compare of the ratio G_E^p/G_M^p with Rosenbluth separation [22] [23] (open and filled triangles.) The dashed curve is a refit of Rosenbluth data [24]. This plot is taken from [25].

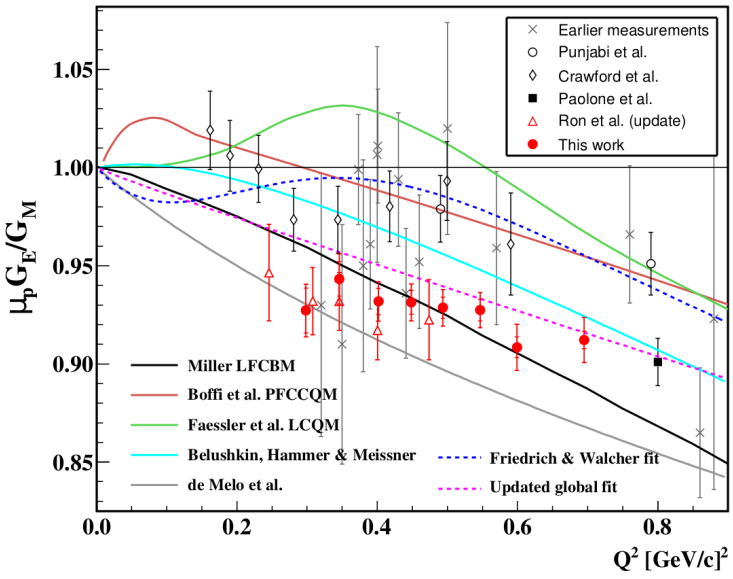

Figure 2-15: Low Q^2 polarization measurement of $\mu_p G_E/G_M$ from ep elastic scattering experiment. This plot is taken from [26].

cross section of doubly polarized elastic scattering can be expressed by [60]:

$$\frac{d\sigma}{d\Omega} = \Sigma + h\Delta, \tag{2.101}$$

where Σ is the unpolarized differential cross section (the Rosenbluth formula Eq. (2.92)), Δ is the spin dependent differential cross section [25] [61]:

$$\Delta = -2\sigma_{Mott}\tan(\theta_e/2)\sqrt{\frac{\tau}{1+\tau}}\Big\{\sqrt{\tau[1+(1+\tau)\tan^2(\theta_e/2)]}\cos\theta^\star G_M^2 + \sin\theta^\star\cos\phi^\star G_E G_M\Big\}, \tag{2.102}$$

where $\theta^\star$ and $\phi^\star$ are the polar and azimuthal angles of the target polarization vector, shown in Fig. 2-13. The physical asymmetry is then defined as

$$A = \frac{\sigma_+ - \sigma_-}{\sigma_+ + \sigma_-} = \frac{\Delta}{\Sigma}, \tag{2.103}$$

where σ_+ and σ_- are the differential cross sections with beam helicity equal to +1 and -1. Substituting Δ and Σ into Eq. (2.103):

$$A = -\frac{2\sqrt{\tau(1+\tau)}\tan(\theta_e/2)}{G_E^2 + \frac{\tau}{\epsilon}G_M^2}\big[\sin\theta^\star\cos\phi^\star G_E G_M + \sqrt{\tau[1+(1+\tau)\tan^2(\theta_e/2)]}\cos\theta^\star G_M^2\big], \tag{2.104}$$

clearly, the G_E/G_M ratio can be extracted from the above equation.

In realistic situations, we don't have 100% polarized electron beam and target, so the measured asymmetry is diluted by the polarization:

$$A_{measure} = P_{beam}P_{target}A, \tag{2.105}$$

where P_{beam} and P_{target} are the polarization of beam and target, respectively. Multiple experiments using double polarization technique have been carried out. The first experiment was performed at the Stanford Linear Accelerator Center (SLAC) using

longitudinally polarized electron beam and polarized protons [62], followed by MIT-Bates [14] [63] [64], MAMI [16], at different Q^2 range.

The theoretical understanding of the electromagnetic form factors of nucleon has a long history but still requires major effort to be made. One important reason is that a direct calculation of the nucleon form factors from the underlying QCD theory is difficult due to the two features of QCD: asymptotic freedom and confinement. Currently, all the theoretical models on nucleon form factors are based on effective theories. They rely on the current available data and usually have many adjustable parameters. There are two major categories of theoretical models: the first category employs the meson degree of freedom in the calculation of interactions with nucleons, the vector meson dominance (VMD) [65] [66] [67], dispersion analyses [68] belong to this category. The second category employs quark and gluon degrees of freedom, includes but not limited to: relativistic constituent quark model (RCQM) [69] [70], cloudy bag [71], generalized parton distribution [72] [73] [74] [75], perturbative QCD [76], and lattice QCD calculation [77] [78] [79]. Among these, the VMD model was the earliest, developed by Sakurai in 1960s [80]. In the VMD model, shown in Fig.

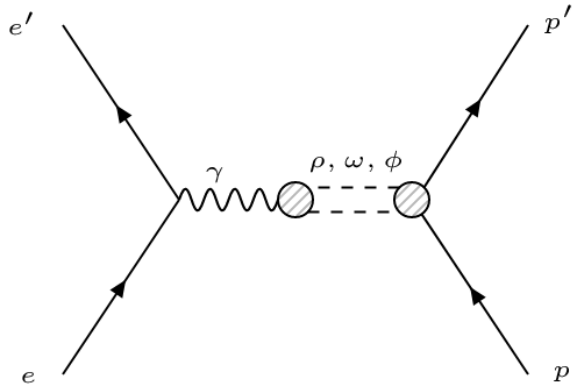

Figure 2-16: The vector meson dominance model for the coupling of the virtual photon to a nucleon. This plot is reproduced from [10].

2-16, the virtual photon in $eN \to eN$ elastic scattering does not directly couple with the nucleon, instead the interaction is dominated by the exchange of vector mesons (isospin = 1) $\rho(770)$, $\omega(782)$, and $\phi(1020)$. These are short-lived resonance particles appeared in scattering experiments. With two vector poles in the above Feynman

diagram contributing oppositely to the form factor [10]:

$$F_{1,2}(q^2) \sim \frac{a}{q^2 - m_{V1}^2} - \frac{a}{q^2 - m_{V2}^2} = \frac{a(m_{V1}^2 - m_{V2}^2)}{(q^2 - m_{V1}^2)(q^2 - m_{V2}^2)}, \tag{2.106}$$

one can write the above form factor into dipole form in approximation:

$$F_{1,2}(Q^2) \sim \frac{1}{(Q^2 + m_V^2)^2},$$

which is the same form with Eq. (2.95) in this section. A fit using VMD model in [66] predicted a linear decrease of the proton G_E^p/G_M^p ratio, which agrees with the result from the polarization transfer experiments [45] [12]. The VMD model was further refined by introducing an intrinsic structure to the nucleon in [81]. For the second category, in the RCQM model, the nucleons are treated as three quark bound states, the predictions of $\mu_p G_E^p/G_M^p$ using RCQM in [82] [83] all had good agreements with the measurements from polarization transfer experiments, see [84]. The lattice QCD has been developing rapidly recently, the precision of calculation for baryon mass such as proton mass in lattice QCD has reached 2% [85]. However, the calculation for nucleon form factor remain challenging, the recent calculation mainly focus on isovector form factors, where the contributions from disconnected diagrams are reduced. The calculation on isoscalar form factor is highly computational intensive [10] [84]. So far, no model can accurately describe all form factors of the nucleon, which is necessary to fully understand the strong interaction. On the other hand, a precise knowledge of nucleon form factors can provide a high precision test for QCD theory.

2.6 Hydrogen Spectroscopy

By the 18th century, physicists had discovered that the light emitted when different substances were put into flames, and observed through prisms, will show different spectra patterns. In 1850s, Bunsen and Kirchhoff [86] developed a new instrument named Bunsen Burner which made observation of spectra from burning substances more effective. Because the Bunsen burner itself emits practically no light, resulted in an improvement by eliminating the contamination light from burning ovens from the spectra of substances being investigated. Many new elements were discovered through this method at that time.

The spectrum of hydrogen consisting of a series of discrete lines [87] hinted that there must be some internal structures that made hydrogen atoms emit lights at such a frequency pattern. In 1913, Niels Bohr and Ernest Rutherford presented a semi-classical model to depict the internal structure of atoms, the model was later named Bohr model [88]. In Bohr model, an atom consists of a small, dense nucleus surrounded by orbiting electrons, the structure is just like the solar system. The electron can only revolve around the nucleus in certain stable orbits without radiating any energy, and no orbit is allowed in between these discrete ones; the angular momentum of the electron is quantized: $m_e vr = n\hbar$, where $\hbar$ is the reduced Planck's constant and n is natural number; electrons can only gain or lose energy by jumping from one allowed orbit to another, emitting or absorbing an electromagnetic radiation with frequency ν determined by the energy difference: $\Delta E = E_2 - E_1 = h\nu$, where h is the Planck's constant. For hydrogen, its nucleus was later named proton by Ernest Rutherford in 1920.

The Bohr model only works for certain selected systems such as the non-relativistic hydrogen atom, and it can be derived as a first order approximation of the hydrogen atom using a classical quantum mechanics model. In order to calculate the leading order of hydrogen electron energy in classical quantum mechanics, it is natural to assume that the nucleus mass is infinite [89], and the electron moves under a Coulomb

potential centered at it. The Schrödinger equation can be expressed as:

$$(-\frac{\boldsymbol{p}^2}{2m} + \frac{Z\alpha}{r})\psi(\boldsymbol{r}) = E\psi(\boldsymbol{r}). \tag{2.107}$$

Here we use natural units $\hbar = c = 1$, and the fine structure constant $\alpha = e^2/4\pi = 1/137$. The solution for the above equation turns out to be a series of discrete energy levels,

$$\psi(\boldsymbol{r}) = R_{nl}(r)Y_{lm}(\frac{\boldsymbol{r}}{r}),$$

$$E_n = -\frac{m(Z\alpha)^2}{2n^2} = -2\pi R_\infty \frac{Z^2}{n^2}, \quad n = 1, 2, 3, ... \tag{2.108}$$

where m is the electron mass, n is called the principle quantum number, and

$$R_\infty = m\frac{\alpha^2}{4\pi}, \tag{2.109}$$

is the Rydberg constant. The finite proton mass effect can be corrected by introducing an effective mass m_r of the two-body system [90], which is defined as:

$$m_r = \frac{mM}{m+M},$$

where m is the electron mass and M is the proton mass. For hydrogen, $m_r \approx 0.9995m$, the energy correction caused by finite mass effect is about 0.05%. Shrödinger's non-relativistic quantum mechanical model is a great success, it explains why we have discrete lines in atomic spectra. The discrete lines in hydrogen spectra corresponds to photons emitted when electrons transit between different energy levels. However, it was soon discovered that these lines are degenerate. A better description of hydrogen model was made through Dirac equations, where the relativistic effect of electron and its spin effect were taken into account. In the first approximation, assume the proton mass is infinite, and use the relativistic relationship for electron:

$$E = \sqrt{p^2 + m^2},$$

the energy eigenvalues from Eq. (2.108) becomes [91]:

$$E_{nj} = mf(n,j), \tag{2.110}$$

where

$$f(n,j) = \left[1 + \frac{(Z\alpha)^2}{\left(n - j - \frac{1}{2} + \sqrt{(j+\frac{1}{2})^2 - (Z\alpha)^2}\right)^2}\right]^{-\frac{1}{2}}, \tag{2.111}$$

with j the sum of orbital and spin angular momentum of the electron. States with the same principle quantum number n but different angular momentum quantum number j now have different energy levels.

Relativistic corrections are self-expressed by an expansion of $f(n,j)$ over $Z\alpha$ [92]:

$$\begin{aligned} E_{n,j} = m - m\frac{(Z\alpha)^2}{2n^2} - m\frac{(Z\alpha)^4}{2n^3}\left(\frac{1}{j+\frac{1}{2}} - \frac{3}{4n}\right) \\ - m\frac{(Z\alpha)^2}{8n^3}\left[\frac{1}{(j+\frac{1}{2})^3} + \frac{3}{n(j+\frac{1}{2})^2} + \frac{5}{2n^3} - \frac{6}{n^2(j+\frac{1}{2})}\right] + ... \end{aligned} \tag{2.112}$$

The first term corresponds to the electron relativistic mass energy, the second term is Bohr energy. The first term already has the correct mass dependence, while the second term needs to be corrected by a factor of m_r/m to reproduce Bohr energy level. The different mass dependence from the two terms shows that we cannot do finite mass corrections to Dirac energy levels by simply substituting m by m_r. An improved theory was given in [89], where an effective Dirac Hamiltonian H^{Dirac} was obtained by introducing a Breit potential:

$$\begin{aligned} V_{Br} = \frac{\pi Z\alpha}{2}\left(\frac{1}{m^2} + \frac{1}{M^2}\right)\delta^3(r) - \frac{Z\alpha}{2mMr}\left(\boldsymbol{p}^2 + \frac{\boldsymbol{r}(\boldsymbol{r}\cdot\boldsymbol{p})\cdot\boldsymbol{p}}{r^2}\right) \\ + \frac{Z\alpha}{r^3}\left(\frac{1}{4m^2} + \frac{1}{2mM}\right)[\boldsymbol{r}\times\boldsymbol{p}]\cdot\boldsymbol{\sigma}, \end{aligned} \tag{2.113}$$

and the Breit Hamiltonian in the external Coulomb field:

$$H_{Br} = \frac{\boldsymbol{p}^2}{2m} + \frac{\boldsymbol{p}^2}{2M} - \frac{Z\alpha}{r} + V_{Br}. \tag{2.114}$$

The Dirac equation result [89] for H_{Br} was presented in the form:

$$E^{tot}_{njl} = m + M + m_r[f(n,j) - 1] - \frac{m_r^2}{2(m+M)}[f(n,j) - 1]^2 + \frac{(Z\alpha)^4 m_r^3}{2n^3 M^2}\left(\frac{1}{j+\frac{1}{2}} - \frac{1}{l+\frac{1}{2}}\right)(1 - \delta_{l0}). \quad (2.115)$$

In the above equation, the third term corresponds to the finite nucleus mass correction to the Dirac energy in a static Coulomb potential field. The last two terms are recoil corrections.

In Eq. (2.115), the major contributions come from the first three terms, so states with the same quantum number n and j are degenerate. In 1947, Lamb and Rutherford [93] measured the energy difference between $2S_{1/2}$ and $2P_{1/2}$, with the result around 1 GHz. And the $2S_{1/2}$ level is actually higher than $2P_{1/2}$ level. The large difference cannot be explained by the l quantum number dependence in Eq. (2.115), because the last term related to l only contributes about 2 kHz. This clearly does not comply with the predictions of Dirac theory. This phenomenon is called the Lamb Shift. The first explanation was given by H. A. Bethe in [94], the major contribution comes from electron self-energy or vacuum polarization, which in Feynman diagrams is represented by an electron emits and then absorbs a virtual photon.

Generally speaking, the "Lamb Shift" refers to any deviation from the energy levels predicted by Dirac equation. The various contributions to Lamb shift can be classified into four groups [90], listing in decreasing order: radiative correction, recoil correction, radiative-recoil, and finite nuclear size correction. Radiative correction is the major contribution, account for QED effects like self-energy, or vacuum polarization; Recoil correction is due to the finite mass of nucleus; Radiative-recoil correction takes into account mixed radiative and recoil contributions; Finite nuclear size correction originates from the fact that nucleus is not point-like.

Determining the proton charge radius r_p or the Rydberg constant R_∞ from hydrogen spectroscopy can be pushed to very high accuracy [95]. The principal methodology usually involves measuring the transition energy between two different energy levels, and the extraction of r_p and R_∞ requires detailed calculation of all the cor-

rection terms to the Dirac energy levels in QED framework, some of these terms are dependent on r_p. A detailed description of this process is given in [96] [37]. Due to the simplicity of the hydrogen atom, theoretical calculations for hydrogen can be carried out with very high accuracy [95], reaching a precision of up to the 12^{th} decimal place, making the Rydberg constant the second most accurately determined fundamental constant next to the electron spin g-factor.

The most precise measurement of r_p was carried out through muonic hydrogen spectroscopy in 2010. Muonic hydrogen is a bound state of a muon orbiting a proton, and it is not stable. The muon itself is an unstable subatomic particle, it decays into at least three particles through weak interaction:

$$\mu^- \rightarrow e^- + \bar{\nu}_e + \nu_\mu, \tag{2.116}$$

where ν_μ is muon neutrino, $\bar{\nu}_e$ is anti electron neutrino. The lifetime for that process is about 2.2×10^{-6} s. The muonic hydrogen spectroscopy experiment was performed at the Paul Scherrer Insitute (PSI) in Switzerland, using its proton accelerator πE5 beam line [1]. To create short-lived muonic hydrogen atoms, the researchers developed a low-energy μ^- source, and attached it to the πE5 beam line [97]. The muon beam was first sent to a 5T solenoid equipped with two muon detectors triggering the arrival signal, and then the through muons were stopped in the following 20 cm long target vessel filled with 1 hPa (hundred Pascal) H_2 gas, where highly excited μp atoms ($n \approx 14$, where n is the principle quantum number) were formed (see Fig. 2-17). About 99% of the muonic atoms de-excite into the $1S$ state immediately, around 1% stay at the long-lived $2S$ state ($\tau_{2S} \approx 1$ μs). Then a short laser pulse with a wavelength around $\lambda \approx 6\mu m$ enters the cavity, pumping up the muonic hydrogen from $2S$ state to $2P$ state, and then the $2P$ state ($\tau_{2P} = 8.5$ ps) μp immediately de-excite into $1S$ state, emitting a 1.9 keV X-ray. The researchers obtained a resonance curve by measuring the pumping laser wavelengths when the 1.9 keV X-rays occur in time-coincidence. Through this method, they obtained a resonance curve centred at 49,881.88(70) GHz, with a width of 18.0(2.2) GHz. This frequency corresponds

to an energy of $\Delta E = 206.2949(32)$ meV, leading to a proton charge radius of $r_p = 0.84184(36)(56)\ fm$ [1]. This result is 10 times more precise than the previous normal hydrogen spectroscopy, and 26 times more precise than the previous electron proton elastic scattering.

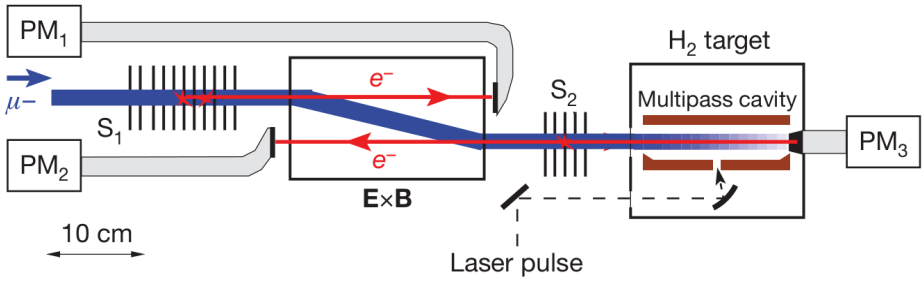

Figure 2-17: Muon Beam [1]. S_{1-2} are ultra-thin carbon foils, electrons will be emitted from these foils when μ^- pass through, the red electrons will be separated from μ^- beam by $E \times B$ drift, and then reach the scintilators. PM_{1-3} are photomultiplier tubes, reading signals from the scintilators. The μ^- beam is stopped in the Multipass cavity, where μp atom will be generated.

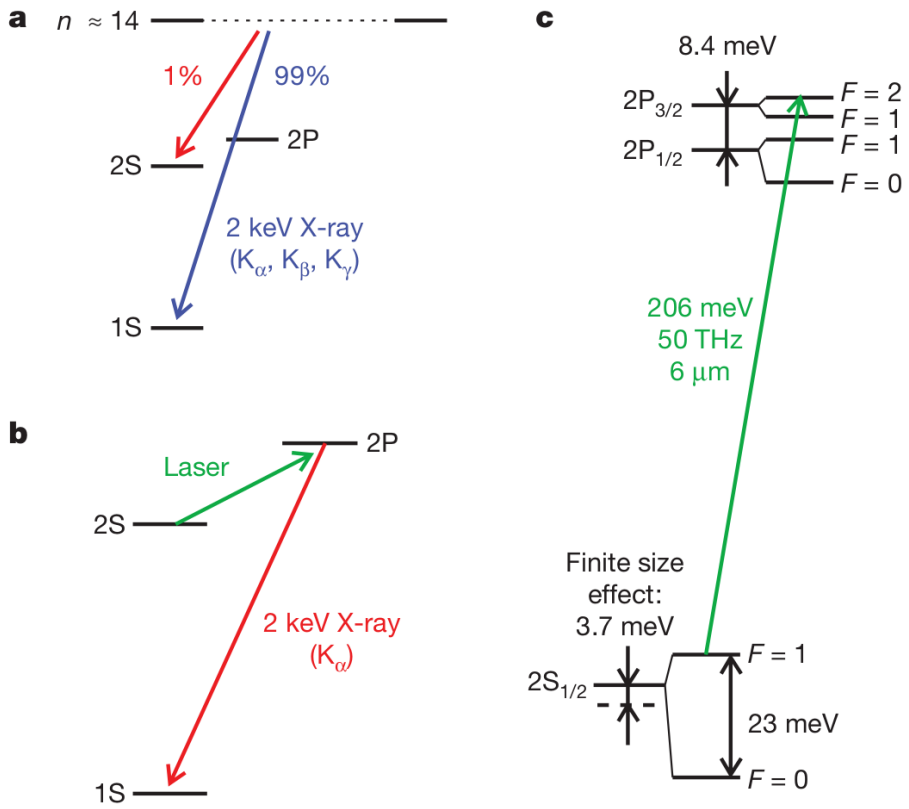

Figure 2-18: Muonic hydrogen energy levels [1], cascade and experimental principle in Muonic Hydrogen. (a) about 99% of muonic hydrogen de-excite directly to 1S state, 1% remain in the metastable 2S state. (b) 2S state muonic hydrogen are pumped into 2P state using $\lambda = 6\ \mu m$ laser, 2P state immediately de-excite to 1S sate. (c) Vacuum polarization dominates the μp Lamb shift.

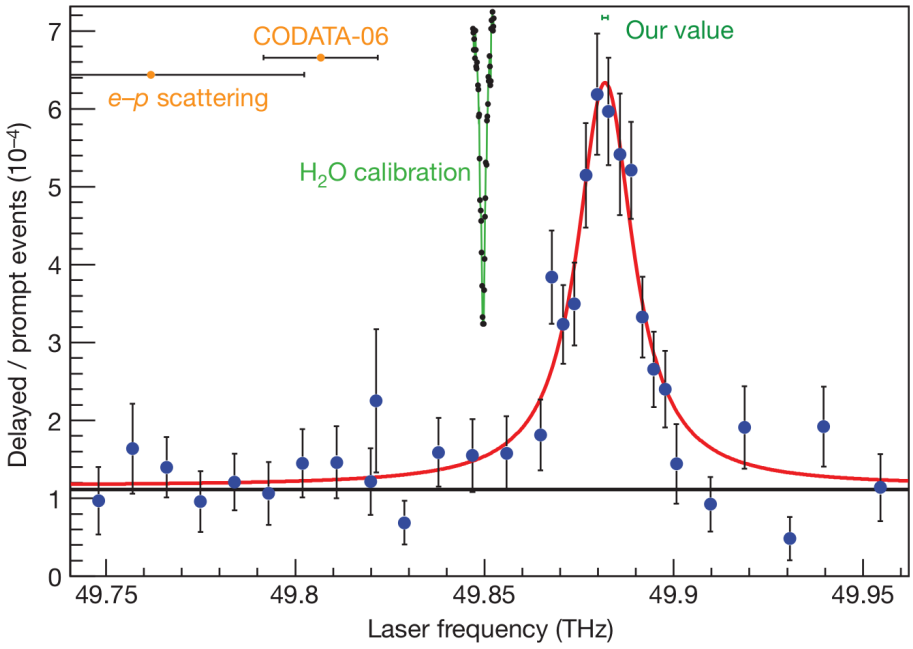

Figure 2-19: Resonance measured in the μp proton radius determination [1]. The resonance spectrum for pumping laser measured in coincidence with K_α X ray. Black dots are the calibration measurements using water absorption. The expected resonance position using the proton radius of CODATA-06 and $e-p$ scattering are shown for comparison.

Chapter 3

The PRad Experiment

3.1 Overview

The PRad experiment (E12-11-106) [11] was designed to investigate the proton charge radius crisis using electron proton (ep) elastic scattering. Compared with previous ep scattering experiments, the innovative part of PRad is that it would not use the bulky magnetic spectrometers. Due to the large volume of these spectrometers, it is usually difficult to reach very forward scattering events. The PRad experiment was performed at Jefferson Lab (JLab) in Hall B in June, 2016. It used two beam energies, 1.1 GeV and 2.2 GeV. Both its electron beam and cryo-cooled hydrogen gas target were un-polarized. It was the first physics experiment after the 12 GeV upgrade of Jefferson Lab was completed.

The Q^2 (4 momentum transfer squared) coverage of PRad is around $2.1 \times 10^{-4} - 0.06$ $(\mathrm{GeV}/c)^2$. The goal of PRad is to measure proton charge radius within sub-percent precision. A series of techniques were designed to control experimental uncertainties. First, in order to reduce the background coming from target cells, which is a major source of systematic uncertainty for previous scattering experiments, a windowless gas flow target was used for PRad. The hydrogen gas continuously flows into the target cell, and then exits the cell through two orifices on the two ends of the cell. The beam would pass through these orifices without hitting anything but the target gas. Second, the ep cross section is normalized to the Møller cross section

(electron electron scattering, ee). Electrons are elementary particles, they have no internal structure, and the Møller cross section can be calculated with high precision in QED (see Chapter 2). The Møller scattering and ep scattering are detected using the same detector setup simultaneously, thus the normalization process cancels the necessity of beam luminosity normalization. Last, in order to reduce the background from beam-line, PRad utilized a two stage vacuum box between its target and detectors.

A pair of high efficiency, high resolution GEM chambers for improving position detection of the scattered electrons was used. These GEM chambers were designed and constructed by UVa detector group in 2015. The radiation length X_0 of GEM chambers is low, thus secondary scatterings from GEM chamber materials were negligible. The energy detection was from a hybrid calorimeter (HyCal). In this chapter, we will describe all the components of the PRad setup except the GEM chambers. The GEM chambers will be discussed in detail in the next chapter.

3.2 The Experiment Setup

The PRad experimental setup is shown in Fig. 3-1. The electron beam goes from left side to right side. Starting from the left side, the main components of the setup include:

1) The photon tagger. The photon tagger [98] was used to generate a photon beam out of the electron beam, which was used during HyCal calibration run. The photon tagger is composed of a thin foil radiator in the front and a single dipole magnetic (shown in red color) in the back. When the electron beam passes through the radiator, photons are generated by the Bremsstrahlung effect. Then the electron is deflected away from its original direction by the magnets, leaving only photons to continue along the beam line. Under the dipole magnet is a hodoscope. The hodoscope contains two planar arrays of plastic scintillators to detect energy-degraded electrons from the radiator. The first layer of 384 partially overlapping small scintillators (E-counters) detects the electron energy; the second layer of 61 larger scintillators (T-counters) provides the timing signal. The timing signal is necessary to form a co-

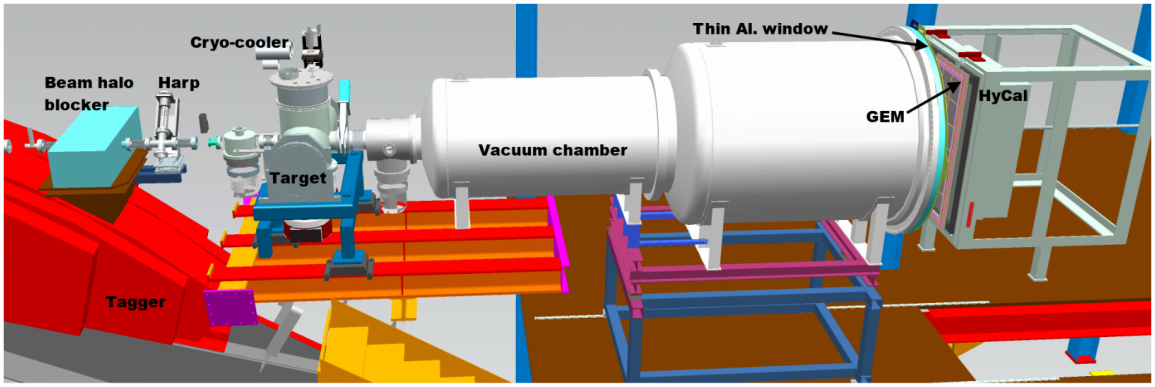

Figure 3-1: The PRad experimental setup.

incidence with signals from the corresponding nuclear interactions triggered by the tagged photon. The energy of the photon can be determined by the difference between the original beam energy and the electron energy from the E-counters:

$$E_\gamma = E_{beam} - E_c, \tag{3.1}$$

where E_c is the electron energy measured by E-counters. The energy resolution of E_γ is around $10^{-3}E_{beam}$. The timing resolution is about 110 ps. The photon tagger was not used in production runs.

2) The beam halo blocker. The beam halo blocker is a cylinder made of nickel with an inner diameter around 1.27 cm (smaller than the beam pipe inner diameter 4.75 cm) and an outer diameter around 9.91 cm. The length is 29.97 cm. It is used to block the beam halo electrons (electrons outside the core beam with very low density, $< 10^{-6}$ compared to the core beam). However, due to the fact that the electron beam has an approximately 25 micro rad divergence, there were some electrons hitting the edge of the halo blocker and introducing a higher background rate at the forward angle. A detailed Geant4 simulation was carried out for the halo blocker and will be discussed in later chapters.

3) The harp scanner. The harp scanner [27] was used to determine the beam position and profile. It consists of a vacuum tube and a "fork" (aluminum support frame) inside it. Two or three tungsten wires are rigidly held on the fork. Two

perpendicular wires can be seen in Fig. 3-2. while in operation, the fork is slowly

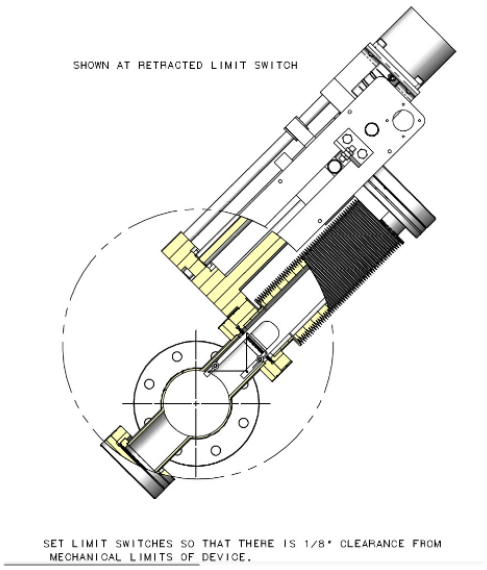

Figure 3-2: The harp structure [27].

moved by a stepping motor; the wires hanging on it will be hit by the beam. At different position, different part of the beam profile hits the wire, resulting a different charge deposition on the wire. Thus by measuring the charges collected by the wire, one can determine the beam position and profile. An example harp scan is shown in Fig. 3-3.

After the harp scanner, there are 4) PRad gas flow target, 5) vacuum chamber, 6) GEM detectors, and 7) HyCal calorimeter. These components will be discussed in the following sections.

3.3 The Electron Beam

The electron beam was provided by the Continuous Electron Beam Accelerator Facility (CEBAF) at Jefferson Lab (JLab). Jefferson Lab finished its 12 GeV upgrade program [99] in 2014[1]. After the upgrade, there are 4 experimental Halls: A, B, C

[1]The accelerator finished upgrade in 2014, while the experimental equipment upgrade continued in the following years.

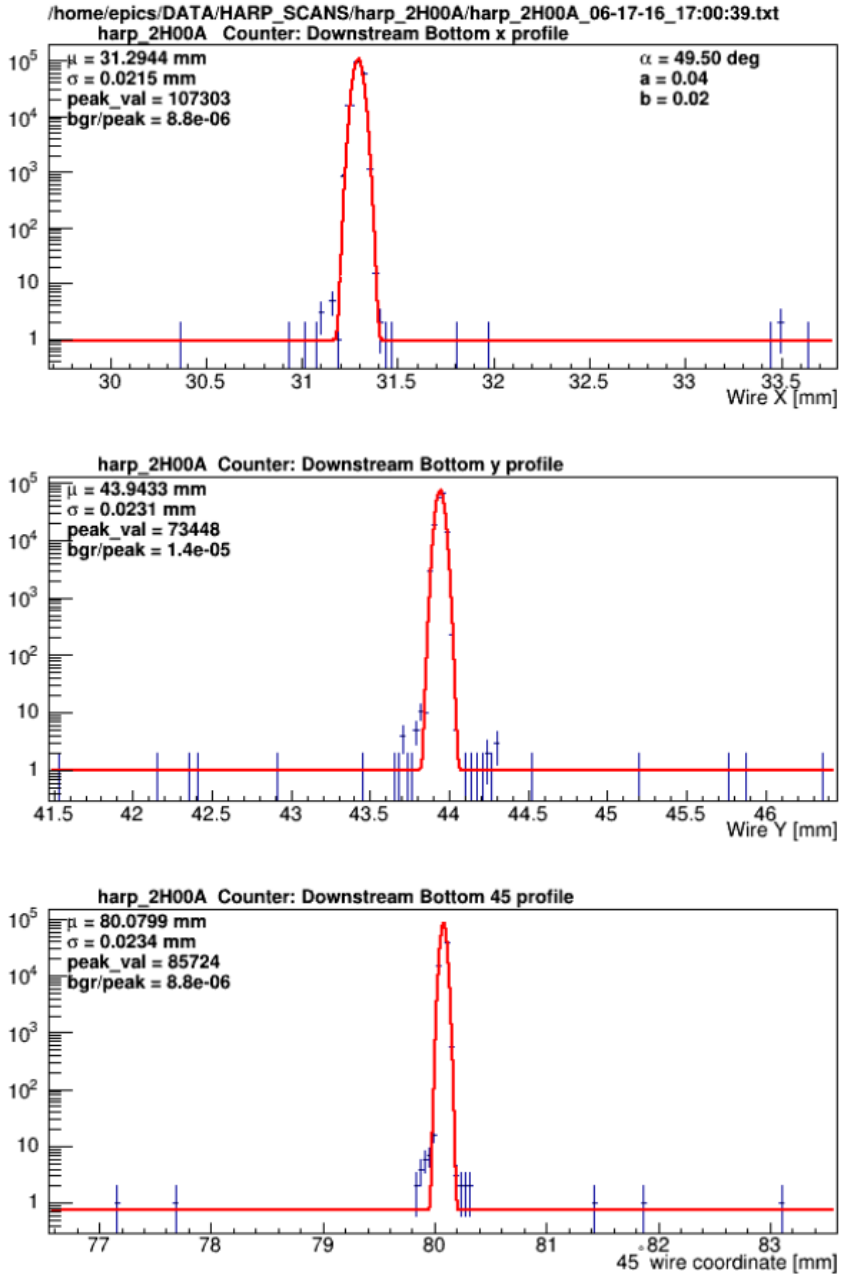

Figure 3-3: Beam profile from harp scan. The top plot shows the beam profile in X direction; the middle plot is for Y direction; the bottom plot shows the beam profile in the inclined direction 45° to the X axis. The red line is a Gaussian fit to the measured data.

and D (see Fig. 3-4). CEBAF can provide different beams to different Halls concurrently. CEBAF is a recirculating linear accelerator (linac) [99]; it consists of two linac sections and two recirculating arc sections. A linac section consists of 20 cryomodules before the upgrade, each cryomodule contains 8 superconducting RF cavities. One cryomodule can add 25 MeV acceleration to the electron, with the 20 modules adding a total around 0.5 GeV acceleration. One pass contains 2 linac sections providing a total of 1 GeV to the accelerated electrons. The recirculating arcs contain quadrupole and dipole magnets, it recirculates the electron beam back to the linac section for continued acceleration. There are 5 lines of recirculating arcs, which gives a maximum of 5 GeV with actual performance up to 6 GeV for the electron beam after 5 pass.

After the upgrade [100], one cryomodule can add up to 100 MeV acceleration to the electron (compared to 25 MeV before the upgrade), and 5 more cryomodules were added to each linac section. Under normal operation, each linac is now capable of adding 1.1 GeV acceleration. With 2 linac sections in each pass, and a total of 5 pass can provide 11 GeV acceleration with actual performance up to 12 GeV to Halls A, B, C and D.

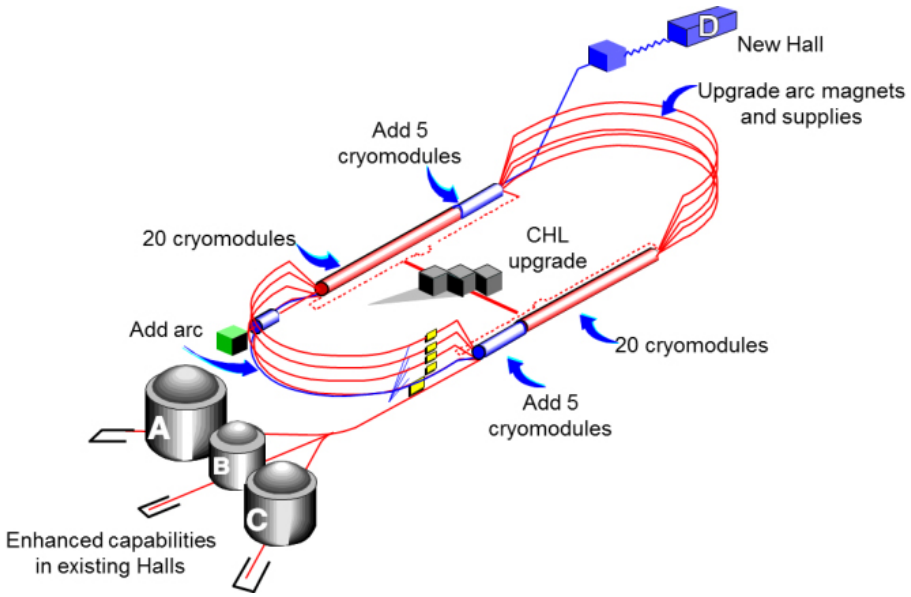

Figure 3-4: Jefferson Lab accelerator beam line.

PRad experiment was carried out in Hall B with two beam energies, 1.1 GeV and 2.2 GeV. The calibrated beam energies for the runs are given in Table 3.1: Due to the

Beam Energy (MeV)	Uncertainty (MeV)
1101.0	0.5
2143.0	1.5

Table 3.1: Beam energy.

higher elastic cross section at lower energies, the beam current for 1.1 GeV runs were 10 nA and 15 nA; while 2.2 GeV runs mostly had 55 nA, with a few runs at 15 nA, 25 nA and 40 nA for calibration runs using carbon foil target. The beam position was constantly monitored by Beam Position Monitors (BPM) installed behind HyCal. The beam profile was monitored by the harp scanner before the target, as indicated in the previous section.

3.4 The Windowless Hydrogen Target

The target for PRad was a windowless hydrogen gas flow target. The target cell was made of high conductivity copper C101, with a length of 4 cm, as shown in Fig. 3-5. The two ends of the cell was sealed by Kapton foils with orifices at the center. During operation, cold H_2 gas (temperature around 20 K) continuously flowed into the target cell, and exited the cell through the two orifices. The electron beam will pass through the orifices without hitting anything. Thus eliminating the possibility for background coming from target cell windows.

The target cell was installed inside the target chamber, Fig. 3-6. Three Pfeiffer 3200 turbo pumps were installed around the target chamber to remove the H_2 gas and maintain a stable gas pressure. The target cell was suspended in the chamber using a carbon fibre tube. Its position could be adjusted through a 5-axis motion controller. In each run, before the data taking the target cell position was fine-tuned to ensure that its orifices were aligned with beam line.

The target gas was cooled to a a temperature around 20 K by a Cryomech pulse tube refrigerator PT810 before it flowed into the target cell. The temperature and pressure of the target gas was continuously monitored by various gauges installed in different locations inside the target chamber. For production runs, the pressure in

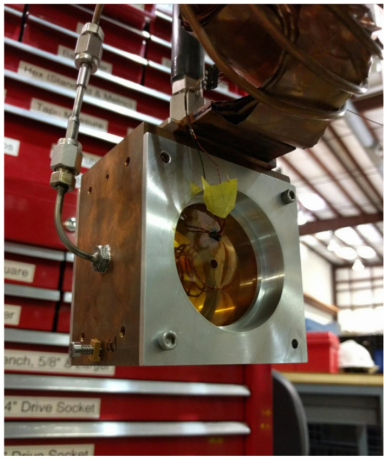

Figure 3-5: PRad target cell. The orifice can be seen in the middle of the Kapton foil.

target cell was maintained at around 480 mTorr, with an areal density corresponding to about 2×10^{18} H atoms/cm^2. In the rest of the regions of the target chamber, the gas pressure was about 2.5 mTorr.

3.5 The Hybrid Calorimeter

The hybrid calorimeter (HyCal) consisted of 1152 PbWO4 modules and 576 Pb-glass modules. The 1152 PbWO4 (crystal) modules were arranged in a 34 by 34 array, taking up the inner area. There was a hole in the center of the array, equivalent to an area of 2 by 2 crystal modules. The hole allowed the beam pipe to pass through. The 576 Pb-glass modules were divided into 4 parts, each part was arranged into a 6 by 24 array, and placed on one side of the crystal area. The layout is shown in Fig. 3-7.

The size of one crystal module is $2.076 \times 2.076 \times 18$ cm^3 (see Fig. 3-8); the radiation length of it is around 20 X_0. In order to improve the light collection efficiency, each crystal module was wrapped with a 100 μm thick VM2000 reflective material and a 36 μm Tedlar foil.

The size of one Pb-glass module (see Fig. 3-8) is $3.815 \times 3.815 \times 45$ cm^3, corresponding to a radiation length of around 17 X_0. The Pb-glass modules are also

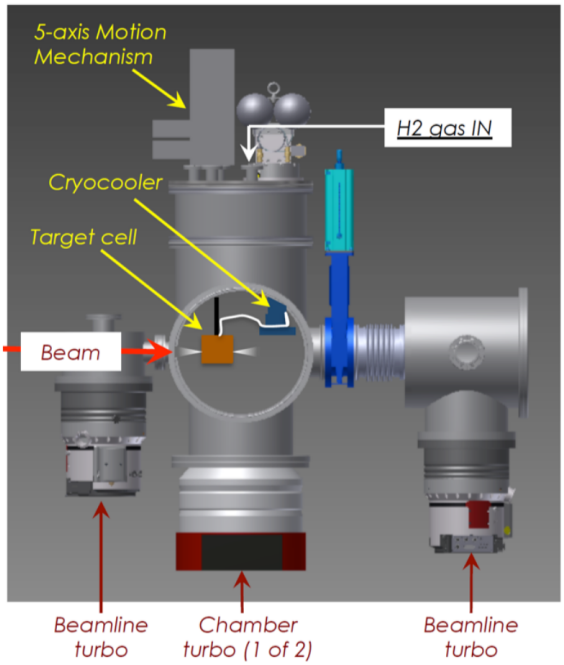

Figure 3-6: PRad target chamber schematic.

wrapped with 25 μm aluminized mylar foil.

A cubic tungstate absorber is placed in front of the HyCal around the hole area, covering up 12 crystal modules of the most inner layer. The tungstate absorber can partially block scattered events going to the most inner layer, hence protect the most inner layer from ultra-high scattering event rate. In PRad setup, the scattering angle for the most inner layer was around 0.6°, a cut was used in physics analysis to remove electrons below this angle.

Electromagnetic calorimeters measure particle energy through electromagnetic shower effect [101]. They are designed to completely stop the incident particles, so that the energy of the incident particle can be completely deposited in the calorimeter and converted to light. The crystal module is of a scintillating material, the charged particles in the shower produce fluorescent light through ionization effect; the Pb-glass module is a Cherenkov calorimeter, the charged particles in the shower produce light through Cherenkov effect. The light was collected by a PMT (photon multiplier tube) attached to the back of each module. The amplitude of the PMT output signal is proportional to the energy deposited in the module. A proportionality constant is

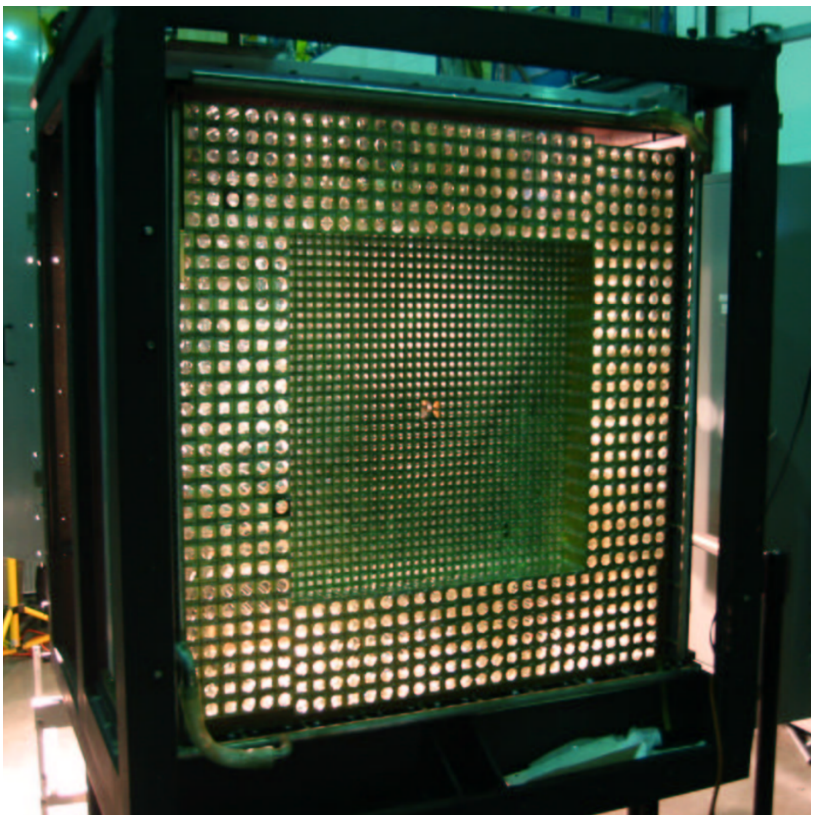

Figure 3-7: HyCal front side view. The center are crystal modules and sides are Pb-glass modules.

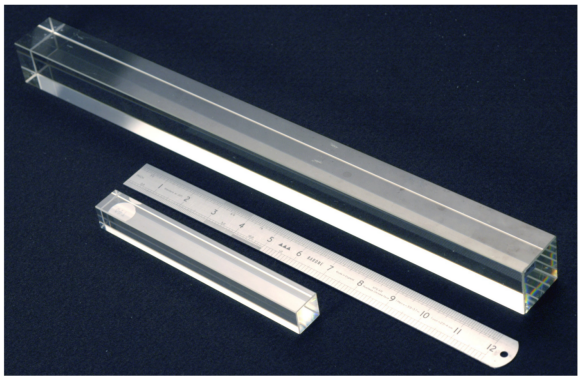

Figure 3-8: HyCal modules, the smaller one is the PbWO4 crystal module, the larger one is Pb-glass module.

used so that the deposited energy can be determined using the PMT signal amplitude. These constants are usually obtained through a specific calibration run. For Hycal, during the calibration run, a photon beam with known energy was sent to the face of the detector and is perpendicular to the face, the calibration constant was obtained for each module.

During the experiment, the calibration constant may change with time. A light monitoring system (LMS) was developed to monitor the stability of the calibration constant for each module. The system had a pulsed nitrogen laser, the light produced by the laser was sent to each HyCal module through a bundle of optical fibres. These fibres were attached to the front side of each module. Meanwhile, the laser light was also sent to three reference PMTs. One can monitor the ratio between the reference PMT signal and HyCal module signal, and if this ratio changes, a correction factor to the calibration constant can be achieved by the following formula:

$$g_i(t) = \frac{(A_i/A_r)_t}{(A_i/A_r)_0}, \tag{3.2}$$

where A_i is the signal amplitude from the i^{th} module of HyCal, A_r is the signal amplitude from the reference PMT. The subscript 0 represents the initial measurement, the subscript t represents the measurement at time t.

3.6 DAQ system

The Jefferson Lab Hall B CEBAF Online Data Acquisition (CODA) was used for PRad data acquisition (DAQ). The CODA system records data from detector electronics and writes them to disk in binary format (evio format). A total volume around 1 PB (Petabytes) of raw data was recorded. Considering this large volume, the data was moved to Jefferson Lab silo tape system after preliminary check during the experiment. The schematic of PRad DAQ system is shown in Fig. 3-9. The trigger is from a HyCal total sum of all its PMT signals. Both the dynode signals and anode signals from each module's PMT were used. The dynode signal was used for timing,

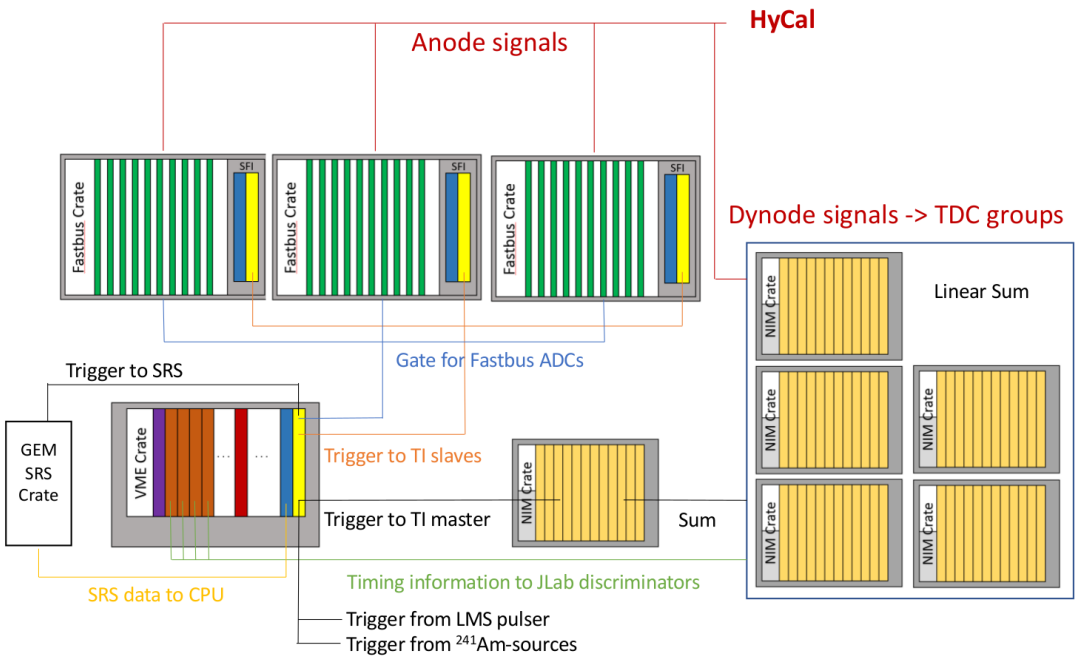

Figure 3-9: The schematic layout of PRad DAQ system. This plot is from Chao Peng at Duke University.

the anode signal was written to the data stream after being digitized.

Three FastBus protocol crates were used for recording anode signals, these FastBus crates were reused from the previous PrimEx experiment. A total of 30 LeCroy ADC1881M modules installed in these crates were deployed to record anode signals from all 1728 HyCal modules. The integral time window for the anode signals was 280 ns. Then the anode signals were digitized and written to the data stream.

The dynode signals from the 1728 modules were grouped into 52 Time Digital Converter (TDC) groups. Signals in one TDC group were summed together linearly using UVA120A summing modules. The generated 52 TDC signals were recorded by the CAEN v1990 TDC modules, and saved in the data stream. These TDC signals contain HyCal cluster timing information. At the same time, a copy of the 52 TDC groups were all summed together forming a total sum signal. The total sum signal serves as the trigger for the whole experiment. The signal was first sent to a NIM level-translator module and was converted to ECL level. Then the ECL level signal was sent to the Trigger Interface (TI) master. The TI master distributes this trigger

signal to different TI slaves which are synchronized with it. The TI slaves provide triggers to different components of the experiment including GEM detectors.

The Experimental Physics and Industrial Control System (EPICS) information was also recorded in the data stream. The EPICS monitors beam line conditions and other experimental conditions, such as beam position, beam current, detector gas pressure, gas flow rate, etc. The EPICS event was taken periodly. Approximately 8000 physics events follow one EPICS event. EPICS events continuously monitor the running conditions. If an EPICS event behaves abnormally, the batch of physics events closest to this EPICS event would be discarded.

The DAQ dead time was monitored by scaler events. Every 20 to 50 seconds, a 2.0 MHz pulser sent a series of events to the DAQ system, the dead time was estimated using:

$$t_{dead} = \frac{N_{gated}}{N_{total}}, \tag{3.3}$$

where N_{total} is the total counts from the pulser, and N_{gated} is the total counts while the DAQ system is occupied. During PRad experiment, the typical live time ($t_{live} = 1 - t_{dead}$) for production run was around 80% to 90%, for empty target run was around 95%.

The beam charge was recorded by a Faraday cup installed in the beam dump. The uncertainty of the charge measurement was approximately 0.1%. The live charge was calculated using

$$C_{live} = (1 - t_{dead}) \times C_{total}. \tag{3.4}$$

This live charge was used in background subtraction during physics analysis.

Chapter 4

GEM Detector

The Gas Electron Multiplier (GEM) detector was first introduced by Fabio Sauli in 1997 [102]. Similar to Resistive Plate Chamber (RPC) detector [103] and Multiwire Proportional Chamber (MWPC) detector [104], GEM detector also belongs to the Micro Pattern Gaseous Detector (MPGD) type of detectors. Compared to MWPC or RPC, GEM is designed to survive the high rate, high resolution environment in modern high energy and nuclear physics experiments. The spatial resolution of GEM is typically around 50 - 100 μm, and it can survive a particle rate around a few MHz per square centimeter. GEM detectors can be built into various sizes and shapes. They are widely used as the tracker part for modern spectrometers, such as COMPASS [105] and SBS (Super BigBite Spectrometer) [106] [107] [108]. The PRad experiment utilized a pair of GEM detectors for scattered electron position detection. The detectors were designed and constructed at UVa detector Lab in 2015, the size of each was around 55 cm by 120 cm. At the time these were the largest GEM detectors in the world. In this chapter, we will give a detailed description of the PRad GEM detectors.

4.1 GEM Overview

The key components of GEM detectors are GEM foils. The GEM foil has a sandwich-like structure [109] [110], as shown in Fig. 4-1. It is made of a 50 ± 1 μm thick Kapton

foil with a 5 ± 1 μm copper/chromium coating on both sides. During operation, the GEM foils are installed in a chamber filled with Argon/CO2 gas mixtures.

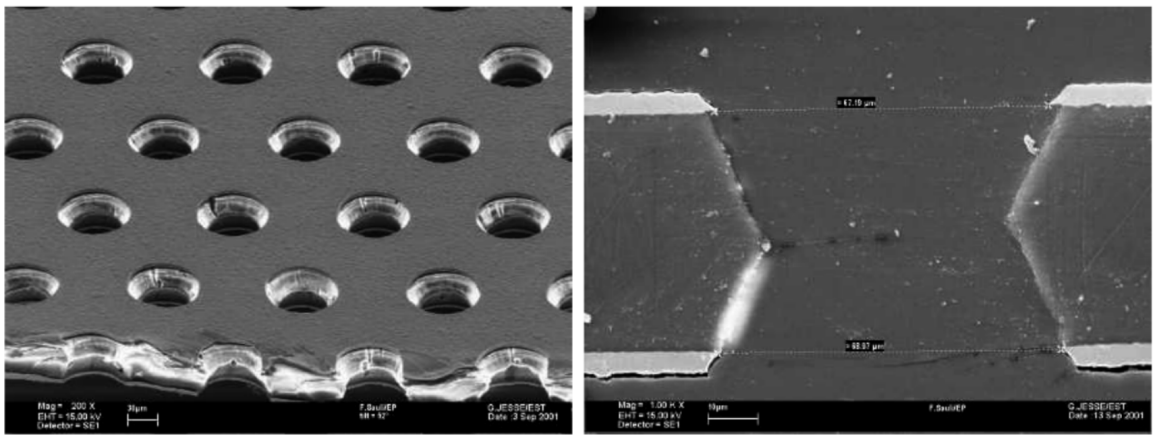

Figure 4-1: Microscopic picture of a GEM foil. The left plot shows the distribution of the double conical shaped holes; the right plot is a cross section plot for the hole structure.

GEM foils have double conical shaped holes etched through using lithography technology. The typical diameter of the hole is 70 ± 5 μm on the two ends, and 50 ± 5 μm in the middle, the pitch (typical distance between two holes) is approximately 140 μm.

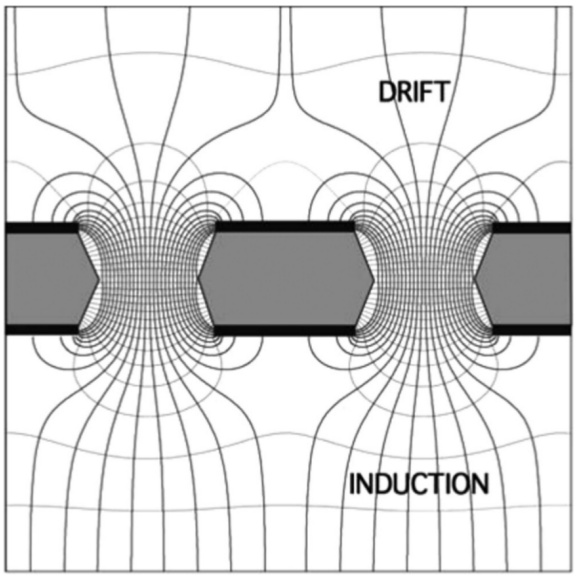

Figure 4-2: Electric field and equipotential line in the area of a GEM hole.

During operation, an electric potential difference around 200 V - 300 V is applied

on the two metal layers of the GEM foil, see Fig. 4-2. The potential difference creates a strong electric field inside the holes. Electrons released in the upper region will drift towards the hole and gain sufficient energy in the hole area and causing more ionizations of the molecules of the filling gas. The electrons released from the ionizations again acquire sufficient energy from the field and continue the process. This process is called electron avalanche, see Fig. 4-3. The avalanche electrons will be collected by the readout strips under the GEM foil, and then the electric current signal on the strips can be interpreted by the front end electronics.

The working gas used for PRad GEMs was a mixture of 70% (by volume) Argon and 30% carbon dioxide. The noble gas Argon serves as the ionization gas which releases electrons during avalanche. However, in the collision process between the accelerated electron and the filling gas molecule, the gas molecule may be raised to an excited state but not ionized. Then photons can be produced by gas de-excitation, these photons are capable of causing secondary ionizations elsewhere by interacting with less-tightly bound electrons and intensify the avalanche. Since photons cannot induce electric signals in the readout strips, thus the electron gain is limited to 10^3 before continuous discharge (sparking) occurs [111], discharges can easily damage GEM foils and the readout strips. Hence CO2 gas was added to serve as a quencher. It absorbs photons and dissipates energy through dissociation and elastic collision.

A GEM detector contains multiple layers of GEM foils. The PRad GEM chamber is a COMPASS-like triple foil detector, as shown in Fig. 4-4. It consists of three layers of GEM foils separated 2 mm away, and a drift cathode layer 3 mm above the top GEM foil, and then a readout board 2 mm below the bottom GEM foil.

The primary ionization happens in the drift area, as shown in Fig. 4-4, which is induced by the interaction between incident particles and the filling gas. In PRad case, the incident particles mainly include electrons and photons. The ratio of counts of photons to electrons was about 0.4% - 0.5%, which had been measured in the GEM efficiency study. For electron, the energy deposition in GEM region is mainly through collision (Moller scattering) and radiative effect (Bremstrahlung effect, higher order loop contribution etc). When the electron energy is low (smaller than a few tens

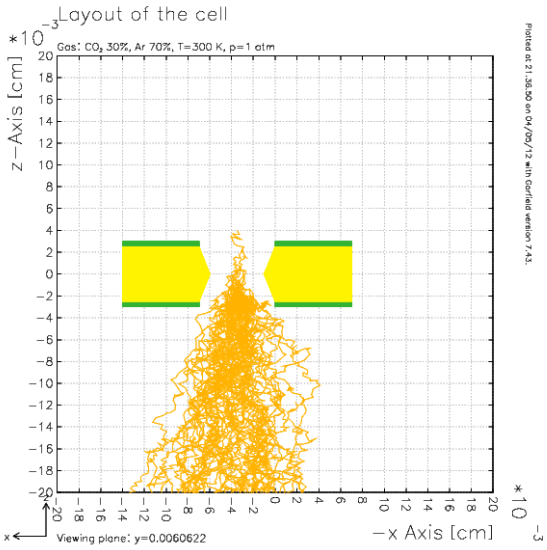

Figure 4-3: A Garfield [28] simulation for the avalanche process inside GEM hole, the brown lines represent for ionized electrons, the electric field was calculated using a finite element analysis package neBEM.

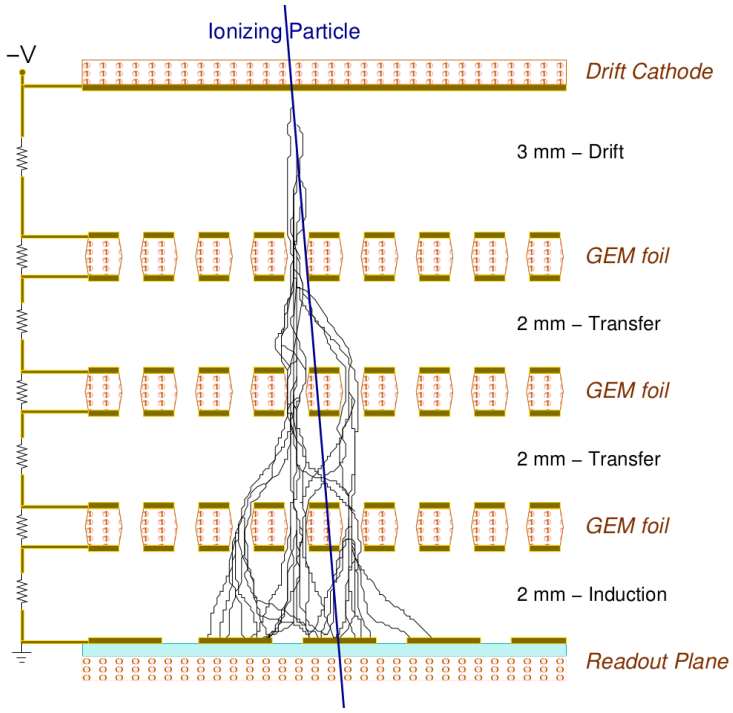

Figure 4-4: The typical structure of a triple foil GEM detector.

of MeV), the collision effect dominates, when the energy is high, the radiative effect dominates. The energy deposition for relativistic electron through matter is described by the Bethe-Bloch formula, Eq. (33.23) in [112] :

$$\langle -\frac{dE}{dx} \rangle = \frac{1}{2} K \frac{Z}{A} \frac{1}{\beta^2} \Bigg[\ln \frac{m_e c^2 \beta^2 \gamma^2 m_e c^2 (\gamma - 1)/2}{I^2} + (1 - \beta^2) - \frac{2\gamma - 1}{\gamma^2} \ln 2 + \frac{1}{8} \left(\frac{\gamma - 1}{\gamma} \right)^2 - \delta \Bigg], \quad (4.1)$$

where $-dE/dx$ is called the stopping power (typically in the unit of MeV/cm), Z is the charge number of the matter, A is the atomic mass number, I is the mean excitation energy, β is electron velocity, $K = 4\pi N_A r_e^2 m_e c^2$ with $r_e = e^2/(4\pi\epsilon_0 m_e c^2)$ being the classical electron radius, and $\gamma = 1/\sqrt{1-\beta^2}$. The mass stopping power (stopping power divided by density) of Argon for electron passage is shown in Fig. 4-5. For gas mixtures, the stopping power is weighted by the following formula:

$$\langle \frac{dE}{dx} \rangle = \sum_i w_i \langle \frac{dE}{dx} \rangle_i, \quad (4.2)$$

where w_i is the weight ratio, and i sums over all types of gas in the mixture. The number of total electron-ion pairs is given by:

$$n = \frac{\Delta E}{W_I}, \quad (4.3)$$

where ΔE is the total energy deposition, W_I is the average energy required to generate one electron-ion pair. For Ar/CO2 (70:30) gas mixture, $W_I \approx 26\ eV$.

After the creation of electron-ion pairs in the drift area, as shown in Fig. 4-4, the ions drift upward towards the cathode, and the electrons drift towards the opposite direction to the readout plane. As we already mentioned, when the electrons go through the holes of the GEM foils, they will be accelerated by the strong field inside the holes and collide again with the gas molecules. Further ionizations will be induced, the process repeats and finally causes the avalanche. For these ionizations,

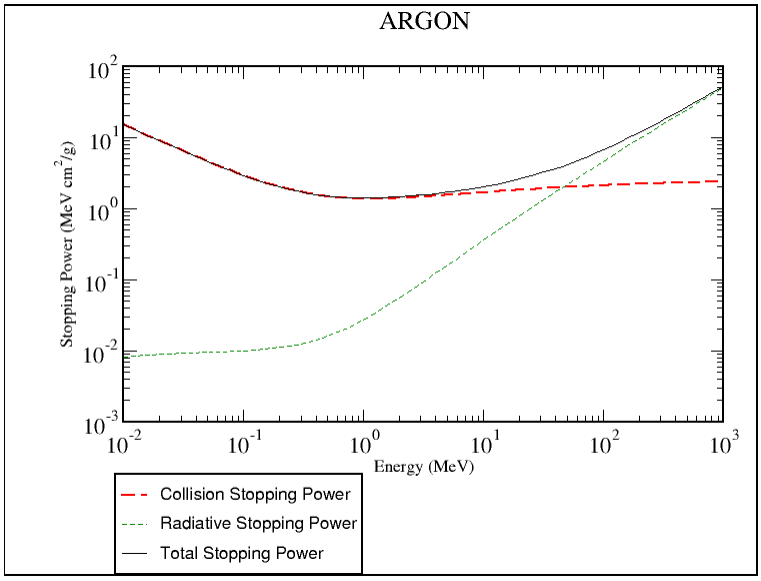

Figure 4-5: The mass stopping power of Argon for electron passage [29]. This plot was produced from the NIST website.

the majority part of the ions will be collected by electrodes on the GEM foil, thus reducing the large detector dead time caused from ion back drifting.

The potential difference on each foil was carefully configured using a resistor voltage divider, resulting in a gain factor for each foil to be around 20. After three layers of amplification, the total gain was around 8000. Then the avalanche electrons were collected by the readout strips. For PRad, a Cartesian $X - Y$ readout pattern was used, see Fig. 4-6. The readout strips were connected to the APV25 [113] electronic front-end boards. Each APV25 chip has 128 channels, and a total of 72 APV25 electronic boards were used in the experiment. The signals from all channels were sampled concurrently and pre-amplified on the APV25 boards. A multiplexer inside the APV25 chip reorganized the signal data from its 128 channels according to a predefined sequence, and then forwarded them serially to an ADC board through HDMI cables. The ADC board was connected to a FEC (Front End Concentrator) board which directly sent the digitized data to the DAQ PC through a RJ45 interface. More details will be discussed in section 4.3.

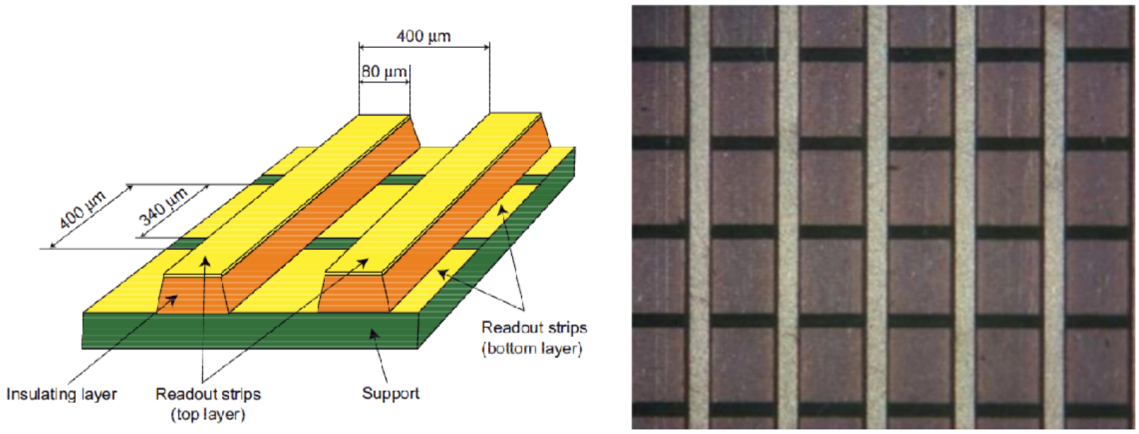

Figure 4-6: Readout board for GEM detectors. The left plot shows the size and structure, the right plot is an image from microscope inspection, where the vertical thin brighter strips are top readout strips, the horizontal wider brighter strips are bottom readout strips. The readout strips are etched from copper layers. The insulation between the top and bottom strips is of Kapton material.

4.2 Design & Construction

The detector was designed by the UVa physics detector group, and assembled in a class-1000 clean room at the UVa physics department. The foils were manufactured by CERN, and the frames were fabricated in a commercial factory in Belgium.

Each gem foil has 64 sectors, each sector has an area around 100 cm^2. Before the construction, the GEM foils were first checked using a microscope in the clean room visually. The purpose for this step is for quality check and broken area localization. After the visual check, the foil were installed in a high voltage box filled with nitrogen, and a 550V potential difference was applied to each sector, one at a time. The purpose was to check the leakage current for every sector. The pass criteria was that the leakage current for each sector was less than 5 nA.

The frames were made of fiberglass-reinforced epoxy material Permaglas[1], and were re-polished before the assembly. Frames consist of wide (15 mm) fringes and inner thin spacers (300 μm), as shown in Fig. 4-7. The spacers and the inner side of the fringes were carefully polished using a fine-grade sand paper, the purpose for this step was to remove all protruding glass fiber ends in case they damage the GEM foil.

[1]From Permali, distributed by Resarm Engineering Plastics in Belgium, http://www.resarm.com

Then the frames were cleaned in an ultra-sonic washing machine filled with de-ionized water for 15 minutes. The cleaned frame was thoroughly dried after 3 to 4 days. Then the frame was moved to the varnish room for varnish (Polyurethane, Nuvovern LW + Hardener[2]) coating. The purpose for varnish was to prevent surface irregularites, residual fiber ends or sharp edges. After varnish, the frames were moved to the clean room for assembly.

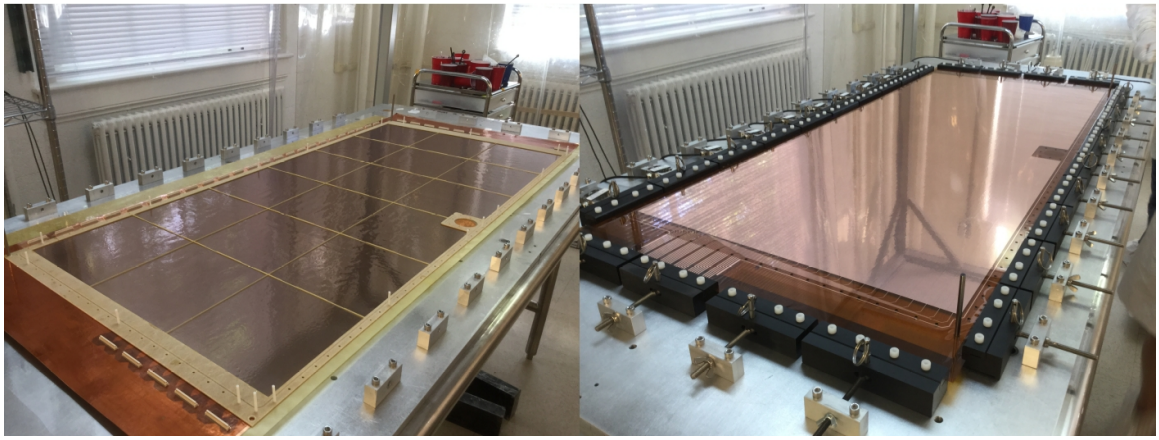

Figure 4-7: The left plot shows a GEM frame glued on top of the readout board, the thin grids are spacers. The right plot shows the assembly of the GEM foil stretcher and a stretched GEM foil sitting on it ready for gluing. The aluminum blocks in both plots are anchors for clamps. The black blocks in the right plot are clamps used in stretching. The tension gauges can be seen in the right plot by the left edge of the stretcher.

During the assembly, each foil was glued[3] onto a corresponding frame. In order to do this, the GEM foils first needed to be stretched. A 188 $cm \times 86$ cm stretcher was designed and manufactured by the UVa detector group for this purpose. In the stretching process, the foils were placed on the stretcher and held in place by plastic clamps, as shown in Fig. 4-7. The clamps were fastened three times to ensure a tight contact with the GEM foil. Clamps on two out of the four sides of the stretcher were connected with force sensors. During stretching, the tension applied on each clamp was around 5.8 N/cm. The tension was fine-tuned for each clamp to remove wrinkles and ripples on the foil.

[2]Distributed by Walter Mäder AG, http://www.maederlacke.ch
[3]A resin epoxy (Araldite AY103 + HD991 Hardener.)

In the gluing process, a thin layer of glue was first applied to the frame edges using a syringe. Then the frame was aligned with the stretched foil using four dwell pins and pressed onto the foil with the glue side facing the foil. In order to maintain a tight contact between the GEM foil and the frame, a 1 cm thick poly-carbonate plate was placed on top of the frame, and then a number of lead bricks were placed on top of the cover along the frame edges. It took 24 hours for the glue to dry. The GEM foils, cathode foils, readout foils, and gas windows were all glued using this method.

Beside the gas window on top of the chamber, we also designed a bottom gas window to be attached underneath the readout plane. The bottom gas window was used to balance the gas pressure applied on top of the readout board. During the PRad operation, the gas flow rate was set to around 5 litres per hour considering its large volume, which is twice the flow rate of normal SBS GEM chamber commissioning. This would introduce a relatively high pressure inside the chamber. In order to ensure that the readout board does not bend under the pressure (which will cause a Z position error), we introduced the bottom gas window. The bottom gas window used an independent gas flow line in order to keep the GEM chamber gas line intact. The gas window also used the gluing technique during assembly.

When the gluing for each foil was finished, they were glued together to close the chamber. This process was performed in another station inside the clean room. The bottom gas window was placed on the station first with the frame side on top, then a thin layer of glue was again smeared on the frame surface, and the readout board was directly glued on top of it. A 24 hour time period was set for the glue to dry. The GEM foils were processed in a specific sequence, so that when the frame gluing was finished for each foil, it could be directly installed on the chamber assembly station. Chamber would be closed with gluing the final top gas window.

The last step inside the clean room was gas connector installation. The connectors were also glued to the chamber. For PRad chamber, there are 6 gas connectors designed on each of the two shorter sides of one frame, see Fig. 4-7, one side for gas inlet, the other for gas outlet. It also took 24 hours for the glue to dry.

Once all gluing was finished, the chamber was taken out of the clean room into a

detector lab to continue assembly. In the detector lab, a thin layer of sealing material was smeared on the four edges in order to avoid gas leaking. After that the chamber was inspected for gas leaking using a CO2 gas sensor. Then the chamber was flushed with nitrogen gas to maintain a low humidity inside the chamber.

After the sealing was done, another leakage current check with high voltage was performed for each GEM foil. This step served two purposes. The first one was to check that the foils are still intact after assembly; the second purpose was to burn all tiny particles inside the closed chamber using high voltage. The final step was soldering. Each gem foil needs a resistor divider board to accept the high voltage. The board was soldered directly on the copper pads on GEM foils.

The whole assembly for each chamber took about 3 weeks, and a total of two chambers were made. After the assembly, a quick cosmic test was performed in the UVa detector lab. Then the chamber was sent to Jefferson Lab for installation and commission. The final setup at Jefferson Lab is shown in Fig. 4-8.

4.3 DAQ

The scalable readout system (SRS) [114] [30] [115] was used to serve as the DAQ system for PRad GEM detectors. SRS was developed by RD51 collaboration [115] for R&D on MPGD gas detectors. It was originally configured with CERN DATE/Amore DAQ software. During PRad commission, we integrated the SRS system to Jefferson Lab CODA DAQ software. In order to do this, both the firmware and driver package need to be modified. The firmware modification was done by Jefferson Lab staff Benjamin Raydo, and the driver package was developed by Jefferson Lab staff Bryan Moffit.

The SRS system consists of 1) Analog Pipeline, Voltage mode (APV) hybrid boards for reading analog signals from GEM detectors; 2) Analog Digital Converter (ADC) boards for converting analog signals to digital signals; 3) Front End Concentrator (FEC) cards for organizing the digitized data into TCP/IP packets; 4) Scalable Readout Unit (SRU) for transferring the data to DAQ PC and receiving

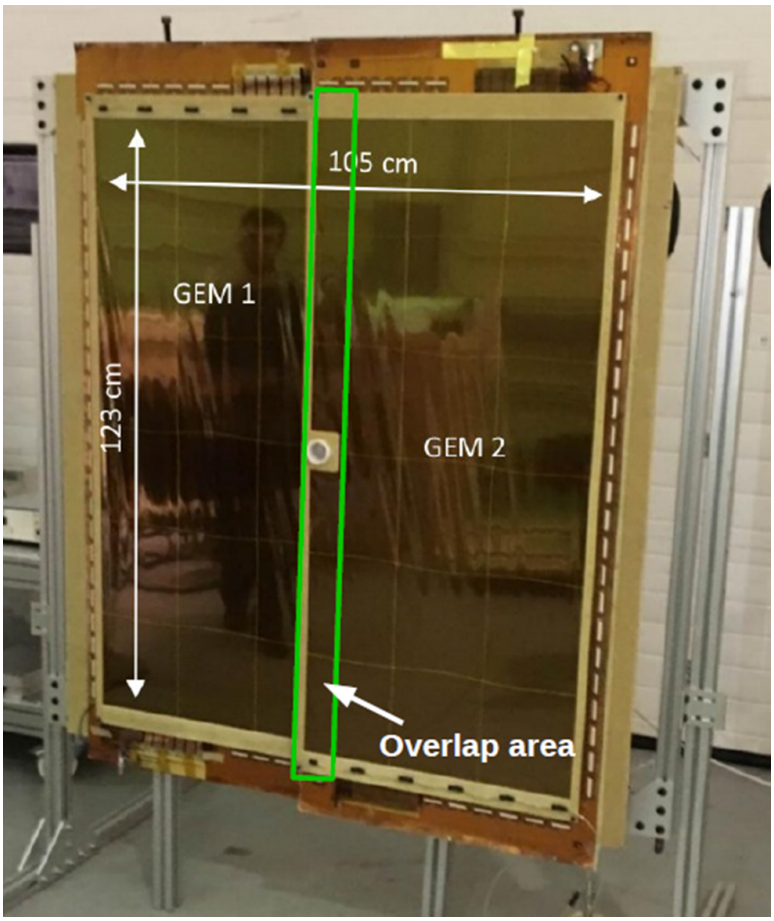

Figure 4-8: PRad GEM detector setup at Jefferson Lab. The central hole is for beam pipe to pass through.

trigger signals; and 5) Data Acquisition (DAQ) PC housing the InfiniBand adapter for data throughput and a TI-PCIe card for trigger process. The architecture for SRS is shown in Fig. 4-9. The trigger system setup is shown in Fig. 4-10.

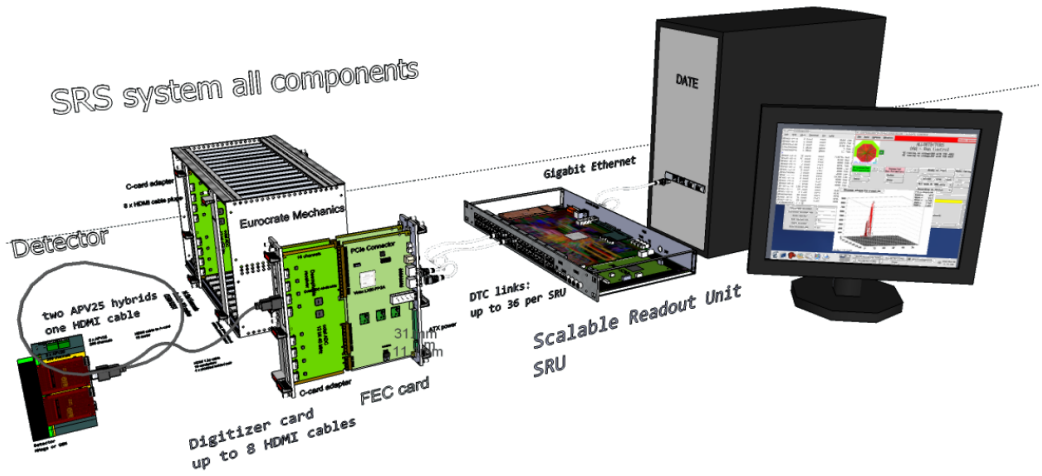

Figure 4-9: The SRS architecture [30].

For PRad setup, the two GEM chambers have a total of 9216 readout channels/strips; which required 2 SRU units, one for each chamber. Each SRU processed data from 1 SRS crate; and one SRS crate housed 4 FEC cards. A total of 2 SRS crates were used in the experiment. Every FEC card was paired with one ADC board. One ADC board held 8 HDMI interfaces, where each HDMI interface has 2 ADC channels. One ADC channel corresponded to one APV hybrid board, where one APV board has 128 channels. In order to read the 9216 channels, a total of 72 APVs were used. The event rate during the experiment was around 4 kHz, and the total data transfer rate was about 200 MB/s to 300 MB/s. A 10 Gbps fibre link was used to transfer data to DAQ PC.

The APV hybrid board [113] is a circuit board housing an APV25-S1 chip. The APV25 (Analog Pipeline, Voltage mode) chip is an ASIC (application specific integrated circuit) type chip customized for multi-channel strip readout detectors, one APV chip contains 128 channels. Each channel consists of a pre-amplifier and a shapper circuit. The 128 channels in the APV chip drives a 192 column analogue memory. During operation, the APV chip constantly sample signals at a 40 MHz

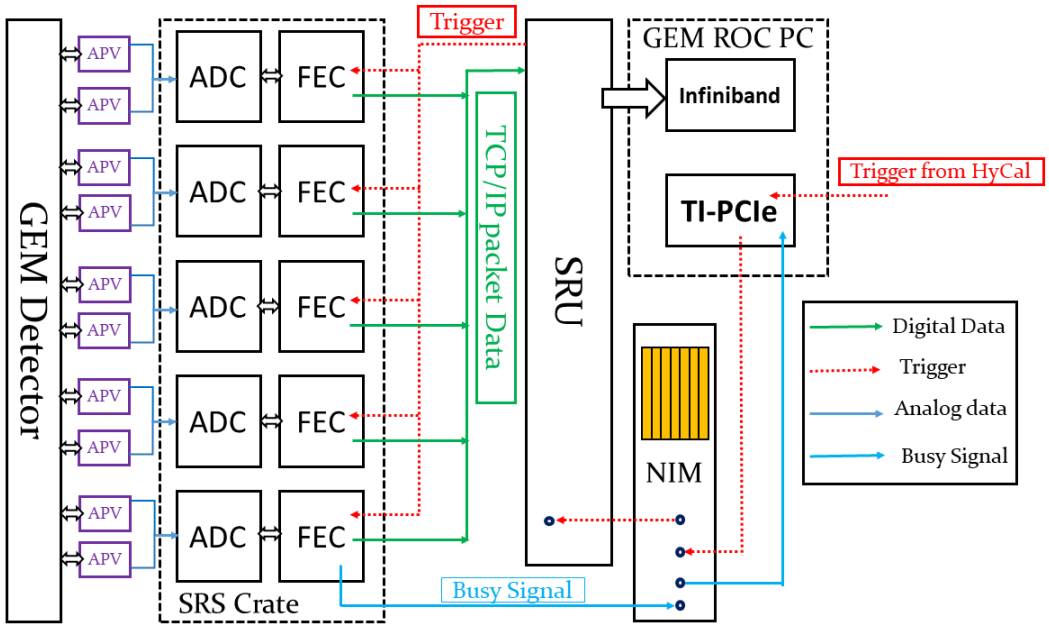

Figure 4-10: PRad GEM DAQ trigger setup.

frequency (25 ns period), which is the same as the CERN beam line accelerated particle bunch frequency, such that a synchronization can be achieved between the beam line and the APV sampling. However, in general, one usually don't have 40 MHz frequency incident particles, thus there's usually a $\pm 12.5\ ns$ timing jitter. The jitter usually doesn't matter if one take more than 3 time samples for every signal, as 3 time samples have enough redundancy to accommodate the timing jitter.

The 192 column analogue memory is organized in a circular loop form, with APV constantly write data into this memory. When the memory is full, the earliest data in the column will be overwritten by the latest writing. This mechanism ensures that the APV memory always contains the most recent data. A data access mechanism was designed to access the memory. It allows marking and queuing of specific locations of the memory. After receiving the trigger, the FEC can decide which location (offset) of the APV memory to be read out for the current event. The memory offset value is set from slow control commands, it depends on the timing difference between the external trigger and the APV timing. It is carefully tuned in the experiment by searching for the optimum latency between them.

The ADC board and FEC card combination receives data from APV hybrid cards. The two boards are connected back to back, the combination takes up the volume of 1U in a Eurocrate, as shown in Fig. 4-9. The ADC board houses a 8-channel 12-bit ADC converter, designed by the RD51 for APV25 readout. The key module of the FEC card is a Xilinx Virtex-5 LX50T FPGA chip [115]. It allows 16-bit read/write transaction at a 400 MHz data rate. The FPGA chip organizes data into UDP packets, and then send the data to DAQ PC through TCP/IP interface. During PRad operation, initially the UDP processing of APV data was coupled with APV sending data, which would have limited the event ratio to no more than a few hundred Hz. Therefor the FPGA was reprogrammed for PRad. A memory space in the FPGA was reserved for trigger buffering, thus the APV sending data and UDP processing can be executed asynchronously. This improved the event rate to 4 kHz with a live time around 90%. The test result is shown in Fig. 4-11.

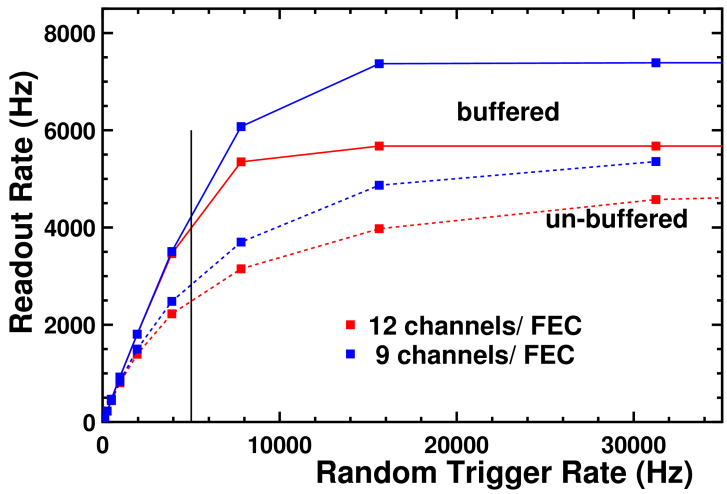

Figure 4-11: Trigger rate throughput capability. The vertical line marks the PRad experiment rate requirement, the 9 channels buffered line (top) was used for PRad. This plot was produced using test data provided by Ben Raydo in the Jefferson Lab fast electronic group and Kondo Gnanvo at University of Virginia. The plot was made by Prof. Dipangkar Dutta at Mississippi State University.

The SRU unit acts more like a hub, it collects all the FEC data and send them to the DAQ PC through a 10 Gbps fibre link. The SRU and FEC cards all have specific assigned IP addresses. As shown in Fig. 4-10, the external trigger is the same with other detectors in PRad setup, namely the HyCal total sum. The external trigger was first processed by a TI-PCIe (Trigger Interface using PCI-express data bus) interface card [116] designed by Jefferson Lab DAQ group. This card first check the busy signal from FEC cards, if it is not occupied, then it sends the trigger to the SRU for data recording. The TI-PCIe card accepts ECL level, a level converter was used to covert electric signal levels between NIM and ECL. The SRU dispatches the trigger signal to all the housed FEC cards through a Fan-in/Fan-out NIM module, and the latency between these triggers was written into APV cards through slow control commands.

4.4 Calibration

The GEM detectors improved PRad position resolution by at least 20 times in comparison with HyCal. In physics analysis, all HyCal reconstructed cluster positions were replaced by the corresponding GEM cluster positions through matching. Thus GEM detectors played a key role in improving PRad scattering angle and Q^2 resolution. In this section, we will give a detailed discussion on GEM cluster reconstruction, efficiency, resolution, offset correction, and a few other issues such as cross talk.

4.4.1 Cluster Reconstruction

As already mentioned in the DAQ section, there were a total of 9216 channels in PRad GEM detectors, 128 channels for each APV. During operation, signals from all these channels were recorded and analyzed. The signals from one strip is shown in Fig. 4-12, where 15 time samples were used, each time sample takes 25 ns. The red line is a fitting using

$$V = A \times \frac{t-\mu}{\tau} e^{-(t-\mu)/\tau}, \tag{4.4}$$

where A is the signal amplitude, μ is the time offset between the first time sample which has non-zero ADCs and the APV start-sampling time, τ is the time constant for the decay of the signal. In reality, it is not necessary to take 15 time samples. For PRad, 3 time samples were used to reduce the sampling time and improve event rate. Fig. 4-13 shows the recorded signals (the composition of the signals can be found in [117]) from the 128 channels in one APV card, where 6 time samples were used, this data is taken from PRad commissioning.

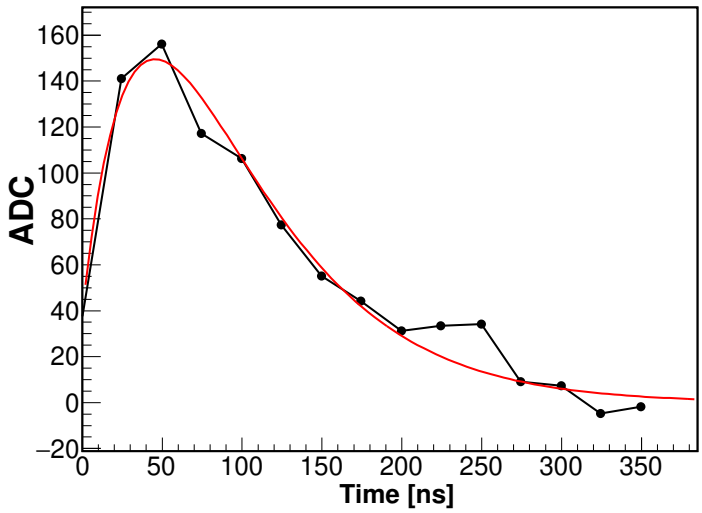

Figure 4-12: Signals from one strip. In this plot, 15 time samples were used.

In Fig. 4-13, the dotted red line indicates the common mode level, which depends on the electric potential applied on the APV chip. The two dotted black lines mark the range of noise fluctuation. The large downward pointing lines in each time sample are the ADC signals from fired strips. The multiple vertical lines between each two time samples are header signals produced by APV chip, which have a specific characteristic ADC value (<1500 in this case, the 1500 was set as the APV header ADC level), this is to provide marks for separating different APV time samples.

In order to do clustering, one needs common mode correction, zero suppression, and strip mapping. A pedestal run was designed for this purpose. During a pedestal run, the beam was turned off, so that there would be no fired strips due to incident beam electrons. The GEM voltage and gas flow rate were kept the same. Consid-

ering the running conditions were slightly changing over the time during the PRad experiment, we took 20,000 events as pedestal events at the beginning of each run. These events were used for common mode and noise level estimation. The common mode level was taken as the ADC average from all time samples for each strip. The noise level was taken as the RMS value of all time samples from the 20,000 events after subtracting the common mode for each strip. This analysis was done strip by strip, and the analysis results was used in signal extraction.

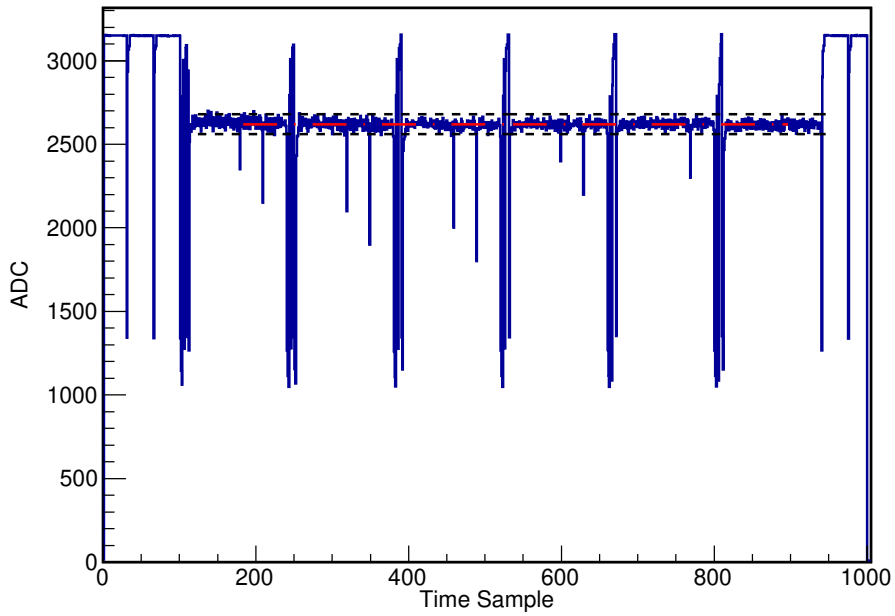

Figure 4-13: The output from one APV card in one event. The X axis is samples, Y axis is ADC. There are a total of 6 time samples in this plot, each time sample contains 128 channels. The red dotted line represents the common mode, the two black dotted lines mark the range of noise fluctuation.

The average noise is defined as the RMS (σ) value of the noise ADC distribution after common mode subtraction, the value of σ for each strip in PRad experiment was around 6 - 14 ADCs. A 5σ cut criteria was required for a strip to be recognized as fired:

$$\mathrm{ADC}_{\mathrm{strip}} > 5 \times \sigma. \tag{4.5}$$

During zero suppression, for each strip, the common mode offset was first subtracted

from its raw ADC, then the remaining value was compared with 5σ. If the remaining ADC is smaller than 5σ, then the ADC value was set to 0 for that sample of that strip; otherwise the remaining value was taken intact as the signal ADC. The zero suppression was done time sample by time sample. In PRad case, 3 time samples were collected for each strip. If the strip was fired, there would be 3 ADCs, one ADC for each time sample, among which the maximum one was taken as the ADC amplitude of the strip signal and the other two were discarded.

After zero suppression, only the fired strips were kept for cluster reconstruction. However, as we mentioned in section 4.1, there's a multiplexer inside the APV chip which takes data from the 128 channels concurrently and output the data in a serial mode, one channel at a time clock. The multiplexer has a tree structure, it does not output channel data in their original sequence. Instead it follows

$$\text{Channel No.} = 32 \times (n \bmod 4) + 8 \times \text{INT}(n/4) - 31 \times \text{INT}(n/16), \tag{4.6}$$

where n is the order in which the channel appears in the output. Thus, one has to do a mapping between the output index and the input index to reconstruct the original order.

Besides the mapping inside APV chip, there's another mapping need to be taken care of. The APV chips are connected to GEM readout strips through a Panasonic connector, the Panasonic connector was soldered to the readout board during fabrication. The way it connects to the readout strips differs detector by detector, for example, the SBS GEM chamber has a same order between Panasonic connector and readout board strips. For PRad, the orders are different due to a special geometry requirement for the readout boards.

After the two-stage strip mapping, all fired strips were aligned in the order following their positions in the readout board. Then the consecutive fired strips are grouped together as a cluster. The cluster position was determined as the charge

gravity center of the cluster:

$$X_{cluster} = \frac{\sum_i^N X_i^{strip} C_i}{N}, \tag{4.7}$$

where $X_{cluster}$ is the reconstructed cluster position, X_i^{strip} is the strip position in readout board, C_i is the strip ADC, and i runs over all strips in this cluster. In PRad case, the average number of strips in one cluster was in the range of 3 - 4.

In case the incident particles are too close that the clusters don't have enough separation between them (for example during calibration runs, the high energy photon beam can induce pair production, of which the electron and the positron are very close in space when they hit GEM detector, and their fired strips are consecutive), a cluster split mechanism was introduced. For each group of the ordered strips, the cluster split

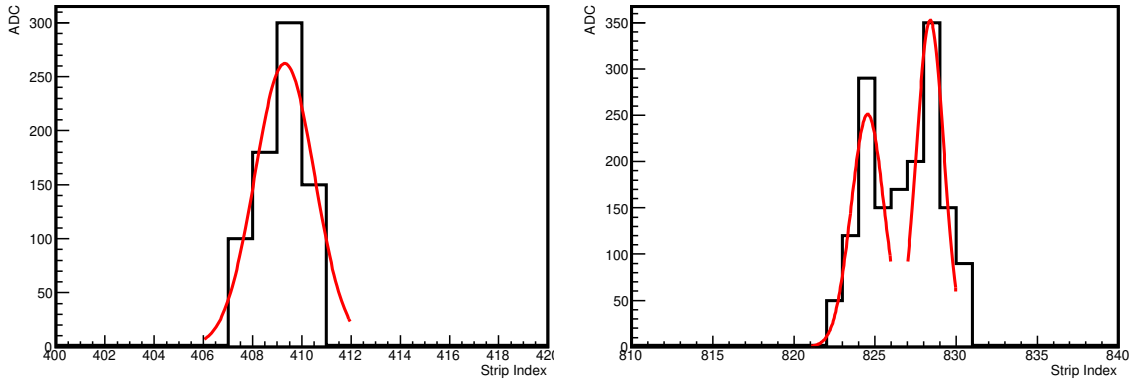

Figure 4-14: Clustering and Cluster split.

algorithm will search for a valley strip. A valley strip is defined as when its ADC value is smaller than both its adjacent strips. If no valley strip is found, then we have normal clustering, like the left plot in Fig. 4-14; if the valley strip exists, then the ADC of the valley strip will be split evenly, the two neighboring clusters get 1/2 of it each, as shown in the right plot of Fig. 4-14.

4.4.2 Cross Talk

Unlike the cross talk signals induced by capacitive, inductive or conductive coupling [118], the cross talk for APV is different. It is caused by imperfections in the timing synchronization between the APV25 clock and the SRS reading clock, which only happens on the APV25 chip level. Channels in different APVs do not have cross talk issues. When a channel has a large enough signal, its neighbouring channels, either precedent or succedent in time, will have a small parasitic signal which is usually about 10% of the original large signal. If the channel signal is not large enough, the parasitic signals usually will be cut off in the zero suppression stage.

During the readout stage, data from the 128 channels on one APV25 chip will be multiplexed out into a pipeline with a 40 MHz clock sequence. When this clock is not perfectly synchronized with the DAQ reading clock, part of the signal in one channel will fall into its adjacent channels, as shown in Fig. 4-15.

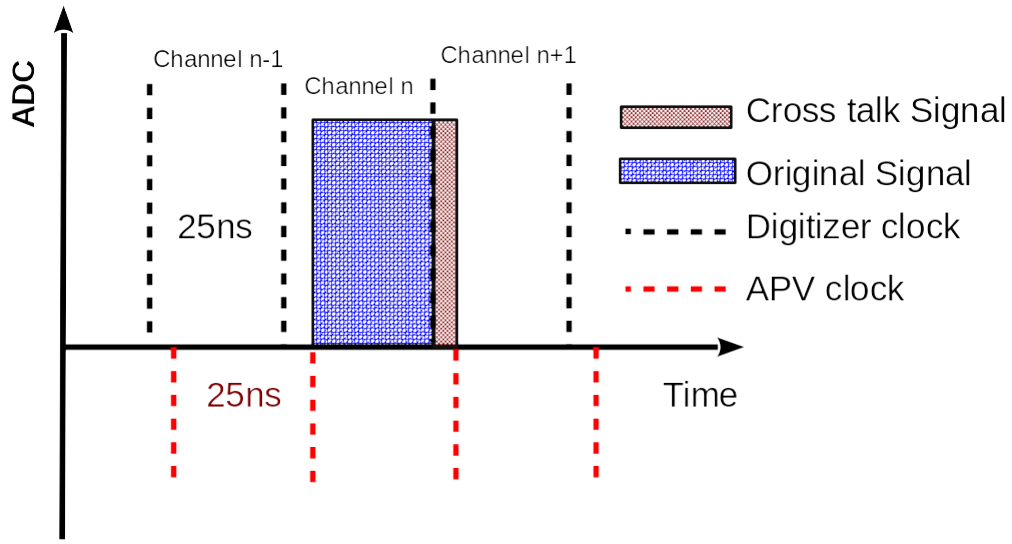

Figure 4-15: Cross Talk Issue. This plot was reproduced from the Ph.D thesis of Danning Di at University of Virginia.

The neighbouring channels on the APV chip, and also the neighbouring channels in the data stream are not physical neighbouring strips in the detector due to the multiplexer's tree structure, as shown in Eq. 4.6. To check the existence of the cross talk signals in PRad data, we checked the ADC ratio of every pair of neighboring

channels that already passed the zero suppression for one APV card. The results are shown in Fig. 4-16. Except for the unlikely case of getting two valid hits in the strip locations corresponding to two neighboring channels, both members of a pair would have valid ADC values only if a) a channel induced cross talk in its neighbour, or b) both channels had high enough pedestal noise to pass the 5σ cut. In Fig. 4-16, the peak around 12 is due to the cross talk issue. The peak at 1 is due to channel noise.

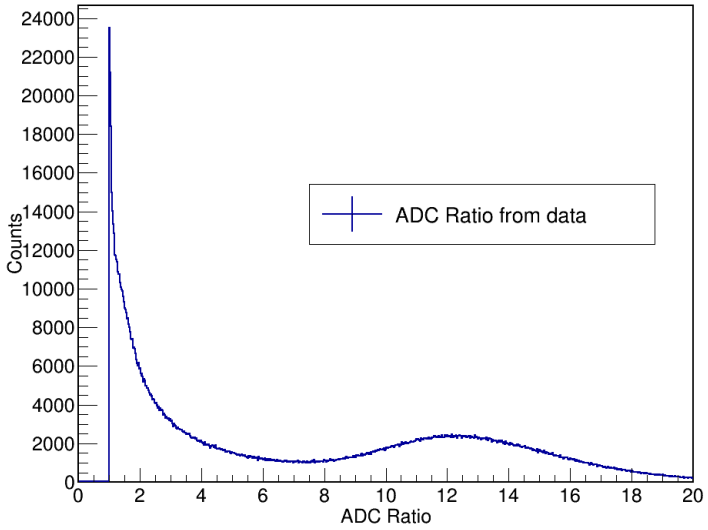

Figure 4-16: Cross talk ADC ratio between two adjacent strips from PRad experiment data. Cross talk only happens on APV chip level, this plot shows the result form one single APV chip (containing 128 channels). For this APV, we checked every pair of two adjacent channels (APV level), see if they passed zero suppression, for those pairs which passed zero suppression, take the ratio of the larger ADC over smaller ADC. In this plot, the peak around 12 is due to the cross talk issue. The peak around 1 is due to noise, which has been confirmed using a simulation as shown in Fig. 4-17.

A simulation for cross talk was also performed. In the simulation, we assumed no large signals, in other words, no channel has large enough ADC that could induce a cross talk hit large enough to pass 5σ cut. Random pedestal noise ADC was added to all channels. The noise was modeled to follow a Gaussian distribution with its mean value at 6 ADC to mimic the pedestal level of PRad data, and the ADC ratio was taken for every neighbouring channel pair that passed the zero suppression. The simulation result is shown in Fig. 4-17. As we can see in the figure, there's only one

peak at around 1, which explains the sharp peak in Fig. 4-16. The width of the two ratio=1 peaks of the two plots do not exactly agree, this is due to the fact that in the simulation we used a mean noise (6 ADC) for every channel, while in reality, different channels have different ADC mean values.

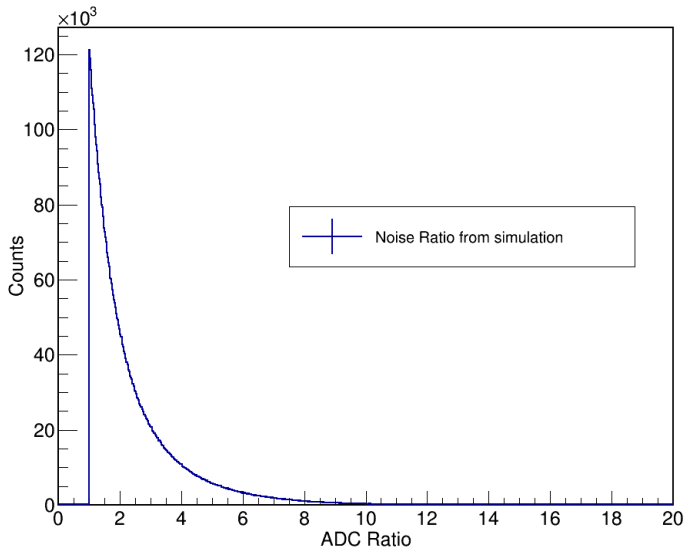

Figure 4-17: Cross talk simulation, a Gaussian noise model was used.

Due to the fact that cross talk channels are not physical neighbours, if we don't remove them before clustering, we will have fake cluster reconstructions. Thus an algorithm was introduced to remove them. The algorithm first check all neighbouring channels inside the APV chip, and then compare the ADC ratio (small over big). If the ratio is smaller than 10%, then the channel with the small ADC will be considered as a cross talk channel and discarded; otherwise it is kept intact. For PRad, since we have a GEM HyCal matching mechanism, the contamination of fake cross talk clusters is negligible after matching, around 0.012%. The possibility of real clusters being removed accidentally in this process has also been considered. The PRad GEM chambers were normally operated under a low event rate (2 kHz - 4 kHz) on the central 10 cm by 10 cm area (outer area was even lower), at this rate the possibility of false removal of a real cluster is negligible.

4.4.3 Detector Alignment

The GEM detectors were used to correct the offsets in the experimental detector setup. The offsets include 1) the offset between two GEM chambers; 2) the offset between beam line and GEM chambers; 3) the offset between HyCal and GEM chambers. Since the beam position was fluctuating from run to run, an offset table was generated for each run. The offset between the two GEM chambers was corrected first, then after aligning the two GEM chambers, the offset between beam and GEM chamber, and that between HyCal and GEM chamber were corrected.

As shown in Fig. 4-8, there's an overlapping area between the two GEM chambers. The overlap area was about 44 mm in width and 1.2 meters in height. This overlapping area played a key role in detector alignment. We developed two different methods for offset correction between the two GEM chambers, one using Møller scattering events, the other one using *ep* scattering events, both methods utilized the overlapping area.

For the Møller method, one can reconstruct the beam center using two Møller scattering events, as shown in Fig. 4-18. In this method, one collects all the Møller

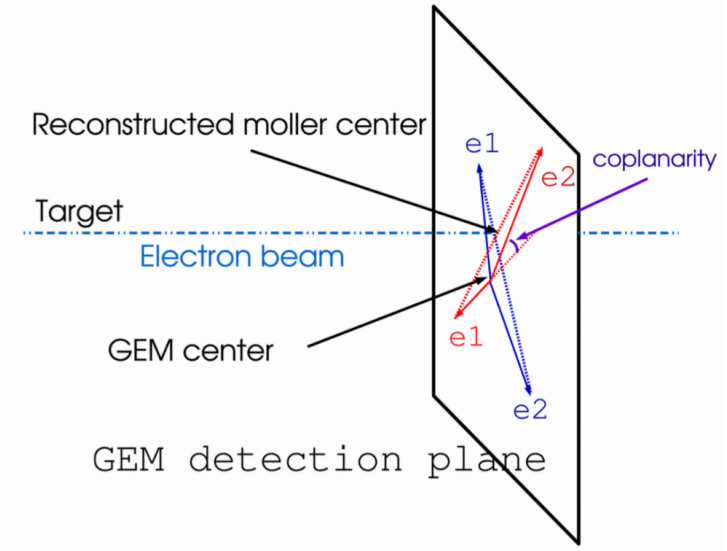

Figure 4-18: Beam position reconstruction using two Møller events.

events detected by one GEM chamber (say GEM chamber 1) in a complete production run, and group them into pairs by time order. There are two electrons in one Møller

event, so a pair of Møller events have 4 electrons. In Fig. 4-18, $e1$ and $e2$ in red color are from one Møller event detected by GEM chamber 1, $e1$ and $e2$ in blue color are from the other Møller event in this pair detected by the same GEM chamber. One can draw a line between two Møller electrons of the same event as shown by the dotted line in Fig. 4-18, then there appears an intersection point from the two dotted lines. This intersection point is called the Møller center. Since in one Møller event, the two outgoing Møller electrons form a lepton scattering plane, and the beam line (also shown in the Fig. 4-18) lies in this plane, which is true for all Møller events, so the Møller center formed in this way must be the real beam line position (X_1, Y_1) reconstructed from GEM chamber 1. The reason for using time-adjacent events (group by time order) is to avoid the beam position fluctuation issue. Similarly for GEM chamber 2, we get (X_2, Y_2). These two coordinates represent the beam line position in local GEM chamber coordinates separately. The offset between the two GEM chambers would be $(X_1 - X_2, Y_1 - Y_2)$. The disadvantage of this method is that the Møller events that can be detected by a single chamber mostly lie in the overlapping area, where we have a relatively large Y coordinate range, but a very narrow (44 mm) X range, the reconstructed Møller center usually have a large uncertainty on X direction.

The other method is using the scattered electrons from ep events (as mentioned earlier, the 4-momentum transfer in PRad experiment is low, the recoil of the proton is small, so protons were not detected in PRad experiment), as shown in Fig. 4-19. The Z positions of the two GEM chambers are from Jefferson Lab survey group with high precision. The Z difference between them is 40 mm. In order to estimate the offset between the two GEM chambers, one can project the coordinates detected by GEM1 to GEM2 from the target, then the difference between the projected position and the GEM2 measured position should be the offset between the two chambers. This method can only be applied in the overlapping area, same as the Møller method. However, the statistical uncertainty from this method is much better on both X and Y direction compared with Møller method. The reason is that the angular coverage for detecting two electrons of one Møller event in a single GEM chamber is very

limited: $< 2.5°(5.5°)$ for 2.2(1.1) GeV beam, and mostly only the symmetric Møller events[4] were used; while most of the scattered *ep* electrons are in small scattering angle, which is covered by the overlapping area.

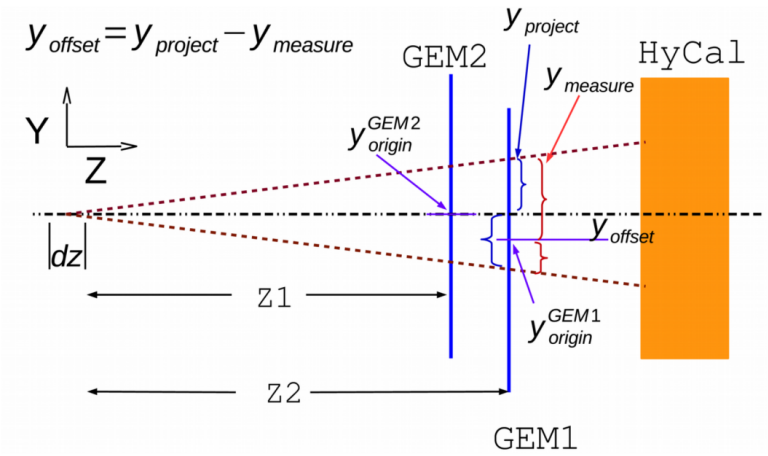

Figure 4-19: Offset correction using *ep* events.

After aligning the two GEM chambers, the beam line positions and HyCal offsets are all corrected using Møller events relative to GEM detectors. The *ep* method for HyCal is defective and discarded due to the fact that HyCal Z is not easy to accurately determine because of the shower depth effect.

After GEM detector alignment, the reconstructed beam position using Møller method is shown in Fig. 4-20, the beam position stability is shown in Fig. 4-21, the fluctuation of beam position mean value is within 50 μm in X direction, and within 35 μm in Y direction.

4.4.4 Resolution

The spatial resolution for multi-layer trackers like GEMs can be studied using a geometric mean method [119] [120], where a linear fit for the tracks composed by the coordinates found on these layers were performed. A two stage fitting technique was used. Stage one is fitting the tracks composed of coordinates from all detectors, including the one under inspection; stage two is fitting the tracks after removing

[4] A Møller event with its two electrons having the same scattering angle value.

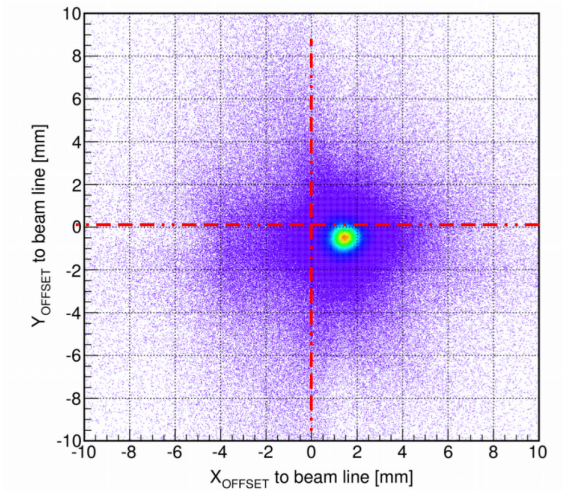

Figure 4-20: The reconstructed beam line position on GEM detection plane.

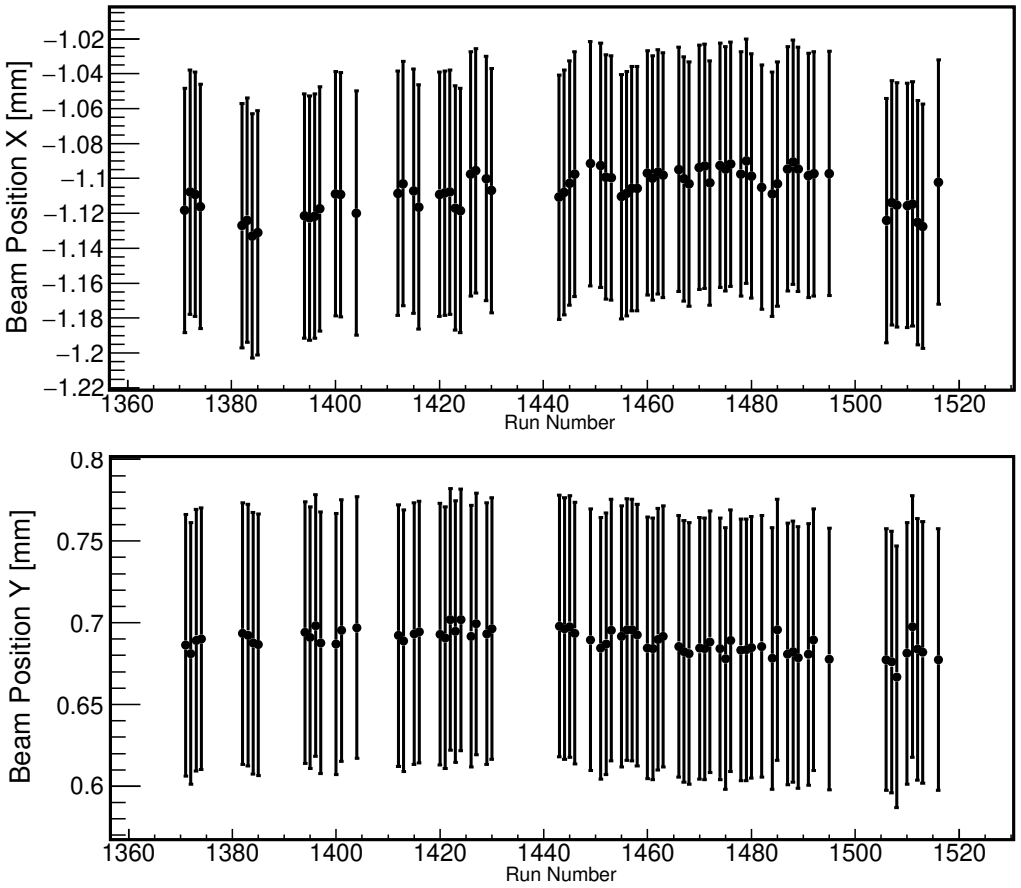

Figure 4-21: Beam position stability.

coordinates from the detector under inspection. Then a residue study using the fitted-track projection and the measured position on the detector was performed. The two fittings can give two resolutions σ_{in} and σ_{ex}, the real detector resolution would be:

$$\sigma = \sqrt{\sigma_{ex}\sigma_{in}}, \tag{4.8}$$

where $\sigma_{in}(\sigma_{ex}$) is the resolution extracted with(without) the inspected detector.

For PRad case, we did not have time for this study, instead we used PRad experimental data for estimation of resolution. In order to study the resolution, all detectors were aligned first. After the alignment, the cluster position detected by GEM1 was projected to GEM2 from target, and a residue study between the projected position and GEM2 measured position was performed, as shown in Fig. 4-22. The detector resolution was extracted from a Gaussian fitting on the residue study. The sigma from the Gaussian fitting should be a quadratic sum of the two detector resolutions:

$$\sigma_{Fit} = \sqrt{\sigma^2_{GEM1} + \sigma^2_{GEM2}}. \tag{4.9}$$

It is reasonable to assume that $\sigma_{GEM1} = \sigma_{GEM2}$, and then the GEM resolution would be:

$$\sigma_{GEM} = \sigma_{Fit}/\sqrt{2}. \tag{4.10}$$

The fitting result is shown in Fig. 4-23. This method only works in the overlapping area, however the GEM resolution should be uniform no matter the location on GEM detector. The fitting for X direction is a bit asymmetric due to the narrow range (44 mm) on the horizontal direction of the overlapping area. The extracted resolution is around 56 μm for both direction, which is consistent with Super Bigbite (SBS) GEM chambers.

4.4.5 Efficiency

Three types of events were used for GEM efficiency study: double arm Møller ($ee2$), single arm Møller ($ee1$), and ep events. The efficiency from different types of events

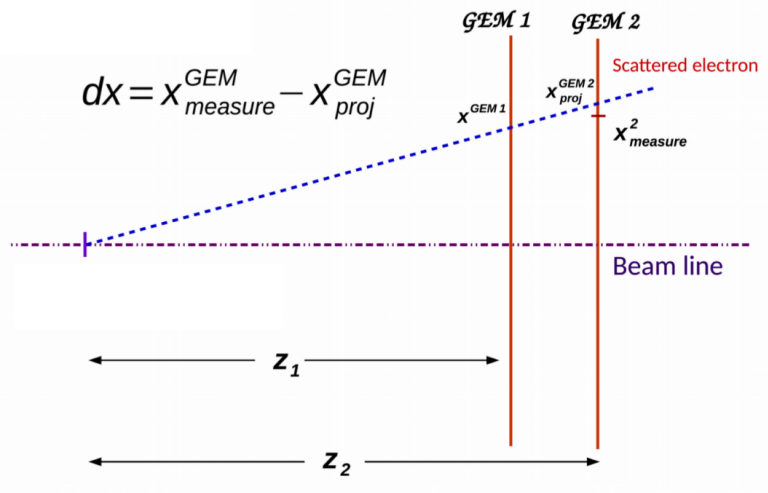

Figure 4-22: Projection method used for resolution study.

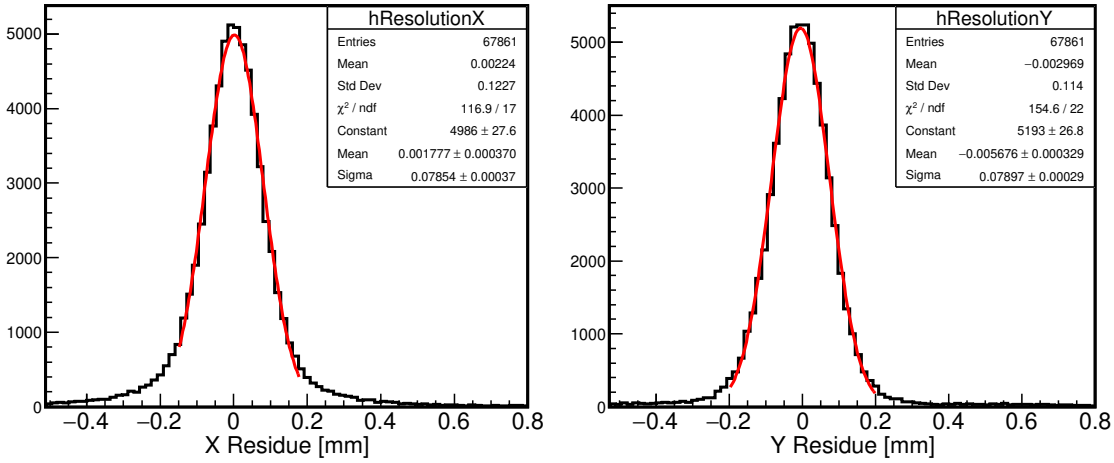

Figure 4-23: GEM Resolution. The Red line is a Gaussian Fit. The disagreement between the Fit and the data could be accounted by the target Z ambiguity.

can also be used as cross checks and systematic checks. Since there was only one layer of GEM chambers in PRad setup, the efficiency of GEM was measured relative to HyCal. The events were first selected by HyCal detectors, which is 40 cm behind the GEM detector. Then the selected clusters were projected to GEM detector, and see if there's a matching GEM cluster around the projection. This is called the GEM-HyCal matching, the mechanism is shown in Fig. 5-6 in next Chapter, where the details of the matching mechanism is discussed. In order to mitigate the deficiency from the matching mechanism, a relatively large matching radius was used, $R_{match} = 6 \times \sigma_{HyCal}$, where σ_{HyCal} is HyCal position resolution, which is more than 20 times larger than GEM position resolution.

In PRad experiment environment, there are three major background sources that can lead to an underestimated GEM efficiency: 1) high energy photon, 2) cosmic rays and 3) the beam line background. Among these, the cosmic contribution has been studied using specific cosmic runs. Two machine learning algorithms were developed for cosmic study: one is using an unsupervised auto-encoder algorithm [121] developed by Duke group, the other one is supervised convolutional neural network algorithm [122] developed by UVa group. Both algorithms confirmed that under our standard cuts, the contribution from cosmic is negligible.

High energy photon can cause a deficiency since GEM is mostly blind to neutral particles, the contribution from high energy photons is studied by Geant4 simulation. A generator with next-to-leading order radiative corrections was developed. The generator can produce hard photons with energy up to the full beam energy. The cut off energy for Bremsstrahlung photons is configurable in the generator. By varying this cut-off energy, once can choose whether or not to have hard photons in the generated events. The contribution is estimated to be aound 0.06% in Pb-glass region and <0.01% in PbWO4 region. When generating the efficiency table for physics analysis, a very tight energy cut (1σ) was also used to remove the contribution from photons.

The beam line background was studied using empty target runs, and a background subtraction (production run - background run) was implemented to remove

its contribution.

For *ep* and single arm Møller events, the efficiency is defined as the ratio of the count of matching GEM clusters over the count of HyCal clusters, with background subtraction:

$$\epsilon = \frac{N_{GEM}^{prod} - C \cdot N_{GEM}^{ety}}{N_{HyCal}^{prod} - C \cdot N_{HyCal}^{ety}}, \tag{4.11}$$

where the subscript GEM(HyCal) represents counts from GEM(HyCal) detector, the superscript prod(ety) represents production(empty target) run, and C is the live charge ratio between empty target run and production run. A Poisson error was used for statistical uncertainty. For the double arm Møller event, since it requires two electron clusters to be detected simultaneously, the double Møller event efficiency is not the same with GEM detection efficiency (ϵ_{GEM}), instead it should be ϵ_{GEM}^2. In order to make it consistent with *ep*, a different calculation method was used. In this method, HyCal still require two Møller electrons, however we did not require two electrons on GEM, the two HyCal electrons will be projected to GEM separately, and also calculated separately in efficiency study.

The zero suppression (as mentioned in section 4.4.1) during clustering also had an effect on GEM efficiency. The effect was studied using clean double arm Møller events, the result is shown in Fig. 4-24. The pedestal means the noise average (the sigma[5]) from the pedestal run. During this study, the raw data was processed (mainly cluster reconstruction and zero suppression) 4 times, each time with a different pedestal cut, and the efficiency from different process were compared. The result shows that if we loosen the pedestal sigma cut by 1σ, the efficiency increases by 0.5%. Based on the usage of SBS GEM testing experience, pedestal cut smaller than 5σ significantly introduces false noise clusters, and the volume of the processed data also becomes huge. In PRad physics analysis, a standard 5σ pedestal cut was used.

The relationship between efficiency and HyCal cluster energy cut has also been studied. As we already know, tighten the HyCal cluster energy cut can mitigate the contamination from hard photons, and in efficiency study, the most strict 1σ cut was

[5]Refer to the clustering subsection 4.4.1 in this chapter for its definition.

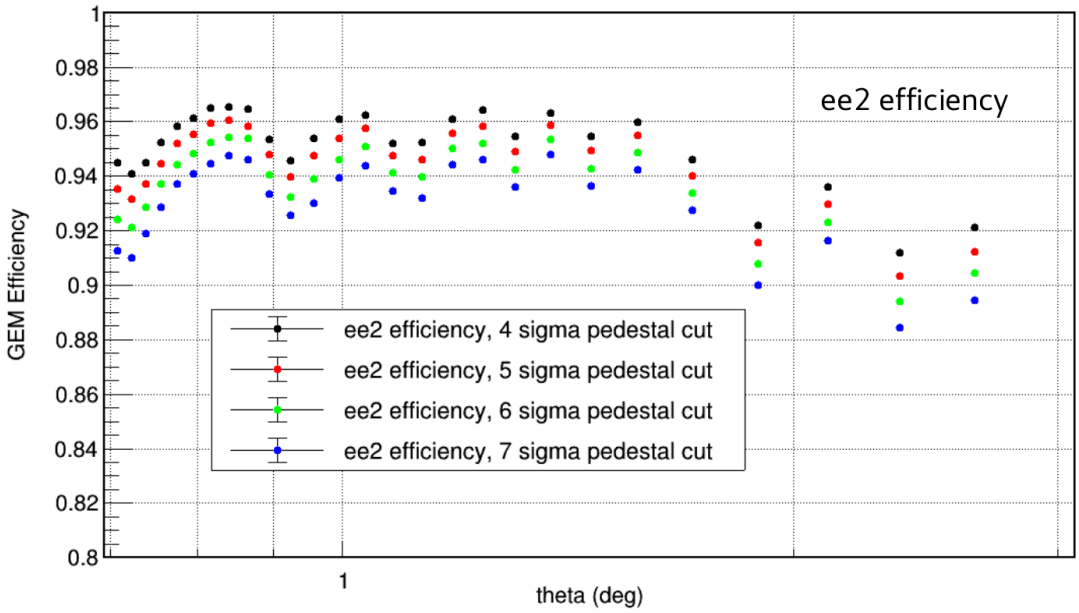

Figure 4-24: GEM efficiency extracted from clean double-arm Møller events (ee2) vs pedestal cut. Y axis is efficiency, X axis is scattering angles. Different colors are for different pedestal cuts.

used. In this study, we checked the efficiency against different HyCal cluster energy cut, the result is shown in Fig. 4-25. All types of events had been checked. As the result shows, when one gradually tighten the cut (from right to left in Fig 4-25), the GEM efficiency will finally reach a plateau. The approaching speed is different due to the fact that different type of events have different cuts, however the converged value is consistent.

The spacers and high voltage sectors inside the chamber also caused efficiency drop. In order to check the contributions from these factors, we compared the efficiency with/without spacers and high voltage sectors. To remove events around the spacers, the HyCal clusters were first projected to GEM plane. If the projected cluster is within a $\pm 2 \times \sigma_{HyCal}$ (HyCal spatial resolution) range to the spacer center, then the event was discarded. The spacer removal effect is shown in Fig. 4-26. The removal width of each spacer is different due to different HyCal resolutions in different areas. A more general comparison is given in the 2-D efficiency map, see Fig. 4-27, where the GEM detection plane was divided into different sections that follow the size of

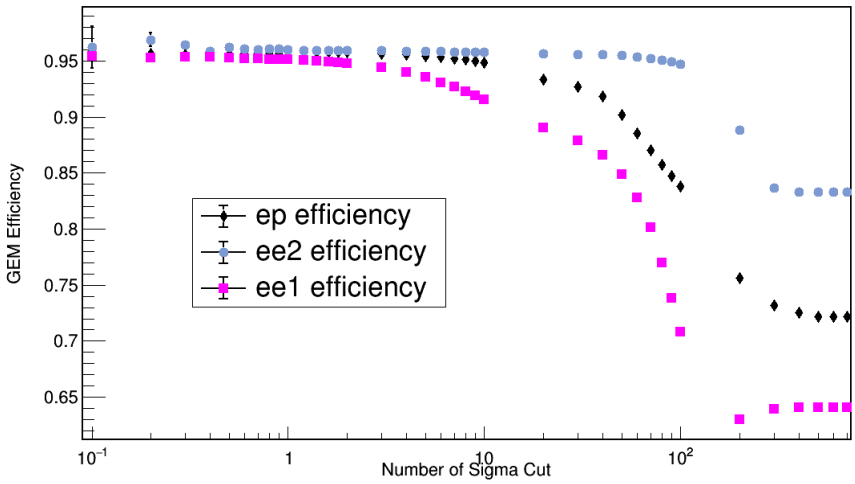

Figure 4-25: GEM efficiency vs HyCal cluster energy cut.

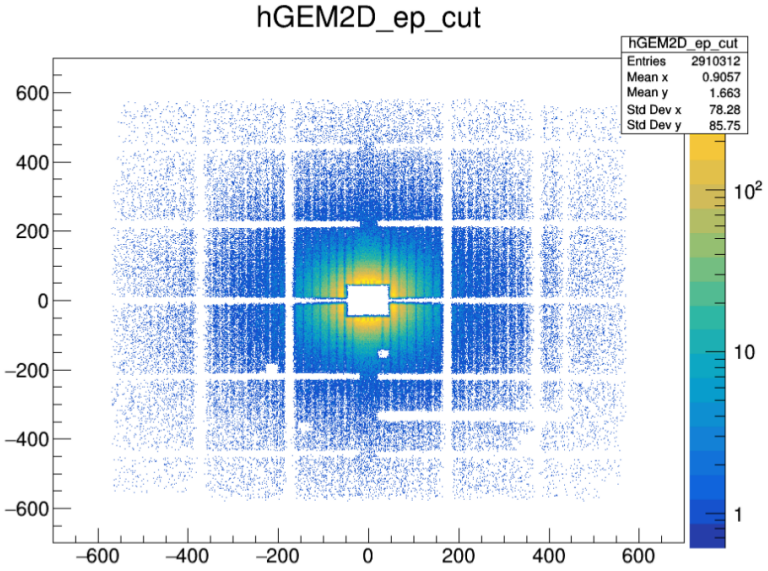

Figure 4-26: Spacer Removal. The extra horizontal and vertical empty band in the right side of the plot is due to broken readout strips. The white spots are due to HyCal dead modules.

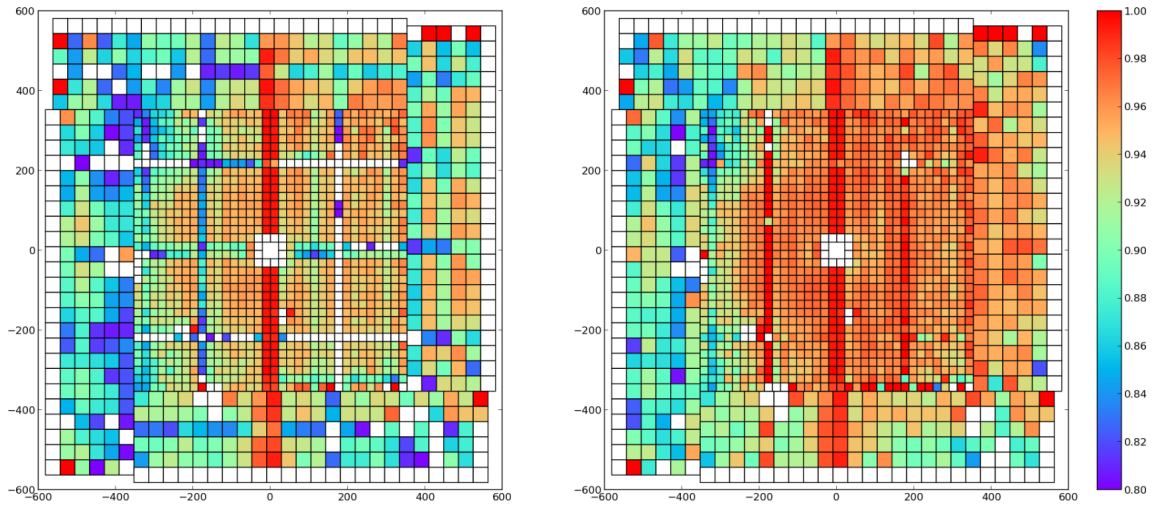

Figure 4-27: Efficiency compare between with/without spacer removal. The left plot has spacers, the right plot has spacers removed. The low efficiency area on the left side of each plot is due to a FEC card malfunction.

HyCal modules behind them. The efficiency value is shown in color code.

The overall GEM efficiency in different scattering angle bins are shown in Fig. 4-28 and Fig. 4-29. Among these, Fig. 4-28 did not remove GEM dead areas (spacers, high voltage sector margins and broken area). Up to 3°, the efficiencies from *ep*, single arm Møller and double arm Møller are consistent. The single arm Møller events start to drop beyond 3°, which is due to the fact that in this area Møller electrons usually have very low energies, and the HyCal resolution is worse when energy is low. The double arm Møller events did not exceed 3° due to kinematics limitation.

Fig. 4-29 shows the *ep* efficiency after removing all dead areas. The binning is different due to that we combined the bins from Fig. 4-28 to increase the statistics. The statistics reduction due to GEM dead area cut is especially significant at large scattering angles. As the plot shows, the efficiency at low scattering angle ($< 3°$) is almost flat after dead area cut. However, there's a 5% efficiency drop starting from 3° all the way up to 6°, which is due to a malfunction FEC card. This issue was studied using a simulation, which will be discussed in detail in next section.

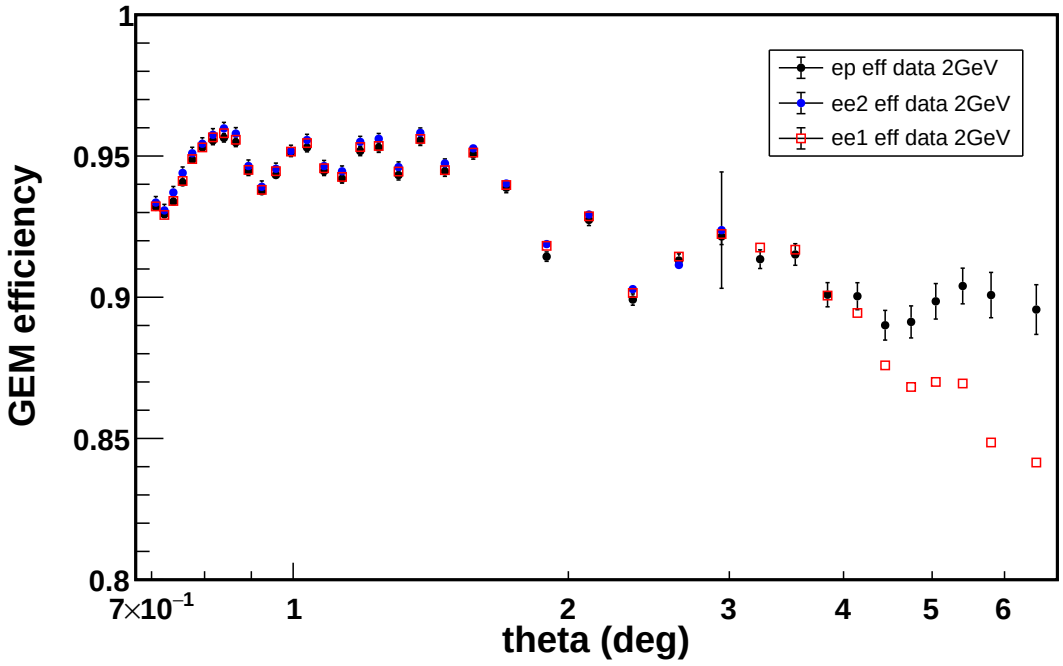

Figure 4-28: GEM efficiency from different types of events as a function of scattering angle.

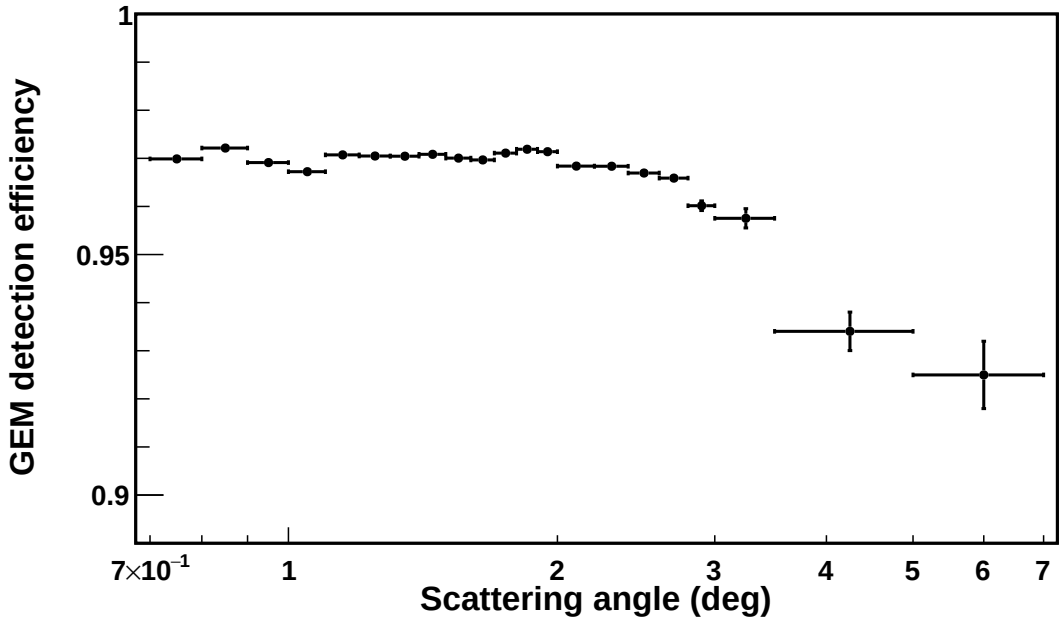

Figure 4-29: The average GEM efficiency from *ep* events as a function of scattering angle after removing dead areas, the dead areas include spacer, high voltage margin and broken area.

4.5 GEM Efficiency Simulation

The efficiency drop at large scattering angles was due to an electronics issue. During the experiment, all the channels parallel to the Y direction in the range of around X = (-460 mm, -200 mm) on the left GEM chamber were connected to a malfunction FEC card. The common mode level of this malfunction FEC card was raised by almost 100 ADCs, which led to an early saturation for all APV cards that connected to it. The output ADC of the affected channels became smaller. Thus the efficiency in this area was more sensitive to pedestal cut, and the overall efficiency in this affected area dropped by almost 10%. This effect was confirmed by simulation.

In the simulation, we modeled all dead areas from spacers, high voltage sectors, and broken areas following PRad data. An assumption that GEM should have uniform intrinsic efficiency for all unaffected area was used. This intrinsic efficiency was extracted from PRad data using the overlapping area, the value was around 99.2%.

For the dead area, we assumed a 30% event loss probability for high voltage (HV) sector margins, and each HV margin will cause a 2 mm wide low efficiency area in the readout board. A 100% event loss rate was used for dead areas from spacers, the width of each being 3 mm. Lastly, a 100% event loss rate was used for the broken area. In order to model the malfunction electric board behaviour, we assumed a 90% intrinsic GEM efficiency for the area between X = (-460 mm, -200 mm). The consistency between data and simulation are shown in Figs. 4-30, 4-31 and 4-32. Fig. 4-30 shows a comparison for the accumulated electron event counts on GEM Y direction. A 2D comparison for efficiency at different GEM locations is given in Fig. 4-31. Fig. 4-32 shows a comparison of efficiency vs. scattering angle between data and simulation. Two simulation results are shown in Fig. 4-32, the first one assumed all FEC cards performed normally and the intrinsic efficiency being 99.2% everywhere; the second one took into account of the FEC issue and assumed a 9.2% efficiency drop in the affected area. As one can see, after the FEC correction, the simulated efficiencies are consistent with data within uncertainties.

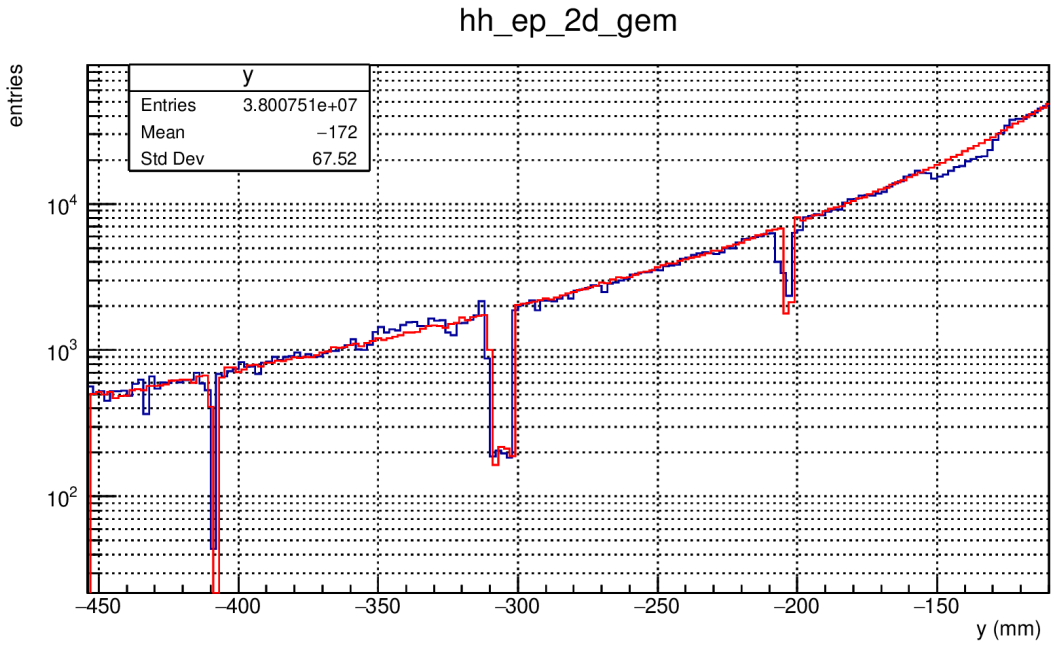

Figure 4-30: Comparison between simulation and data for *ep* event count on Y direction, the red line is from simulation, the blue line is PRad data.

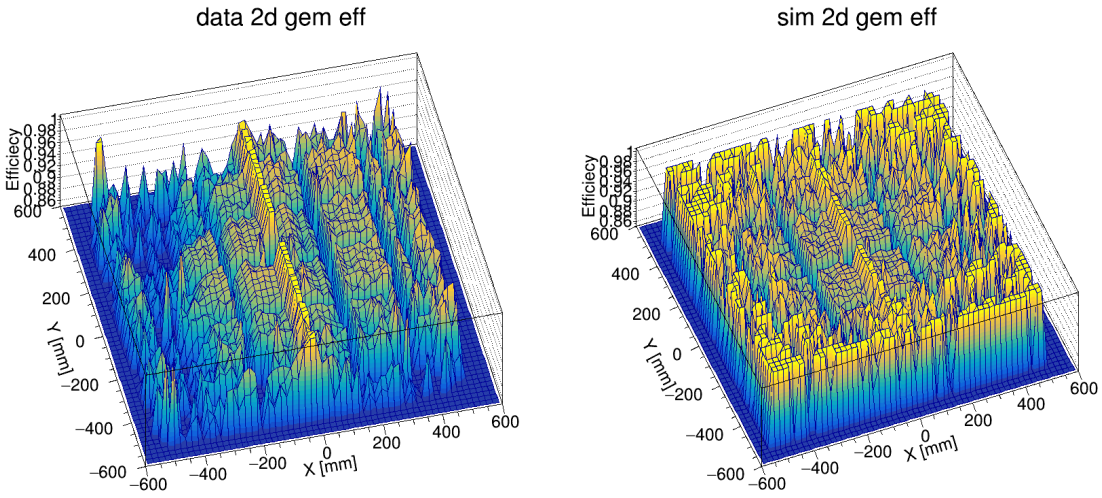

Figure 4-31: Comparison between data and simulation for efficiency in each divided cell on GEM detection plane. The left plot is from data, the right plot is from simulation. The low efficiency area due to electronics is more obvious in the top left corner of the left plot. The high ridge at $X = 0$ is due to the GEM overlap area.

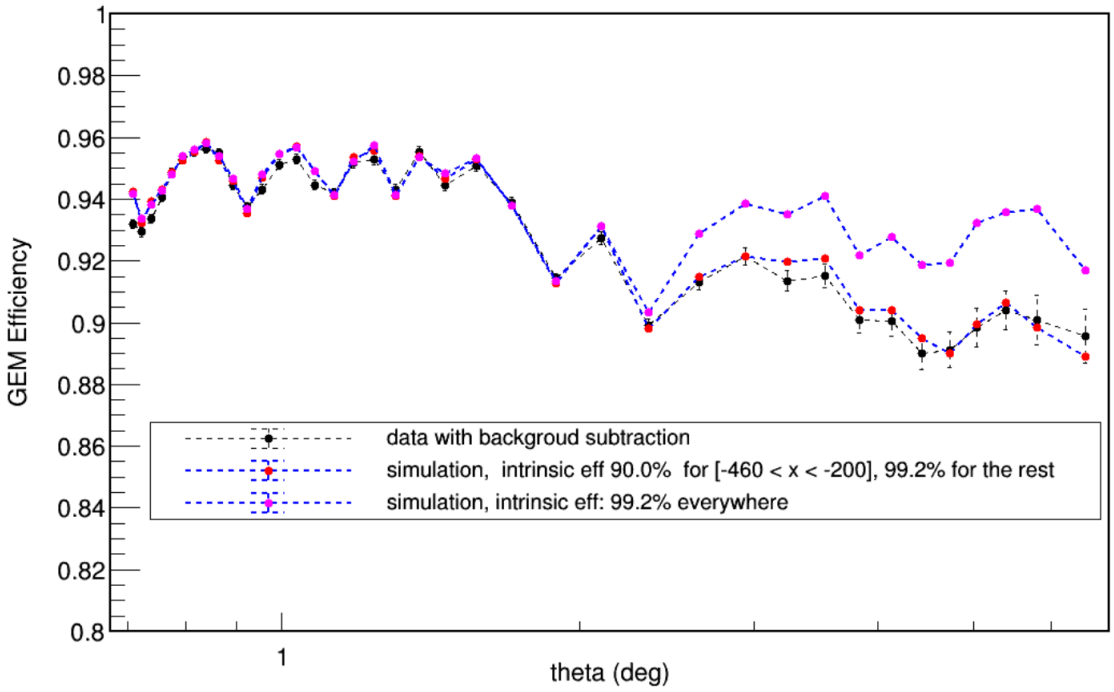

Figure 4-32: Efficiency simulation. The black dots are from PRad data; the pink dots are from simulation assuming an intrinsic GEM efficiency 99.2% everywhere; the red dots are from simulation, which also take into account the FEC issue, assumed a 9.2% efficiency drop in the affected area.

Chapter 5

Data Analysis

5.1 Overview

The overall analysis procedure includes: 1) detector calibration, 2) event selection, 3) background subtraction, 4) radiative correction, 5) cross section extraction, 6) form factor extraction, and 7) proton radius extraction. The detector calibration includes both GEM and HyCal. The GEM calibration was discussed in the previous chapter. The calibration of HyCal was done by groups from Mississippi State University, North Carolina A&T University and Duke University, and we will briefly summarize their results in this chapter. Except for the extraction of the proton radius, which will be presented in Chapter 6, all other analysis steps will be presented in this chapter.

In a nutshell, as mentioned in Chpater 2, the proton charge radius is related to the slope of the proton electric form factor as a function of Q^2 at $Q^2 = 0$,

$$R \equiv \left(-6 \frac{dG_E^P(Q^2)}{dQ^2} \Big|_{Q^2=0} \right)^{1/2}, \tag{5.1}$$

where G_E^P is typically extracted from the Born level differential cross section, Eq. (2.92). In PRad analysis, in order to reduce the uncertainties coming from the luminosity, the ep cross section was normalized to the Møller cross section. The measured differential cross sections have radiative effects; in order to reach the Born level cross sections (one photon exchange), a radiative correction was performed using a Geant4-

based Monte-Carlo simulation. An event generator that includes the next-to-leading order radiative effects for both ep and ee scattering was developed for this purpose. A super ratio was defined:

$$SR \equiv \frac{(ep/ee)_{data}}{(ep/ee)^{RC}_{sim}}. \tag{5.2}$$

where $(ep/ee)_{data}$ is the ratio of ep vs ee scattering yield measured from data and $(ep/ee)^{RC}_{sim}$ is that from simulation with radiative effects. If the radiative correction was done properly, with the proper G_E and G_M model in the generator, SR should should be consistent with 1 for every scattering angle bin.

For the PRad Q^2 range of $2.1\times10^{-4}-0.06$ $(\mathrm{GeV}/c)^2$, the contribution from G_M^P to the ep cross section is negligible: at the highest(lowest) Q^2 covered in the experiment, the G_M^P contribution to the cross section was less than 10%(0.04%). Therefore, a Kelly form factor parameterization [9] for G_M^P was used in the generator; and a systematic uncertainty contribution due to G_M^P was added to the final results. The optimum G_E^P model was achieved using an iterative method. First, an initial $G_E^{\mathrm{P,\ model}}$ was set in the generator, then a full Geant4 simulation was performed. Combining the simulation and experimental data through Eq. (5.2), an electric form factor $G_E^{\mathrm{P,\ extract}}$ was extracted from the data. At the same time, if $SR = 1$ did not hold for the $G_E^{\mathrm{P,\ model}}$, then the $G_E^{\mathrm{P,\ model}}$ in the generator would be replaced by $G_E^{\mathrm{P,\ extract}}$; this procedure was repeated, until the condition $SR = 1$ was reached. The details of this procedure will be discussed in the following sections in this chapter.

5.2 HyCal Calibration

As described in last chapter, HyCal (Hybrid Calorimeter) consists of two types of modules: PbWO4 (crystal) modules and Pb-glass modules. Each PbWO4 module was wrapped with a 100 μm thick VM2000 reflective material to impreove the light collection and a 36 μm thick Tedlar for light isolation; each Pb-glass module was wrapped with a 25 μm thick aluminized mylar foil. The electrons and photons that reach the calorimeter produce a shower inside it. The shower develops around the hit center, with the number of modules having energy deposition in the range of 2 -

50. The number of modules with energy deposition depends on the incident particle energy. The photons in the shower in each module were reflected by the wrapping foils surrounding each module, and collected by the PMT tube connected to the back of each module. Signals from PMTs were sent to an ADC board through an amplifier. The ADC values were recorded by the DAQ system.

In order to correctly reconstruct the energy deposition of the incident particle from ADC values, a calibration constant for each module needs to be determined. A specific calibration run for this purpose was carried out at the beginning of the data taking process, where the calorimeter was moved across the beam spot in a "snake-like" pattern. A tagged photon beam with its energy ranging from 220 MeV to 1050 MeV was used for this calibration run. The photon beam was produced by the 1.1 GeV electron beam hitting a thin wire target, then the electron beam was deflected from the beam line by the magnet of the photon tagger system [98], leaving only photons passing along the beam line. In addition to determining calibration constants, there are two more major objectives for HyCal calibration: to study the trigger efficiency of the calorimeter using triggers from the photon tagger; and to perform HyCal non-linearity calibration. The non-linearity effect arises due to the fact that the calorimeter response depends on the incident particle energy. The calibration constants need to be slightly corrected based on the incident particle energy.

As shown in Fig. 5-1, during the calibration run, the photon beam spot was fixed. The calorimeter was mounted to a transporter which moved on the $X - Y$ plane. In order to calibrate each module in HyCal, the transporter moved in a snake-like pattern so that the photon beam was focused on each module. For each module, approximately 20 minutes of data were taken with different incident photon energies.

For every event, a HyCal reconstruction algorithm was applied to reconstruct the incident photon energy. The algorithm first identifies the group of fired modules that belong to a cluster, then it multiplies the ADC value from each fired module in that group by the corresponding calibration constant and sums them together. The calibration constant for each module is tuned iteratively so that the sum finally equals to the energy of the incident photon determined by the tagger system, as shown in

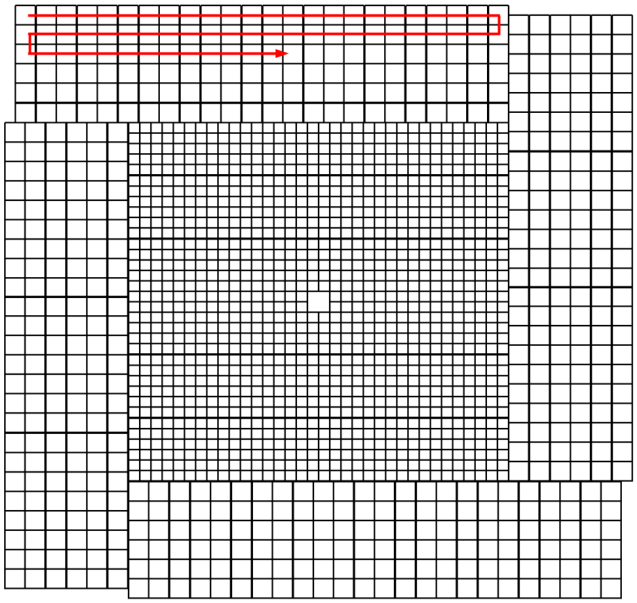

Figure 5-1: "Snake" run for HyCal calibration. HyCal was mounted on a transporter, the transporter moved in the way a snake moves, as shown by the red arrow, so that each module could be centered on the photon beam. Data for each module accumulated for about 20 minutes. The trigger was provided by the photon tagger in the Hall B beam line.

Fig. 5-2. This calibration process was performed by Maxime Lavilain from North Carolina A&T State University, Li Ye from Mississippi State University, Weizhi Xiong and Chao Peng from Duke university. The initial algorithm was adopted from the PrimEx experiment [123]. We will briefly summarize their work in this section.

If the calorimeter were to have perfect linearity, a single calibration constant for each module could be used at all energies. However, due to light attenuation properties of a module and the electronics pedestal cut, the calibration constant obtained at a given energy cannot be applied directly to other energies, and a correction must be made. For PRad, the correction factors were studied using photons. The non-linear effect was studied using E_{rec}/E_{γ} as a function of E_{γ}, as shown in Fig. 5-3, where E_{rec} is the calorimeter reconstructed energy using a single constant, and E_{γ} is the energy of incident photon. In Fig. 5-3, the black dots are from measurement, the red line is a polynomial fit:

$$\frac{E_{rec}}{E_{\gamma}} = 1 + \sum_{i=1}^{N} \alpha_i (E_{rec} - E_{cali})^i, \tag{5.3}$$

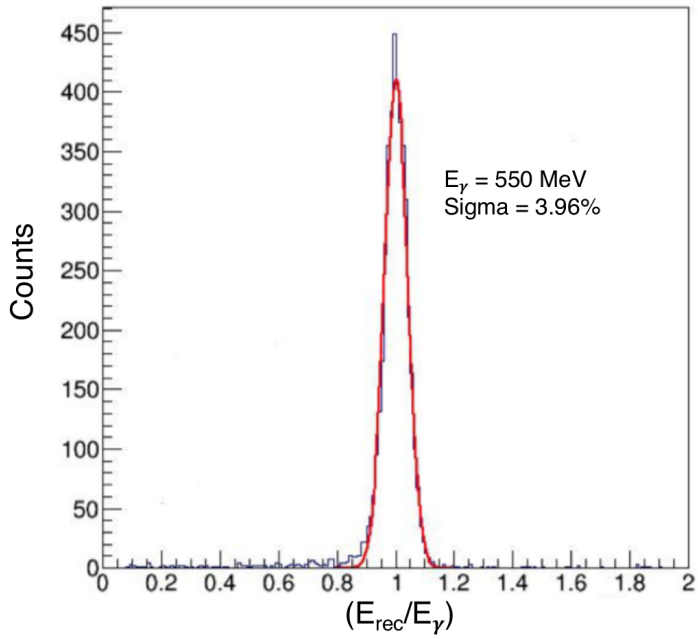

Figure 5-2: The reconstructed energy over the incident photon energy (black) for 550 MeV photons. The red line is a Gaussian fit. This plot is from Li Ye.

where E_{cali} is the energy where the calibration constant was obtained, α_i are parameters to be determined, and N is the order that depends on the desired precision. For PRad case, the response is close to linear, so $N = 1$ was used. The correct energy would be:

$$E_{corr} = \frac{E_{rec}}{1 + \alpha_1(E_{rec} - E_{cali})}, \tag{5.4}$$

where E_{corr} gives the true energy of the incident particle.

After correcting the non-linear effect, the resolution of HyCal was studied. The resolution for PbWO4 modules (shown in Fig. 5-4) was around $2.5\%/\sqrt{E}$. The resolution for Pb-glass module was worse, around $6.2\%/\sqrt{E}$, with E in GeV.

HyCal trigger efficiency was also studied in the snake run. The trigger efficiency was defined as the number of events recorded in HyCal over the total number of triggers. The total number of trigger was recorded by the photon tagger. The efficiency for some PbWO4 modules and some Pb-glass modules is shown in Fig. 5-5. For photon energies greater than 400 MeV, the efficiency pleataued at 99.9%.

The position resolution of HyCal was also calibrated using GEM detectors. Con-

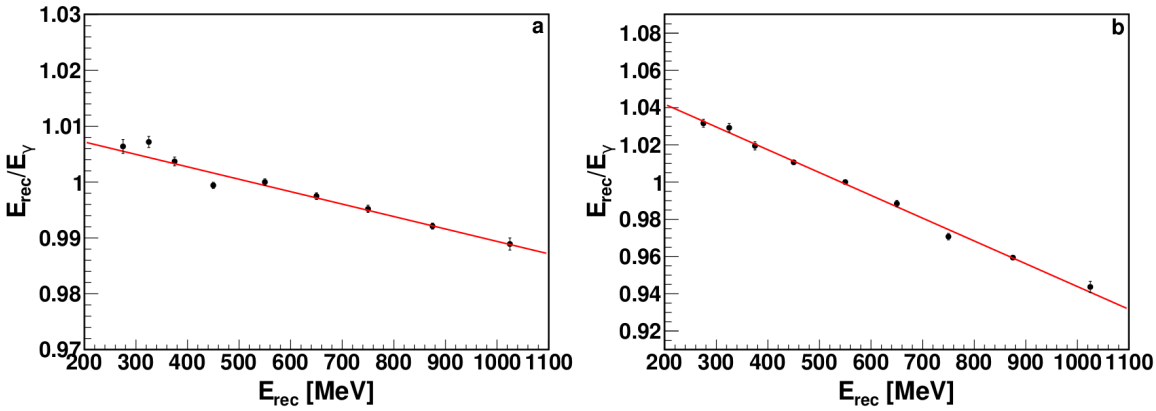

Figure 5-3: The non-linearity of a typical PbWO4 module (left) and a typical Pb-glass module (right). The red line is a linear fit. This plot is from Weizhi Xiong.

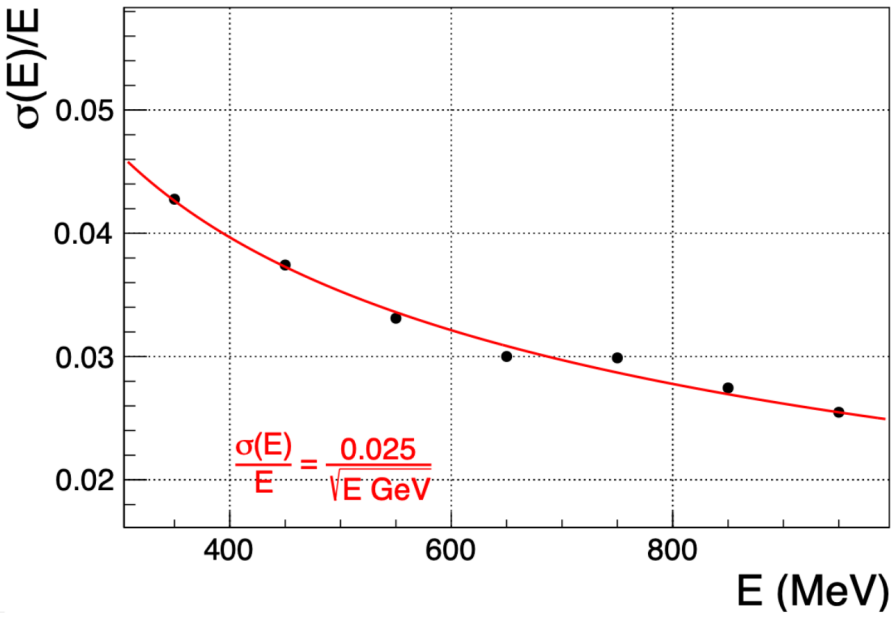

Figure 5-4: The energy resolution of PbWO4 module. This plot is from Maxime Lavillain.

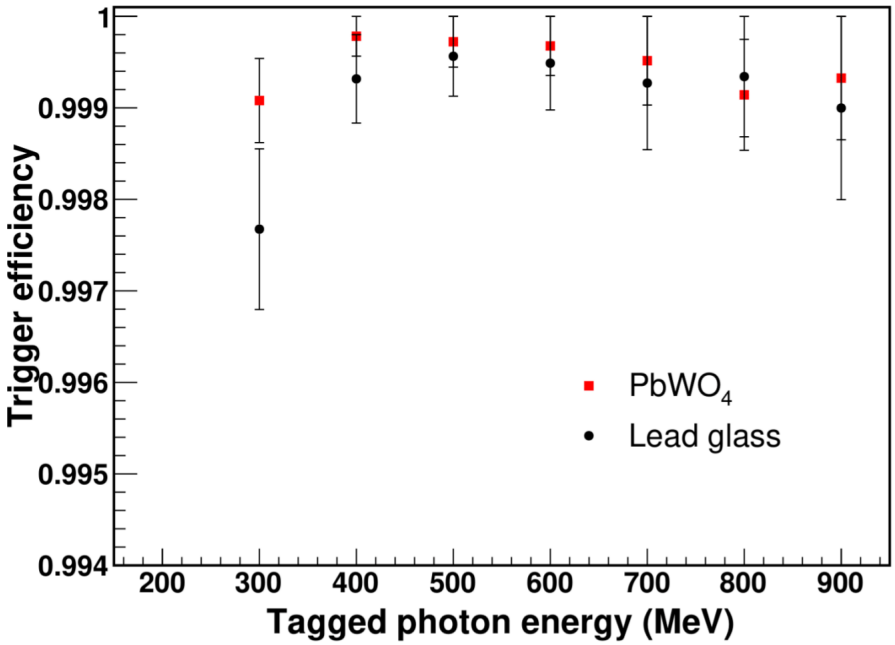

Figure 5-5: The trigger efficiency for PbWO4 modules and Pb-glass modules v.s. incident photon energy. This plot is from Weizhi Xiong.

sidering the different run conditions between the snake run and the production runs, the calibration constants and non-linearity factors were fine-tuned using production *ep* and *ee* events. The energy and position resolution of HyCal are summarized in Table 5.1:

Module type	Energy resolution (%)	Position resolution (mm)
PbWO4	$2.4/\sqrt{E(\text{GeV})}$	$2.4/\sqrt{E(\text{GeV})}$
Pb-glass	$6.2/\sqrt{E(\text{GeV})}$	$6.5/\sqrt{E(\text{GeV})}$

Table 5.1: Energy and position resolution of different HyCal modules. E is the energy of incident particle in GeV.

5.3 Event Selection

The majority particles that are detected by the PRad setup are photons and electrons, muons from cosmic rays are negligible. Electrons were originated from Møller scattering, *ep* elastic scattering, *ep* inelastic scattering, and pair production. The sources of photons include Bremsstrahlung and gas molecule de-excitation. The particles useful

for PRad measurement are elastic *ep* and Møller electrons. Although HyCal does not distinguish electrons from photons, the GEM detectors are mostly blind to photons. The matching between GEM and HyCal removed most of the photon signals.

As discussed in last chapter, there is only one GEM detector layer in PRad setup, and the clustering of GEM signals are performed over the readout strips in X and Y direction separately. In order to get the 2D position information of where electrons hit GEM detectors, a matching between X clusters and Y clusters is needed. However, for many scattering events in PRad, there were usually more than one electrons hitting GEM detectors (for example, there are two electrons from every Møller scattering event); and these electrons all have similar GEM ADC amplitudes. Thus, the usual way of matching X and Y clusters using ADC amplitudes cannot be used in the PRad situation. In order to avoid accidentally missing the real electron coordinate, all matching combinations between X and Y clusters were saved. Take a Møller event for example, there are two electrons hitting GEM detector simultaneously, both X direction and Y direction would be reconstructed as two clusters: X_1 and X_2 in X direction, Y_1 and Y_2 in Y direction. In total there are thus four possible combinations for the two electron coordinates: (X_1, Y_1), (X_1, Y_2), (X_2, Y_1), (X_2, Y_2). Among the four combinations, only two are real. To filter out the real coordinates, the reconstructed position information from HyCal sitting closely behind the GEM detector was used. During a HyCal GEM matching process, as shown in Fig. 5-6, the coordinates from GEM and HyCal were projected to a common Z-surface (usually the HyCal crystal surface), and then a circular search area with $r = 6 \times \sigma$ around the projected HyCal coordinates were established, where σ is HyCal position resolution for that hit. The GEM coordinates combination that falls into this circle were selected as the real electron coordinates. If there were more than one combination within the circle, the closest one to the center would be chosen. Thus, HyCal played a key role in position reconstruction. In this section, we will mainly describe the event selection on HyCal.

Multiple cuts were used for choosing elastic *ep* and *ee* events from HyCal. As shown in Fig. 5-7, the energy deposition of *ep* and *ee* is clearly separable down to 0.6°. However, in our analysis, due to the multiple scattering (electrons with

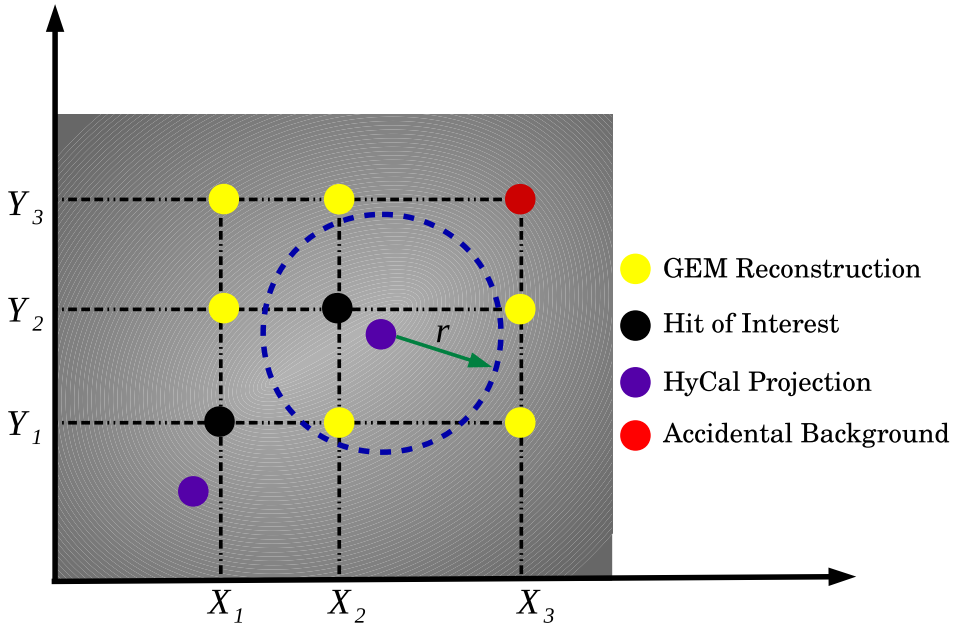

Figure 5-6: Matching between GEM and HyCal projected clusters.

scattering angle $\theta > 0.3°$ could hit the beam pipe and bounce into the acceptance), pile-up effect (Møller electrons landing on some low energy background resulting in a higher detected energy) and the energy leakage in the HyCal most inner layer of PbWO4 modules, a slightly larger angle cut was used in the analysis. The scattering angle range used in physics analysis is given in Table 5.2.

beam energy	angle used in analysis
1.1 GeV	$0.75° - 7.0°$
2.2 GeV	$0.7° - 7.0°$

Table 5.2: Scattering angle range used in analysis.

The most effective cut was using the energy cut, see Eq. (5.5). A general description on the energy cut is shown in Fig. 5-8, where the reconstructed energy was from HyCal, and the reconstructed scattering angle was from GEM.

$$|E_{rec} - E_{expect}| < N \times \sigma_E, \tag{5.5}$$

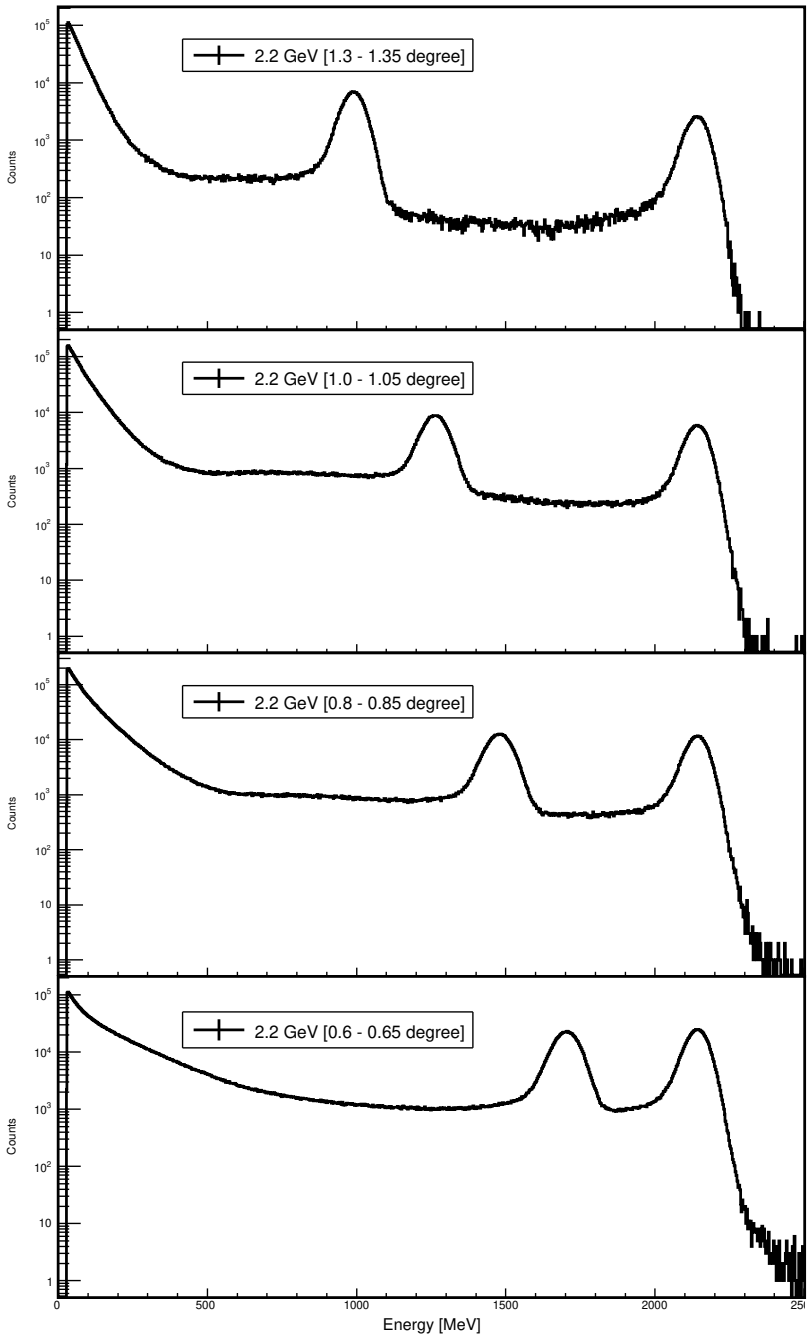

Figure 5-7: Energy spectrum for a series of angle bins from HyCal. The scattering angles are arranged in a decreasing order from top to bottom. The peak on the right most side is from *ep* elastic, the second peak on its left side is Møller elastic. As shown in the bottom plot, the separation between *ee* and *ep* is still clear down to approximately 0.6°.

where E_{rec} is the reconstructed energy, E_{expect} is the calculated energy expected for elastic ep and ee for that scattering angle, σ_E is the HyCal energy resolution. Since HyCal consists of crystal and Pb-glass modules, the energy resolution is different in different areas. So the cut on cluster energy varies in different angle bins, as shown by the red line in Fig. 5-8. Due to the contamination of inelastic events, the energy cut criteria are slightly different in PbWO4, Transition and Pb-glass areas. The transition area is where PbWO4 and Pb-glass modules are neighbouring each other, the clusters reconstructed in this area usually contain both types of HyCal modules, the energy resolution in this region (5.0%) is better than pure Pb-glass region (6.0%), but worse than that in the pure PbWO4 region (2.5%). In the transition and Pb-glass regions, it is difficult to reject all inelastic ep events due to the larger energy resolution, thus, we used a slightly stricter energy cut on the left side of the elastic peak, as shown in Table 5.3.

A HyCal cluster module number cut ($\geqslant 2$) was also applied to reject the ADC signals due to PMT discharges, in which case a single isolated module was fired.

events	HyCal Area	Cuts
ep/ee	Energy cut in PbWO4	$-3.5\sigma_E < E_{rec} - E_{exp} < 3.5\sigma_E$
	Energy cut in Transition	$-2.5\sigma_E < E_{rec} - E_{exp} < 4.0\sigma_E$
	Energy cut in Pb-glass	$-2.0\sigma_E < E_{rec} - E_{exp} < 4.0\sigma_E$

Table 5.3: Energy cut for ep/ee in different HyCal regions.

For elastic ee events, the double arm Møller requirement that both electrons are detected was used in the analysis. This allowed us to better reject backgrounds. Besides the energy cut applied in each electron similar to the ep case, the following extra cuts were also applied for ee:

- **The elasticity cut:**

$$|E_{e1} + E_{e2} - E_b - m_e| < N \times \sigma_E, \tag{5.6}$$

where E_{e1} and E_{e2} are the measured energy for the two electrons, E_b is the beam energy, m_e is electron mass, and σ_E is the energy resolution. Since double arm Møller

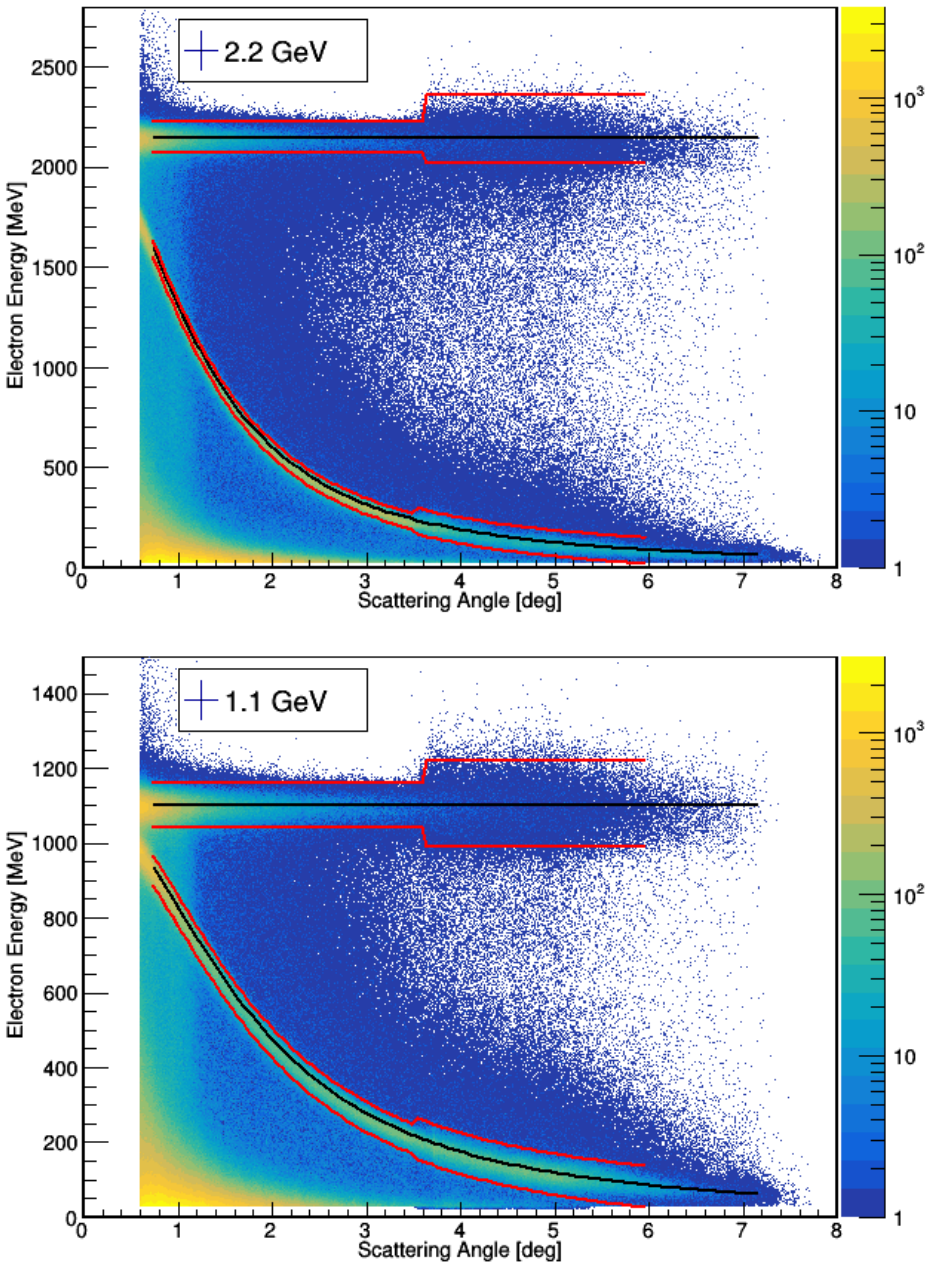

Figure 5-8: Reconstructed electron cluster energy vs scattering angle. The top plot is for 2.2 GeV beam, bottom plot is for 1.1 GeV. The nearly horizontal black line in each plot represents *ep* elastic energy, and the lower black curve shows *ee* elastic energy. The red line represents the elasticity cut of Eq. (5.5) and Eq. (5.6) for *ep* and *ee*. The cut size is dependent on HyCal energy resolution, see Table 5.3.

events all reside in PbWO4 region of HyCal, we used $N = 4.5$ everywhere for this cut.

- **The coplanarity cut:**

$$|\phi_{e1} - \phi_{e2} - \pi| < 15^{\circ}. \tag{5.7}$$

Theoretically, the azimuth angle difference of the two electrons must be 180°. Considering the resolution of detectors, we required the reconstructed angle difference to be within ±15° of 180°.

- **The vertex Z cut:**

The vertex Z_{rec} position can be reconstructed from Møller events (see Appendix A.3 for Z_{rec}):

$$Z_{rec} = \sqrt{(m_e + E_b)R_1R_2/(2m_e)}, \tag{5.8}$$

R_1 and R_2 are the perpendicular distances to the beam line from the two electron hit locations. A vertex Z cut was also applied for Møller:

$$|Z_{rec} - Z_{target}| < 500\ (mm). \tag{5.9}$$

where the Z_{target} was from Jefferson Lab survey group, and cross checked with Møller analysis.

A fairly large cut for Z vertex and coplanarity was used just to reject the tails. The comparison of reconstructed Z vertex and coplanarity between simulation and data is shown in Fig. 5-9.

5.4 Background Subtraction

The background sources for PRad experiment mainly included: 1) residual gas in target chamber; 2) residual gas in vacuum chamber; 3) the re-scattering of very forward angle (< 0.7°) electrons; 4) the collimator located approximately 2 meters away from the target on the upstream side; 5) the beam pipe; 6) photons that induce

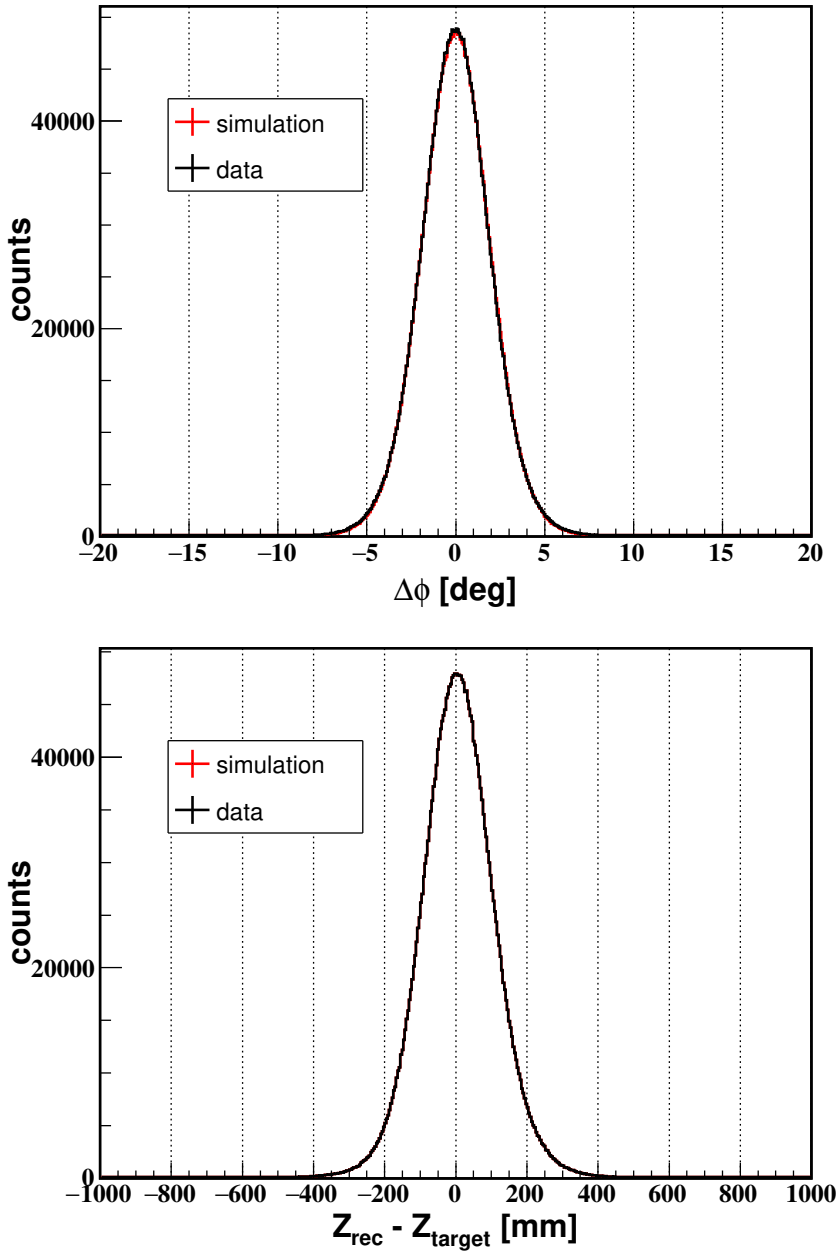

Figure 5-9: The reconstructed coplanarity and Z vertex distribution. The two plots are using HyCal coordinates since all cuts need to be done on HyCal.

signals on GEM detectors through pair production or Compton scattering; and 7) the inelastic $e-p$ scattering contribution.

Among these, the first two sources increased the yield of scattered electrons. The 3^{rd} source (re-scattering) was found to be negligible using a Geant4 simulation. The 4^{th} one (collimator) was a major background source for ep and single arm Møller yields at small scattering angle, which increased the background level from a few percent to 10 - 20% level for small angles. This was fully studied using a Geant4 simulation. The 5^{th} one (beam pipe) is due to beam halo [124] and beam divergence (beam in Jefferson Lab Hall B has a 25 micro radians divergence). Contribution from the 6^{th} one (photons) was also found to be negligible, using a Geant4 simulation. The last one (ep inelastic) was studied using multiple inelastic models through simulation, and was found to contribute less than 2%(0.2%) in the HyCal Pb-glass region for 2.2(1.1) GeV beam, and negligible in the HyCal PbWO4 region ($< 3.5°$).

Most of the background sources are related to the beam line, including item 1, 2, 4 and 5. In order to subtract this kind of backgrounds, background runs were carried out with different types of target configurations, as shown in Fig. 5-10. During the experiment, each run (including both production run and background run) took 1 hour; and every 3 production runs were followed by one empty target cell run with the same beam conditions and the same detector configurations. The target was the only difference between the two types of runs. During production runs, H_2 gas was directly filled into the target cell, and then the gas escaped into the target chamber through the orifices on both sides of the target cell; while in empty target runs, the H_2 gas was filled into the target chamber through another gas inlet instead, in order to mimic the gas situation in target chamber during production runs.

The ep and ee yields from production runs were subtracted by the corresponding yields from empty target runs normalized by live charge, see Fig. 5-11. The percentage of ep and ee yields from empty target runs over production runs are shown in Figs. 5-12, 5-13, 5-14, 5-15 for 2.2 GeV ep, ee, 1.1 GeV ep and ee, respectively. For 2.2 GeV ep events, the background level at small scattering angles less than 1.1° was relatively large, around 10% level. This was due to a collimator installed around

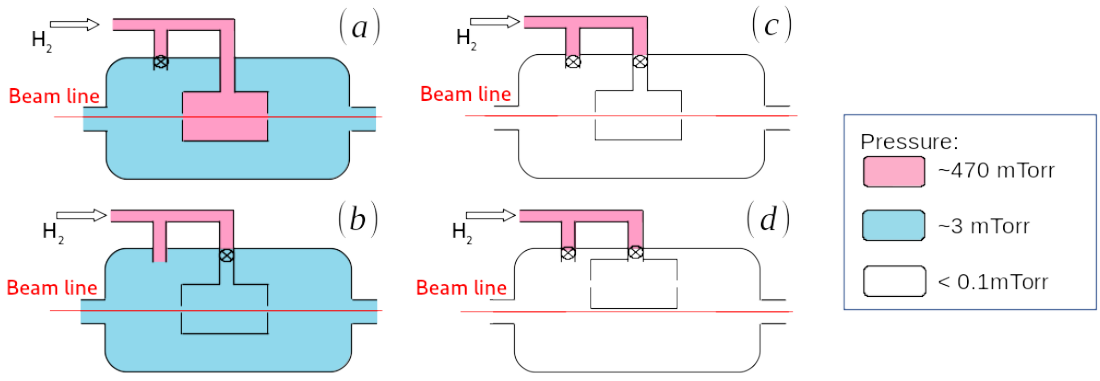

Figure 5-10: Target configurations in PRad experiment. (a) Production run configuration, pink area is H_2 gas directly filled into the cell. Blue area is the background H_2 gas from the orifices of the cell. (b) Empty target run configuration, H_2 gas was directly filled into target chamber area to mimic the background H_2 from orifices, this configuration was used for background subtraction. (c) Empty chamber run with cell in. (d) Empty chamber run with cell out. The last two configurations were used to study background contributions from individual sources.

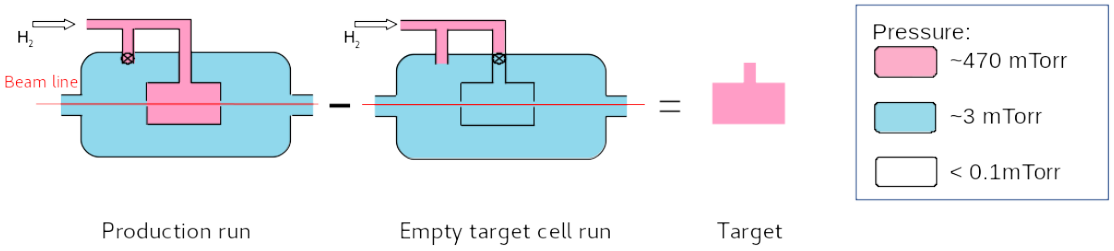

Figure 5-11: Background subtraction. Production run subtracted by empty target cell run remains the yield from target H_2.

2 meters upstream of the target cell. The purpose for this collimator was to block beam halo. However, due to the fact that the beam in Hall B had a ±25 micro radians angular spread [124], a very small portion (less than 10^{-8}) of beam electrons hit the exit edge of the collimator. The collimator is made of nickel. Even though the electrons hitting its edge was rare, the yield generated from the collimator was still significant when compared with the low target gas density. We performed a dedicated simulation to study this issue, which will be discussed in the following section. For scattering angles beyond 1.1°, the background level was less than 2%. For *ee* yield, the background level was less than 1% in every angle bin due to the fact that we have more kinematic restrictions on Møller events compared to *ep* events. For both *ep* and *ee*, the contribution from background residual H_2 gas was low and stable, less than 2% as shown in the plots.

For 1.1 GeV beam, the background situation was worse than that for the 2.2 GeV setting. This was due to the worse beam conditions at the early stage of the experiment, for example, we had larger beam halo counts, and larger fluctuations in beam position for the 1.1 GeV case. For *ep* from the 1.1 GeV beam, the background level was around 25% at forward scattering angles less than 1.1°, and dropped to 5% at large angle. The *ee* case was much better due to the same reason as for the 2.2 GeV case; and the background level for 1.1 GeV *ee* stayed at 2% at every angle bin and was very stable. The high *ep* background level at forward scattering angles was also due to the upstream collimator, similar to the 2.2 GeV case. The rising slope at forward angle in Fig. 5-14 was thought to be due to the reason that in this scattering angle range ($0.7° \sim 1.0°$), the counts of scattered electrons from *ep* elastic increases more drastically than that from beam halo hitting the collimator edge. The *ep* yield contribution from the collimator can be subtracted cleanly by the background subtraction method since the collimator stayed unchanged for all runs in the experiment. The subtraction results, as shown in Fig. 5-12 and Fig. 5-14 also supported this point. For both 1.1 GeV and 2.2 GeV beam, the background level flattened out at forward scattering angles after background subtraction.

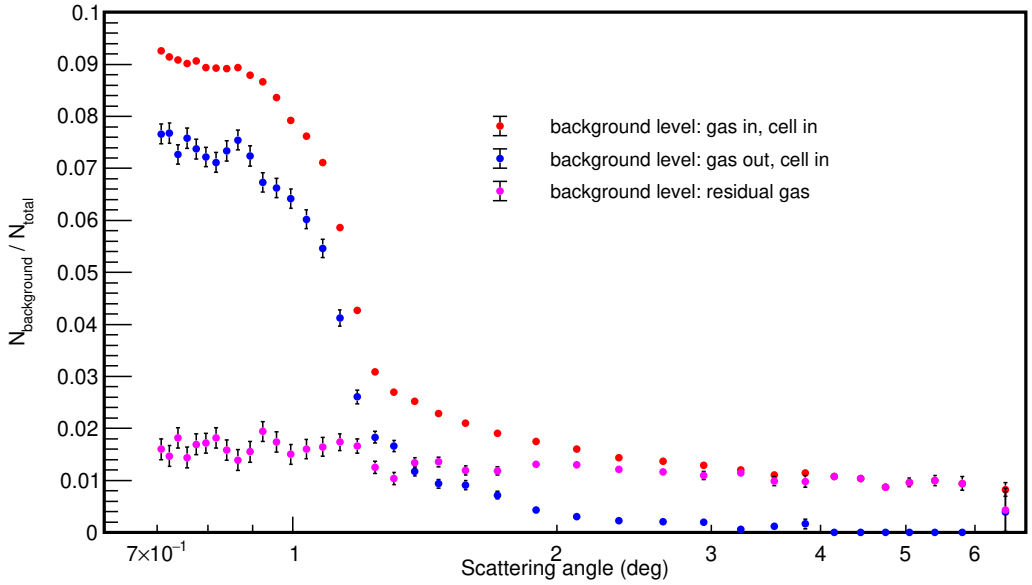

Figure 5-12: 2.2 GeV *ep* yield from background runs normalized by the yield from production runs. The red dots represent the ratio of yield from target configuration (b) divided by the yield from target configuration (a); the blue is for (c)/(a); the purple is for ((b)-(c))/(a), as shown in Fig. 5-10.

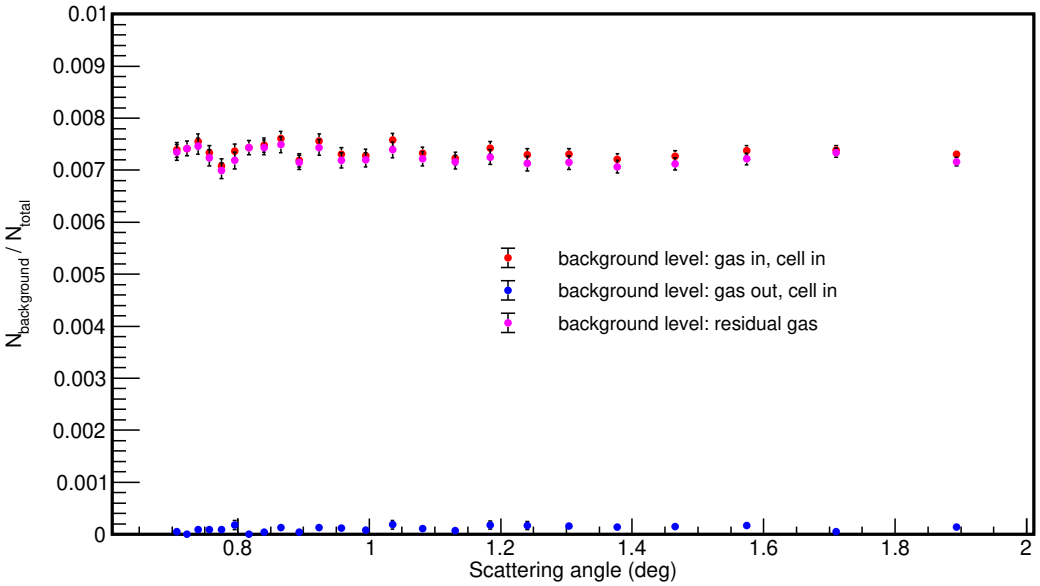

Figure 5-13: 2.2 GeV *ee* yield ratio. The red represents target configuration (b)/(a); the blue is (c)/(a); the purple is ((b)-(c))/(a) as shown in Fig. 5-10.

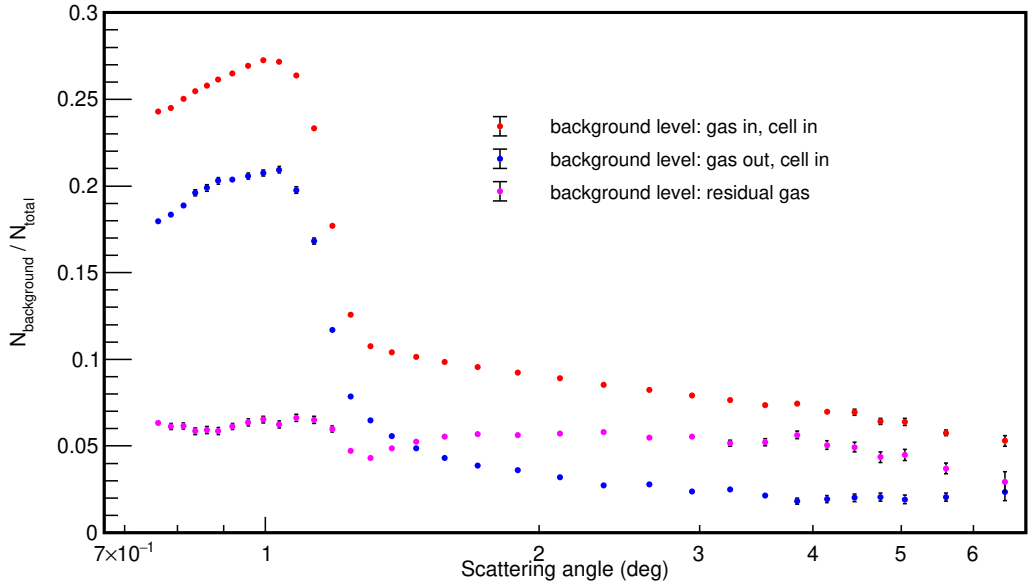

Figure 5-14: 1.1 GeV *ep* yield ratio. The red represents target configuration (b)/(a); the blue is (c)/(a); the purple is ((b)-(c))/(a) as shown in Fig. 5-10.

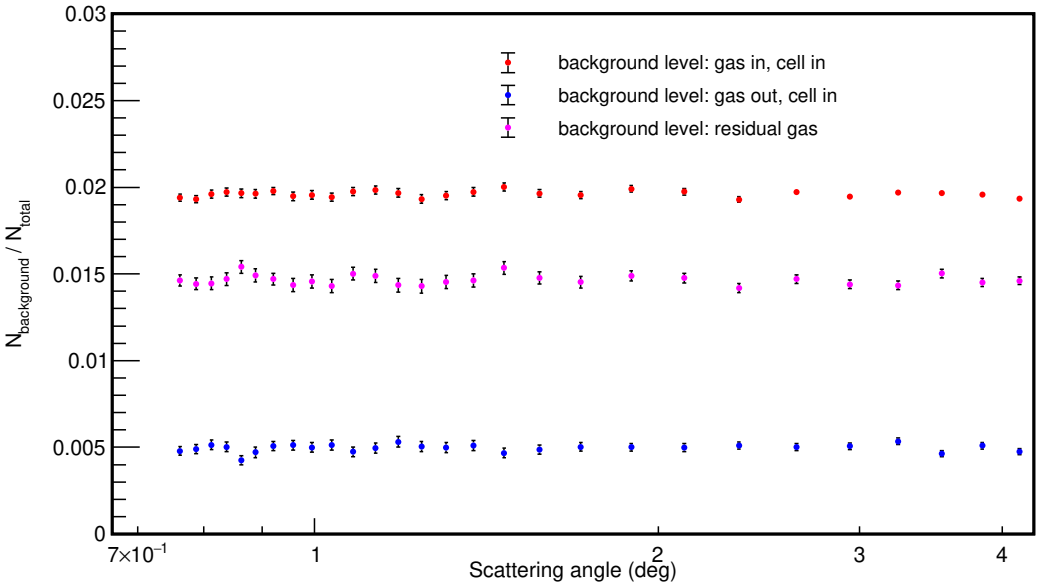

Figure 5-15: 1.1 GeV *ee* yield ratio. The red represents target configuration (b)/(a); the blue is (c)/(a); the purple is ((b)-(c))/(a) as shown in Fig. 5-10.

5.4.1 Background simulation

In order to investigate the cause of the high background ratio at forward scattering angles for *ep* electron counts as shown in Fig. 5-12 and Fig. 5-14, a full beam-on-target Geant4 simulation was developed. The beam profile in the simulation was adopted from [124], a 2D Gaussian distribution in the radial coordinate with $\sigma = 0.04\ mm$ was implemented for the main beam and a flatter Gaussian distribution with $\sigma = 0.4\ mm$ was used for beam halo. The amplitude ratio between the main beam and the beam halo was set to 10^6. A divergence of ± 25 mrads was also added to the beam.

Background from the upstream collimator

A collimator (see Fig. 5-16) made of nickel was placed 2.03 meters upstream of the target cell. The rest of the simulation setup is the same code as the one we used for the main PRad simulation, except for the target gas density profile. A gas density profile for empty target was employed[1] in the background simulation. The *ep* counts from the scattering of electrons off the collimator were taken from a beam-on-target simulation, using the Geant4 intrinsic generator. The *ep* counts from residual gas in the empty target (scattering of electrons off the residual gas in target chamber) were taken from the same *ep* generator as the one we used in the PRad simulation. The two counts were summed together with the same luminosity, and then the summed counts were scaled to the yield of empty target run from the experiment. The simulation showed that the collimator performed very well at blocking beam halo electrons. The electrons hitting the front (upstream) or inner surface of the collimator were stopped inside the collimator body completely. Only the electrons hitting the exit edge of the collimator could escape and reach the detectors, as shown in Fig. 5-16. However, considering the low target gas density for empty target run in PRad experiment, the scattered electrons from collimator still dominated the background yield in the forward scattering angles.

The simulation result is shown in Fig. 5-17. As one can see in the plot, after

[1]The empty target gas profile was also developed by Yang Zhang from Duke university using COMSOL along with the production gas density profile.

the contribution from collimator was added, the bump at forward scattering angles overlaps very well between the simulation and the experiment data Fig. 5-12 and Fig. 5-14. The bump ends at 1.1° for both 1.1 GeV and 2.2 GeV beams, because the scattered electrons from collimator beyond 1.1° were completely stopped by the following 2-meter-long beam pipe and the steel target assembly in the downstream direction.

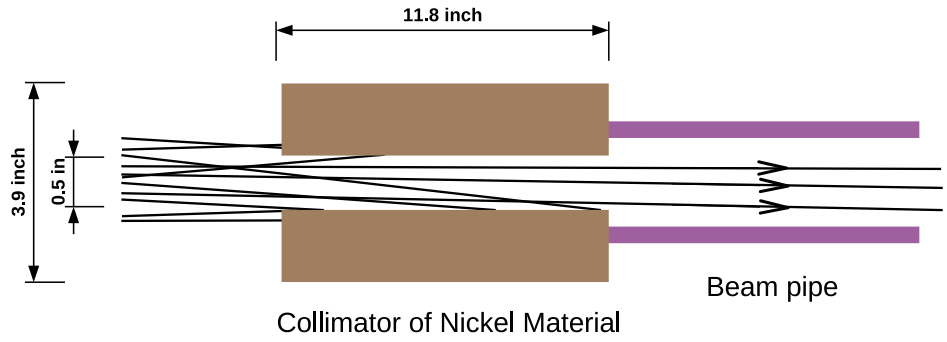

Figure 5-16: A collimator was used to block beam halo. The halo electrons that hit the inner corner on the right side of the collimator escaped along with the main beam, caused a higher background level at forward angle. The lines show possible trajectories of electrons hitting the collimator and those pass through.

Background from inelastic *ep* scattering

Another significant background contribution was from inelastic *ep* scattering. Unlike the background related to beam line, inelastic contamination cannot be removed by simply subtracting yields from background runs. We studied different inelastic *ep* scattering models to fit our data and to estimate its contribution. For the 2.2 GeV beam, the inelastic peak was around $E' = 1820$ MeV at all angles. To evaluate the the agreement between data and different inelastic *ep* models, a χ^2 was defined:

$$\chi^2 = \sum_{i=1} \frac{(N^i_{data} - N^i_{sim})^2}{(\sigma^i_{data})^2 + (\sigma^i_{sim})^2}, \tag{5.10}$$

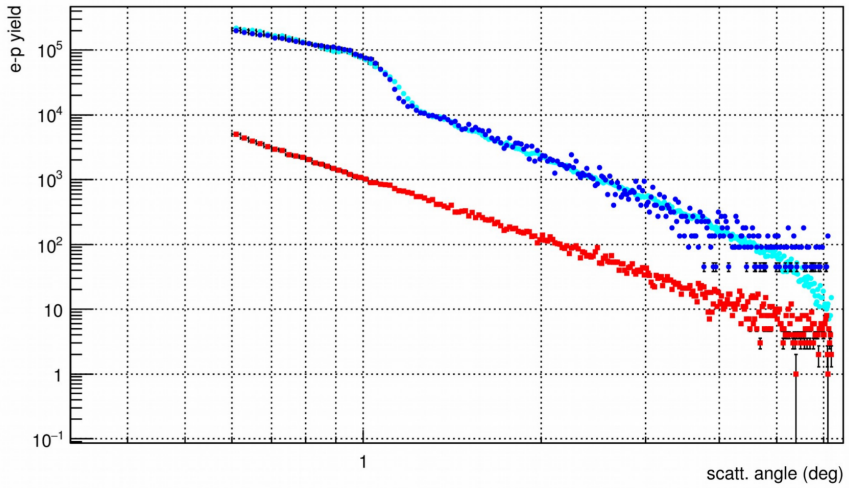

Figure 5-17: Beam on target simulation for collimator. The red dots are simulated *ep* yields from residue gas in target chamber without collimator; The cyan dots are elastic *ep* yields from empty chamber run from experiment (target configuration (b) in Fig. 5-10); The blue dots are the simulated *ep* yields from residue gas plus collimator.

where index i represents all energy bins from 1700 MeV to 1850 MeV, a region where the inelastic peak is visible. The luminosity for PRad data had a relatively large uncertainty due to the gas flow target. Thus, in order to compare the simulation with data, the spectrum from the simulation was scaled to that from the data by a factor of α, which equals the ratio of amplitudes of the two elastic peaks instead of luminosity. The inelastic simulation was scaled to the elastic simulation by luminosity, since both of them were precisely known in simulation. For Eq. (5.10), the N^i stands for the counts of electrons in i^{th} bin for both data and simulation, and σ represents their statistical uncertainty, which follows a Poisson distribution. For each inelastic model, a scale factor and a stretch factor were applied. The scale factor increased or decreased the amplitude of the model, and the stretch factor shifted the peak of the model to the left or right side. For each pair of the two factors, a full simulation and a χ^2 calculation were performed. The search of the minimum of χ^2 was executed through a series of scans for the two-factor pairs. The best model that fits our data should be the one whose minimum χ^2 appears when both factors are closest to 1. Through this method, we found out that the Christy 2018 model [31] best describes PRad data.

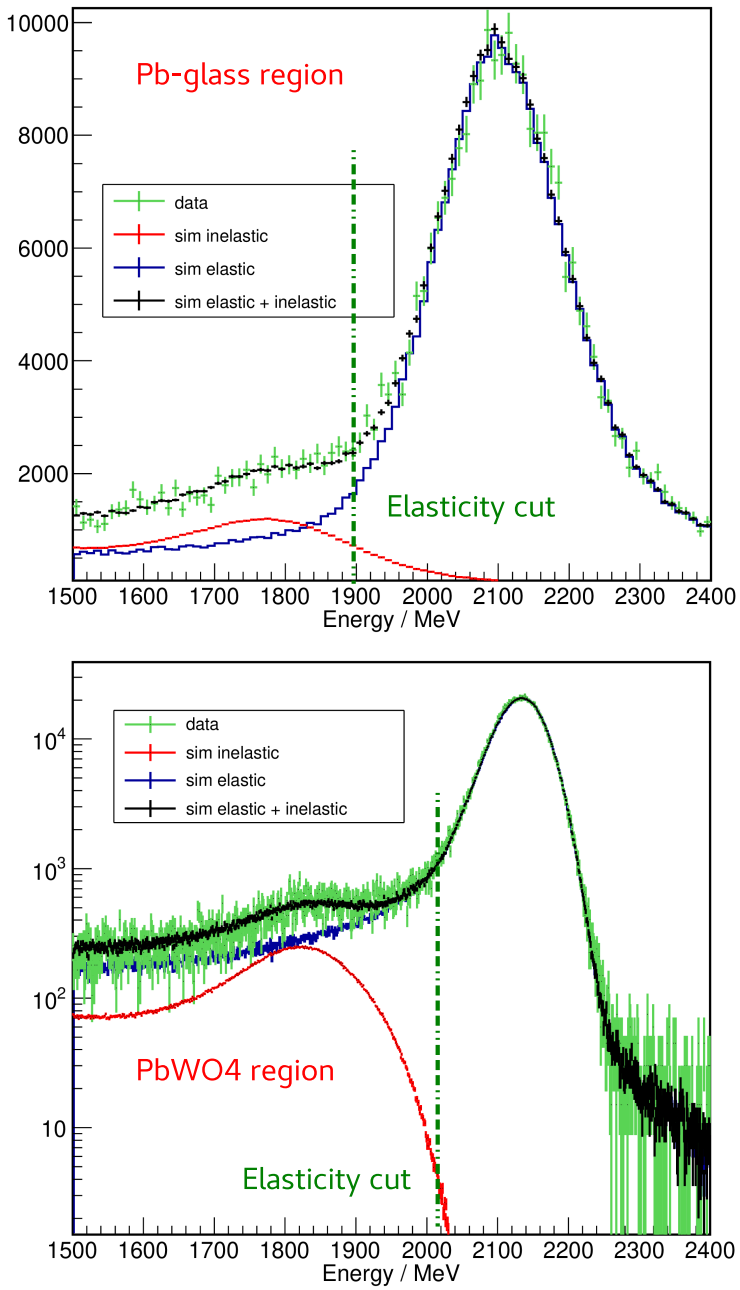

Figure 5-18: Comparison of the reconstructed energy spectrum in Pb-glass region (top) and PbWO4 region (bottom) between data and simulation. The green line is PRad data; the blue line is pure elastic simulation; the red line is the pure inelastic simulation using Christy 2018 model [31]; the black line is the sum of inelastic and elastic simulation. The bottom plot is in log scale to show the agreement.

Using Christy 2018 model, the estimated contribution from the inelastic scattering was found to be negligible for the HyCal crystal region, because the crystal region had a sufficient energy resolution to cleanly reject inelastic electrons from the elastic cut region, see the bottom plot in Fig. 5-18. The cut is tighter when energy resolution is better, see Table 5.3. The contribution was larger in the large Q^2 region where Pb-glass modules dominated cluster reconstruction, see the top plot in Fig. 5-18. In this region, the inelastic *ep* contribution was up to 2% for the 2.2 GeV beam, and up to 0.2% for the 1.1 GeV beam,

Background from photons

Background source 6), the contribution from photons, has also been investigated using Geant4 simulation. In most cases, photons were rejected by the matching between GEM and HyCal since GEMs are mostly sensitive to charged particles only. The matching required that for each GEM hit that originated from the target, its projected position on HyCal must be within a 6σ range around the HyCal reconstructed position, where σ is HyCal position resolution at that point, it was location dependent due to HyCal had different resolutions in different regions. However, there's around 1.5% - 2% chance that a HyCal signal induced by a photon could trigger matching signals in GEM. These signals on GEM were caused by electrons generated from Compton scattering or pair production that happened in GEM frames, GEM foils, the 1.6 mm thick aluminum vacuum foil, and also the electrons back-scattered from HyCal. The ratio of these photon relative to electrons was estimated in GEM efficiency study by varying different pedestal cuts. This ratio was evaluated to be 0.4% - 0.5%, see Fig. 4-24 in last Chapter. The contamination is thus the photon to electron ratio multiplied by the chance that the photons induce matched GEM signals. The upper bound for background 6) was around 0.01%.

Background from multiple scattering

Lastly, although we could reach electron scattering angles down to 0.6°, the angular acceptance range used in physics analysis was set to around $0.7° \sim 7.2°$, see Table

5.2. Because the detector energy and position resolutions deteriorated in the $< 0.7^\circ$ region due to energy leakage and the tungstate absorber in front of the HyCal. The materials in this region closely around the beam line, such as beam pipe, the vacuum box window inner fringe, GEM frame, the tungstate absorber right in front of HyCal, could cause secondary scatterings. Thus, the scattered electrons at $< 0.7^\circ$ could go through multiple scatterings inside these materials and reach the physics acceptance range. Most of these electrons were rejected through GEM and HyCal matching, and only the GEM efficiency was affected. For this efficiency issue, we had two different cross checks. One was through the cross check of GEM efficiency from different types of events: the efficiency from *ep* events was contaminated by this background but the *ee* efficiency stayed intact because it required two electrons satisfying the Møller kinematics. The other way was during the *ep*, *ee* normalization process, where we used a bin by bin method for small scattering angle bins; in this bin by bin method, the GEM efficiency canceled out in the *ep*/*ee* ratio. Thus, the GEM efficiency in this region was not used.

5.5 Simulation

The PRad analysis required a very detailed, realistic and comprehensive simulation. This was critical due to two important reasons, (1) the electric form factor G_E was determined with the aid of the simulation using an iterative method; (2) the studies of background, acceptance, radiative effects, bin center correction, systematic uncertainties etc, were also performed through simulation. Thus a simulation package based on Geant4 was developed by the Duke and the UVa groups in the collaboration. The geometry and material setup in the simulation followed exactly the PRad experiment. In the simulation, each GEM detector was composed of three layers of GEM foils with NEMA G10/FR4 material frames around them; each GEM foil included two 5 μm-thick copper layers and one 60 μm-thick kapton layer. The HyCal detector model consisted of 1156 PbWO4 crystal modules and 576 Pb-glass modules. The 100 μm VM2000 reflective material foil and the 36 μm Tedlar foil wrapping the PbWO4

modules, the 25 μm aluminized mylar foil wrapping the Pb-glass modules were also implemented. A tungstate absorber was placed right in front of HyCal around the beam line. The vacuum box included a two-stage steel cylinder and a 1.6 mm thick sealing aluminum window at the downstream end; the upstream side of the vacuum box was connected to the target assembly. The 4 cm long target cell was made of copper, the kapton orifices on both sides of the target cell were also implemented. A 2-inch-diameter beam pipe connected the target to the upstream collimator located at around 2 meters upstream of the target, the collimator was made of nickel material. All the sizes followed exactly the actual detector sizes, and the relative positions between detectors followed the survey data from the Jefferson Lab survey group.

A digitization package for the calorimeter was also developed. The digitization package translated the deposited energy in simulation into ADC values, and saved the ADC values for each module to an evio file, in the same format as the files generated with PRad experimental data. Then the same reconstruction code used for PRad experimental data was used to analyze the simulation output. This ensured that the same cut criteria were used for both simulation and data analysis.

Geant4 has intrinsic generators. The interactions between scattering particles and materials have been grouped into different physics lists. The standard EM physics list we adopted in the PRad simulation includes effects from ionization, Bremsstrahlung, Compton scattering, pair production, Rayleigh scattering etc. However, in PRad simulation, these effects were only used to simulate the external radiation effect. In order to better describe PRad data, and also to speed up simulation, two ep/ee generators based on Akushevich [8] and Gramolin's work [32] were developed. Both generators included radiative effects, which satisfied the precision requirement of PRad experiment. Thus, instead of directly shooting electron beams into the target and accumulating the scattered simulated electrons in the Geant4 beam-on-target method, the electrons from the generators were used. Considering the small cross section of ep and ee scattering, a beam-on-target simulation was very low in efficiency, since most of the electrons go straight or scatter into very forward angles outside the detector acceptance. Using an independent generator (which outputs scattered electrons for a

specific angular range) greatly improved simulation efficiency.

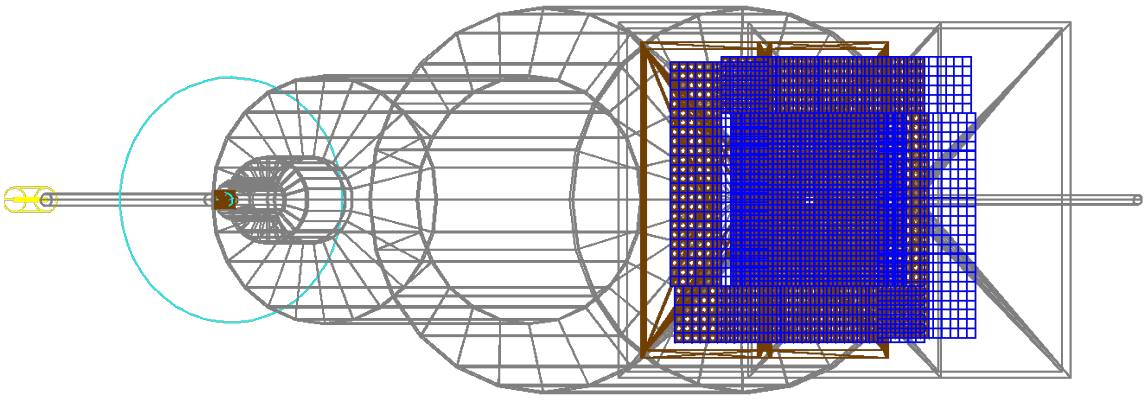

Figure 5-19: A Geant4 simulation for the PRad experiment. The blue is for the HyCal detector, consisting of 1728 modules; the brown frames in front of HyCal are for GEM detectors; The grey cylinders represent the two-stage vacuum box; the cyan circle at the left side is the target assembly; The yellow cylinder on the most left side is the collimator.

A gas density profile for the target was also developed using COMSOL[2] software to best mimic the realistic running conditions. In PRad, a series of pressure gauges, flow meters, and temperature sensors were installed in the target assembly to monitor the target running status. All input parameters that were used in COMSOL were from measurements of these sensors. The electrons from the generators passed through the target gas with a density distribution following the calculated profile (see Fig. 5-20), and interactions (including all the effects in the standard EM physics list mentioned above) between the generator electrons and the target gas were taken as the external radiative contribution.

[2]This COMSOL simulation was done by Yang Zhang from Duke Group.

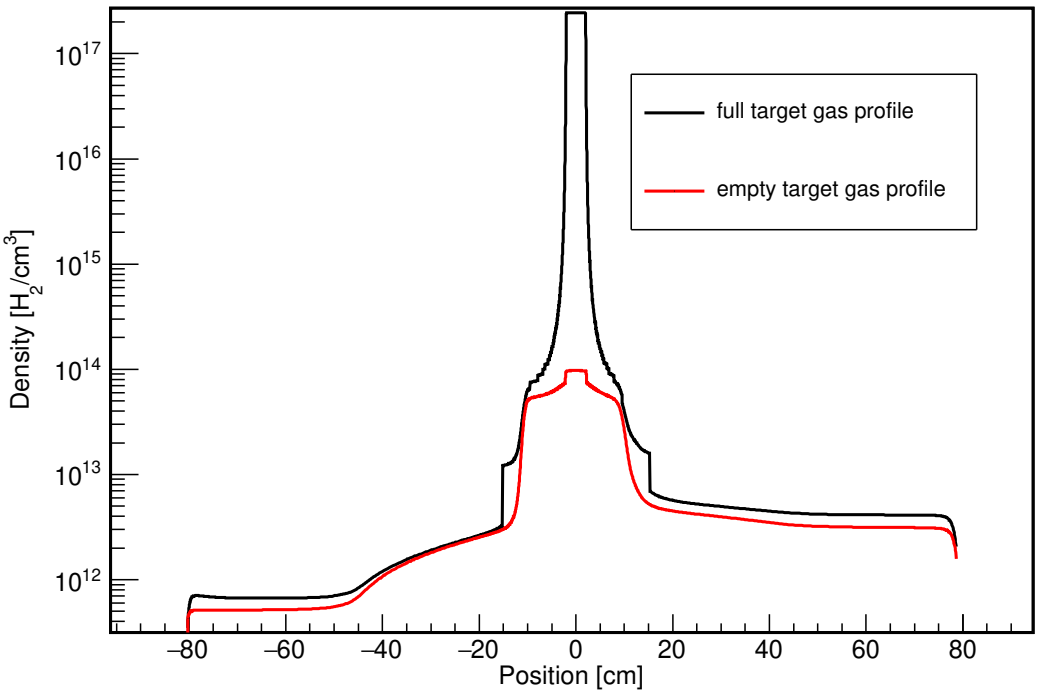

Figure 5-20: Target gas density profile calculated using COMSOL software, the X-axis origin refer to the target center. Target is a 4 cm long cylinder. The black is production target gas profile; red is empty target gas profile.

5.5.1 Radiative Corrections

For the internal radiative correction, two independent generators [32] [8] were developed to calculate the next-to-leading order contribution to the Born level cross section. Due to the high precision required by PRad experiment, both generators did not use the ultra relativistic approximation that neglects the electron mass in calculation. Both generators generated hard photons [125] without using the peaking approximation, an assumption that hard photons are emitted either along the direction of the incident electron or the scattered electron [126]. Not using this approximation was crucial since the calorimeter cannot distinguish photons from electrons, and accumulates their deposited energy together if the emitted photons not separated far enough from the electrons. The results from the two generators were cross checked against each other. In our simulation the discrepancy between the two generators was negligible.

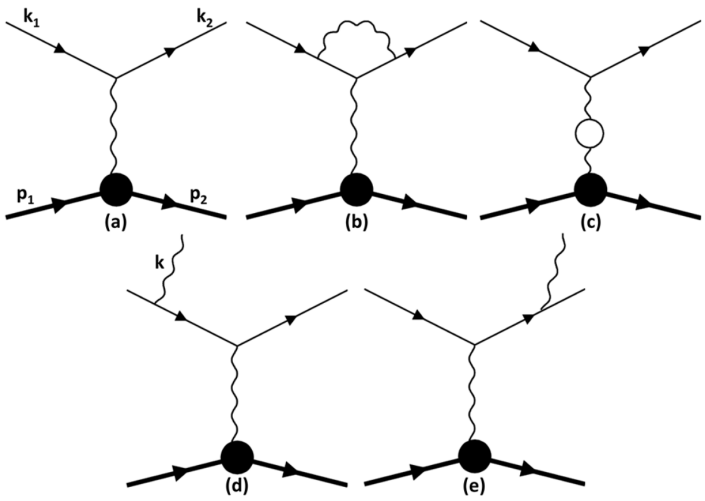

Figure 5-21: Feynman diagrams for *ep* elastic scattering [8], including the Born level (a), and the next-to-leading order radiative corrections on the lepton line: (b) vertex correction, (c) vacuum polarization, (d)-(e) Bremsstrahlung photons.

The generator from [8] included contributions from Feynman diagrams as shown in Fig. 5-21 for *ep* and Fig. 5-22 for *ee*. The generator from [32] also included contributions from Bremsstrahlung photons originated from the proton line, as shown in Fig. 5-23, which was usually neglected in other generators. However, due to the heavy

mass of proton, the contribution from it was negligible at PRad kinematics, which was cross checked in our simulation. The two-photon-exchange (TPE) contribution was also estimated using [32] [127] [128] [129], which was less than 0.2% of the Born level cross section in PRad kinematics range.

5.5.2 Angular and Q^2 Resolution

The angular and Q^2 resolution of PRad experiment was also studied using the same Geant4 simulation package, see results shown in Fig. 5-24. This study was necessary since the resolution determined how fine binning that we could have. In this study, the position of the scattered electrons was determined by GEM. Since the scattering was elastic, the Q^2 only rely on the scattering angle θ and beam energy. Beam in Jefferson Lab Hall B has about ± 0.5 MeV and ± 1.5 MeV uncertainty around the central value for 1.1 GeV and 2.2 GeV. Beam energy spread is around $\pm 3 \times 10^{-5}$.

5.6 Cross Section

The experimental differential cross section for the ep scattering process at a particular angle bin θ_i is defined as:

$$\langle \frac{d\sigma_{ep}^{e,r}(\theta_i)}{d\Omega} \rangle = \frac{N_{ep}^{e,r}(\theta_i)}{L \cdot g_{ep}^{e,r}(\theta_i) \cdot \epsilon_{ep}^{e,r}(\theta_i)}, \tag{5.11}$$

where the $\langle\rangle$ operator means the cross section is averaged in a specific bin θ_i, L is the integrated luminosity: $L = N_{beam}^{e-} \cdot N_{target}^{H}$; N_{beam}^{e-} is the total number of the incident electrons, N_{target}^{H} is the target areal density. g is detector acceptance; ϵ represents for detector efficiency. $N_{ep}^{e,r}(\theta_i)$ means the yield of ep events in angle bin θ_i received by the detector. The superscript e means measurement in experiment; r means with radiative correction; the subscript i means the i^{th} bin.

Similarly for the Møller differential cross section we have:

$$\langle \frac{d\sigma_{ee}^{e,r}(\theta_j)}{d\Omega} \rangle = \frac{N_{ee}^{e,r}(\theta_j)}{L \cdot g_{ee}^{e,r}(\theta_j) \cdot \epsilon_{ee}^{e,r}(\theta_j)}. \tag{5.12}$$

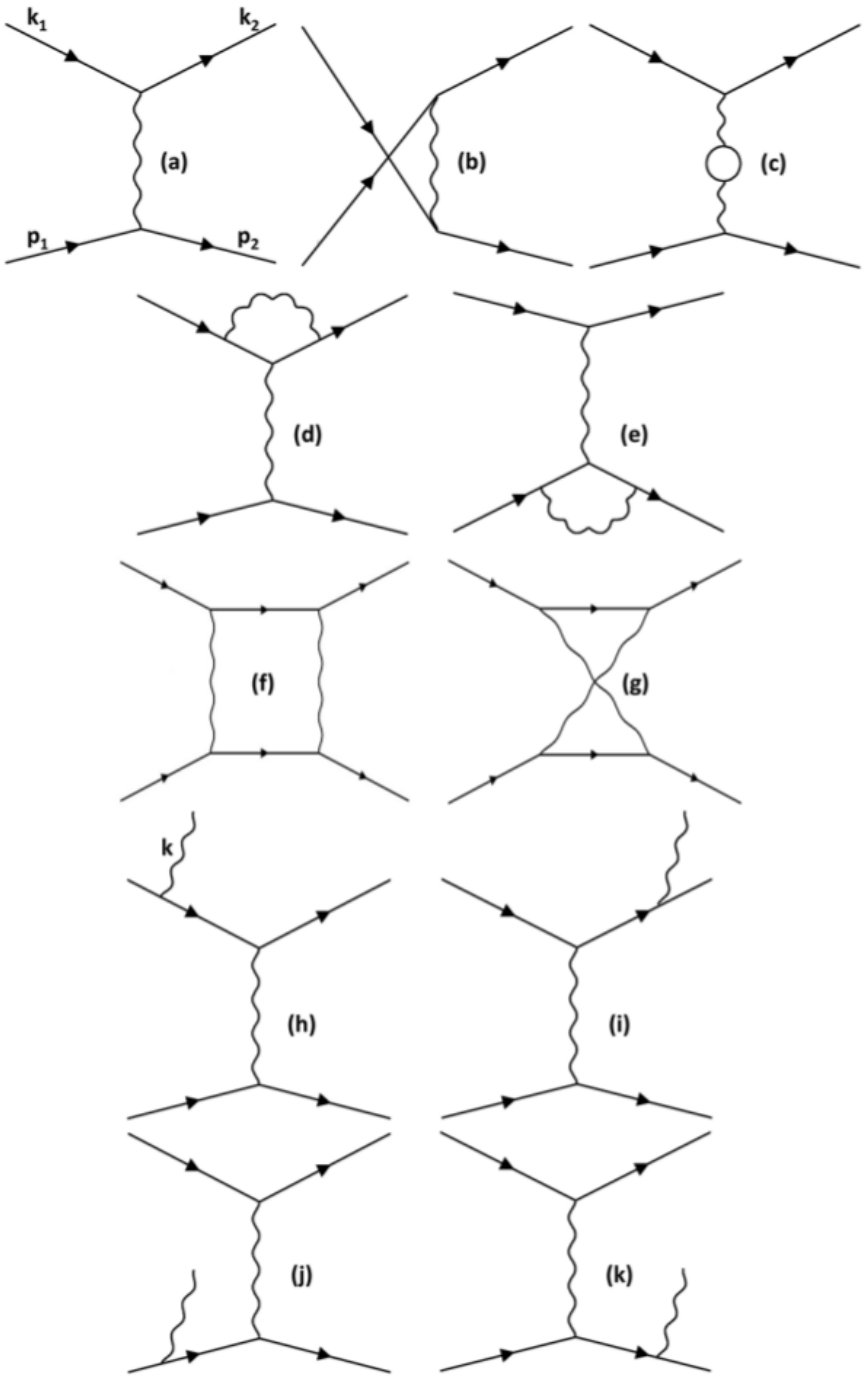

Figure 5-22: Møller scattering Feynman diagrams [8], include the Born level (the top left) and the next-to-leading order radiative corrections; (c) vacuum polarization, (d)-(e) vertex correction, (f)-(g) TPE (two photon exchange) effect, (h)-(k) Bremsstrahlung photons.

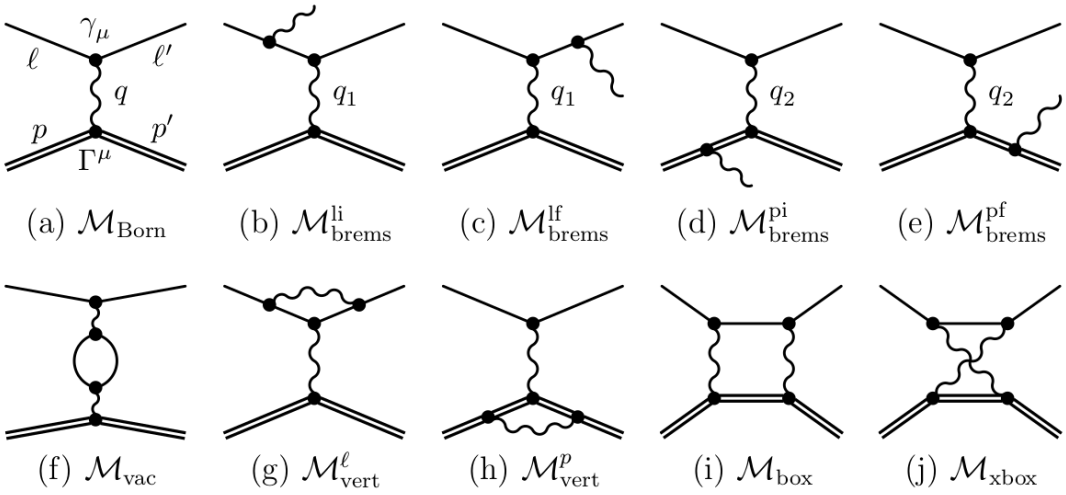

Figure 5-23: Feynman diagrams for ep elastic scattering [32]. (a) Born level; (b)-(e) the first order Bremsstrahlung process $l^{\pm}p \to l^{\pm}p\gamma$ from external lines, include both lepton and hadron; (f)-(j) virtual-photon correction, where (f) vacuum polarization, (g) lepton (h) proton vertex correction and (i) (j) two photon exchange correction.

In this analysis, the $e-p$ elastic cross section was normalized to the Møller cross section by dividing Eq. (5.11) over Eq. (5.12), so the luminosity L cancels out, leaving only efficiency and acceptance factors:

$$\begin{aligned}\langle\frac{d\sigma^{e,r}_{ep}(\theta_i)}{d\Omega}\rangle &= \frac{N^{e,r}_{ep}(\theta_i)}{g^{e,r}_{ep}(\theta_i)\epsilon^{e,r}_{ep}(\theta_i)}\Big/\frac{N^{e,r}_{ee}(\theta_j)}{g^{e,r}_{ee}(\theta_j)\epsilon^{e,r}_{ee}(\theta_j)}\cdot\langle\frac{d\sigma^{e,r}_{ee}(\theta_j)}{d\Omega}\rangle \\ &= \frac{N^{e,r}_{ep}(\theta_i)}{N^{e,r}_{ee}(\theta_j)}\cdot\frac{g^{e,r}_{ee}(\theta_j)\epsilon^{e,r}_{ee}(\theta_j)}{g^{e,r}_{ep}(\theta_i)\epsilon^{e,r}_{ep}(\theta_i)}\cdot\langle\frac{d\sigma^{e,r}_{ee}(\theta_j)}{d\Omega}\rangle,\end{aligned} \tag{5.13}$$

In order to extract the form factors, the Born level differential cross sections was needed. The measured cross section from experimental data contained radiative corrections, thus a radiative correction (RC) factor was needed to get Born level cross sections from experimentally measured cross sections. This factor was calculated in simulation using Eq. (5.14):

$$\text{RC} = \langle\frac{d\sigma^{s,b}_{ep}(\theta_i)}{d\Omega}\rangle\Big/\langle\frac{d\sigma^{s,r}_{ep}(\theta_i)}{d\Omega}\rangle, \tag{5.14}$$

where superscript s represents for simulation; b means Born level; and r means with

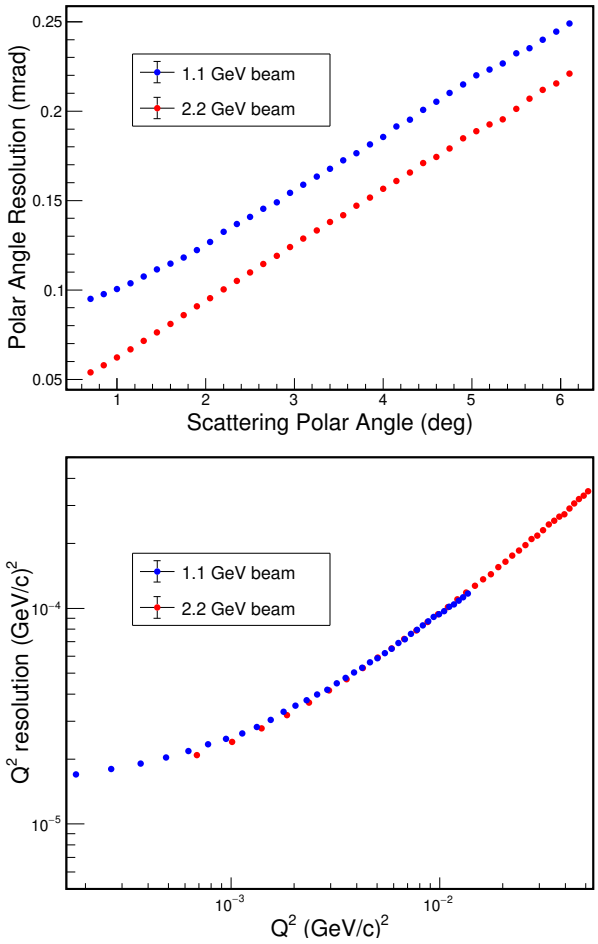

Figure 5-24: Scattering angle (top) and Q^2 (bottom) resolution of PRad experiment. The red is for 2.2 GeV beam, blue is for 1.1 GeV beam. The angle smearing in simulation is caused by the multiple scattering happened in residue gas, vacuum aluminum foil, etc. The detector resolution and target length also contributes.

radiative correction.

Besides radiative corrections, we also need a bin centering correction to get the cross section at the bin center from the averaged cross section at that bin. This bin center correction factor was also obtained from the simulation:

$$\mathrm{BCC} = \left(\frac{d\sigma_{ep}^{s,b}(\theta_i)}{d\Omega}\right) \Big/ \left\langle \frac{d\sigma_{ep}^{s,b}(\theta_i)}{d\Omega} \right\rangle, \tag{5.15}$$

where the numerator with the operator () is evaluated at the center value θ_i and the denominator is evaluated over the whole bin.

Combing all these factors, one could get the Born level cross section in simulation:

$$\left(\frac{d\sigma_{ep}^{s,b}(\theta_i)}{d\Omega}\right) = \mathrm{BCC} \times \mathrm{RC} \times \left\langle \frac{d\sigma_{ep}^{s,r}(\theta_i)}{d\Omega} \right\rangle, \tag{5.16}$$

where BCC means bin center correction factor; RC represents radiative correction factor. Equation (5.16) works for both simulation and data.

For averaged *ep* cross section with RC in simulation, it was also normalized by *ee* cross section in the simulation:

$$\left\langle \frac{d\sigma_{ep}^{s,r}(\theta_i)}{d\Omega} \right\rangle = \frac{N_{ep}^{s,r}(\theta_i)}{N_{ee}^{s,r}(\theta_j)} \cdot \frac{g_{ee}^{s,r}(\theta_j)\epsilon_{ee}^{s,r}(\theta_j)}{g_{ep}^{s,r}(\theta_i)\epsilon_{ep}^{s,r}(\theta_i)} \cdot \left\langle \frac{d\sigma_{ee}^{s,r}(\theta_j)}{d\Omega} \right\rangle. \tag{5.17}$$

For Møller, we had a very accurate QED calculation for its cross section, including radiative corrections up to next-to-leading order, very well suited for PRad experiment precision; so we would assume data and simulation have the same Møller cross section. Therefore we can replace *ee* simulation cross section by data *ee* cross section in Eq. (5.17).

$$\left\langle \frac{d\sigma_{ep}^{s,r}(\theta_i)}{d\Omega} \right\rangle = \frac{N_{ep}^{s,r}(\theta_i)}{N_{ee}^{s,r}(\theta_j)} \cdot \frac{g_{ee}^{s,r}(\theta_j)\epsilon_{ee}^{s,r}(\theta_j)}{g_{ep}^{s,r}(\theta_i)\epsilon_{ep}^{s,r}(\theta_i)} \cdot \left\langle \frac{d\sigma_{ee}^{e,r}(\theta_j)}{d\Omega} \right\rangle. \tag{5.18}$$

Substituting Eq. (5.18) back into Eq. (5.13), one obtains:

$$\left\langle \frac{d\sigma_{ep}^{e,r}(\theta_i)}{d\Omega} \right\rangle = \frac{N_{ep}^{e,r}(\theta_i)}{N_{ee}^{e,r}(\theta_j)} \cdot \frac{g_{ee}^{e,r}(\theta_j)\epsilon_{ee}^{e,r}(\theta_j)}{g_{ep}^{e,r}(\theta_i)\epsilon_{ep}^{e,r}(\theta_i)} \cdot \frac{N_{ee}^{s,r}(\theta_j)}{N_{ep}^{s,r}(\theta_i)} \cdot \frac{g_{ep}^{s,r}(\theta_i)\epsilon_{ep}^{s,r}(\theta_i)}{g_{ee}^{s,r}(\theta_j)\epsilon_{ee}^{s,r}(\theta_j)} \cdot \left\langle \frac{d\sigma_{ep}^{s,r}(\theta_i)}{d\Omega} \right\rangle. \tag{5.19}$$

Since we had exactly the same detector setup in simulation and in experiment, the

detector acceptance coefficients ($g_{ep}^{s,r}$ and $g_{ee}^{s,r}$, $g_{ep}^{e,r}$ and $g_{ee}^{e,r}$) would cancel out, and we only need to correct the detector efficiency ($\epsilon's$) for data.

After correcting the detector efficiency for data, the efficiency factors in Eq. (5.19) canceled out:

$$\langle\frac{d\sigma_{ep}^{e,r}(\theta_i)}{d\Omega}\rangle = \frac{N_{ep}^{e,r}(\theta_i)/N_{ee}^{e,r}(\theta_j)}{N_{ep}^{s,r}(\theta_i)/N_{ee}^{s,r}(\theta_j)} \cdot \langle\frac{d\sigma_{ep}^{s,r}(\theta_i)}{d\Omega}\rangle. \tag{5.20}$$

For the Born level cross section in data, one could use the correction factors obtained in Eq. (5.16):

$$\begin{aligned}(\frac{d\sigma_{ep}^{e,b}(\theta_i)}{d\Omega}) &= \text{BCC} \times \text{RC} \times \langle\frac{d\sigma_{ep}^{e,r}(\theta_i)}{d\Omega}\rangle \\ &= \text{BCC} \times \text{RC} \times \frac{N_{ep}^{e,r}(\theta_i)/N_{ee}^{e,r}(\theta_j)}{N_{ep}^{s,r}(\theta_i)/N_{ee}^{s,r}(\theta_j)} \cdot \langle\frac{d\sigma_{ep}^{s,r}(\theta_i)}{d\Omega}\rangle.\end{aligned} \tag{5.21}$$

Substitute Eq. (5.16) into Eq. (5.21), one could get the Born level $e-p$ scattering cross section for data:

$$(\frac{d\sigma_{ep}^{e,b}(\theta_i)}{d\Omega}) = \frac{N_{ep}^{e,r}(\theta_i)/N_{ee}^{e,r}(\theta_j)}{N_{ep}^{s,r}(\theta_i)/N_{ee}^{s,r}(\theta_j)} \cdot (\frac{d\sigma_{ep}^{s,b}(\theta_i)}{d\Omega}), \tag{5.22}$$

Keep in mind that one need to correct detector efficiencies for Eq. (5.22), unless the $e-p$ efficiency canceled out with $e-e$ efficiency when using bin by bin method, namely bins $i=j$. The ratio appeared in Eq. (5.22)

$$R \equiv \frac{N_{ep}^{e,r}(\theta_i)/N_{ee}^{e,r}(\theta_j)}{N_{ep}^{s,r}(\theta_i)/N_{ee}^{s,r}(\theta_j)}. \tag{5.23}$$

is called the super ratio between data and simulation.

This method put a very strict requirement for the simulation: the *ep* cross section in simulation needs to be exactly the same as that from the experiment. This could be achieved using an iterative method, by tuning the form factors that were used in simulation iteratively, until the simulation converged with data and the super ratio $R=1$ was approached.

The iteration procedure is as follows: 1) set up both the electric and magnetic form factor models/parameterizations in simulation (knowing the form factors means

we know exactly the Born level cross section in simulation); 2) do a full Geant4 simulation, with radiative corrections for both $e-p$ and $e-e$; 3) use Eq. (5.23) to obtain the super ratio between data and simulation; 4) use Eq. (5.22) and the Born level cross section in simulation, obtain the Born level cross section for data, then extract the form factors from the Born level cross section for data; 5) if the super ratio in step 3 converged to 1 at every scattering angle bin, then the extracted form factors in step 4 would be taken as the final result; otherwise replace the form factors in simulation with the one we extracted in step 4, and repeat the full Geant4 simulation starting step 2; 6) repeat steps 1 - 5 until the super ratio converged to 1.

5.6.1 Super Ratio

As described by Eq. (5.22) in the last section, the Born level cross section was determined from the simulation, using the super ratio between PRad experimental data and simulation and the iteration method. In order to determine the super ratio, the elastic *ep* and *ee* counts in each scattering bin needs to be calculated, and the background in each bin needs to be removed. In realistic situations of an experiment, the running conditions cannot be kept the same all the time. For example, in PRad case the change of beam position and current, the replacement of APV cards in GEM detectors, and the swap for ADC boards in HyCal detector etc, all caused changes in experimental running conditions. It is therefore erroneous to subtract a fixed background run from different production runs. During PRad, every three production runs were followed by one empty target run. And during the analysis, the background subtraction of production runs was always based on the background run nearest in time. The production runs and empty runs were normalized by live charge, which was determined from a Faraday cup installed in the beam line:

$$N_{ep}^{e,r}(\theta_i) = N_{ep}^{e,r}(\theta_i)|_{prod} - \frac{C_{prod}}{C_{empty}} N_{ep}^{e,r}(\theta_i)|_{empty}, \tag{5.24}$$

$$N_{ee}^{e,r}(\theta_i) = N_{ee}^{e,r}(\theta_i)|_{prod} - \frac{C_{prod}}{C_{empty}} N_{ee}^{e,r}(\theta_i)|_{empty}, \tag{5.25}$$

where $C_{prod/empty}$ represents the ratio of live charge detected from the Faraday cup, and $N(\theta_i)$ are the elastic ep, ee counts in bin θ_i from production ($|_{prod}$) and background ($|_{empty}$) runs.

The elastic counts of ep and ee for simulation also need to be calculated, as already described in section (5.5). In order to reach the closest similarity between simulation and data, radiation corrections and inelastic contribution must be taken into account in the simulation generator. Our ep and ee generators already included the next-to-leading order radiative contribution [8] [32] from both electron line and proton line. The inelastic contribution was simulated independently using Christy empirical model [31]. The inelastic yield was added to elastic yield with the same luminosity.

The super ratio (Eq. 5.23) was defined as the ratio of ep yield over ee yield between data and simulation. In PRad experiment, there were two types of Møller events: double arm Møller and single arm Møller events. Double arm Møller events required two electrons to be detected simultaneously, while single arm Møller events only required one. Double arm Møller had more kinematic cuts, resulting in a much cleaner selection. Thus, in analysis, the ep/ee ratio was calculated using double arm Møller[3]. The ep and Møller yields were corrected by GEM efficiency. The weakness of this method was that the double Møller events have limited angular coverage. This was due to the detector acceptance: for the majority of the scattered Møller events, the electron in forward angle passed through the beam hole beyond the detector acceptance.

	ep	ee	ee integral range	Møller edge
1.1 GeV	$0.7° \sim 7.2°$	$0.7° \sim 4.0°$	$1.338° \sim 3.092°$	$3.092°$
2.2 GeV	$0.7° \sim 7.2°$	$0.7° \sim 2.5°$	$1.338° \sim 2.0°$	$1.634°$

Table 5.4: Møller, ep events meaningful angular coverage; for Møller, there are very limited events beyond 2.5° (2.2 GeV) or 6.0° (1.1 GeV). The ee integral range means the scattering angle range that we used for integration in the integral method. The Møller edge means beyond this angle, we start to use integral method, smaller than this angle, we use bin by bin method.

[3]The symbol $ee2$ refers to double arm Møller in this thesis, single arm will be denoted as $ee1$. The symbol ee also refers to double arm Møller unless specifically pointed out for other meanings.

As mentioned in section 5.6, there were two different ways to get the ep/ee ratio, one was through bin by bin method, the other one was using integral method. Bin by bin method means that the ep yield was divided by the ee yield in the same bin: θ_j/θ_j; integral method means the ep yield in θ_j was divided by the integral of Møller yields in a range (θ_i, θ_f). Bin by bin method canceled out the effect from detector efficiency, thus there's no need to correct GEM efficiency for ep and ee yields in this method. The need of the second method was due to the limited double arm Møller coverage. As shown in Table 5.4, there were very few double arm Møller events exist beyond 2.5° (2.2 GeV) or 6.0° (1.1 GeV), so it was impossible to use bin by bin method for all bins. The integral method relied more on knowing the GEM efficiencies. The luminosity were canceled in the ep/ee ratio for both methods.

Starting from 1.634° (2.2 GeV) and 3.092° (1.1 GeV), the integral method was used for ep/ee ratio. The integral angle range for Møller events was set to (1.338° $\sim$ 3.092°) and (1.338° $\sim$ 2.0°) for 1.1 GeV and 2.2 GeV beam separately. Using other angle ranges had some small difference, for the super ratio, the difference between choosing different angle ranges was within 0.05%. A systematic uncertainty regarding different angle ranges were also added in the result. The reason behind this small effect was due to the detector conditions in different angle ranges. For the current integral angle range, GEM detector has almost no dead area cut, and there was no dead module cut for HyCal either. The GEM efficiency was known to a very high precision, minimizing the systematic uncertainties introduced by the GEM efficiency.

As described in Eq. (5.22), the Born level cross section was determined through an iteration method, as shown in Fig. 5-25. By adjusting the electromagnetic form factor models/parameterizations that we used in the simulation, we could finally reach a result where the super ratio $R \approx 1$ for every angle bin, as shown in Fig. 5-26. The details of form factors in simulation will be discussed in the following sections.

5.6.2 Born Level ep Elastic Scattering Cross Section

After getting the super ratio, the Born level cross section was extracted using Eq. (5.22). The extracted differential cross section was shown in Fig. 5-27 and Fig. 5-28,

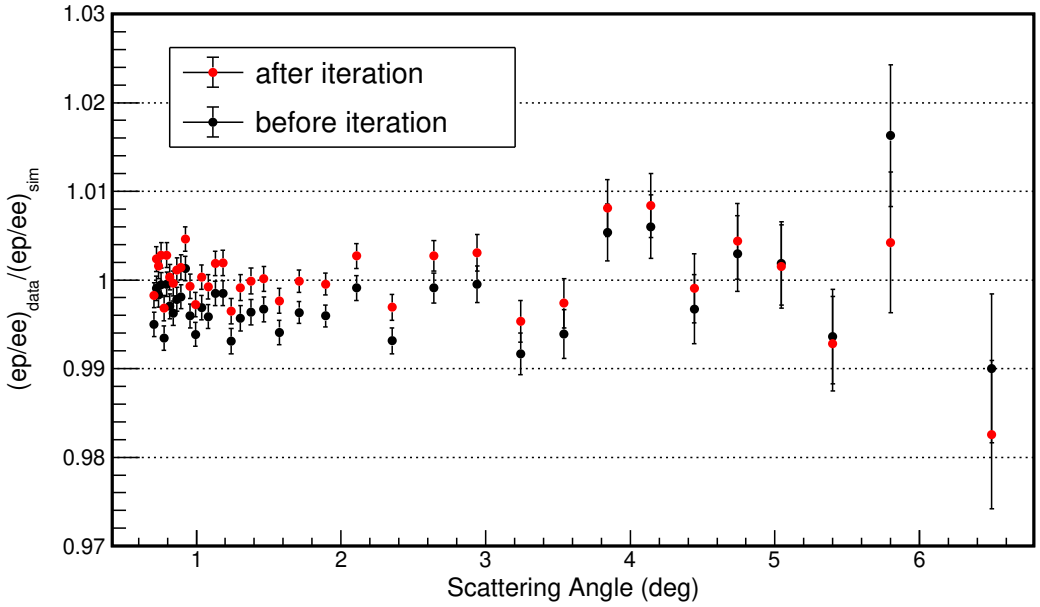

Figure 5-25: The super ratio over iteration. The black line is before iteration, the red line is after iteration. The red line is more converged to 1.

and the cross section table is given in Appendix A.4. There are two bands in the bottom part of each plot, the top band represents for the statistical uncertainty, the bottom band is the systematic uncertainty. For 1.1 GeV beam, there are a total of 33 points, covering the Q^2 range from 2.1×10^{-4} $(\mathrm{GeV}/c)^2$ to 1.6×10^{-2} $(\mathrm{GeV}/c)^2$. The statistical uncertainty increased from 0.2% in small Q^2 to almost 1% in large Q^2, due to that the statistics decreased in large scattering angles. The systematic uncertainty was around 0.3% to 0.5%, which combined contributions from beam line, background subtraction, and GEM efficiency.

For 2.2 GeV *ep* elastic scattering cross section, as shown in Fig. 5-28, there are a total of 38 bins, covering the Q^2 range from 7.0×10^{-4} $(\mathrm{GeV}/c)^2$ to 5.9×10^{-2} $(\mathrm{GeV}/c)^2$. The statistical uncertainty is around 0.15% in forward angle and increased to around 0.8% at large angle, which is slightly lower than the 1.1 GeV case, this was due to that we accumulated more events for 2.2 GeV beam.

The systematic uncertainty at forward angle ($< 3.5^\circ$) is around 0.25% to 0.32%, and around 1.1% at large angle. The slightly larger systematic uncertainty at large angle was partially due to inelastic contribution. For 2.2 GeV beam, the inelastic

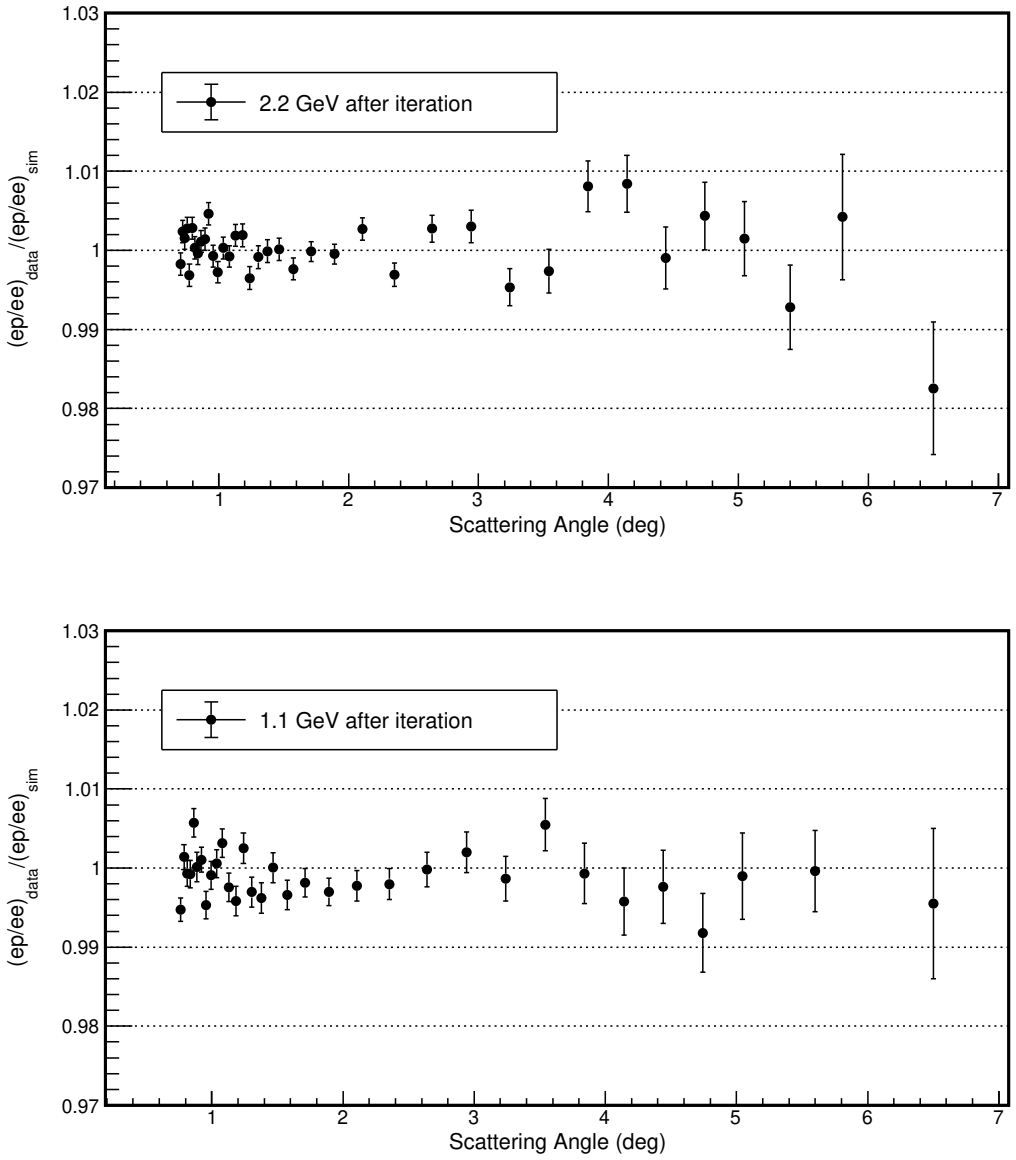

Figure 5-26: Super ratio for 2.2 GeV beam (top) and 1.1 GeV beam (bottom) after iteration finished.

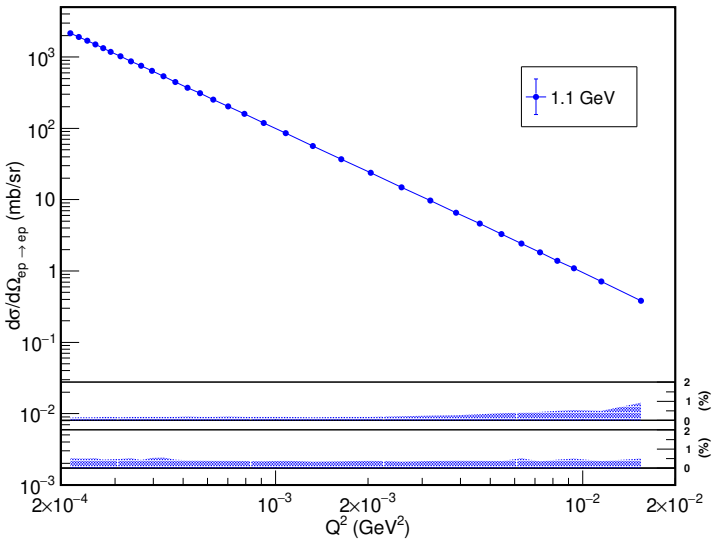

Figure 5-27: The *ep* elastic scattering Born level differential cross section for 1.1 GeV beam. The top band shows the statistical uncertainty, the bottom band is systematic uncertainty. The uncertainties are in the unit of percentage relative to the cross section at each point.

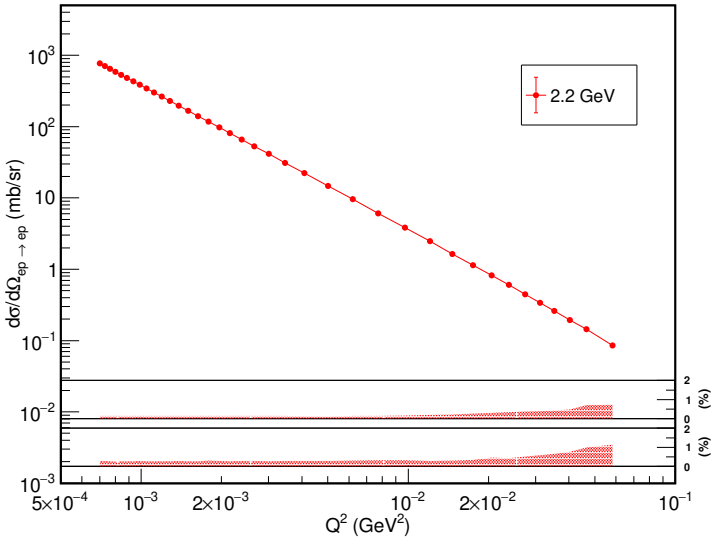

Figure 5-28: The Born level differential cross section for 2.2 GeV beam *ep* elastic scattering. The top band shows the statistical uncertainty, the bottom band is systematic uncertainty. The uncertainties are in the unit of percentage relative to the cross section at each point.

contribution for ep yield is around 2.0% at large angle, while for 1.1 GeV beam, the inelastic contribution at large angle is around 0.2%. The inelastic contribution is negligible for scattering angle $< 3.5°$ for both 1.1 and 2.2 GeV beams, this was due to the fact that for angles $< 3.5°$, HyCal crystal modules dominated the cluster reconstruction, while in area $> 3.5°$, Pb-glass played a key role. The energy resolution for crystal modules was about 3 times better than Pb-glass modules. Thus, the subtraction of inelastic ep yield resulted in a slightly larger uncertainty on the cross sections at large angles. The details of systematic uncertainty estimation will be discussed in the following chapter on radius result.

5.7 Form Factors

As described by the Rosenbluth formula (Eq. (2.92)), the differential cross section for ep elastic scattering includes the contribution from both electric form factor G_E^p and magnetic form factor G_M^p. While in low Q^2 region, namely the PRad case, G_E^p dominates. This is because τ approaches to 0, and ϵ approaches to 1, as shown in Eq. (2.94). Since the contribution from G_M^p is small, it is reasonable to use some known magnetic form factor models or parameterizations as the input, and extract the electric form factor from cross section. A systematic error should be added to the extracted G_E^p regarding the magnetic form factors.

In PRad experiment, different G_M^p models and parameterizations [130] [131] [132] [133] [134] [135] were tested. The first is the dipole model:

$$G_{M,dipole}^p = \mu_p \frac{1}{(1 + \frac{Q^2}{0.71(GeV/c)^2})^2}, \tag{5.26}$$

where $\mu_p = 2.793\ \mu_N$ is the proton magnetic moment, $\mu_N = e\hbar/(2m_p)$ is the nuclear magneton.

There is also the polynomial model:

$$G_{M,polynomial}^p = 1 + \sum_i^n a_i Q^{2i}, \tag{5.27}$$

where a_i are the parameterizations. There is also the Kelly form factor [9] which was used to extract the G_E^p for PRad, our result for G_E^p is shown in Fig. 5-29. The relative difference of extracted G_E^p between using Kelly magnetic form factor and using other G_M^p models or parameterizations (defined in Eq. (5.28)) is shown in Fig. 5-30 using the following formula:

$$\frac{\Delta G_E^p}{G_E^p|_{G_M^p(\text{Kelly})}} = \frac{G_E^p|_{G_M^p(\text{Kelly})} - G_E^p|_{G_M^p(\text{other model})}}{G_E^p|_{G_M^p(\text{Kelly})}}, \tag{5.28}$$

where G_M^p(Kelly) is the Kelly magnetic form factor for proton; G_M^p(other model) is other model or parameterization of magnetic form factor for proton (see Fig. 5-30); $G_E^p|_{G_M^p(\text{Kelly})}$ is the extracted proton electric form factor from PRad data using Kelly magnetic form factor. The relative difference at $Q^2 = 0.06$ (GeV/c)^2 (the largest Q^2 that PRad reached) is less than 0.3%, and less than 0.01% in $Q^2 < 0.01$ (GeV/c)^2 region.

The systematic uncertainties for proton electric form factor G_E^p due to magnetic form factor G_M^p assumptions is less than 0.07% (0.03%) at $Q^2 = 0.06$ (GeV/c)^2 , and less than 0.015% (0.028%) in $Q^2 < 0.01$ (GeV/c)^2 region for 2.2 (1.1) GeV beam.

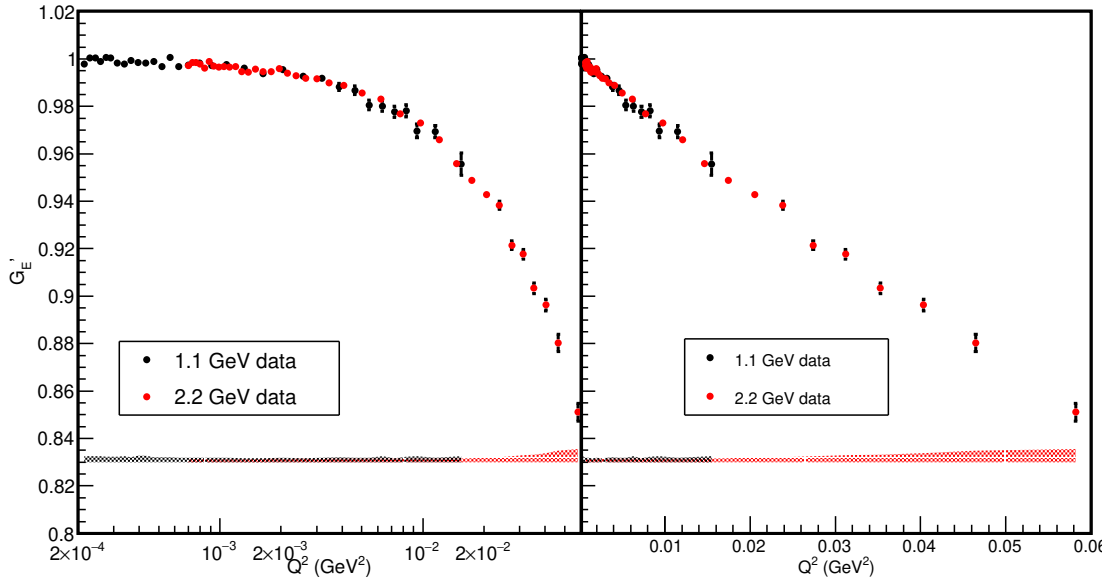

Figure 5-29: The extracted electric form factor G_E^p for 1.1 GeV (black) and 2.2 GeV (red) beam. Statistical uncertainties are shown as the error bar, systematic uncertainties are shown as the band in the bottom.

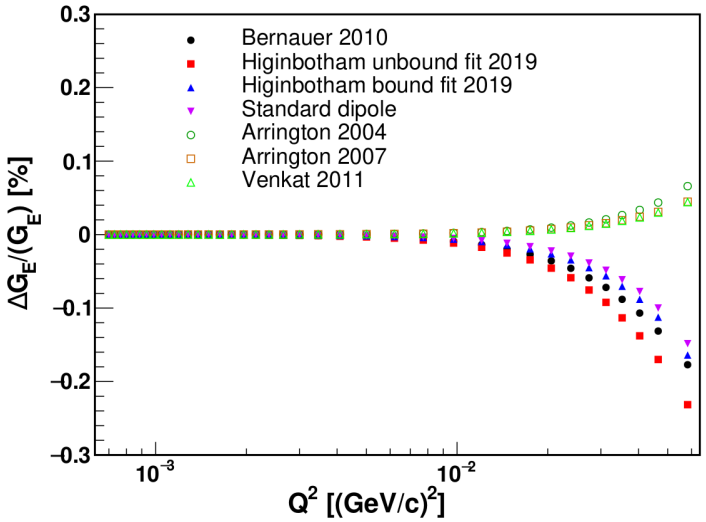

Figure 5-30: The relative G_E^p difference between using Kelly magnetic form factor (G_M^p) and other G_M^p models or parameterizations (This plot is from Weizhi Xiong).

Chapter 6

Results and Conclusion

As described in chapter 1, the proton charge radius is directly related to the slope of the electric form factor $G_E^p(Q^2)$ over Q^2 at $Q^2 = 0$.

$$R \equiv \left(-6 \frac{dG_E(Q^2)}{dQ^2} \Big|_{Q^2=0} \right)^{1/2}. \tag{6.1}$$

However, it is impractical to measure $G_E(Q^2)$ all the way to $Q^2 = 0$ due to detector acceptance. Thus to extract the proton charge radius from G_E^p, we need to extrapolate the measured G_E^p from experiments to $Q^2 = 0$.

There are two types of methods to do this extrapolation. The first type is using a multi-parameter polynomial expansion of Q^2 up to an order Q^{2N}. Mathematically speaking, since the $G_E^p(Q^2)$ must be differentiable, there always exist a Fourier transform polynomial expansion which can describe the electric form factor to any precision as long as we put high enough N in the expansion, and this method seems model independent. However, as shown in [136], this method cannot ensure a correct extraction of R when one has to extrapolate the data all the way to $Q^2 = 0$. The second type is using a functional form of G_E^p based on models of proton charge distribution. However, for this method, it is difficult to quantify how the extracted R depends on the model we chose. In order to correctly extract the charge radius, it is critical to use unbiased functional models or parameterizations of G_E^p, and find a robust fitting. This work has been studied and published in [137] for PRad Q^2 range

and uncertainty.

6.1 Robust Fitter

In order to search for the robust fitter for PRad Q^2 range, we tested fittings using different G_E models and parameterizations on a large number of pseudo-data. The pseudo-data were generated using different models and parameterizations from [138] [139] [140] [141] [135] [142] [143], with the radius R set to be an input parameter in these models and parameterizations. In this study, $G_E(Q^2)$ data was generated for each model/parameterization, and then the data was fit using different models/parameterizations. The robust fitter, when used in the fitting, should reproduce the radius that was used in the generator, regardless of which model was used in the generator. As summarized in [137], the functional models and parameterizations used to generate pseudo-data include:

(a) Dipole form:

$$G_E(Q^2) = \left(1 + \frac{Q^2}{p_1}\right)^{-2}, \tag{6.2}$$

where $p_1 = 12/R^2$. This functional form corresponds to an exponential charge distribution: $\rho(r) = \frac{\eta^3}{8\pi} e^{-\eta r}$ [144], where $\eta = \sqrt{12/\langle r_p^2 \rangle}$.

(b) Monopole form:

$$G_E(Q^2) = \left(1 + \frac{Q^2}{p_1}\right)^{-1}, \tag{6.3}$$

where $p_1 = 6/R^2$. This functional form corresponds to a Yukawa charge distribution: $\rho(r) = \left(\frac{\eta^2}{4\pi}\right) e^{-\eta r}/r$ [145], where $\eta = \sqrt{6/\langle r_p^2 \rangle}$.

(c) Gaussian form:

$$G_E(Q^2) = \exp\left(-Q^2/p_1\right), \tag{6.4}$$

where $p_1 = 6/R^2$, this functional form corresponds to a Gaussian charge distribution: $\rho(r) = \left(\frac{\eta}{\pi}\right)^{3/2} e^{-\eta r^2}$ [145], where $\eta = 3/2\langle r_p^2 \rangle$.

(d) Kelly-2004 parameterization [9]:

$$G_E(Q^2) = \frac{1 + a_1\tau}{1 + b_1\tau + b_2\tau^2 + b_3\tau^3}, \tag{6.5}$$

where $\tau = Q^2/4m_p^2$.

(e) Arrington-2004 parameterization [132]:

$$G_E(Q^2) = \left(1 + \sum_{i=1}^{N} p_{2i} Q^{2i}\right)^{-1}. \tag{6.6}$$

(f) Arrington-2007 parameterization [140]:

$$G_E(Q^2) = \frac{1}{1 + \frac{p_1 Q^2}{1 + \frac{p_2 Q^2}{1 + \cdots}}}. \tag{6.7}$$

A fifth-order continued-fraction (CF) expansion was used, see Eq. (6.15).

(g) Venkat-2011 parameterization [141]:

$$G_E(Q^2) = \frac{1 + a_1\tau + a_2\tau^2 + a_3\tau^3}{1 + b_1\tau + b_2\tau^2 + b_3\tau^3 + b_4\tau^4 + b_5\tau^5}. \tag{6.8}$$

(h) Bernauer-2014 parameterization [109]:

$$G_E(Q^2) = 1 + \sum_{i=1}^{10} p_i Q^{2i}. \tag{6.9}$$

(i) Parameterization from a fit to the world data by Ye[133]; and the model by Alarcon and Weiss [142].

The models and parameterizations that we tested for fitting the pseudo-data include:

1. Dipole form:

$$f_{dipole}(Q^2) = p_0 G_E(Q^2) = p_0 \left(1 + \frac{Q^2}{p_1}\right)^{-2}, \tag{6.10}$$

where $R = \sqrt{12/p_1}$.

2. Monopole form:

$$f_{monopole}(Q^2) = p_0 G_E(Q^2) = p_0 \left(1 + \frac{Q^2}{p_1}\right)^{-1}, \tag{6.11}$$

where $R = \sqrt{6/p_1}$

3. Gaussian form:

$$f_{Gaussian}(Q^2) = p_0 G_E(Q^2) = p_0 \exp\left(-Q^2/p_1\right), \tag{6.12}$$

where $R = \sqrt{6/p_1}$.

4. Multi-parameter polynomial-expansion over Q^2:

$$f_{polyQ}(Q^2) = p_0 G_E(Q^2) = p_0 \left(1 + \sum_{i=1}^{N} p_i Q^{2i}\right), \tag{6.13}$$

where $R = \sqrt{-6p_1}$.

5. Multi-parameter rational-function of Q^2

$$f_{rational}(Q^2) = p_0 G_E(Q^2) = p_0 \frac{1 + \sum_{i=1}^{N} p_i^{(a)} Q^{2i}}{1 + \sum_{j=1}^{M} p_j^{(b)} Q^{2j}}, \tag{6.14}$$

where $R = \sqrt{6(p_1^{(b)} - p_1^{(a)})}$.

6. Continued-Fraction (CF) expansion [133]:

$$f_{CF}(Q^2) = p_0 G_E(Q^2) = p_0 \frac{1 + a_1\tau + a_2\tau^2 + a_3\tau^3}{1 + b_1\tau + b_2\tau^2 + b_3\tau^3 + b_4\tau^4 + b_5\tau^5}, \tag{6.15}$$

where $R = \sqrt{6p_1}$.

7. Multi-parameter polynomial-expansion of z [146]:

$$f_{polyZ}(Q^2) = p_0 G_E(Q^2) = p_0 \left(1 + \sum_{i=1}^{N} p_i z^i\right), \tag{6.16}$$

where p_0 is normalization factor, z is a transformation over Q^2:

$$z = \frac{\sqrt{T_c + Q^2} - \sqrt{T_c - T_0}}{\sqrt{T_c + Q^2} + \sqrt{T_c - T_0}}, \tag{6.17}$$

where $T_c = 4m_\pi^2$, $m_\pi = 140$ MeV is the mass of π^0 meson, T_0 is a free parameter representing the point mapping onto $z = 0$ ($T_0 = 0$ in this study). In this express, $R = \sqrt{-3p_1/2T_c}$.

In order to account for the normalization factor, a free parameter p_0 was added to each model/parameterization during the fitting. For PRad case, since 1.1 GeV and 2.2 GeV beam have different normalization factors, two separate free parameters were used in fitting.

In the generated pseudo-data, a bin-by-bin and an overall fluctuation were added to the $G_E(Q^2)$ data. The bin-by-bin fluctuation was to mimic the noise of the data from experiment, the overall fluctuation was to account for the normalization factor. 150,000 times of fitting were performed for each pair of (generator model, fitting model), each time with regenerated bin-by-bin and overall fluctuations. A radius R was extracted from each fitting, and then the 150,000 R's were evaluated using a Gaussian distribution. To test the fitting quality of each model, a root mean square error (RMSE) quantity was defines as:

$$\text{RMSE} \equiv \sqrt{\text{bias}^2 + \sigma^2}, \tag{6.18}$$

where *bias* is the difference between R in the generator and the mean value from the 150,000 fittings; and σ is the RMS value. The best model/prameterization should give the smallest RMSE, the testing result for RMSE is shown in Fig. 11 of [137].

During the test, it was found that the following three parameterizations have the

most robustness:

I. Rational (1, 1):

$$G_E(Q^2) = p_0 \frac{1 + p_1 Q^2}{1 + p_2 Q^2}. \tag{6.19}$$

II. Second order z transformation:

$$G_E(z) = p_0(1 + p_1 z + p_2 z^2). \tag{6.20}$$

III. Second order continuous-fraction (CF):

$$G_E(Q^2) = p_0 \frac{1}{1 + \frac{p_1 Q^2}{1 + p_2 Q^2}}. \tag{6.21}$$

Among the above three parameterizations, the rational (1, 1) and the 2^{nd}-order CF parameterization are the same after a mathematical transformation. The RMSE testing result of rational (1, 1) is slightly better than the 2^{nd}-order z transformation parameterization. Thus, the rational (1, 1) parameterization was used in PRad analysis. The test results for different fitters are shown in Figs. 6-1, 6-2, 6-3 and 6-4.

6.2 Proton Radius Results

Based on the study of robust fitter in the previous section, the PRad data was fit using rational (1, 1) parameterization. The 1.1 GeV and 2.2 GeV data were fit simultaneously. Two independent normalization parameters n_1 and n_2 (they are p_0's in Eq. (6.14); one for 1.1 GeV, the other one for 2.2 GeV) were assigned to the $G_E(Q^2)$ model considering the different normalization factors for the two beam energies. The Q^2 dependence is the same for both beam energies. The results are:

$$R_p = 0.833 \pm 0.007_{stat.} \pm 0.012_{syst.}\ fm, \tag{6.22}$$

$$n_1 = 1.0002 \pm 0.0002_{stat.} \pm 0.0020_{syst.}, \tag{6.23}$$

$$n_2 = 0.9983 \pm 0.0002_{stat.} \pm 0.0013_{syst.}. \tag{6.24}$$

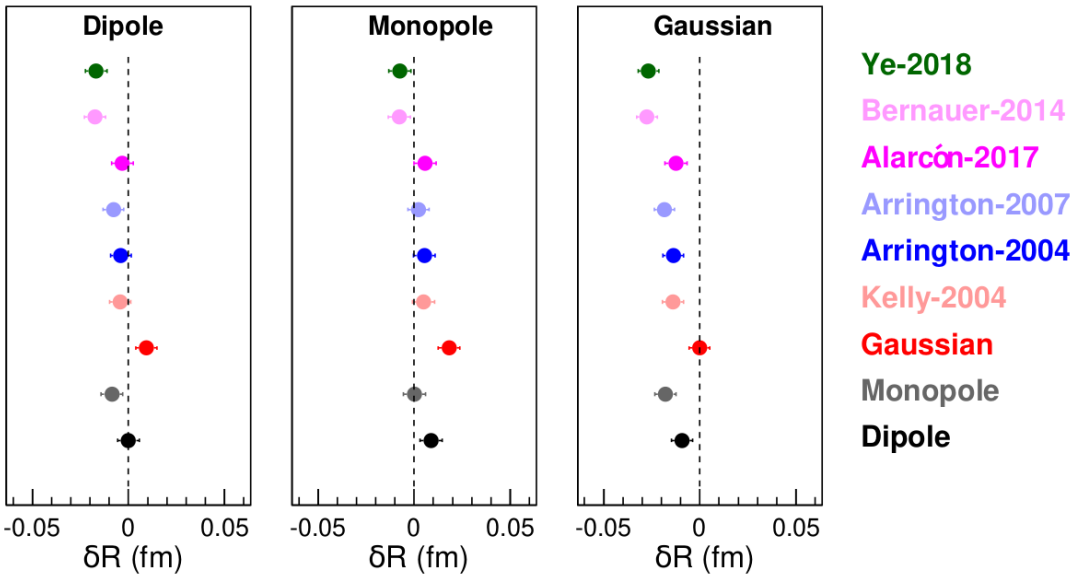

Figure 6-1: Test for using Dipole, Monopole, and Gaussian models in fitter. The RMS is shown as the error bar, the bias is the distance from the vertical dotted line which represents the input R in the generator. The models used for generating the pseudo-data are listed on the right. The binning, Q^2 range and uncertainties followed PRad experimental data.

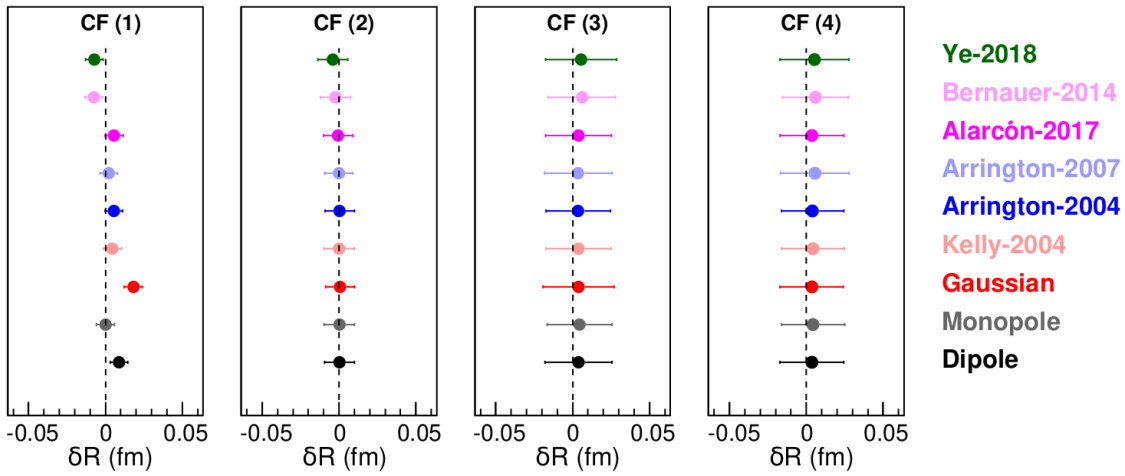

Figure 6-2: Test for using different order CF parameterizations in fitter. The RMS is shown as the error bar, the bias is the distance from the vertical dotted line which represents the input R in the generator. The models used for generating the pseudo-data are listed on the right. The 2^{nd}-order CF parameterization yields R values that are the closest to the dotted lie and with the smallest error bars.

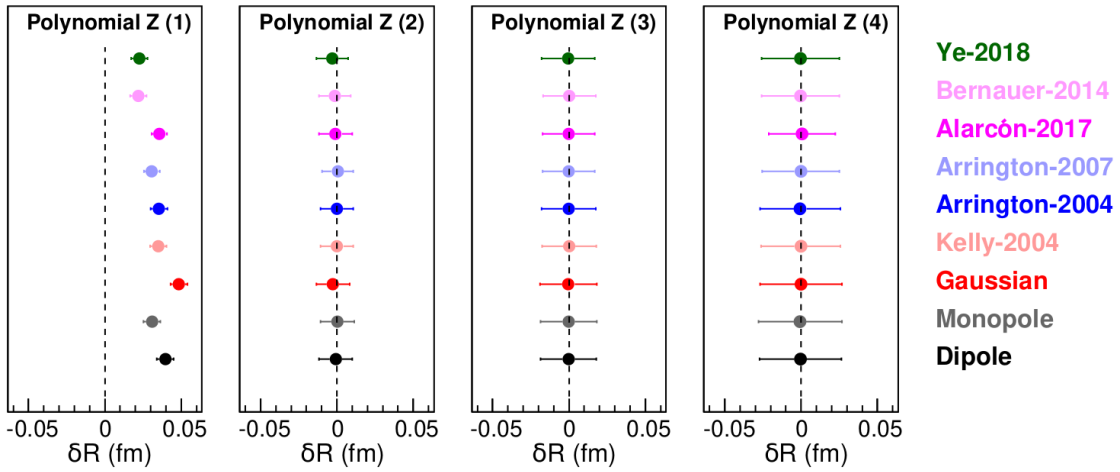

Figure 6-3: Test for using different order polynomial Z parameterizations in fitter. The RMS is shown as the error bar, the bias is the distance from the vertical dotted line which represents the input R in the generator. The models used for generating the pseudo-data are listed on the right. The 2^{nd}-order polynomial Z parameterization gives the best RMSE value.

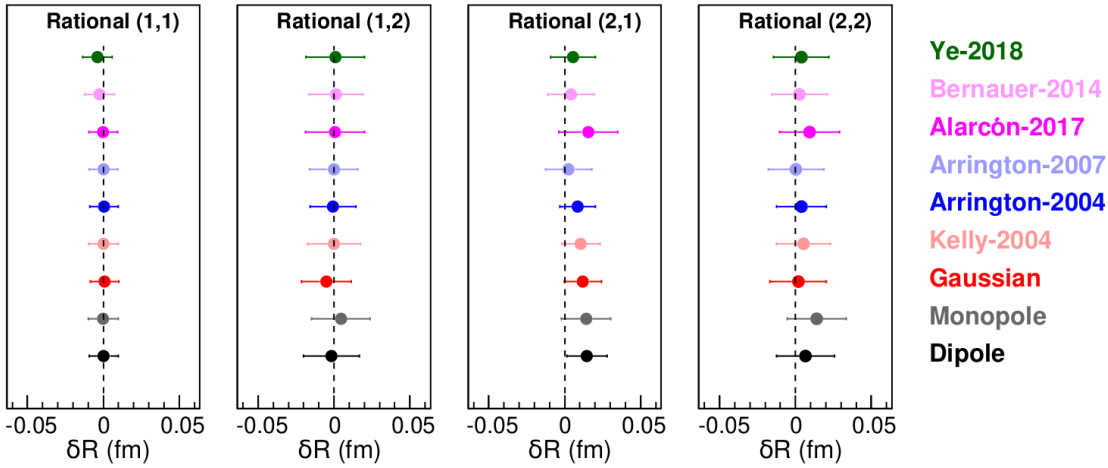

Figure 6-4: Test for using different order rational (N, M) parameterizations in fitter. The RMS is shown as the error bar, the bias is the distance from the vertical dotted line which represents the input R in the generator. The models used for generating the pseudo-data are listed on the right. The rational (1, 1) parameterization gives the best RMSE value.

The quality of the fit and the pull distribution [147] defined as:

$$g_i = \frac{G_E^p(Q_i^2)|_{\text{measure}} - G_E^p(Q_i^2)|_{\text{fit}}}{\sigma_i^{\text{stat}}} \tag{6.25}$$

which is expected to be standard Gaussian, has been checked in Fig. 6-6.

As shown in Fig. 6-6, using rational (1, 1) parameterization, the difference between the fitting and the PRad G_E data are within 2.5 standard deviations. The point-wise 95% confidence band (considering only statistical uncertainty) from PRad rational (1, 1) fitting is shown in Fig. 6-7. Other fitting parameterization has also been tested by the Duke Group, such as the second order z transformation [148]. From their study, the second order z transformation fitting is very similar to rational (1, 1) fitting. The results from second order z transformation fitting is $R_p = 0.830 \pm 0.008_{stat.} \pm 0.013_{syst.}$ (fm). The consistency of the extraction of R_p has also been tested by the Duke group by choosing only a subset of the data in the fitting. In their study, data from different Q^2 range, such as $Q^2 < 0.016$ $(\text{GeV}/c)^2$ or $Q^2 > 0.002$ $(\text{GeV}/c)^2$; data from only 1.1 GeV or 2.2 GeV; data from only PbWO4 modules etc, were all tested separately in the fitting, and all sub data sets produced consistent radius results.

6.3 Systematic Uncertainties on the Proton Radius

The full systematic uncertainty for R_p was studied by the Duke group using Geant4 simulation method. A few items such as the uncertainties from event selection, detector efficiency were cross checked by the UVa group. Table 6.1 lists all systematic sources and are explained below.

The event selection uncertainty was due to the criteria that we used in filtering elastic events for both *ep* and *ee*. The elastic *ep* events were mainly from applying cuts on HyCal reconstructed clusters. For each cluster from HyCal, we had a cluster size cut to remove the discharge channels and a 4σ energy cut to choose elastic events, where σ is the HyCal energy resolution. For *ee* elastic events, besides the same cuts that were applied on selecting *ep* events, the coplanarity cut, vertex Z cut, Møller

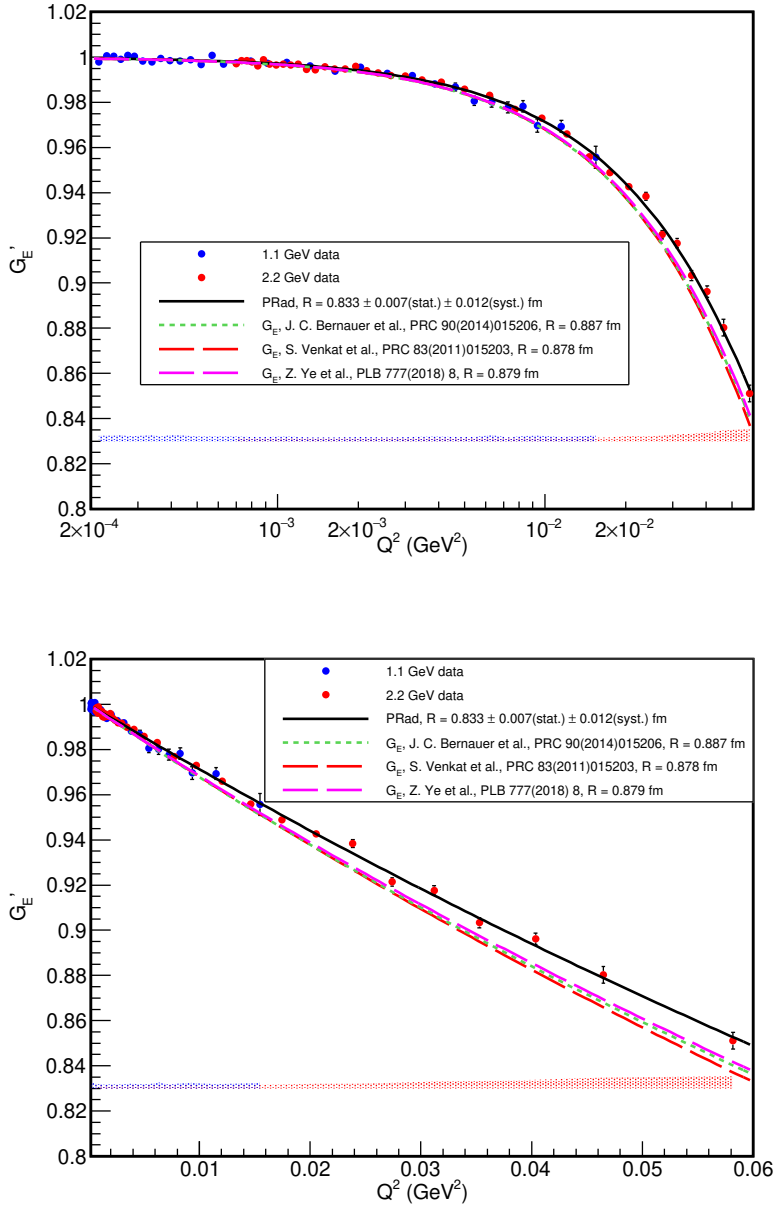

Figure 6-5: Extraction of R_p from PRad $G_E^p(Q^2)$ data. The top plot Q^2 axis is in log scale, the bottom plot Q^2 axis is in linear scale. The $G_E(Q^2)$ was normalized by the free normalization parameters n_1 and n_2. The statistical uncertainties are shown as the error bar, the systematic uncertainties are shown as the color band in the bottom. The blue points are 1.1 GeV data, the red points are 2.2 GeV data. The $G_E^p(Q^2)$ data from a few other models are also shown for comparison.

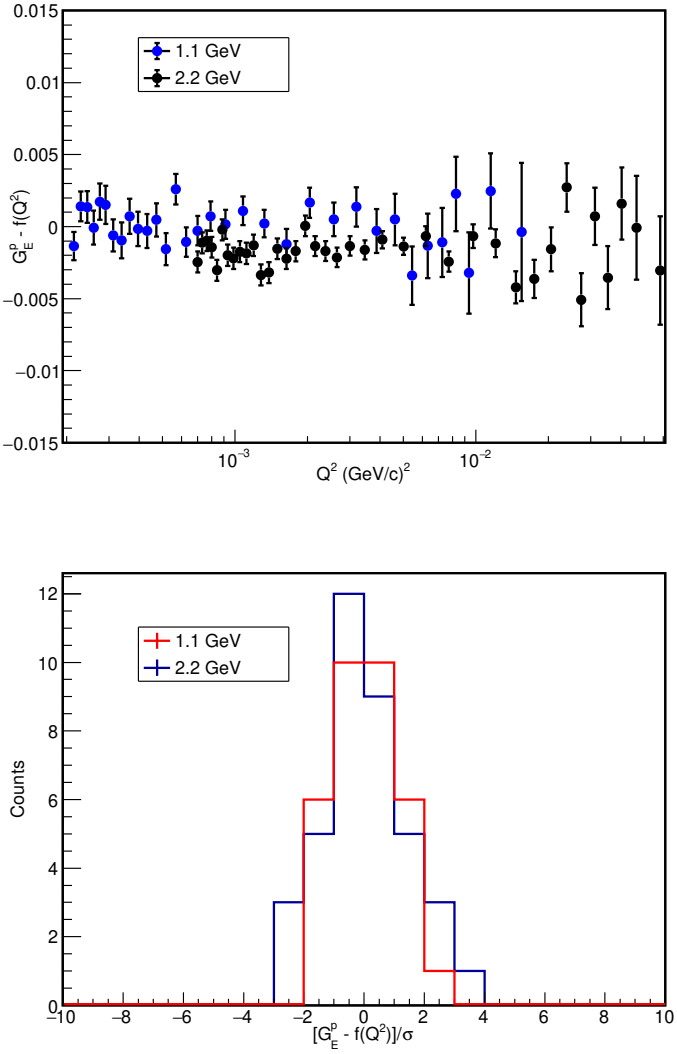

Figure 6-6: The top plot shows the difference between the PRad G_E and the fitting value; the bottom plot shows the difference (in the top plot) divided by the statistical uncertainty (the pull distribution).

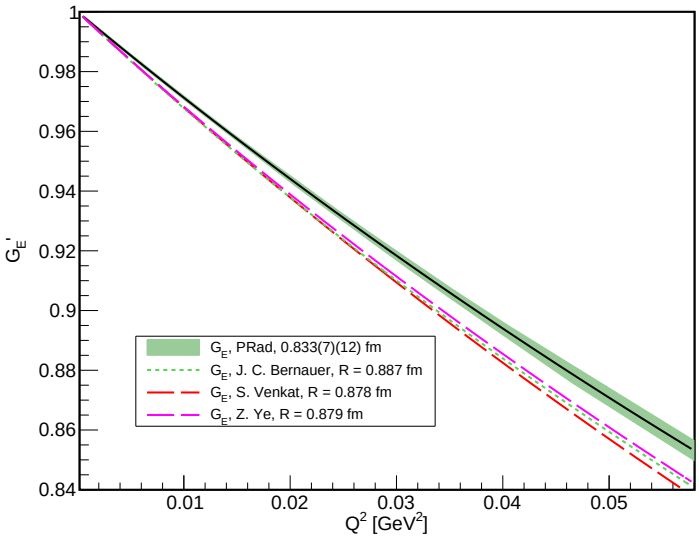

Figure 6-7: The point-wise 95% confidence band from PRad rational (1,1) fitting, along with a few extracted radius results from previous *ep* scattering measurements.

kinematics cut were also applied. The uncertainty from this source was estimated by varying the $e-p$ and $e-e$ cut criteria by around 20% (1.1 GeV) and 50% (2.2 GeV) of the standard cuts (see Table 5.3) for both data and simulation. Then a series of different cuts within this [-20%(-50%), 20%(50%)] of the original cut range were selected. For each set, a cross section and radius were calculated and extracted, the RMS value was taken as the systematic uncertainty. All uncertainties from different cuts were summed together quadratically, and the combined value is given in Table 6.1.

The uncertainty related to radiative correction came from high order contributions. The next-to-leading order contribution has been calculated accurately using non-ultra-relativistic approximation (electron mass was not neglected). However, for higher order contributions (next-to-next-to-leading order and above), such as multi photon emission and multi loop processes, the contribution was approximated using the method introduced by [149] for both *ep* and *ee*.

Detector efficiency includes HyCal trigger efficiency and GEM detection efficiency. Both were determined from the experiment. This systematic source arose from the statistical uncertainty from measurement for both efficiencies. The statistical un-

certainty follow Binomial distribution. For HyCal, the trigger efficiency has been measured within 0.03% for each module, and the total effect is negligible. The GEM efficiency did not cause any uncertainty since we used bin-by-bin method at forward angles. Only at large scattering angles GEM efficiency played a role where integrated method was used. At large angles, the statistical uncertainty for GEM efficiency was determined within 0.3%. It is worth pointing out that the HyCal cluster energy cut used in GEM efficiency calculation was $\pm 1\ \sigma_E$ (see section 4.4.5), where σ_E is HyCal energy resolution, which is much narrower than the cuts used in physics analysis (see Table 5.3). This provided a clean GEM efficiency table for physics analysis. In the integrated method, both *ep* and *ee* yield were corrected by GEM efficiency. The systematic uncertainty of R_p was estimated by smearing the GEM efficiency in each bin multiple times using a Gaussian model with $\mu = \epsilon$ and $\sigma = 0.3\%\epsilon$, where ϵ is the original efficiency. The R_p was extracted for each smearing. The RMS value was taken as the systematic uncertainty.

Beam background systematic uncertainty was mainly from background subtraction. Three major items were studied. The 1^{st} item was the background fluctuation over time, which was studied by using different combinations of empty target runs during background subtraction. This one was found to be negligible. The 2^{nd} item was the uncertainty from live charge measurement. For PRad case, the live charge uncertainty was around 0.1%. The 3^{rd} item was due to the target gas profile, studied by using different models of gas profile. The quadratic sum of the uncertainties from the three items was taken as the systematic uncertainty from beam background.

The HyCal response uncertainty was due to the fact that the calorimeter energy response for different energies was different — the non-linearity effect, which could arise from pedestal cut, light attenuation, back scattering particles etc. The linearity is better when incident particle has higher energy, and usually get worse with lower energy particles due to the pedestal cut. A non-linearity correction algorithm was developed by Weizhi Xiong, Maxime Levillain and Li Ye during the analysis, and the systematic uncertainties related to this method were also summarized in this table.

The acceptance uncertainty was related to the uncertainty of detector positions

and the dead area cut for both GEM and HyCal. The detector positions were from Jefferson Lab survey group, and cross checked using Møller events. The uncertainty from detector position was studied using simulation by slightly varying detector positions in Geant4 detector setup. The uncertainty from the dead area cut was studied by using different methods of cuts, and was found to be negligible.

For the uncertainty due to beam energy, which was related to the uncertainty in beam energy from Hall B: ± 0.5 MeV for 1.1 GeV beam and ± 1.5 MeV for 2.2 GeV beam. The systematic uncertainty from this item was studied by running a series of simulations using different beam energies. The R_p was extracted for each beam energy setting, and the RMS value was taken as the systematic uncertainty.

For the inelastic ep part, the Christy 2018 empirical fit model for ep inelastic scattering was used in the simulation to fit PRad data. The systematic uncertainty was studied by scaling the amplitude and stretching the width of the peak, each scale or stretch generated one set of simulation data. The scaling and stretching factors were within 10% and 0.5% of the original values, respectively. The uncertainty from magnetic form factors were studied during fitting, using different parameterizations and models as described in the last section. The contributions from each item is summarized in Table 6.1.

Item	R_p uncertainty (fm)	n_1 uncertainty	n_2 uncertainty
Event Selection	0.0070	0.0002	0.0006
Radiative Correction	0.0069	0.0010	0.0011
Detector Efficiency	0.0042	0.0000	0.0001
Beam Background	0.0039	0.0017	0.0003
HyCal Response	0.0029	0.0000	0.0000
Acceptance	0.0026	0.0001	0.0001
Beam Energy	0.0022	0.0001	0.0002
Inelastic ep	0.0009	0.0000	0.0000
G_M^p parameterization	0.0006	0.0000	0.0000
Total	0.0115	0.0020	0.0013

Table 6.1: Systematic uncertainties for R_p and the two floating normalization parameters n_1 and n_2.

6.4 Conclusion

The proton electric form factor at small Q^2 range is indispensable for reliably extracting the proton charge radius from ep elastic scattering without model dependence. For previous $e-p$ scattering experiments, the bulky magnets used in spectrometers restricted the ability of reaching very small Q^2 ranges, the low Q^2 ever reached was 0.004 $(\mathrm{GeV}/c)^2$ by Mainz collaboration [42], and 0.001 $(\mathrm{Gev}/c)^2$ by IRS experiment [150]. PRad experiment used a novel magnetic-spectrometer-free calorimetric method. A hybrid, high energy resolution calorimeter and a pair of high position resolution (56 μm) GEM detectors were utilized. Both detectors have holes designed in the middle which allowed a beam pipe to pass through. PRad experiment reached an unprecedentedly low Q^2 value, and covered two orders of Q^2 magnitude in one experimental setting: $Q^2 = (2.1 \times 10^{-4} - 0.06\ (\mathrm{GeV}/c)^2)$.

A windowless cryo-cooled hydrogen gas flow target with areal density $\approx 2 \times 10^{18}$ atoms/cm^2 was used, which removed the major background source from target cell walls. The $e-p$ events and Møller events were detected simultaneously within the same detector setting for both beam energies (1.1 GeV and 2.2 GeV), sharing the same integrated luminosity. The $e-p$ cross section was normalized by the well-known Møller cross section. This process eliminated the uncertainties from luminosity.

A rational (1, 1) G_E^p parameterization was found to be most robust in extracting the proton charge radius from PRad G_E^p data, the proton charge radius extracted by this analysis is

$$R_p = 0.833 \pm 0.007_{stat.} \pm 0.012_{syst.}\ (fm),$$

as shown in Fig. 6-8, in comparison with several other measurements from [1] [2] [40] [41] [151] [152] and the CODATA-2014 value combining both hydrogen spectroscopy measurement and $e-p$ scattering measurement. The result presented in this thesis shows a clear difference (around 3σ) from previous $e-p$ elastic scattering measurements. The difference could be accounted by the model independence in radius extraction due to the low Q^2 range and the superior uncertainty control techniques used in PRad experiment. The extracted proton charge radius agrees with the

result from muonic hydrogen spectroscopy measurement within experimental uncertainties, and this result supports no violation to lepton universality in the standard model.

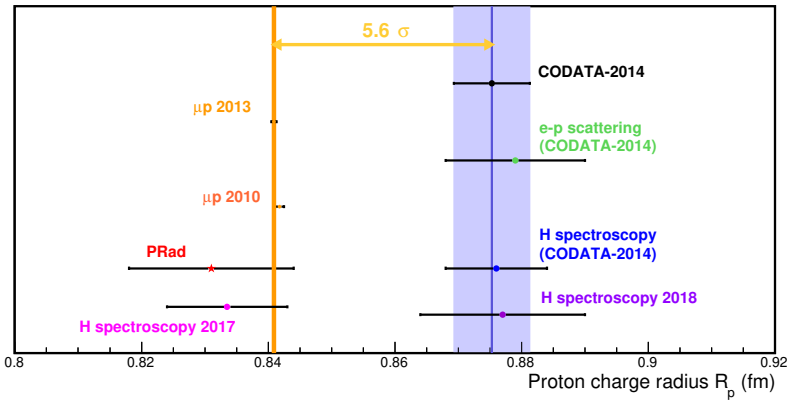

Figure 6-8: The R_p extracted from PRad data along with a few other measurements and the CODATA-2014 value. The PRad R_p agrees with the muonic hydrogen measurement.

The measured PRad G_E^p data in this analysis is shown in Fig. 6-9, where the top plot shows the lowest Q^2 range that was reached prior to PRad experiment. The data was from Mainz collaboration [6], collected by Douglas W. Higinbotham from Jefferson Lab. The bottom plot of Fig. 6-9 shows the G_E^p in the low Q^2 region: $Q^2 < 0.06$ $(\mathrm{GeV}/c)^2$, and overlapped with the G_E^p data collected by PRad shown in red dots. The PRad data has expanded the lowest Q^2 range down to 2.1×10^{-4} $(\mathrm{GeV}/c)^2$. PRad is the first experiment conducted after Jefferson Lab was upgraded to its 12 GeV era. The by-then world largest GEM detectors fulfilled our expectation, which is also a valuable reference for other experiments and large spectrometers such as SBS project at Jefferson Lab that will need large area GEM trackers. Further experiments on the proton charge radius are proposed or scheduled. For example, the follow-up PRad-II experiment which will improve the PRad experiment setup by introducing a second layer of GEM detectors. Two layers of GEM detectors not only improve the uncertainties related to GEM efficiencies, but also can make the Z vertex reconstruction from $e - p$ events possible, which can reject the backgrounds related to the beam line such as the upstream collimators. The muon proton scattering experiment

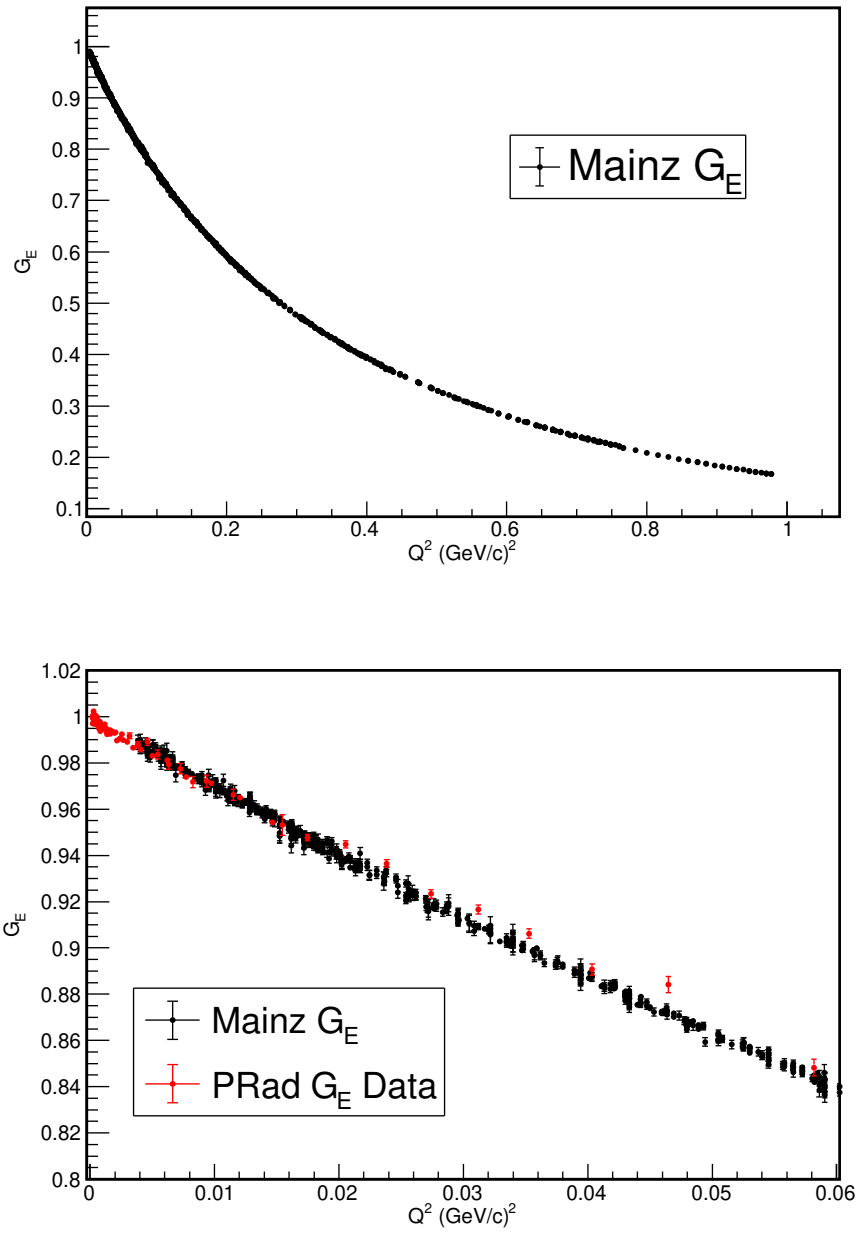

Figure 6-9: Top plot: the combined G_E^p data from Mainz, the top plot shows the Q^2 coverage before PRad experiment. Bottom plot is a zoomed in figure showing the low Q^2 range of Mainz data, the red dots are the G_E^p data measured by PRad experiment. The bottom plot shows the data expansion in low Q^2 range from PRad.

(MUSE) [153] scheduled at the Paul Scherrer Institute (PSI) in Switzerland will directly measure the proton form factors from $\mu - p$ scattering process, and compare them with the form factors measured from $e - p$ scattering. The MUSE experiment will provide a direct test on the lepton universality between electrons and muons.

Appendix A

Appendix A

A.1 Lorentz Invariant Flux

In non-relativistic case, suppose we have two different type of particles a and b moving towards each other at velocity v_a and v_b respectively, then the flux of particle a relative to particle b is

$$n_a n_b (v_a + v_b),$$

where, n_a is particle density of a. when writing out the wave functions of particles, n_a will be normalized together with the volume it occupies, so $n_a = 1$, then the non-relativistic flux is

$$v_a + v_b.$$

In relativistic case, considering the length contraction effect, if we normalized particle density to be 1 (together with the volume it occupies), then the flux is not Lorentz invariant anymore, it can be proved that it will be Lorentz invariant if one normalize to $2E$, so the Lorentz invariant flux is:

$$2E_a 2E_b (v_a + v_b),$$

it is not convenient to carry $\boldsymbol{v}'s$ around in calculation, so we need to express it in $\boldsymbol{p}'s$ and $E's$, suppose $(E, 0)$ is the rest frame F, and $(E, \boldsymbol{p})$ is the moving frame F' at

velocity β, using natural units $\hbar = 1, c = 1$, in the rest frame we have:

$$(E, 0) = (m, 0),$$

using lorentz transform matrix,

$$\begin{pmatrix} E \\ p \end{pmatrix} = \begin{pmatrix} \gamma & -\gamma\beta \\ -\gamma\beta & \gamma \end{pmatrix} \begin{pmatrix} m \\ 0 \end{pmatrix},$$

so we get $E = \gamma m$ and $\boldsymbol{p} = -\gamma\beta m$, the '$-$' sign here is due to frame F' is moving at β relative to F, then the observer in F' will see the object moving at a velocity $-\beta$, so the momentum should have a minus sign for observers in F'.

Anyway, in F' frame,

$$\beta = |\boldsymbol{p}|/E,$$

namely

$$v = |\boldsymbol{p}|/E,$$

using vector form, since two particles are moving towards each other, the Lorentz invariant flux would be :

$$\boldsymbol{F} = 4E_a E_b(\frac{\boldsymbol{p_a}}{E_a} - \frac{\boldsymbol{p_b}}{E_b}),$$

in the same direction with $\boldsymbol{p_a}$, using relativistic mass momentum relationship: $E^2 = \boldsymbol{p}^2 + m^2$ and the 4-momentum $p = (E, \boldsymbol{p})$,

$$p_a \cdot p_b = (E_a E_b - \boldsymbol{p_a p_b}),$$

$$(p_a \cdot p_b)^2 = E_a^2 E_b^2 - 2E_a E_b \boldsymbol{p_a p_b} + (E_a^2 - m_a^2)(E_b^2 - m_b^2),$$

$$(p_a \cdot p_b)^2 - m_a^2 m_b^2 = 2E_a^2 E_b^2 - 2E_a E_b \boldsymbol{p_a p_b} - E_a^2 m_b^2 - E_b^2 m_a^2,$$

$$(p_a \cdot p_b)^2 - m_a^2 m_b^2 = E_a^2 \boldsymbol{p_b}^2 - 2E_a E_b \boldsymbol{p_a p_b} + E_b^2 \boldsymbol{p_a}^2,$$

so we have:

$$F = 4\sqrt{(p_a \cdot p_b)^2 - m_a^2 m_b^2}.$$

A.2 Gordon Identity

Using Dirac equation:

$$(\gamma^\mu p_{2,\mu} - M_p)u(p_2) = 0, \tag{A.1}$$

$$\bar{u}(p_4)(\gamma^\mu p_{4,\mu} - M_p) = 0, \tag{A.2}$$

$$\Rightarrow \bar{u}(p_4)\gamma^\mu\big(M_p u(p_2)\big) = \bar{u}(p_4)\gamma^\mu\gamma^\nu p_{2,\nu}u(p_2), \tag{A.3}$$

$$\big(M_p\bar{u}(p_4)\big)\gamma^\mu u(p_2) = \bar{u}(p_4)\gamma^\nu p_{4,\nu}\gamma^\mu u(p_2), \tag{A.4}$$

Sum the above two equations:

$$2M_p\bar{u}(p_4)\gamma^\mu u(p_2) = \bar{u}(p_4)(\gamma^\mu\gamma^\nu p_{2,\nu} + \gamma^\nu\gamma^\mu p_{4,\nu})u(p_2), \tag{A.5}$$

$$\begin{aligned}
&\Rightarrow 2M_p\bar{u}(p_4)\gamma^\mu u(p_2) = \\
&\bar{u}(p_4)\Big[\gamma^\mu\gamma^\nu\big(\frac{p_{2,\nu}+p_{4,\nu}}{2} + \frac{p_{2,\nu}-p_{4,\nu}}{2}\big) + \gamma^\nu\gamma^\mu\big(\frac{p_{2,\nu}+p_{4,\nu}}{2} - \frac{p_{2,\nu}-p_{4,\nu}}{2}\big)\Big]u(p_2) \\
&= \bar{u}(p_4)\Big[(\gamma^\mu\gamma^\nu + \gamma^\nu\gamma^\mu)\big(\frac{p_{2,\nu}+p_{4,\nu}}{2}\big) + (\gamma^\mu\gamma^\nu - \gamma^\nu\gamma^\mu)\big(\frac{p_{2,\nu}-p_{4,\nu}}{2}\big)\Big]u(p_2),
\end{aligned} \tag{A.6}$$

using

$$\sigma^{\mu\nu} = \frac{i}{2}(\gamma^\mu\gamma^\nu - \gamma^\nu\gamma^\mu), \tag{A.7}$$

$$g^{\mu\nu} = \frac{1}{2}(\gamma^\mu\gamma^\nu + \gamma^\nu\gamma^\mu), \tag{A.8}$$

substitute back into Eq. (A.6),

$$2M_p\bar{u}(p_4)\gamma^\mu u(p_2) = \bar{u}(p_4)\Big[g^{\mu\nu}(p_{2,\nu} + p_{4,\nu}) + i\sigma^{\mu\nu}q_\nu\Big]u(p_2), \tag{A.9}$$

$$\Rightarrow \bar{u}(p_4)\gamma^\mu u(p_2) = \bar{u}(p_4)\Big[\frac{p_4^\mu + p_2^\mu}{2M_p} + \frac{i\sigma^{\mu\nu}q_\nu}{2M_p}\Big]u(p_2). \tag{A.10}$$

A.3 Z Vertex Reconstruction from Møller Events

For Møller scattering $e_1 + e_2 \to e_1' + e_2'$, as shown in Fig. A-1:

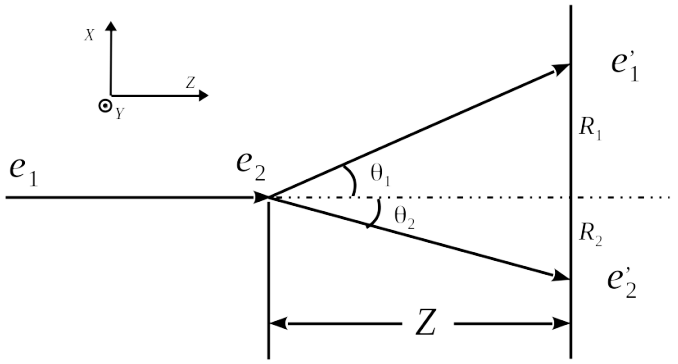

Figure A-1: Møller scattering in Lab frame.

Where:

$$
\begin{aligned}
p_1 &= (E, 0, 0, \mathrm{p}), \\
p_2 &= (m_e, 0, 0, 0), \\
p_3 &= (E_3, \mathrm{p}_3 \sin\theta_1, 0, \mathrm{p}_3 \cos\theta_1), \\
p_4 &= (E_4, -\mathrm{p}_4 \sin\theta_2, 0, \mathrm{p}_4 \cos\theta_2).
\end{aligned}
$$

From momentum and energy conservation:

$$
p_1 + p_2 = p_3 + p_4 \quad \Rightarrow \quad E + m_e = E_3 + E_4. \tag{A.11}
$$

Mandelstam variable u and t:

$$
\begin{aligned}
p_1 - p_3 = p_4 - p_2 \quad &\Rightarrow \quad p_1 \cdot p_3 = p_2 \cdot p_4 \quad \Rightarrow \quad EE_3 - \mathrm{pp}_3 \cos\theta_1 = m_e E_4, \\
p_1 - p_4 = p_3 - p_2 \quad &\Rightarrow \quad p_1 \cdot p_4 = p_3 \cdot p_2 \quad \Rightarrow \quad EE_4 - \mathrm{pp}_4 \cos\theta_1 = m_e E_3.
\end{aligned} \tag{A.12}
$$

Combine Eq. (A.11) and Eq. (A.12):

$$
EE_3 - \sqrt{E^2 - m_e^2}\sqrt{E_3^2 - m_e^2}\cos\theta_1 = m_e(E + m_e - E_3). \tag{A.13}
$$

Solve Eq. (A.13):

$$\sqrt{\frac{E+m_e}{E-m_e}}\sqrt{\frac{E_3-m_e}{E_3+m_e}}=\cos\theta_1, \tag{A.14}$$

and also:

$$E_3=\frac{2m_e}{1-\cos^2\theta_1\frac{E-m_e}{E+m_e}}-m_e. \tag{A.15}$$

where

$$\cos^2\theta_1=\frac{1}{1+\tan^2\theta_1}=\frac{Z^2}{Z^2+R_1^2}. \tag{A.16}$$

Similarly for E_4:

$$E_4=\frac{2m_e}{1-\cos^2\theta_2\frac{E-m_e}{E+m_e}}-m_e. \tag{A.17}$$

$$\cos^2\theta_2=\frac{1}{1+\tan^2\theta_2}=\frac{Z^2}{Z^2+R_2^2}. \tag{A.18}$$

use $E_3+E_4=E+m_e$ and Eqs. (A.15), (A.16), (A.17), (A.18), one get:

$$\frac{2EZ^2+R_1^2(E+m_e)}{2m_eZ^2+R_1^2(E+m_e)}+\frac{2EZ^2+R_2^2(E+m_e)}{2m_eZ^2+R_2^2(E+m_e)}=\frac{E+m_e}{m_e}, \tag{A.19}$$

Z can be solved:

$$Z^2=(E+m_e)R_1R_2/(2m_e).$$

A.4 Cross Section Tables

θ [deg]	Cross Section [mb]	Stat. Uncertainty [mb]	Syst. Uncertainty [mb]
0.7625	2166.7602	3.2659	11.1477
0.7875	1917.1353	3.0616	9.79131
0.8125	1688.1852	2.7015	8.38374
0.8375	1495.2014	2.5424	7.89877
0.8625	1337.7802	2.3929	6.01773
0.8875	1186.5639	2.2528	5.51297
0.92	1028.3933	1.6427	4.92329
0.9575	871.4129	1.5748	4.57167
0.9945	751.5522	1.3529	3.24345
1.0355	640.2742	1.1508	3.43346
1.081	540.3481	0.9687	2.97916
1.131	448.3463	0.8082	2.01126
1.184	372.5844	0.7101	1.52818
1.2405	311.2074	0.5891	1.29366
1.304	253.4070	0.4823	1.02258
1.3775	203.2666	0.3871	0.823192
1.4655	159.2030	0.3020	0.614382
1.574	119.1656	0.2267	0.436159
1.7105	85.5051	0.1538	0.343416
1.8935	56.8132	0.0966	0.192834
2.1065	37.0620	0.0703	0.131133
2.3525	23.7883	0.0451	0.0944054
2.642	14.9433	0.0327	0.0521155
2.942	9.7119	0.0250	0.0372057
3.242	6.5436	0.0182	0.0271079
3.542	4.6077	0.0150	0.018261
3.842	3.2957	0.0124	0.0126205
4.142	2.4212	0.0101	0.0127462
4.442	1.8259	0.0083	0.00650495
4.742	1.3914	0.0069	0.00638368
5.046	1.0875	0.0059	0.00540121
5.6	0.7103	0.0035	0.00273203
6.5	0.3828	0.0035	0.00196581

Table A.1: 1.101 GeV Beam *ep* Cross Section Table.

θ [deg]	Cross Section [mb]	Stat. Uncertainty [mb]	Syst. Uncertainty [mb]
0.7075	769.094	1.0769	2.17985
0.723	708.029	0.9873	2.03674
0.7395	646.377	0.9019	1.78115
0.757	589.199	0.8211	1.53891
0.7755	531.618	0.7453	1.44192
0.7955	482.98	0.673	1.31902
0.817	432.942	0.6047	1.21355
0.84	387.077	0.5409	1.10749
0.8655	343.861	0.4798	0.920646
0.8935	302.743	0.4222	0.811516
0.924	265.489	0.369	0.724408
0.9575	228.941	0.3198	0.629023
0.9945	196.209	0.2746	0.567121
1.0355	167.348	0.2335	0.444601
1.081	140.695	0.1964	0.379336
1.131	117.644	0.1637	0.354157
1.184	97.8801	0.1362	0.283988
1.2405	80.7279	0.1129	0.225065
1.304	66.223	0.0923	0.190508
1.3775	53.1553	0.074	0.157543
1.4655	41.4475	0.0576	0.111579
1.574	31.0065	0.0432	0.0921595
1.7105	22.2218	0.0286	0.0653302
1.8935	14.7381	0.0175	0.043133
2.1065	9.6033	0.0132	0.0295626
2.3525	6.0997	0.009	0.0197922
2.642	3.8244	0.0063	0.0121505
2.942	2.4646	0.005	0.00724614
3.242	1.6418	0.0037	0.00498021
3.542	1.1417	0.0031	0.00383885
3.842	0.8232	0.0025	0.00380399
4.142	0.6017	0.002	0.00256187
4.442	0.4448	0.0016	0.00232811
4.742	0.3394	0.0014	0.00201398
5.046	0.2603	0.0011	0.00172097
5.4	0.1932	0.0009	0.00150317
5.8	0.1441	0.001	0.00143545
6.5	0.0857	0.0006	0.000985776

Table A.2: 2.143 GeV Beam ep Cross Section Table.

Bibliography

[1] R. Pohl et al. The size of proton. *Nature*, 466:213–216, 2010.

[2] Aldo Antognini, François Nez, Karsten Schuhmann, Fernando D. Amaro, François Biraben, João M. R. Cardoso, Daniel S. Covita, Andreas Dax, Satish Dhawan, Marc Diepold, Luis M. P. Fernandes, Adolf Giesen, Andrea L. Gouvea, Thomas Graf, Theodor W. Hänsch, Paul Indelicato, Lucile Julien, Cheng-Yang Kao, Paul Knowles, Franz Kottmann, Eric-Olivier Le Bigot, Yi-Wei Liu, José A. M. Lopes, Livia Ludhova, Cristina M. B. Monteiro, Françoise Mulhauser, Tobias Nebel, Paul Rabinowitz, Joaquim M. F. dos Santos, Lukas A. Schaller, Catherine Schwob, David Taqqu, João F. C. A. Veloso, Jan Vogelsang, and Randolf Pohl. Proton structure from the measurement of 2s-2p transition frequencies of muonic hydrogen. *Science*, 339(6118):417–420, 2013.

[3] Peter J. Mohr, Barry N. Taylor, and David B. Newell. Codata recommended values of the fundamental physical constants: 2010. *Reviews of Modern Physics*, 84(4):1527–1605, Nov 2012.

[4] Peter J. Mohr, David B. Newell, and Barry N. Taylor. Codata recommended values of the fundamental physical constants: 2014. *Reviews of Modern Physics*, 88(3), Sep 2016.

[5] Hofstadter R. et al. The structure of the proton. *Rhys. Rev.*, 92.978, 1953.

[6] Keith Griffioen, Carl Carlson, and Sarah Maddox. Consistency of electron scattering data with a small proton radius. *Physical Review C*, 93(6), Jun 2016.

[7] Herbert Goldstein et al. *Classical Mechanics*. Addison Wesley, 2000.

[8] I. Akushevich et al. Radiative corrections beyond the ultra relativistic limit in unpolarized ep elastic and møller scatterings for the prad experiment at jefferson laboratory. *Eur. Phys. J.*, 51:1, 2015.

[9] J. J. Kelly. Simple parametrization of nucleon form factors. *Phys. Rev. C*, 70:068202, Dec 2004.

[10] V. Punjabi C. F. Perdrisat and M. Vanderhaeghen. Nucleon electromagnetic form factors. *Prog. Part. Nucl. Phys.*, 59.694, 2008.

[11] A. Gasparian et al. High precision measurement of the proton charge radius. *PRad Proposal*, 2011.

[12] O. Gayou, K. A. Aniol, T. Averett, F. Benmokhtar, W. Bertozzi, L. Bimbot, E. J. Brash, J. R. Calarco, C. Cavata, Z. Chai, C.-C. Chang, T. Chang, J.-P. Chen, E. Chudakov, R. De Leo, S. Dieterich, R. Endres, M. B. Epstein, S. Escoffier, K. G. Fissum, H. Fonvieille, S. Frullani, J. Gao, F. Garibaldi, S. Gilad, R. Gilman, A. Glamazdin, C. Glashausser, J. Gomez, V. Gorbenko, J.-O. Hansen, D. W. Higinbotham, G. M. Huber, M. Iodice, C. W. de Jager, X. Jiang, M. K. Jones, J. J. Kelly, M. Khandaker, A. Kozlov, K. M. Kramer, G. Kumbartzki, J. J. LeRose, D. Lhuillier, R. A. Lindgren, N. Liyanage, G. J. Lolos, D. J. Margaziotis, F. Marie, P. Markowitz, K. McCormick, R. Michaels, B. D. Milbrath, S. K. Nanda, D. Neyret, Z. Papandreou, L. Pentchev, C. F. Perdrisat, N. M. Piskunov, V. Punjabi, T. Pussieux, G. Quéméner, R. D. Ransome, B. A. Raue, R. Roché, M. Rvachev, A. Saha, C. Salgado, S. Širca, I. Sitnik, S. Strauch, L. Todor, E. Tomasi-Gustafsson, G. M. Urciuoli, H. Voskanyan, K. Wijesooriya, B. B. Wojtsekhowski, X. Zheng, and L. Zhu. Measurement of G_{E_p}/G_{M_p} in $\overrightarrow{e}\ p \to e\ \overrightarrow{p}$ to $q^2 = 5.6\text{gev}^2$. *Phys. Rev. Lett.*, 88:092301, Feb 2002.

[13] V. Punjabi, C. F. Perdrisat, K. A. Aniol, F. T. Baker, J. Berthot, P. Y. Bertin, W. Bertozzi, A. Besson, L. Bimbot, W. U. Boeglin, E. J. Brash, D. Brown, J. R. Calarco, L. S. Cardman, Z. Chai, C.-C. Chang, J.-P. Chen, E. Chudakov, S. Churchwell, E. Cisbani, D. S. Dale, R. De Leo, A. Deur, B. Diederich, J. J. Domingo, M. B. Epstein, L. A. Ewell, K. G. Fissum, A. Fleck, H. Fonvieille, S. Frullani, J. Gao, F. Garibaldi, A. Gasparian, G. Gerstner, S. Gilad, R. Gilman, A. Glamazdin, C. Glashausser, J. Gomez, V. Gorbenko, A. Green, J.-O. Hansen, C. R. Howell, G. M. Huber, M. Iodice, C. W. de Jager, S. Jaminion, X. Jiang, M. K. Jones, W. Kahl, J. J. Kelly, M. Khayat, L. H. Kramer, G. Kumbartzki, M. Kuss, E. Lakuriki, G. Laveissière, J. J. LeRose, M. Liang, R. A. Lindgren, N. Liyanage, G. J. Lolos, R. Macri, R. Madey, S. Malov, D. J. Margaziotis, P. Markowitz, K. McCormick, J. I. McIntyre, R. L. J. van der Meer, R. Michaels, B. D. Milbrath, J. Y. Mougey, S. K. Nanda, E. A. J. M. Offermann, Z. Papandreou, L. Pentchev, G. G. Petratos, N. M. Piskunov, R. I. Pomatsalyuk, D. L. Prout, G. Quéméner, R. D. Ransome, B. A. Raue, Y. Roblin, R. Roche, G. Rutledge, P. M. Rutt, A. Saha, T. Saito, A. J. Sarty, T. P. Smith, P. Sorokin, S. Strauch, R. Suleiman, K. Takahashi, J. A. Templon, L. Todor, P. E. Ulmer, G. M. Urciuoli, P. Vernin, B. Vlahovic, H. Voskanyan, K. Wijesooriya, B. B. Wojtsekhowski, R. J. Woo, F. Xiong, G. D. Zainea, and Z.-L. Zhou. Proton elastic form factor ratios to $Q^2 = 3.5$ GeV^2 by polarization transfer. *Phys. Rev. C*, 71:055202, May 2005.

[14] B. D. Milbrath, J. I. McIntyre, C. S. Armstrong, D. H. Barkhuff, W. Bertozzi, J. P. Chen, D. Dale, G. Dodson, K. A. Dow, M. B. Epstein, M. Farkhondeh, J. M. Finn, S. Gilad, M. K. Jones, K. Joo, J. J. Kelly, S. Kowalski, R. W. Lourie, R. Madey, D. J. Margaziotis, P. Markowitz, C. Mertz, J. Mitchell, C. F. Perdrisat, V. Punjabi, L. Qin, P. M. Rutt, A. J. Sarty, D. Tieger, C. Tschalær,

W. Turchinetz, P. E. Ulmer, S. P. Van Verst, G. A. Warren, L. B. Weinstein, and R. J. Woo. Comparison of polarization observables in electron scattering from the proton and deuteron. *Phys. Rev. Lett.*, 80:452–455, Jan 1998.

[15] O. Gayou, K. Wijesooriya, A. Afanasev, M. Amarian, K. Aniol, S. Becher, K. Benslama, L. Bimbot, P. Bosted, E. Brash, J. Calarco, Z. Chai, C. C. Chang, T. Chang, J. P. Chen, S. Choi, E. Chudakov, S. Churchwell, D. Crovelli, S. Dieterich, S. Dumalski, D. Dutta, M. Epstein, K. Fissum, B. Fox, S. Frullani, H. Gao, J. Gao, F. Garibaldi, R. Gilman, S. Glamazdin, C. Glashausser, J. Gomez, V. Gorbenko, O. Hansen, R. J. Holt, J. Hovdebo, G. M. Huber, C. W. de Jager, X. Jiang, C. Jones, M. K. Jones, J. Kelly, E. Kinney, E. Kooijman, G. Kumbartzki, M. Kuss, J. LeRose, M. Liang, R. Lindgren, N. Liyanage, S. Malov, D. J. Margaziotis, P. Markowitz, K. McCormick, D. Meekins, Z.-E. Meziani, R. Michaels, J. Mitchell, L. Morand, C. F. Perdrisat, R. Pomatsalyuk, V. Punjabi, R. D. Ransome, R. Roche, M. Rvachev, A. Saha, A. Sarty, E. C. Schulte, D. Simon, S. Strauch, R. Suleiman, L. Todor, P. E. Ulmer, G. M. Urciuoli, B. Wojtsekhowski, F. Xiong, and W. Xu. Measurements of the elastic electromagnetic form factor ratio $\mu_p G_{\rm ep}/G_{\rm mp}$ via polarization transfer. *Phys. Rev. C*, 64:038202, Aug 2001.

[16] Th. Pospischil et al. Measurement of G_E^p/G_M^p via polarization transfer at $Q^2 = 0.4\ GeV/c^2$. *The European Physical Journal A - Hadrons and Nuclei*, 12:125–127, 2001.

[17] S. Dieterich, P. Bartsch, D. Baumann, J. Bermuth, K. Bohinc, R. Bohm, D. Bosnar, S. Derber, M. Ding, M. Distler, I. Ewald, J. Friedrich, J.M. Friedrich, R. Gilman, C. Glashausser, M. Hauger, P. Jennewein, J. Jourdan, J.J. Kelly, M. Kohl, A. Kozlov, K.W. Krygier, G. Kumbartzki, J. Lac, A. Liesenfeld, H. Merkel, U. Muller, R. Neuhausen, Th. Pospischil, R.D. Ransome, D. Rohe, G. Rosner, H. Schmieden, M. Seimetz, I. Sick, S. Strauch, J.M. Udias, J.R. Vignote, A. Wagner, Th. Walcher, G. Warren, and M. Weis. Polarization transfer in the $^4he(e \rightarrow, e'p \rightarrow)^3h$ reaction. *Physics Letters B*, 500:47–52, 2001.

[18] S. Strauch, S. Dieterich, K. A. Aniol, J. R. M. Annand, O. K. Baker, W. Bertozzi, M. Boswell, E. J. Brash, Z. Chai, J.-P. Chen, M. E. Christy, E. Chudakov, A. Cochran, R. De Leo, R. Ent, M. B. Epstein, J. M. Finn, K. G. Fissum, T. A. Forest, S. Frullani, F. Garibaldi, A. Gasparian, O. Gayou, S. Gilad, R. Gilman, C. Glashausser, J. Gomez, V. Gorbenko, P. L. J. Gueye, J. O. Hansen, D. W. Higinbotham, B. Hu, C. E. Hyde-Wright, D. G. Ireland, C. Jackson, C. W. de Jager, X. Jiang, C. Jones, M. K. Jones, J. D. Kellie, J. J. Kelly, C. E. Keppel, G. Kumbartzki, M. Kuss, J. J. LeRose, K. Livingston, N. Liyanage, S. Malov, D. J. Margaziotis, D. Meekins, R. Michaels, J. H. Mitchell, S. K. Nanda, J. Nappa, C. F. Perdrisat, V. A. Punjabi, R. D. Ransome, R. Roché, G. Rosner, M. Rvachev, F. Sabatie, A. Saha, A. Sarty, J. M. Udias, P. E. Ulmer, G. M. Urciuoli, J. F. J. van den Brand, J. R. Vignote, D. P. Watts, L. B. Weinstein, K. Wijesooriya, and B. Wojtsekhowski. Polarization transfer in the

^{4}He$(\vec{e}, e' \vec{p})^3$H reaction up to $Q^2 = 2.6$ (GeV/c)^2. *Phys. Rev. Lett.*, 91:052301, Jul 2003.

[19] B. Hu, M. K. Jones, P. E. Ulmer, H. Arenhövel, O. K. Baker, W. Bertozzi, E. J. Brash, J. Calarco, J.-P. Chen, E. Chudakov, A. Cochran, S. Dumalski, R. Ent, J. M. Finn, F. Garibaldi, S. Gilad, R. Gilman, C. Glashausser, J. Gomez, V. Gorbenko, J.-O. Hansen, J. Hovebo, C. W. de Jager, S. Jeschonnek, X. Jiang, C. Keppel, A. Klein, A. Kozlov, S. Kuhn, G. Kumbartzki, M. Kuss, J. J. LeRose, M. Liang, N. Liyanage, G. J. Lolos, P. E. C. Markowitz, D. Meekins, R. Michaels, J. Mitchell, Z. Papandreou, C. F. Perdrisat, V. Punjabi, R. Roche, D. Rowntree, A. Saha, S. Strauch, L. Todor, G. Urciuoli, L. B. Weinstein, K. Wijesooriya, B. B. Wojtsekhowski, and R. Woo. Polarization transfer in the ^{2}H $(\vec{e}, e' \vec{p})n$ reaction up to $Q^2 = 1.61$ (GeV/c)^2. *Phys. Rev. C*, 73:064004, Jun 2006.

[20] G. MacLachlan, A. Aghalaryan, A. Ahmidouch, B.D. Anderson, R. Asaturyan, O. Baker, A.R. Baldwin, D. Barkhuff, H. Breuer, R. Carlini, E. Christy, S. Churchwell, L. Cole, E. Crouse, S. Danagoulian, D. Day, T. Eden, M. Elaasar, R. Ent, M. Farkhondeh, H. Fenker, J.M. Finn, L. Gan, K. Garrow, P. Gueye, C.R. Howell, B. Hu, M.K. Jones, J.J. Kelly, C. Keppel, M. Khandaker, W.-Y. Kim, S. Kowalski, A. Lai, A. Lung, D. Mack, R. Madey, D.M. Manley, P. Markowitz, J. Mitchell, H. Mkrtchyan, A.K. Opper, B. Plaster, C. Perdrisat, V. Punjabi, B. Raue, T. Reichelt, J. Reinhold, J. Roche, Y. Sato, N. Savvinov, A.Yu. Semenov, I.A. Semenova, W. Seo, N. Simicevic, G. Smith, S. Taylor, S. Stepanyan, V. Tadevosyan, S. Tajima, L. Tang, W. Tireman, P.E. Ulmer, W. Vulcan, J.W. Watson, S.P. Wells, F. Wesselmann, S. Wood, C. Yan, Chenyu Yan, S. Yang, L. Yuan, W.-M. Zhang, H. Zhu, and X. Zhu. The ratio of proton electromagnetic form factors via recoil polarimetry at q2=1.13 (gev/c)2. *Nuclear Physics A*, 764:261 – 273, 2006.

[21] M. K. Jones, A. Aghalaryan, A. Ahmidouch, R. Asaturyan, F. Bloch, W. Boeglin, P. Bosted, C. Carasco, R. Carlini, J. Cha, J. P. Chen, M. E. Christy, L. Cole, L. Coman, D. Crabb, S. Danagoulian, D. Day, J. Dunne, M. Elaasar, R. Ent, H. Fenker, E. Frlez, D. Gaskell, L. Gan, J. Gomez, B. Hu, J. Jourdan, C. Keith, C. E. Keppel, M. Khandaker, A. Klein, L. Kramer, Y. Liang, J. Lichtenstadt, R. Lindgren, D. Mack, P. McKee, D. McNulty, D. Meekins, H. Mkrtchyan, R. Nasseripour, I. Niculescu, K. Normand, B. Norum, D. Pocanic, Y. Prok, B. Raue, J. Reinhold, J. Roche, D. Rohe, O. A. Rondón, N. Savvinov, B. Sawatzky, M. Seely, I. Sick, K. Slifer, C. Smith, G. Smith, S. Stepanyan, L. Tang, S. Tajima, G. Testa, W. Vulcan, K. Wang, G. Warren, F. R. Wesselmann, S. Wood, C. Yan, L. Yuan, J. Yun, M. Zeier, and H. Zhu. Proton G_E/G_M from beam-target asymmetry. *Phys. Rev. C*, 74:035201, Sep 2006.

[22] M. E. Christy, A. Ahmidouch, C. S. Armstrong, J. Arrington, R. Asaturyan, S. Avery, O. K. Baker, D. H. Beck, H. P. Blok, C. W. Bochna, W. Boeglin,

P. Bosted, M. Bouwhuis, H. Breuer, D. S. Brown, A. Bruell, R. D. Carlini, N. S. Chant, A. Cochran, L. Cole, S. Danagoulian, D. B. Day, J. Dunne, D. Dutta, R. Ent, H. C. Fenker, B. Fox, L. Gan, H. Gao, K. Garrow, D. Gaskell, A. Gasparian, D. F. Geesaman, P. L. J. Guèye, M. Harvey, R. J. Holt, X. Jiang, C. E. Keppel, E. Kinney, Y. Liang, W. Lorenzon, A. Lung, P. Markowitz, J. W. Martin, K. McIlhany, D. McKee, D. Meekins, M. A. Miller, R. G. Milner, J. H. Mitchell, H. Mkrtchyan, B. A. Mueller, A. Nathan, G. Niculescu, I. Niculescu, T. G. O'Neill, V. Papavassiliou, S. F. Pate, R. B. Piercey, D. Potterveld, R. D. Ransome, J. Reinhold, E. Rollinde, P. Roos, A. J. Sarty, R. Sawafta, E. C. Schulte, E. Segbefia, C. Smith, S. Stepanyan, S. Strauch, V. Tadevosyan, L. Tang, R. Tieulent, A. Uzzle, W. F. Vulcan, S. A. Wood, F. Xiong, L. Yuan, M. Zeier, B. Zihlmann, and V. Ziskin. Measurements of electron-proton elastic cross sections for $0.4 < Q^2 < 5.5(gev/c)^2$. *Phys. Rev. C*, 70:015206, Jul 2004.

[23] I. A. Qattan, J. Arrington, R. E. Segel, X. Zheng, K. Aniol, O. K. Baker, R. Beams, E. J. Brash, J. Calarco, A. Camsonne, J.-P. Chen, M. E. Christy, D. Dutta, R. Ent, S. Frullani, D. Gaskell, O. Gayou, R. Gilman, C. Glashausser, K. Hafidi, J.-O. Hansen, D. W. Higinbotham, W. Hinton, R. J. Holt, G. M. Huber, H. Ibrahim, L. Jisonna, M. K. Jones, C. E. Keppel, E. Kinney, G. J. Kumbartzki, A. Lung, D. J. Margaziotis, K. McCormick, D. Meekins, R. Michaels, P. Monaghan, P. Moussiegt, L. Pentchev, C. Perdrisat, V. Punjabi, R. Ransome, J. Reinhold, B. Reitz, A. Saha, A. Sarty, E. C. Schulte, K. Slifer, P. Solvignon, V. Sulkosky, K. Wijesooriya, and B. Zeidman. Precision rosenbluth measurement of the proton elastic form factors. *Phys. Rev. Lett.*, 94:142301, Apr 2005.

[24] J. Arrington. How well do we know the electromagnetic form factors of the proton? *Phys. Rev. C*, 68:034325, Sep 2003.

[25] C.F. Perdrisat, V. Punjabi, and M. Vanderhaeghen. Nucleon electromagnetic form factors. *Progress in Particle and Nuclear Physics*, 59(2):694–764, Oct 2007.

[26] X. Zhan, K. Allada, D.S. Armstrong, J. Arrington, W. Bertozzi, W. Boeglin, J.-P. Chen, K. Chirapatpimol, S. Choi, E. Chudakov, and et al. High-precision measurement of the proton elastic form factor ratio $\mu_p g_e/g_m$ at low q^2. *Physics Letters B*, 705(1-2):59–64, Nov 2011.

[27] S. Stepanyan. Hps beamline manual. *JLab wiki documentation*, 2019.

[28] Dorothea Pfeiffer, Lennert De Keukeleere, Carlos Azevedo, Francesca Belloni, Stephen Biagi, Vladimir Grichine, Leendert Hayen, Andrei R. Hanu, Ivana Hřivnáčová, Vladimir Ivanchenko, and et al. Interfacing geant4, garfield++ and degrad for the simulation of gaseous detectors. *Nuclear Instruments and Methods in Physics Research Section A: Accelerators, Spectrometers, Detectors and Associated Equipment*, 935:121–134, Aug 2019.

[29] Nist Stopping Power. https://physics.nist.gov/physrefdata/star/text/estar.html.

[30] RD51 collaboration. Rd51 scalable readout system. *Cern documents server*, August 2010.

[31] M. E. Christy and P. E. Bosted. Empirical fit to precision inclusive electron-proton cross sections in the resonance region. *Physical Review C*, 81(5), May 2010.

[32] A V Gramolin, V S Fadin, A L Feldman, R E Gerasimov, D M Nikolenko, I A Rachek, and D K Toporkov. A new event generator for the elastic scattering of charged leptons on protons. *Journal of Physics G: Nuclear and Particle Physics*, 41(11):115001, Sep 2014.

[33] E. Rutherford. The scattering of α and β rays by matter and the structure of the atom. *Philosophical Magazine.*, 21, 1911.

[34] D. P. Roy. Basic constituents of the visible and invisible matter - a microscopic view of the universe, 2000.

[35] G. Aad, T. Abajyan, B. Abbott, J. Abdallah, S. Abdel Khalek, A.A. Abdelalim, O. Abdinov, R. Aben, B. Abi, M. Abolins, and et al. Observation of a new particle in the search for the standard model higgs boson with the atlas detector at the lhc. *Physics Letters B*, 716(1):1–29, Sep 2012.

[36] David Griffiths. *Introduction to elementary particles.* Weinheim, Germany: Wiley-VCH, 2008.

[37] Aldo Antognini, Franz Kottmann, François Biraben, Paul Indelicato, François Nez, and Randolf Pohl. Theory of the 2s–2p lamb shift and 2s hyperfine splitting in muonic hydrogen. *Annals of Physics*, 331:127–145, Apr 2013.

[38] Renat Kh. Gainutdinov. Proton radius, bound state qed and the nonlocality of the electromagnetic interaction, 2011.

[39] Carl E. Carlson. The proton radius puzzle. *Progress in Particle and Nuclear Physics*, 82:59–77, May 2015.

[40] Axel Beyer, Lothar Maisenbacher, Arthur Matveev, Randolf Pohl, Ksenia Khabarova, Alexey Grinin, Tobias Lamour, Dylan C. Yost, Theodor W. Hänsch, Nikolai Kolachevsky, and Thomas Udem. The rydberg constant and proton size from atomic hydrogen. *Science*, 358(6359):79–85, 2017.

[41] Hélène Fleurbaey, Sandrine Galtier, Simon Thomas, Marie Bonnaud, Lucile Julien, François Biraben, François Nez, Michel Abgrall, and Jocelyne Guéna. New measurement of the 1s - 3s transition frequency of hydrogen: Contribution to the proton charge radius puzzle. *Physical Review Letters*, 120(18), May 2018.

[42] G. G. Simon, F. Borkowski, Ch. Schmitt, and V. H. Walther. The structure of the nucleons. *Nucl. Phys. A*, 333.381, 1980.

[43] Xiaohui Zhan. High precision measurement of the proton elastic form factor ratio at low q^2. *Ph. D. Thesis*, 2010.

[44] Kees de Jager John Arrington and Charles F. Perdrisat. Nucleon form factors - a jefferson lab perspective. *J.Phys.Conf.Ser.*, 2011.

[45] M.K. Jones et al. Gep/gmp ratio by polarization transfer in $\vec{e}p \to e\vec{p}$. *Phys. Rev. Lett.*, 2000.

[46] Andrei Afanasev, Peter Blunden, Douglas Hasell, and B.A. Raue. Two-photon exchange in elastic electron-proton scattering. *Progress in Particle and Nuclear Physics*, 03 2017.

[47] Brian Henderson. Results from the olympus experiment on the contribution of hard two-photon exchange to elastic electron-proton scattering. *Proceedings of XVII International Conference on Hadron Spectroscopy and Structure — PoS(Hadron2017)*, Feb 2018.

[48] Jan C. Bernauer. Measurement of the elastic electron-proton cross section and separation of the electric and magnetic form factor in the q^2 range from 0.004 to 1 $(gev/c)^2$. *Ph. D. Thesis*, 2010.

[49] R. Shankar. *Principles of Quantum Mechanics*. Spinger, 1994.

[50] Mark Thomson. *Modern Particle Physics*. Cambridge University Press, 2013.

[51] Gary l. Catchen Javed Husain and Richard N. Zare. Scattering kinematics: Transformation of differential cross sections between two moving frames. *J. Chem. Phys.*, 69(4):1737–1741, 1978.

[52] Michael E. Peskin and Daniel V. Schroeder. *An Introduction to quantum field theory*. Addison-Wesley, Reading, USA, 1995.

[53] Herbert Goldstein et al. *Quarks and leptons: An introductory course in Modern particle physics*. Francis Halzen, Alan D. Martin, 1984.

[54] R. G. Sachs. High-energy behavior of nucleon electromagnetic form factors. *Phys. Rev.*, 126:2256–2260, Jun 1962.

[55] L. N. Hand, D. G. Miller, and Richard Wilson. Electric and magnetic form factors of the nucleon. *Rev. Mod. Phys.*, 35:335–349, Apr 1963.

[56] J. C. Bernauer, P. Achenbach, C. Ayerbe Gayoso, R. Böhm, D. Bosnar, L. Debenjak, M. O. Distler, L. Doria, A. Esser, H. Fonvieille, and et al. High-precision determination of the electric and magnetic form factors of the proton. *Physical Review Letters*, 105(24), Dec 2010.

[57] A.I. Akhiezer and Mikhail.P. Rekalo. Polarization effects in the scattering of leptons by hadrons. *Sov. J. Part. Nucl.*, 4:277, 1974.

[58] R.G. Arnold, Carl E. Carlson, and Franz Gross. Polarization Transfer in Elastic electron Scattering from Nucleons and Deuterons. *Phys. Rev. C*, 23:363, 1981.

[59] A. J. R. Puckett, E. J. Brash, M. K. Jones, W. Luo, M. Meziane, L. Pentchev, C. F. Perdrisat, V. Punjabi, F. R. Wesselmann, A. Afanasev, and et al. Polarization transfer observables in elastic electron-proton scattering at q2=2.5 , 5.2, 6.8, and 8.5 gev2. *Physical Review C*, 96(5), Nov 2017.

[60] A.S Raskin T.W Donnelly. Considerations of polarization in inclusive electron scattering from nuclei. *Annals of Physics*, 169:247–351, 1986.

[61] Dmitri Diakonov and V.Yu. Petrov. A Theory of Light Quarks in the Instanton Vacuum. *Nucl. Phys. B*, 272:457–489, 1986.

[62] M. J. Alguard, W. W. Ash, G. Baum, J. E. Clendenin, P. S. Cooper, D. H. Coward, R. D. Ehrlich, A. Etkin, V. W. Hughes, H. Kobayakawa, K. Kondo, M. S. Lubell, R. H. Miller, D. A. Palmer, W. Raith, N. Sasao, K. P. Schüler, D. J. Sherden, C. K. Sinclair, and P. A. Souder. Elastic scattering of polarized electrons by polarized protons. *Phys. Rev. Lett.*, 37:1258–1261, Nov 1976.

[63] D.H. Barkhuff et al. Measurement of recoil proton polarizations in the electrodisintegration of deuterium by polarized electrons. *Phys. Lett. B*, 470:39–44, 1999.

[64] C. B. Crawford, A. Sindile, T. Akdogan, R. Alarcon, W. Bertozzi, E. Booth, T. Botto, J. Calarco, B. Clasie, A. DeGrush, T. W. Donnelly, K. Dow, D. Dutta, M. Farkhondeh, R. Fatemi, O. Filoti, W. Franklin, H. Gao, E. Geis, S. Gilad, W. Haeberli, D. Hasell, W. Hersman, M. Holtrop, P. Karpius, M. Kohl, H. Kolster, T. Lee, A. Maschinot, J. Matthews, K. McIlhany, N. Meitanis, R. G. Milner, R. P. Redwine, J. Seely, A. Shinozaki, S. Širca, E. Six, T. Smith, B. Tonguc, C. Tschalaer, E. Tsentalovich, W. Turchinetz, J. F. J. van den Brand, J. van der Laan, F. Wang, T. Wise, Y. Xiao, W. Xu, C. Zhang, Z. Zhou, V. Ziskin, and T. Zwart. Measurement of the proton's electric to magnetic form factor ratio from $^1\vec{\mathrm{h}}\,(\vec{e}, e'p)$. *Phys. Rev. Lett.*, 98:052301, Jan 2007.

[65] G. Höhler, E. Pietarinen, I. Sabba-Stefanescu, F. Borkowski, G.G. Simon, V.H. Walther, and R.D. Wendling. Analysis of electromagnetic nucleon form factors. *Nuclear Physics B*, 114(3):505 – 534, 1976.

[66] F. Iachello, A.D. Jackson, and A. Lande. Semi-phenomenological fits to nucleon electromagnetic form factors. *Physics Letters B*, 43(3):191 – 196, 1973.

[67] M. Gari and W. Krümpelmann. Semiphenomenological synthesis of meson and quark dynamics and the e.m. structure of the nucleon. *Z. Phys. A Atoms and Nuclei volume*, 322:689–693, Dec. 1985.

[68] P. Mergell, Ulf-G. Meißner, and D. Drechsel. Dispersion-theoretical analysis of the nucleon electromagnetic form factors. *Nuclear Physics A*, 596(3-4):367–396, Jan 1996.

[69] P. L. Chung and F. Coester. Relativistic constituent-quark model of nucleon form factors. *Phys. Rev. D*, 44:229–241, Jul 1991.

[70] I.G. Aznauryan. On the q^2-dependence of the $n \to n\gamma$ and $\delta \to n\gamma$ transition form factors in a quark model at $q^2 < 4\text{GeV}^2$. *Physics Letters B*, 316(2):391 – 396, 1993.

[71] D. H. Lu, A. W. Thomas, and A. G. Williams. Electromagnetic form factors of the nucleon in an improved quark model. *Phys. Rev. C*, 57:2628–2637, May 1998.

[72] Xiangdong Ji. Off-forward parton distributions. *Journal of Physics G: Nuclear and Particle Physics*, 24(7):1181–1205, jul 1998.

[73] K. Goeke, M.V. Polyakov, and M. Vanderhaeghen. Hard exclusive reactions and the structure of hadrons. *Progress in Particle and Nuclear Physics*, 47(2):401–515, Jan 2001.

[74] M. Diehl. Generalized parton distributions. *Physics Reports*, 388(2):41 – 277, 2003.

[75] A.V. Belitsky and A.V. Radyushkin. Unraveling hadron structure with generalized parton distributions. *Physics Reports*, 418(1-6):1–387, Oct 2005.

[76] A. V. Belitsky, Xiangdong Ji, and Feng Yuan. Perturbative qcd analysis of the nucleon's pauli form factor $F_2(Q^2)$. *Phys. Rev. Lett.*, 91:092003, Aug 2003.

[77] Kenneth G. Wilson. Confinement of quarks. *Phys. Rev. D*, 10:2445–2459, Oct 1974.

[78] C. Alexandrou, G. Koutsou, J. W. Negele, and A. Tsapalis. Nucleon electromagnetic form factors from lattice qcd. *Phys. Rev. D*, 74:034508, Aug 2006.

[79] Claude Bernard, Tom Burch, Thomas A. DeGrand, Carleton DeTar, Steven Gottlieb, Urs M. Heller, James E. Hetrick, Kostas Orginos, Bob Sugar, and Doug Toussaint. Scaling tests of the improved kogut-susskind quark action. *Phys. Rev. D*, 61:111502, Apr 2000.

[80] J.J Sakurai. Theory of strong interactions. *Annals of Physics*, 11(1):1 – 48, 1960.

[81] R. Bijker and F. Iachello. Reanalysis of the nucleon spacelike and timelike electromagnetic form factors in a two-component model. *Phys. Rev. C*, 69:068201, Jun 2004.

[82] Fabio Cardarelli and Silvano Simula. Su(6) breaking effects in the nucleon elastic electromagnetic form factors. *Phys. Rev. C*, 62:065201, Nov 2000.

[83] E. Santopinto, A. Vassallo, M. M. Giannini, and M. De Sanctis. High Q^2 behavior of the electromagnetic form factors in the relativistic hypercentral constituent quark model. *Phys. Rev. C*, 82:065204, Dec 2010.

[84] A. J. R. Puckett, E. J. Brash, O. Gayou, M. K. Jones, L. Pentchev, C. F. Perdrisat, V. Punjabi, K. A. Aniol, T. Averett, F. Benmokhtar, and et al. Final analysis of proton form factor ratio data atq2=4.0, 4.8, and 5.6 gev2. *Physical Review C*, 85(4), Apr 2012.

[85] Dru B. Renner. Form factors from lattice qcd, 2012.

[86] William B. Jensen. The origin of bunsen burner. *J. Chem. Educ.*, 82(4):518, 2005.

[87] Mihaly Benedict. *Introduction to the physics of atoms, molecules and photons*. Lecture Notes, 2013.

[88] Niels Bohr. On the constitution of atoms and molecules. *Philosophical Magazine*, 1913.

[89] Michael I. et al Eides. Theory of light hydrogenlike atoms. *Phys.Rept.342:63-261,2001*, 2001.

[90] A. Antognini. The lamb shift experiment in muonic hydrogen. *Ph.D. Thesis*, 2005.

[91] J. D. Bjorken and S. D. Drell. *Relativistic quantum mechanics*. McGraw-Hill, Inc, 1964.

[92] J. R. Sapirstein and D. R. Yennie. *Theory of hydrogenic bound states*. Kinoshita, Int., 1990.

[93] Wills E. Lamb and Robert C. Retherford. Fine structure of the hydrogen atom by a microwave method. *Phyical Review*, 72.3, 1947.

[94] H. A. Bethe. The electromagnetic shift of energy levels. *Phyical Review*, 72.339, 1947.

[95] A. Beyer et al. The rydberg constant and proton size from atomic hydrogen. *Science*, 358:79–85, 2017.

[96] R. Pohl et al. 2S-2P splitting in muonic hydrogen, supplemental information for nature. *Nature*, 466:213–216, 2010.

[97] L. Ludhova et al. Muonic hydrogen cascade time and lifetime of the short-lived $2S$ state. *Phys. Rev. A*, 75.040501, 2018.

[98] D.I. Sober et al. The bremsstrahlung tagged photon beam in Hall B at JLab. *Nucl. Instrum. Meth. A*, 440:263–284, 2000.

[99] R D McKeown. The jefferson lab 12 GeV upgrade. *Journal of Physics: Conference Series*, 312(3):032014, sep 2011.

[100] R. D. McKeown. The jefferson lab 12 gev upgrade, 2010.

[101] Christian W. Fabjan and Fabiola Gianotti. Calorimetry for particle physics. *CERN documentation*, 2003.

[102] Fabio Sauli. The gas electron multiplier (gem): Operating principles and applications. *Nuclear Instruments and Methods: A*, 805:2–24, Jan 2016.

[103] Christian Lippmann. Detector physics of resistiveplate chambers. *Thesis*, 2003.

[104] R Alfaro. Construction and operation of a small multiwireproportional chamber. *J. Phys.: Conf. Ser.*, 18:011, 2005.

[105] J. Agarwala, M. Alexeev, C.D.R. Azevedo, F. Bradamante, A. Bressan, M. Büchele, M. Chiosso, C. Chatterjee, A. Cicuttin, P. Ciliberti, and et al. The mpgd-based photon detectors for the upgrade of compass rich-1 and beyond. *Nuclear Instruments and Methods in Physics Research Section A: Accelerators, Spectrometers, Detectors and Associated Equipment*, 936:416–419, Aug 2019.

[106] BOGDAN WOJTSEKHOWSKI. Nucleon form factors program with sbs at jlab. *International Journal of Modern Physics: Conference Series*, 35:1460427, Jan 2014.

[107] Kondo Gnanvo, Nilanga Liyanage, Vladimir Nelyubin, Kiadtisak Saenboonruang, Seth Sacher, and Bogdan Wojtsekhowski. Large size gem for super bigbite spectrometer (sbs) polarimeter for hall a 12 gev program at jlab. *Nuclear Instruments and Methods in Physics Research Section A: Accelerators, Spectrometers, Detectors and Associated Equipment*, 782:77–86, May 2015.

[108] Aiwu Zhang, Vallary Bhopatkar, Marcus Hohlmann, Xinzhan Bai, Kondo Gnanvo, Nilanga K. Liyanage, Matt Posik, and Bernd Surrow. R&d on gem detectors for forward tracking at a future electron-ion collider. *2015 IEEE Nuclear Science Symposium and Medical Imaging Conference (NSS/MIC)*, Oct 2015.

[109] L. Benussi, S. Bianco, G. Saviano, S. Muhammad, D. Piccolo, G. Raffone, M. Caponero, L. Passamonti, D. Pierluigi, A. Russo, F. Primavera, S. Cerbelli, A. Lalli, M. Valente, M. Ferrini, B. Teissandier, M. Taborelli, M. Parvis, S. Grassini, J. Tirilló, F. Sarasini, and A. V. Franchi. Characterization of the gem foil materials, 2015.

[110] A. Karadzhinova, A. Nolvi, R. Veenhof, E. Tuominen, E. Haggstromb, and I. Kassamakov. Impact of gem foil hole geometry on gem detector gain. *J. Inst.*, 18:011, 2015.

[111] Bo Cederwall. Experimental techniques for nuclear and particle physics gaseous detectors.

[112] Particle Data Group. Passage of particles through matter.

[113] Lawrence Jones. Apv25-s1 user guide version 2.2. *Cern document server*, September 2001.

[114] M. L. Purschke. Readout of gem stacks with the cern srs system. In *2012 18th IEEE-NPSS Real Time Conference*, pages 1–3, 2012.

[115] J Toledo et al. The front-end concentrator card for the rd51 scalable readout system. *Journal of Instrumentation*, 6:C11028, 2011.

[116] William Gu. Description and technical information for the pci-express trigger interface (tipcie) module. *Jefferson Lab DAQ group documentation*, 2016.

[117] CERN Atlas. SRS - Short User Guide. *CERN Document*, 2002.

[118] P. V. Hunagund and A. B. Kalpana. Crosstalk noise modeling for rc and rlc interconnects in deep submicron vlsi circuits, 2010.

[119] T Alexopoulos, G Iakovidis, S Leontsinis, K Ntekas, and V Polychronakos. Examining the geometric mean method for the extraction of spatial resolution. *Journal of Instrumentation*, 9(01):P01003–P01003, Jan 2014.

[120] R.K.Carnegie M.S.Dixit J.Dubeau D.Karlen J.-P. Martin H.Mes K.Sachs. Resolution studies of cosmic-ray tracks in a tpc with gem readout. *Nuclear Instruments and Methods in Physics Research Section A*, 538:372 – 383, Feb 2005.

[121] Mark A. Kramer. Nonlinear principal component analysis using auto associative neural networks. *AICHE Journal*, 37:233–234, 1991.

[122] Keiron O'Shea and Ryan Nash. An introduction to convolutional neural networks, 2015.

[123] I. Larin, D. McNulty, E. Clinton, P. Ambrozewicz, D. Lawrence, I. Nakagawa, Y. Prok, A. Teymurazyan, A. Ahmidouch, A. Asratyan, and et al. New measurement of the π^0 radiative decay width. *Physical Review Letters*, 106(16), Apr 2011.

[124] A. P. Freyberger. Large dynamic range beam profile measurements. *Proceedings of the 2003 Particle Accelerator Conference*, 4:2565–2567, 2003.

[125] A. Bonasera, R. Coniglione, and P. Sapienza. High-energy probes. *Eur. Phys. J. A*, 30:47–64, 2006.

[126] Y. S. TSAI L. W. MO. Radiative corrections to elastic and inelastic ep and μp scattering. *Reviews of Mordern Physics*, 41:205–235, 1969.

[127] Oleksandr Tomalak. Two-photon exchange correction in elastic lepton–proton scattering. *Few-Body Systems*, 59(5), May 2018.

[128] O. Tomalak and M. Vanderhaeghen. Two-photon exchange correction in elastic unpolarized electron-proton scattering at small momentum transfer. *Physical Review D*, 93(1), Jan 2016.

[129] O. Tomalak and M. Vanderhaeghen. Subtracted dispersion relation formalism for the two-photon exchange correction to elastic electron-proton scattering: Comparison with data. *The European Physical Journal A*, 51(2), Feb 2015.

[130] Scott K. Barcus, Douglas W. Higinbotham, and Randall E. McClellan. How analytic choices can affect the extraction of electromagnetic form factors from elastic electron scattering cross section data, 2019.

[131] J. Arrington. Implications of the discrepancy between proton form factor measurements. *Phys. Rev. C*, 69:022201, Feb 2004.

[132] Siddharth Venkat, John Arrington, Gerald A. Miller, and Xiaohui Zhan. Realistic transverse images of the proton charge and magnetization densities. *Phys. Rev. C*, 83:015203, Jan 2011.

[133] Zhihong Ye, John Arrington, Richard J. Hill, and Gabriel Lee. Proton and neutron electromagnetic form factors and uncertainties. *Physics Letters B*, 777:8–15, Feb 2018.

[134] Ingo Sick. On the rms-radius of the proton. *Physics Letters B*, 576(1-2):62–67, Dec 2003.

[135] J. C. Bernauer, M. O. Distler, J. Friedrich, Th. Walcher, P. Achenbach, C. Ayerbe Gayoso, R. Böhm, D. Bosnar, L. Debenjak, L. Doria, and et al. Electric and magnetic form factors of the proton. *Physical Review C*, 90(1), Jul 2014.

[136] E. Kraus, K. E. Mesick, A. White, R. Gilman, and S. Strauch. Polynomial fits and the proton radius puzzle. *Phys. Rev. C*, 90:045206, Oct 2014.

[137] Xuefei Yan, Douglas W. Higinbotham, Dipangkar Dutta, Haiyan Gao, Ashot Gasparian, Mahbub A. Khandaker, Nilanga Liyanage, Eugene Pasyuk, Chao Peng, and Weizhi Xiong. Robust extraction of the proton charge radius from electron-proton scattering data. *Phys. Rev. C*, 98:025204, Aug 2018.

[138] F. Borkowski, G.G. Simon, and V.H. et al. Walther. On the determination of the proton rms-radius from electron scattering data. *Z Physik A*, 275:29–31, March 1975.

[139] J. J. Kelly. Simple parametrization of nucleon form factors. *Phys. Rev. C*, 70:068202, Dec 2004.

[140] John Arrington and Ingo Sick. Precise determination of low-qnucleon electromagnetic form factors and their impact on parity-violatinge-pelastic scattering. *Physical Review C*, 76(3), Sep 2007.

[141] Siddharth Venkat, John Arrington, Gerald A. Miller, and Xiaohui Zhan. Realistic transverse images of the proton charge and magnetization densities. *Physical Review C*, 83(1), Jan 2011.

[142] J. M. Alarcón and C. Weiss. Nucleon form factors in dispersively improved chiral effective field theory. ii. electromagnetic form factors. *Physical Review C*, 97(5), May 2018.

[143] J. M. Alarcón and C. Weiss. Nucleon form factors in dispersively improved chiral effective field theory: Scalar form factor. *Phys. Rev. C*, 96:055206, Nov 2017.

[144] Jesse R. Stryker and Gerald A. Miller. Proton charge extensions. *Physical Review A*, 93(1), Jan 2016.

[145] J. D. Carroll, A. W. Thomas, J. Rafelski, and G. A. Miller. Proton form-factor dependence of the finite-size correction to the lamb shift in muonic hydrogen, 2011.

[146] Gabriel Lee, John R. Arrington, and Richard J. Hill. Extraction of the proton radius from electron-proton scattering data. *Physical Review D*, 92(1), Jul 2015.

[147] Demortier L. and Lyons L. Everything you always wanted to know about pulls. *CDF Note 5776*, April 2008.

[148] Weizhi Xiong. A high precision measurement of the proton charge radius at jlab, PhD Thesis, 2020.

[149] A. B. Arbuzov and T. V. Kopylova. On higher order radiative corrections to elastic electron–proton scattering. *The European Physical Journal C*, 75(12), Dec 2015.

[150] M. Mihovilovič, A.B. Weber, P. Achenbach, T. Beranek, J. Beričič, J.C. Bernauer, R. Böhm, D. Bosnar, M. Cardinali, L. Correa, and et al. First measurement of proton's charge form factor at very low q2 with initial state radiation. *Physics Letters B*, 771:194–198, Aug 2017.

[151] N. Bezginov, T. Valdez, M. Horbatsch, A. Marsman, A. C. Vutha, and E. A. Hessels. A measurement of the atomic hydrogen lamb shift and the proton charge radius. *Science*, 365(6457):1007–1012, 2019.

[152] Miha Mihovilovic, Patrick Achenbach, Tobias Beranek, Jure Bericic, Jan C. Bernauer, Ralph Bohm, Damir Bosnar, Matteo Cardinali, Loup Correa, Luka Debenjak, Achim Denig, Michael O. Distler, Anselm Esser, Maria I. Ferretti Bondy, Helene Fonvieille, Jan M. Friedrich, Ivica Friscic, Keith Griffioen, Matthias Hoek, Simon Kegel, Yvonne Kohl, Harald Merkel, Duncan G. Middleton, Ulrich Muller, Josef Pochodzalla, Bjorn S. Schlimme, Matthias Schoth, Florian Schulz, Concettina Sfienti, Simon Sirca, Samo Stajner, Michaela Thiel,

Alexey Tyukin, Marc Vanderhaeghen, and Adrian B. Weber. The proton charge radius extracted from the initial state radiation experiment at mami. *arXiv:1905.11182*, 2019.

[153] R. Gilman, E. J. Downie, G. Ron, A. Afanasev, J. Arrington, O. Ates, F. Benmokhtar, J. Bernauer, E. Brash, W. J. Briscoe, K. Deiters, J. Diefenbach, C. Djalali, B. Dongwi, L. El Fassi, S. Gilad, K. Gnanvo, R. Gothe, D. Higinbotham, R. Holt, Y. Ilieva, H. Jiang, M. Kohl, G. Kumbartzki, J. Lichtenstadt, A. Liyanage, N. Liyanage, M. Meziane, Z. E. Meziani, D. G. Middleton, P. Monaghan, K. E. Myers, C. Perdrisat, E. Piasetzsky, V. Punjabi, R. Ransome, D. Reggiani, P. Reimer, A. Richter, A. Sarty, E. Schulte, Y. Shamai, N. Sparveris, S. Strauch, V. Sulkosky, A. S. Tadepalli, M. Taragin, and L. Weinstein. Studying the proton "radius" puzzle with μp elastic scattering, 2013.